Wind turbine control
Advances for load mitigations and hydraulic drivetrains

Mulders, Sebastiaan

DOI
10.4233/uuid:521577f0-a361-4f92-94c5-02a3bc61ef44

Publication date
2020

Document Version
Final published version

WIND TURBINE CONTROL

Advances for load mitigations and hydraulic drivetrains

S.P. Mulders

WIND TURBINE CONTROL: ADVANCES FOR LOAD MITIGATIONS AND HYDRAULIC DRIVETRAINS

WIND TURBINE CONTROL: ADVANCES FOR LOAD MITIGATIONS AND HYDRAULIC DRIVETRAINS

Proefschrift

ter verkrijging van de graad van doctor
aan de Technische Universiteit Delft,
op gezag van de Rector Magnificus prof. dr. ir. T.H.J.J. van der Hagen,
voorzitter van het College voor Promoties,
in het openbaar te verdedigen op 31 maart 2020 om 15:00 uur

door

Sebastiaan Paul MULDERS

ingenieur in de systeem- en regeltechniek, Technische Universiteit Delft, Nederland,
geboren te IJmuiden, Nederland.

Dit proefschrift is goedgekeurd door de promotoren:

Prof. dr. ir. J.W. van Wingerden
Prof. dr. ir. M. Verhaegen

Samenstelling promotiecommissie:

Rector Magnificus	voorzitter
Prof. dr. ir. J.W. van Wingerden	Technische Universiteit Delft, promotor
Prof. dr. ir. M. Verhaegen	Technische Universiteit Delft, promotor

Onafhankelijke leden:

Prof. dr. ir. D.A. von Terzi	Technische Universiteit Delft
Prof. dr. ing. D. Schlipf	Hochschule Flensburg, Duitsland
Prof. A. Croce	Politecnico di Milano, Italië
Dr. ir. H. Polinder	Technische Universiteit Delft
Prof. dr. ir. J. Hellendoorn	Technische Universiteit Delft, reservelid

Overig lid:

Dr. ir. N.F.B. Diepeveen	Delft Offshore Turbine (DOT) B.V., Nederland

TU Delft Delft University of Technology

Rijksdienst voor Ondernemend Nederland

Keywords: wind turbine control, open-source controller, individual pitch control, model predictive control, hydraulic drivetrain

Printed by: Gildeprint

Front & Back: Floor Bollee

ISBN 978-94-6402-183-7

An electronic version of this dissertation is available at
`http://repository.tudelft.nl/`.

"Does this spark joy?" If it does, keep it. If not, dispose of it.

– Marie Kondo

ACKNOWLEDGEMENTS

"I am a wind turbine", I said, somewhere halfway my MSc graduation presentation, with my arms wide, imitating a wind turbine with two blades. My arms were turning to show how the pitch mechanism works. Up until this day, the quote, together with the stance, haunts me. And for good reason!

During and after my graduation I promised myself: no more university life, no more exam stress, no more thesis writing, no more LaTeX and MATLAB. On the 26th of November 2015 at 20:39, I received an e-mail from Jan-Willem, in which he wrote something like: "Dear Sebastiaan, everything okay? I have an open position on a very exciting Ph.D. project, interested? Jan-Willem". The e-mail felt random and surreal to me, as I totally did not expect it. And even though I made that promise to myself, I got curious, and as would turn out not much later, I stayed curious for the 4 years to come.

This section is of course only for a small part devoted to myself. During my PhD, I got support from a great variety of people. I will elaborately acknowledge and describe their contributions, knowing that I will inevitably miss out on some of them.

First, my supervisor Jan-Willem, thank you for your continuous support and dedication during the PhD project. You always gave me freedom to decide for myself on which things to work on, and I am very grateful that you gave me a huge sense of trust on how to manage my time. In the first year of my PhD, I really enjoyed to burn my hours with DOT, and to cooperate with them in commissioning and programming a real-world prototype wind turbine. This allowed me to develop myself from a practical point of view. I admire your endless enthusiasm, wide interest and optimism towards ideas of me and other students. When needed, you manage to combine these qualities with a certain degree of sternness. I take an example on your way of motivating people, and your approach of acknowledging everyone's efforts in everything.

My PhD started in cooperation with Delft Offshore Turbine. The learning curve at DOT was steep for a fresh master graduate, but especially in those first months, I learned and gained tremendous amounts of knowledge and skills. I want to thank all the people I cooperated with from DOT. Niels, you have been a great supervisor, and still a good friend. Your direct and (sometimes) rude way of communicating is a thing I really liked, especially during feedback sessions and the random chats. Your endless enthusiasm for DOT projects, and your commitment to employee and student work is a great thing that characterizes you. Furthermore, I had great times with Jacob, Gerrit, Robert (Pssssshhhh, really liked our Python course!), Han and Thijs, especially at the Maasvlakte when we were commissioning the DOT turbine. I learned a lot from all of you, and as a team effort, we made that turbine burn some energy! I also want to thank *de Keuken* (Jannie, Thomas, Wink, and all others) for the delicious meals and cakes!

In my last year, I got the opportunity to visit NREL (National Renewable Energy Laboratory) in Boulder, US. I am very thankful to Paul, Allan, Nikhar, Paula, Eric, Emmanuel, Misha, Dan, Senu (and all others!) for being so welcoming. I had a great times collab-

orating with you, but I also enjoyed the BBQing, hiking, seeing fireworks and playing ultimate frisbee.

I started my PhD in an office together with Tim. Due to my common absence during the first PhD year, my forgotten tomato went alive, got a name (Tommy the Sad Tomato), created an e-mail address (tommydetreurigetomaat@gmail.com), and started sending me e-mails:

> *Alsjeblieft. Ik verveel me. Ik weet dat je lekkere lunches hebt in de bieb maar ik ben zo klaar om opgegeten te worden!*
>
> *– Je tomaat.*

I got to know Tim better later on: a pragmatic guy, with a very open mindset, and a good sense of humor. Later Wouter joined the office. Although our research projects did not align, I learned a lot from both of you. I enjoyed being with you both in a single office, and I liked our nerdy discussions about obscure programming languages.

After 2 years, I moved to the office at the opposite side: the office of Reinier and Sjoerd. Reinier always has some interesting thoughts on subjects. I always enjoyed sharing the office with you, and liked you elaborate visions on manners. Your ideas on how to solve and approach problems has always been very helpful to me.

Sjoerd! Even though we didn't know each other that well when I joined the office, we became very good colleagues, and friends later on. You are passionate, and have a strong opinion and vision on how things should go in work and everyday life. We had (and still have) endless discussions on such manners, which I really enjoy. You helped me a lot by giving advice on how to deal with all kinds of situations. Thanks Sjoerd, I had a great time with you!

After Sjoerd and Reinier both left the office, Bart joined. In 2016, you started your PhD a couple of months after I began, and you will without a doubt graduate shortly after my defense. In the beginning, you intimidated me with your way too fast typing skills: producing those simulation results and papers like a non-stop machine! We stayed together in Cork, Boulder and Philadelphia for quite some time and I discovered that you know people everywhere. I like that we share a similar mindset on dedication to work, but at the same time taking things not too seriously. And not to forget the all-day eating sprees: Everything for the gains, keep on growing Bart!

The other KLASBAKKEN: Joeri, Daan, Maarten and Atin. Although you all focus on wind farm control, I enjoyed the collaborations we had. I had a great time with you during the PhD, and while we stayed together in Cork. Remember to keep the chimney smoking guys! Finally Yichao joined the wind group: an awesome and cheery guy, always in for a good laugh. Good luck to you all in the years to come!

Teaching and supervising students was also a fun part of the PhD. Thank you Stéphane, Atindriyo, Gianmarco, Jan, Rens, Rogier and Sebastiaan for your ideas, creativity and the hard work you put in your master theses. Thank you Sander and Raf for the fun conversations and the nice cooperation we had in teaching Signal Analysis. Also a big thanks to Michiel Zaayer for your great sense of humor, your cooperation in making the FASTTool to a big succes, and your endless energy and dedication to educate students with Wind Turbine Design knowledge. I really appreciate the collaboration we had and the personal engagement you showed when we met.

Just to mention a few quotes: "Doe je wel je best?", "Ik vind dit echt niet normaal!", "Snapt-ie niet, gaat-ie kijken!", "Ik kan je hier wel iets meer over vertellen...", "Hoe zie je dat? Moet je goed kijken!", "Het is me wat; allemaal wat!", "Is dit kip? Nee, dooie kip.", "... Maar er is niemand thuis, zou ze een auto-immuun ziekte hebben?" and many, many more! I learned to know Arno and Steven (Stevie) when I was 20 years old, in a bar in Delft. Our friendship grew, with trips to Stockholm (Sweden, Africa) to attend the Melodifestivalen, towards getting excited for the EuroVision song contest a few months later. I had more great trips with Stevie to Malága and Bilbao. Our occasional events, including *concept-eten*, is a thing I very much enjoy. You are awesome friends, with a great ability to empathize, and never holding back to speak up. I greatly appreciate the support and friendship you have shown me. Also a big thanks, kisses and love to Rob, Joost, Abbas, Jasper and Christof!

I remember that I met Erica when we went on bachelor's introduction camp. We cooperated in a contest to fit as many people in a way too small car. Half a year later, we became friends. We endured the Physics minor together, which was an non-trivial task. At the end, you started a petition to prove the minor's bad quality, and we went back to let them know our disgrace ("Gadverdamme, wat stinkt het hier!"). Now, studies are over, you are married to Paul and bought a huge house in Berkel en Rodenrijs. Respect Erica T.!

In the same period that I met Erica, I slowly got introduced to Jana and Erik. I did not like Jana at first (ik vond je stom), but nonetheless, we became friends quite rapidly. Your ability to concentrate and getting stuff done is unprecedented. I love your directness and your tendency to enjoy creating awkward situations. Like Jana, Erik does not like to speak in vague terms, but clear language. I like your way of persuading your own opinion as a matter of fact.

Koen, David and Mandy have been good friends since primary school. Koen has always been a super cheery guy: never a dull moment, and always something to talk about. You met Linda during studies at the tennis course. I think you are a great couple, and you recently bought a house in Utrecht. Although we do not see each other that often, I really enjoy our drinks in Rotterdam and Utrecht, and I am sure that we will keep on doing this in the years to come. David, I think it is great to see that you went to chase your dream: running your video production company with friends that share the same passion. You worked hard to make your vision happen. With your enthusiasm and skills of leadership, I am sure that your possibilities are endless. Mandy is a great friend and mother. A few years after you met Emiel, you announced the birth of Fenn, and not much later of his sister Lily. It is great to see that you both are such great parents. I also have much respect for Emiel: you are building your *The Practical Engineer* YouTube community, and I enjoy to see your dedication, enthusiasm and hard work.

Up until my 18th year, I lived with my parents (Paul and Karin) and sister (Britt) in Velserbroek: a town near Haarlem and IJmuiden. I am very grateful for all the support I got from you during all the stages. You care about me, listen to my stories, and ever so often we have nice and relaxed days/weekends together in Rotterdam or Velserbroek. I am proud of Britt that she recently found a nice home in IJmuiden, that she is doing great things as a nurse, and is going strong overall in life. I am also very proud of my mother, who has been through a difficult time. After a long trajectory, you now flourish

and are happier than ever before. Currently, you help mentally affected elderly people in a nursing home. I know for sure you give and treat the people with all the caring and love you always provided to us. My father is relaxed and has an endless patience. Besides personal conversations, I appreciate the fact that we can have more technical discussions. I very much like your ability for relativisation, and your special interest in the things that I tell. I love you all, and am very thankful for having such a supportive and understanding family.

Floor, I would like to thank you for your help designing this thesis cover, and your always caring and welcoming attitude. I had fantastic times with Louis at parties, and inspiring (Instagram) conversations with Peter. I would like to express my gratitude to the DCSC secretary: Marieke for your determination in getting things done, Heleen, Kiran and Erica for your helpfulness and welcoming attitude, and Kitty for all the support during my master and personal interest afterwards.

At the 5th of June 2016, I went on a coffee date with Coty, at Nine Bar near the station of Rotterdam Blaak. The date wasn't too awkward and we made a city trip. What followed were endless more dates. Through the years, the joy in our relationship has only grown. I love your vision of realism and the way you encourage me to constantly make the next step in life. You provide me with advice on how to deal with difficult decisions, and I adore the love you give to me. And although I not always show, you put a smile on my face. Therefore, Coty, my final big thank you goes to you.

Sebastiaan Paul Mulders
Rotterdam, January 2020

TABLE OF CONTENTS

SUMMARY

In the last decades, tremendous efforts have been put in advancements of wind turbine technology by scientific research and industrial developments. One of the focal areas has been the upscaling of turbines to increase power capacity. However, by enlarging turbine sizes, the square-cube law dictates rising costs per unit of power capacity. To break this trend of increased expenses, more advanced control techniques are key in facilitating load reductions and system level advances. The synthesis of novel controller designs, and advancements of existing strategies, are in this thesis effectuated by leveraging well-established control theory. This method resulted in analysis tools, that gave rise to practical applicable implementations, of which some are evaluated on real-world setups. The employed approach has thereby shown to stimulate further advancements of wind turbine technology.

Numerical software tools have become essential for the development and evaluation of technological advancements. The proper assessments of novel algorithms and innovations, relies on the availability of baseline simulation software, reference models, and controller code. While the former two mentioned ingredients are broadly available and accepted, a go to baseline controller is still lacking. For this reason, the first contribution to the thesis objective is to provide the wind community with a universal wind turbine controller. The developed controller provides adequate baseline performance, and is easy to use, well-documented, community-driven and widely applicable. In addition to the baseline controller that is written in a high-level programming language, a graphical MATLAB Simulink controller design environment has been developed. The design tool facilitates in the convenient and rapid development of control algorithms.

With the discussed software tools at hand, and by exploiting well-developed methods from classical control theory, control advances have been posed for solving practically prevailing design problems. As a result, a frequency domain-based analysis tool has been developed for individual pitch control (IPC) design. IPC is a well known technique for periodic blade load reductions, and exploits the turbine's ability of setting the blade pitch angles to distinct values. Proper implementation of IPC results in extended blade life spans, enabling more cost effective rotor designs. The scheme's contributions to the pitch control signals are often based on measured blade root bending moments, in a feedback control structure incorporating the multiblade coordinate (MBC) transformation. However, this feedback scheme is prone to the introduction of coupling in the considered multivariable system, leading to reduced or adverse performance consequences. By disregarding the coupling, the application of IPC can even lead to increased fatigue loads, opposing the scheme's intent and accelerating structural damage. To cope with the phenomenon of coupling, the effect of an additional controller design variable – called the azimuth offset – is analyzed in detail, and is shown to decouple the system

under consideration. The azimuth offset is a crucial design parameter for (higher harmonic) IPC implementations, especially when applied to larger rotors with more flexible blades. Improvements are recognized in terms of actuator duty cycle, and increased and more consistent load reduction performance.

The previously described IPC strategy is based on traditional controller designs. The proposed advances optimize the performance levels possible for such architectures. However, more advanced and predictive model-based control methods form an opportunity for further improvements, and provide ways to efficiently solve more complex trade-offs. Advanced algorithms can play an enabling role in the application of low-mass and cost effective *soft-soft* tower configurations. However, *soft-soft* towers are more flexible, and commonly have their fundamental fore-aft and side-side frequencies in the below-rated operational domain. Nevertheless, such towers are needed as upscaling conventional designs would lead to impractical mass levels and unacceptable costs. Limiting the excitation of critical resonances, by trading off power capture, is thus a critical controller design challenge. Towards solving this problem, a novel model predictive frequency skipping control framework has been proposed. The approach consists of a model demodulation operation, combined with an efficient quasi-linear parameter varying (qLPV) model predictive control (MPC) scheme. The technique reduces the effect of resonance excitation, by its ability to define an operational speed exclusion zone. To this end, the scheme makes an optimal trade-off between produced energy and fatigue loading according to user-defined weights.

Besides the methods for fatigue load mitigations, in the same framework, control strategies have been developed for a real-world wind turbine with a hydraulic drivetrain, based on the Delft Offshore Turbine (DOT) concept. DOT aims at the simplification of wind turbines and wind farms, by minimizing the number of drivetrain components, and by collectively harvesting the power of multiple turbines at a centralized location. The controller design – for a wind turbine with a fundamentally different drivetrain configuration – has been established based on the lessons learned by the development of the baseline wind turbine controller. In-field evaluations and measured data analysis show the effectiveness of the hydraulic control strategies, in terms of stability, simplicity, and the maximization of energy efficiency.

The combined contributions of this thesis stimulate advancements in wind turbine technology, and ultimately aim at lowering the cost of wind energy. The standardization of a baseline wind turbine control strategy, supports all disciplines to properly assess and accelerate their pace of innovations. The proposed control technological advancements are based on thorough analysis using well-established theories. The fatigue load mitigating strategies enable the more economical use of materials, resulting in turbines with higher specific powers. The approach stimulates the development and deployment of next-generation wind turbines. Additionally, the employed design philosophy has led to the successful synthesis of a control system for a wind turbine with a hydraulic drivetrain configuration.

SAMENVATTING

In de afgelopen decennia zijn technologische ontwikkelingen van windturbines het resultaat geweest van overweldigende inspanningen uit wetenschappelijk onderzoek en bijdragen uit de industrie. Turbines hebben zich in de afgelopen jaren in hoog tempo verbeterd door het bieden hogere nominale vermogens. Echter, bij het opschalen van de grootte, dicteert de *kwadratisch–derde-machtswet* verhoogde energiekosten. Om deze trend van toenemende kosten te doorbreken, spelen meer geavanceerde regeltechnische technieken een belangrijke rol. In deze thesis zijn nieuwe regeltechnische ontwerpen, en verdere verbeteringen van bestaande strategieëen ontwikkeld, door het uitbuiten van gevestigde regeltechnische theorieën. Deze ontwikkelmethode heeft geresulteerd in analytische hulpmiddelen, die aanleiding hebben gegeven tot praktisch toepasbare regeltechnische implementaties, waarvan een aantal beproefd is op werkelijke opstellingen. De aanpak heeft daarmee laten zien verdere technologische ontwikkelingen voor windturbines te bevorderen.

Numerieke programmatuur is onontbeerlijk geworden voor het implementeren en evalueren van technologische innovaties. Het adequaat beoordelen van de effectiviteit van nieuwe algoritmes of systematische verbeteringen, is afhankelijk van een set aan hulpmiddelen, bestaande uit: gestandaardiseerde simulatieprogrammatuur, referentie windturbine modellen, en basis regeltechnische code. Hoewel de twee eerstgenoemde aspecten wijdverspreid beschikbaar zijn, mist er een breed geaccepteerd en gestandaardiseerd windturbine aansturingsprogramma. Om deze reden is de eerste contributie aan het hoofddoel van deze thesis het publiekelijk beschikbaar stellen van een dergelijk universeel basisprogramma. Het ontwikkelde aansturingsprogramma biedt adequate prestaties, en is breed inzetbaar, eenvoudig te gebruiken, goed gedocumenteerd, en gemeenschapsgedreven. Naast het programma dat is ontwikkeld in een hogere programmeertaal, is er een grafische MATLAB Simulink ontwikkelomgeving gerealiseerd voor het snel en inzichtelijk ontwerpen van regeltechnische programmatuur.

Met de hierboven genoemde hulpmiddelen, en met behulp van gevestigde klassieke regeltechnische theorieën, zijn er regeltechnische verbeteringen uitgewerkt voor het oplossen van geldende praktische problemen. Een van de resultaten is een frequentiedomein gebaseerd analysehulpmiddel voor het ontwerpen van afzonderlijke bladhoek aansturing (ABA) implementaties. Afzonderlijke bladhoek aansturing (ABA) is een welbekende techniek voor het reduceren van periodieke bladbelastingen. De techniek buit de mogelijkheid van de turbine rotor uit om de bladen naar verscheidene hoeken te verstellen. Een correcte ABA-implementatie resulteert in een verlengde levensduur van turbine bladen, hetgeen meer kosteneffectieve rotorontwerpen mogelijk maakt. De contributies aan de bladhoeksignalen worden vaak gevormd door een terugkoppelingslus gebaseerd op de gemeten bladmomenten, waarbij de zogeheten meerdere-blad coör-

dinatentransformatie wordt gebruikt. Echter, de algemene manier van implementatie van deze regeltechnische structuur, is gevoelig voor de introductie van koppeling in het beschouwde meerdere-variabelen systeem, met nadelige gevolgen voor de beoogde belastingverminderingen. Het in de wind slaan van de koppeling, kan er zelfs toe leiden dat het toepassen van ABA verhoogde vermoeiingsbelastingen tot gevolg heeft, wat het doel van de implementatie bestrijdt en het ontstaan van permanente schade versnelt. Om met dit probleem om te gaan, is er een additionele afstellingsvariabele geïntroduceerd, die aangeduid wordt als de azimut afstand. Het effect van de afstandsvariabele is tot in detail bestudeerd, en kan gebruikt worden om het beschouwde systeem te ontkoppelen. De azimut afstand is een cruciale variabele voor hoger harmonische ABA-implementaties, in het bijzonder wanneer de techniek wordt toegepast op grotere rotors met flexibele bladen. Verbetering zijn evident op vlakken van actuator aansturingscycli, en verbeterde en meer consistente verminderingen van de vermoeiingsbelastingen.

De beschreven ABA-strategie is gebaseerd op traditionele methoden voor het ontwerp van regeltechnische implementaties. De voorgestelde verbeteringen resulteren in de optimale prestaties die mogelijk zijn voor dergelijke architecturen. Meer geavanceerde aansturingsalgoritmes bieden potentie voor verdere prestatieverbeteringen, en hebben de mogelijkheid om complexe prestatieafwegingen efficiënt op te lossen. Geavanceerde algoritmen kunnen de toepassing van lichtere en meer kosteneffectieve *zacht-zacht* torenconfiguraties mogelijk maken. Echter, deze torenconfiguratie is meer flexibel, en laat daardoor vaak een of meerdere toren-eigenfrequenties samenvallen met operationele omwentelingsfrequenties. Toch zijn dergelijke torens nodig, omdat het verder opschalen van conventionele torenontwerpen zou leiden tot onpraktische gewichtsniveaus en exorbitante kosten. Het limiteren van de excitatie van kritische resonanties, door vermogenswinsten af te wegen, is daarom een belangrijke regeltechnische uitdaging. Er is een oplossing middels geavanceerde regeltechniek ontwikkeld voor dit probleem, door een nieuwe methodiek voor het uitsluiten van omwentelingsfrequenties. De aanpak bestaat uit een model-demodulatie operatie, resulterend in een quasi-lineair paramater variërend (LPV) systeem. Het optimalisatieprobleem wordt opgelost door een efficiënte methodiek voor voorspellende regeltechniek. De techniek reduceert de excitatie van resonantie(s), door langdurige operatie op een bepaalde omwentelingssnelheid te vermijden. De techniek maakt een optimale afweging tussen belastingen en energieproductie, op basis van door de gebruiker gedefinieerde wegingsvariabelen.

Naast de besproken vermoeiingbelasting reducerende methodieken, zijn er – in hetzelfde raamwerk – aansturingsstrategieën ontwikkeld voor een werkelijk bestaande windturbine met hydraulische aandrijflijn, gebaseerd op het Delft Offshore Turbine (DOT) concept. De doelstelling van DOT is het vereenvoudigen van windturbines en windparken, door het aantal componenten in de aandrijflijn te minimaliseren. De hydraulisch-energetische bijdragen van meerdere turbines worden op een centraal punt gecombineerd en omgezet in elektrische energie. Het regeltechnische ontwerp – voor een windturbine met een fundamenteel afwijkende aandrijflijn – is tot stand gebracht op basis van de lessen die getrokken zijn uit de ontwikkeling van het basis aansturingsprogramma. Praktische testen op een werkelijk bestaand prototype, en verdere analyse van de testresultaten, laten de effectiviteit van de nieuwe hydraulische aansturingstechnieken zien, op vlakken van stabiliteit, eenvoud, en het maximaliseren van de energetische efficiënte.

De gecombineerde bijdragen in deze thesis stimuleren de verdere technologische ontwikkeling van windturbines, met als uiteindelijk doel om de kosten van windenergie te verlagen. Het ontwikkelde basis windturbine aansturingsprogramma, ondersteunt de gehele gemeenschap in het deugdelijk toetsen en versnellen van innovaties. De beschreven regeltechnische verbeteringen komen voort uit grondige analyses, die gebaseerd zijn op gevestigde regeltechnische theorieën. De vermoeiingbelasting reducerende methodieken maken het mogelijk om meer spaarzaam met materialen om te gaan, wat resulteert in turbines met een hoger specifiek vermogen. De aanpak faciliteert de ontwikkeling en uitrol van volgende generatie-windturbines. Bovendien heeft de aangewende ontwikkelstrategie geleid tot het ontwerp van een regeltechnisch systeem voor een windturbine met hydraulische aandrijflijn.

PROLOGUE

This thesis starts with a prologue giving a high-level elaboration on the consequences of climate change and global warming, and underlines the importance of transitioning from fossil towards renewable energy sources. Afterwards, an evolutionary historical overview of wind turbine concepts with conventional mechanical-electrical and hydraulic drive-trains is given. The intent of separating these subjects from the introduction, is to provide a more concise and compact thesis problem statement and thesis goal in the next chapter.

CONSEQUENCES OF CLIMATE CHANGE

For at least 1 million years, the Earth has been oscillating in a temperature limit cycle. The trajectories in Figure 1 show that warmer interglacial states are alternated with cooler glacial periods (Rockström, 2018). The Earth has endured several journeys through this complete cycle, with time periods between 80,000 and 120,000 years (Philander, 2008), and is now in the midst of the interglacial period. The inner trajectory – called the Holocene – is the only proven state capable of supporting the needs for our modern world. However, the current approach of meeting humanity's energy needs by the usage of fossil fuels, has started to push Earth towards the outer boundaries of the interglacial state. While mechanisms are naturally present to counteract temperature increases, these buffers begin to saturate, leading to what is commonly known as global warming.

Therefore, after the Holocene epoch, the Anthropocene is the proposed present-day era. The Anthropocene commences from the time when humans and their industries started to significantly impact the Earth's geology and ecosystems (Borenstein, 2014). The start date of the Anthropocene has not yet been established, however, the moment of nuclear fallout from the Trinity weapons testing in 1945 seems to be in favor (Waters et al., 2016).

Research suggests that when fundamental human intervention stays out, the Earth could be pushed over a threshold, preventing stabilization at an intermediate and stable

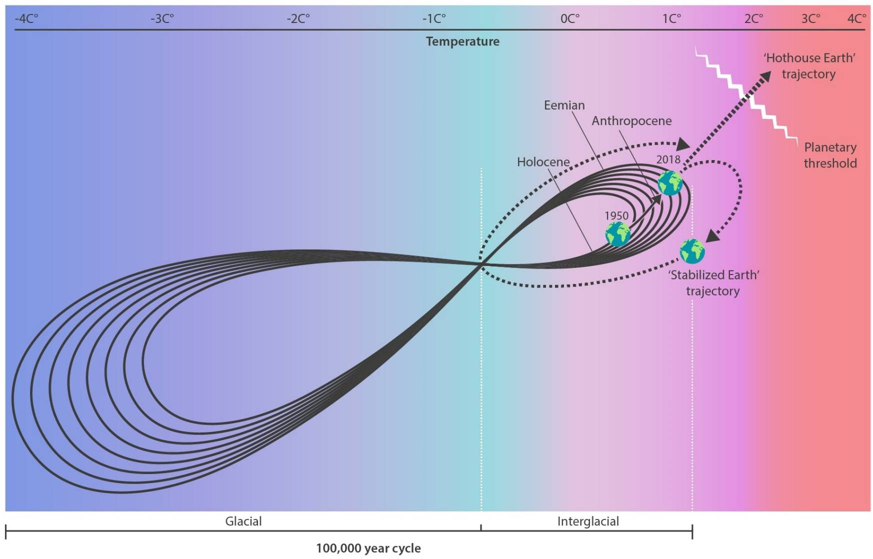

Figure 1: The Earth periodically alternates between colder glacial and warmer interglacial states (Rockström, 2018). In the visualized limit cycles, the inner Holocene path is the most stable trajectory. However, since the 1950s, humanity is actively interfering with Earth's natural stable states. A new era implying the human influences on the Earth geology and ecosystems is called the Anthropocene. Persistently challenging the Earth resilience, could lead to destabilization towards a *Hothouse Earth* trajectory, with severe consequences.

temperature trajectory (Steffen et al., 2018). Figure 1 illustrates that continued greenhouse gas emissions could cause climate change to follow a *Hothouse Earth* pathway, even when emissions are reduced. This Hothouse scenario would lead to an even higher global average temperature, resulting in reduced agricultural production, exceeded adaption limits, increased prices, and an even bigger inequality between poor and rich parts of the world (Pachauri and Meyer, 2014). Interventions in terms of technological innovation, behavior, and governance are needed to impede the discussed scenario (Rockström et al., 2017; Geels et al., 2017; O'Brien, 2018). An exact quantification of the temperature threshold is yet unknown: Staying below the temperature increase limit dictated by the Paris Agreement, does not guarantee to prevent the irreversible *Hothouse Earth*-pathway.

TRANSITIONING TOWARDS RENEWABLE ENERGY SOURCES

The Paris Agreement is an agreement within the United Nations Framework Convention on Climate Change (UNFCCC) with 197 signatories as of October 2019. The members agreed upon restraining the global average temperature increase well below 2 degrees Celsius as compared to pre-industrial levels, with the ultimate goal to limit the increase to 1.5 degrees Celsius. The latter number significantly reduces the risks and consequences of global warming.

With the Paris Agreement in mind, the Dutch government came up with ambitious national climate goals, established in the so called *Klimaatakkoord* (Rijksoverheid, 2019a). The Netherlands envisions a greenhouse gas reduction of 49 % by 2030 as compared to emissions in the year 1990, and a reduction of 95 % by 2050. Simultaneously, the Dutch government aims for a 55 % reduction in 2030 for the entire European Union.

The higher European number shows that the Dutch transition towards renewable

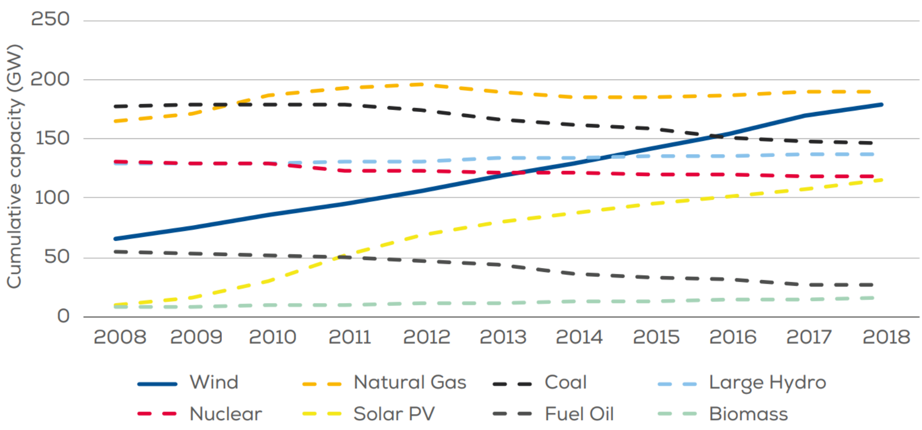

Figure 2: Installed European capacity of conventional and renewable electrical energy sources in the last decade. Solar photovoltaic (PV) and wind energy systems show a strong increase in cumulative capacity (WindEurope, 2019).

energy sources has to get up steam. The Netherlands aims at a renewable penetration of 14 % and 27 % by 2020 and 2030, respectively, and a near full transition to clean sources in 2050 (Rijksoverheid, 2018). To reach these goals, power generation through offshore wind turbines is considered as one of the most important contributors. Recent figures show an offshore installed capacity of 1 GW in 2019, which is extended to 11 GW by 2030, accounting for 40 % of the current Dutch electricity consumption.

THE CASE FOR MORE WIND ENERGY

In the European Union, and as shown in Figure 2, solar photovoltaic (PV) and wind energy see a strong increase in installed cumulative capacity (WindEurope, 2019). It is expected that wind overtakes natural gas in 2019, to become the largest form of power generation capacity.

For wind to be competitive with traditional sources of energy, the lifetime costs divided by the total revenue (price per unit of energy), needs to be minimized (Manwell et al., 2010). This indicator is often referred to as the levelized cost of energy (LCOE), and includes the total costs of deployment, operation and maintenance of an energy system over the expected life time (Department of Energy (DOE), 2015). The LCOE allows for comparison of different fossil and renewable energy sources with dissimilar life spans.

Scientists and industry put great efforts in improving the reliability, efficiency, and power capacities of wind turbines to facilitate the sustained growth of wind energy. The strategy aims at minimizing the levelized cost of electrical energy, and has proven to be fruitful: The construction of the first subsidy free wind farm in the North Sea will be finalized in 2022 (Rijksoverheid, 2019b).

DEVELOPMENTS IN WIND TURBINE TECHNOLOGY

The technologically advanced wind turbines of present day, are a result of the long-term development of wind systems, converting captured wind energy into rotational energy. A few centuries ago, traditional wind mills were typically used to mill grain and/or to pump water (Gregory, 2005). Figure 3 shows the oldest and still operating mills, that were built back in 1628 in the UK. Innovations and the incrementally acquired knowledge on rotor aerodynamics, led to the far more advanced and efficient turbines of present day (Jamieson and Hassan, 2011).

In the last couple of decades, the amount and variety of (proposed) wind turbine concepts is overwhelming. Therefore, and in line with the designs covered in this thesis, this section presents the evolutionary history of only two turbine concepts. The first section gives a brief history on wind turbines with a mechanical-electrical drivetrain, also highlighting some more exotic concepts. Then, the subsequent section considers wind turbines with a different drivetrain approach, substituting the mechanical-electrical with a hydraulic configuration.

TURBINES WITH CONVENTIONAL MECHANICAL-ELECTRICAL DRIVETRAINS

This section addresses the developments of mechanical-electrical wind turbines that have been remarkable and influential. Only horizontal-axis turbines with a conventional drivetrain are considered, i.e., wind turbines of which the rotor axis is mechanically cou-

Figure 3: The Jack and Jill (Clayton) windmills in Sussex, England (Blaikie, 2007).

pled to the electric generator, optionally through a gearbox.

The first successful turbine: Probably the most notable and early-day electricity generating turbine, was the 1.25 MW Smith-Putnam wind turbine, shown in Figure 4a. The turbine was developed and built in 1942 in Vermont, United States (Putnam, 1947). The two-bladed turbine with a rotor diameter of 53 m, was the pioneering turbine supplying power to the electrical grid. After subsequent failures of the main bearing and rotor blades, caused by structural weaknesses and the steel shortage during wartime, the turbine was dismantled in 1945.

After the Smith-Putnam and other two-bladed turbines, the three-bladed turbine began its uptake. Three-bladed rotors attain a slightly higher efficiency, emit less noise by the reduced optimal tip-speed ratio, possess a more favorable dynamic behavior, and have a more symmetric appearance while rotating (Hau, 2013).

Direct drive turbines: A drivetrain concept obviating the need for a gearbox, is the direct drive configuration. While the presence of a gearbox does not necessarily decrease production costs or increase reliability (Hau, 2013; Polinder et al., 2013), it eliminates a potentially bothersome component from the drivetrain. Enercon is a wind turbine manufacturer specializing in direct drive wind turbines. Figure 4b shows their landmark E-126 turbine: a 7.58 MW direct drive wind turbine, with a 135 m hub height, a 12 m generator diameter, and a rotor diameter corresponding to the model number. The generator technology of Enercon involves a wound rotor configuration, where the windings are magnetized by external excitation (Jamieson and Hassan, 2011). In general, this configuration is heavier than the – nowadays more prevalent – permanent magnet generator

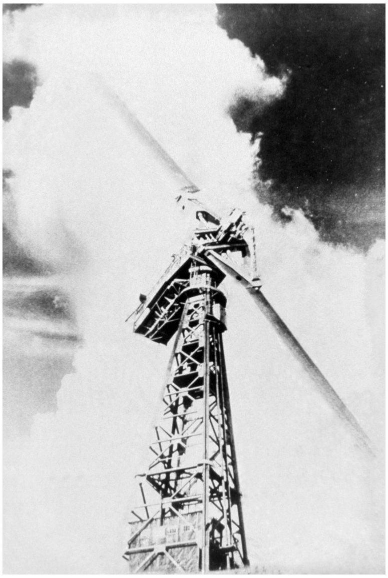

(a) Smith-Putnam turbine (Putnam, 1947)

(b) Enercon E-112 nacelle (van Kuik et al., 2008)

(c) Vestas multi rotor (van der Laan et al., 2019)

(d) GE Haliade-X (General Electric Renewable Energy, 2019)

Figure 4: Various wind turbine concepts and configurations. (a) The first grid-connected system is the two-bladed Smith-Putnam wind turbine with a power rating of 1.25 MW. (b) Direct drive wind turbines eliminate the need for a gearbox, simplifying the drivetrain. (c) For future wind turbines, the multi rotor concept might pose opportunities for scalability and component standardization. (d) The largest wind turbine with a power rating of 12 MW for offshore deployment, is currently being prototype tested in the Netherlands.

(PMG). PMGs are currently embraced for reasons of increased partial load efficiency, and their potential for upscaling direct drive turbines.

Multi rotor turbines: Another approach for increasing the size and power rating of wind turbines, is by applying multiple rotors on a single support structure. The multi rotor concept originates from the historic lack of modern materials, inhibiting the possibilities for upscaling. To date, the potential advantages for scalability and component standardization, are still seen as interesting opportunities (Jamieson and Hassan, 2011). Structural load considerations by imbalances, can be coped with using control of the individual rotors, while naturally, the torque imbalance on the support structure is alleviated by operating the rotors in counter-rotating directions. Furthermore, aerodynamic interactions between rotors do not seem to have adverse effects on the power production efficiency (Smulders et al., 1984).

In April 2016, Vestas built a multi rotor demonstrator turbine consisting of four 225 kW rotors, as shown in Figure 4c. The purpose of the turbine is to explore the potential of cost reductions by the advantage of scaling (Vestas, 2016). The multi rotor concept does not yet see a widespread adoption, however, it could form a solution for capacities that are beyond realizable with single rotor turbines. Moreover, the concept could facilitate denser spacing in a wind farm through faster wake recovery characteristics (van der Laan et al., 2019).

The largest wind turbine: At the time of writing, a prototype of the largest turbine in terms of size and power capacity, is being deployed at Maasvlakte II, the Netherlands. Figure 4d shows the General Electric (GE) Haliade-X with a power rating of 12 MW, a rotor diameter of 220 m (General Electric Renewable Energy, 2019), and a direct drive PMG drivetrain setup.

Controller technologies aiming at wind turbine (fatigue) load reductions, prominently facilitate the upscaling of wind turbines. As will become clear later, this thesis contributes in the development and the maturing of such control algorithms.

TURBINES WITH HYDRAULIC DRIVETRAINS

The operational costs for conventional turbines suffer from the maintenance needs of powertrain components. An 11 year lasting reliability study over a large number wind turbines in Denmark and Germany (Tavner et al., 2007; Sheng, 2013), shows that the rotor, power converter, generator, and gearbox have the highest failure rates. While the number of gearbox and generator failures do not stand out from the rest of the subassemblies, the resulting downtime on occurrence is substantially higher (Spinato et al., 2009). It is also noted in the same work that gearbox are a matured technology, and it is unlikely that groundbreaking innovations will lead to a substantially improved reliability. Furthermore, components part of the drivetrain and rotor assembly are the most expensive to repair (Sheng, 2013).

For the above-stated reasons, besides conventional wind turbines with a mechanical-electrical configuration, a variety of turbines with a hydraulic drivetrain have been proposed. Hydraulic turbines form an opportunity in reducing the maintenance requirements for wind turbines. Hydraulics are known for their high torque and inertia to

(a) Bendix SWT-3 (Rybak, 1981; Hau, 2013)

(b) Mitsubishi Heavy Industries SeaAngel (*SeaAngel 7 MW*)

Figure 5: The oldest and most recent hydraulic wind turbines. *(a)* The Bendix SWT-3 turbine, employed with a 3 MW drivetrain, however, was decommissioned shortly after it became operational. *(b)* The nacelle of the 7 MW MHI SeaAngel turbine, with the high-efficiency digital displacement pump developed by Artemis.

weight ratio (Merritt, 1967), and have the potential to significantly reduce the nacelle mass. In the 80s, it was already acknowledged that the application of positive displacement pumps reduces the number of maintenance critical components in the nacelle, by removing the gearbox and relocating the generator (Salter and Rea, 1984). Other notable benefits of hydraulic components are the robustness and compactness. The advantages are the reason for their wide application in auxiliary systems, such as the pitch and yaw mechanisms (Burton et al., 2001).

This section summarizes the hydraulic turbine developments and concepts that have been considered in the past: The most remarkable models, test setups, and turbines are discussed. The final paragraph describes the Delft Offshore Turbine hydraulic concept, which is part of this thesis.

Bendix SWT-3: The first 3 MW wind turbine with a hydrostatic power transmission was the SWT-3, developed and built from 1976 to 1980 by Bendix (Rybak, 1981), and shown in Figure 5a. The configuration with 14 fixed-displacement oil pumps in the nacelle, and 18 variable-displacement motors at the tower base, proved to be overly complex, unreliable and inefficient. Because of the losses, a maximum generated power output of only 1.1 MW was attained (Nelson, 2013). The turbine was disassembled shortly after it became operational.

ChapDrive: In 2004, the ChapDrive hydraulic drivetrain, of which the working principle illustrated in Figure 6a, was developed with the aim of driving a synchronous generator. The low-speed shaft is connected to a fixed-displacement oil pump, which directs pressurized fluid flow to a variable-displacement oil motor (Chapple et al., 2011; Thom-

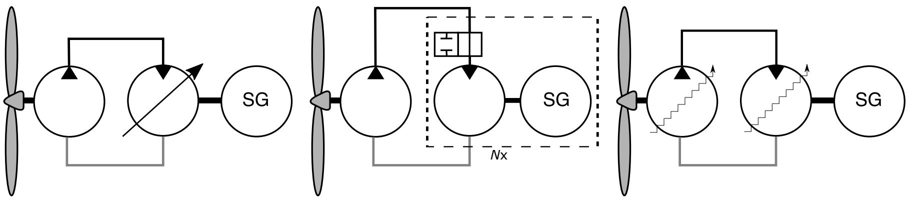

(a) Continuous variable displacement configuration

(b) Switching the number of fixed-displacement components

(c) Discrete displacement ratio through cilinder control

Figure 6: Hydraulic diagrams of the most prominent wind turbines with hydraulic drivetrains. All configurations are similar: a pump is connected to the rotor shaft, which hydraulically drives a motor mechanically coupled to a synchronous generator. Main differences are found in the application of fixed or variable displacement components, and the use of single or multiple parts to optimize the drivetrain efficiency for variable-speed operation.

sen et al., 2012). The angular speed of the output shaft is regulated for the application of a synchronous generator. Although the company acquired funding from Statoil for a 5 MW concept, the company ceased operations.

Hägglunds / Statoil: In cooperation with Hägglunds, Statoil modeled a drivetrain with hydrostatic transmission. The set-up, of which the working principles are illustrated in Figure 6b, consists of a single fixed-displacement oil pump connected to the rotor and six fixed-displacement motors at ground level (Skaare et al., 2011; Skaare et al., 2013). Half the motors can be enabled or disabled to obtain a discrete transmission ratio to drive either one or two synchronous generators. The reason for this configuration is that hydraulic components generally have a narrow region of high efficiency, and the ability of switching ensures operation in a more favorable regime. The discrete drivetrain configuration somewhat affects the aerodynamic efficiency, however, increases the overall power generating efficiency.

Artemis / Mitsubishi Heavy Industries: In 2005, Artemis Ltd. developed a digital displacement pump, meaning that the volume displacement can be adjusted in a digital way by enabling and disabling individual cylinders (Figure 6c) (Rampen, 2006; Artemis Intelligent Power, 2018). The product was originally intended for application in the automotive industry, however, in 2010, Mitsubishi acquired Artemis Intelligent Power. In contrast to variable displacement components operated by swash plates, the feature of controlling individual cylinders has a positive impact on the partial load efficiency. In 2012, Mitsubishi successfully installed a 2.4 MW turbine employing Artemis' technology (Umaya et al., 2013). Figure 5b shows a 7 MW demonstrator with the hydraulic power drive technology, called the SeaAngel, and was deployed by Mitsubishi Heavy Industries (MHI) in 2013 (Sasaki et al., 2014).

Institute for Fluid Power Drives and Systems: The Institute for Fluid Power Drives and Systems (IFAS) situated in Aachen, Germany, focuses on the development of new cost-

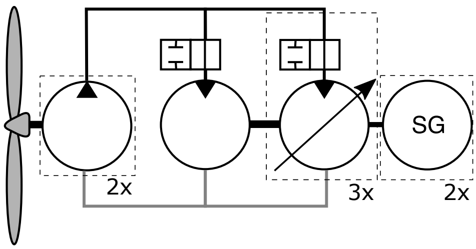

(a) Hydraulic diagram

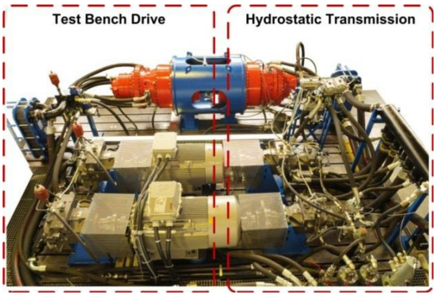

(b) Photograph

Figure 7: The megawatt-scale IFAS test bench, for the system-level and controller development of an efficient hydrostatic wind turbine drivetrain. The set-up consists of a single fixed-displacement oil pump in conjunction with oil motors: a single fixed-displacement motor and three smaller variable-displacement units. Altering the drivetrain configuration according to the operating conditions improves the efficiency in the partial load region (Vukovic and Murrenhoff, 2015).

effective hydraulic architectures, and holistic design methodologies. The IFAS group recognizes the often inefficient configurations of hydraulic systems, and attributes this to two main factors (Vukovic and Murrenhoff, 2015). The first cause is related to economic reasons of efficient systems being more expensive. The second reason is poor system designs where efficient components are forced to operate in unfavorable efficiency regions. To this end, as shown in Figure 7, a 1 MW hydraulic test bench for the development of a hydrostatic wind turbine drivetrain has been developed (Schmitz et al., 2012). Tests with this set-up have proven efficiency enhancements, by switching between pumps and motors depending on the current operating point. Moreover, experiments have shown the feasibility of torque control strategies, and reduction of drivetrain peak loads as a result of hydraulic dampening effects.

Delft Offshore Turbine: The above described concepts aim to eliminate power electronics from the turbine for the use of a synchronous generator, and therefore use a mechanism to vary the hydraulic gear ratio. However, to date, none of the full hydraulic concepts have made their way to a commercial product. All concepts use oil as the hydraulic medium because of the favorable fluid properties and component availability, but therefore also need to operate in a closed circuit. Closed-circuit operation for an offshore wind application using oil is required to minimize the risk of environmental pollution, but also to abandon the need for a continuous fresh oil supply to the circuit. Furthermore, often an additional cooling circuit is needed when losses in hydraulic components are significant and natural heat convection to the surroundings is insufficient.

A novel and patented hydraulic concept with an open-circuit drivetrain using seawater as the hydraulic medium is the Delft Offshore Turbine (DOT) (van der Tempel, 2009), as shown in Figure 8. The open circuit is enabled by the use of preconditioned seawater and alleviates the need for a cooling circuit by the continuous fresh supply. The DOT concept only requires a single seawater pump directly connected to the turbine rotor. The pump replaces components with high maintenance requirements in the nacelle,

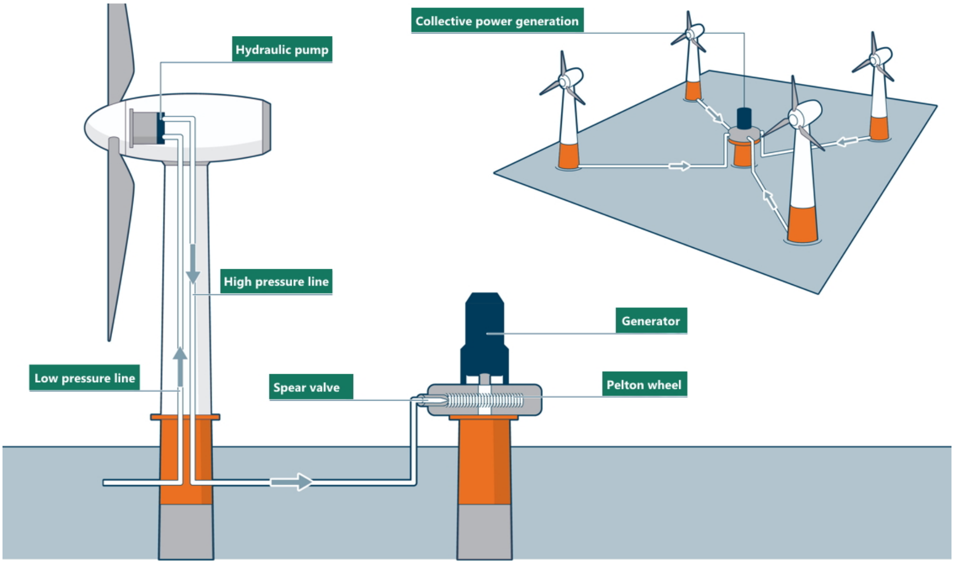

Figure 8: Schematic overview of an ideal DOT hydraulic wind turbine configuration. A radial piston seawater pump is coupled to the rotor in the nacelle. The flow is converted to a high-velocity water jet by a spear valve, and a Pelton turbine-generator configuration harvests the hydraulic into electric energy. Multiple turbines can be connected to the central power generation platform.

which reduces the weight, support structure requirements, and turbine maintenance frequency. All maintenance-critical components are located at sea level, and the centralized generator is coupled to a Pelton turbine. Turbines collectively drive the Pelton turbine to harvest the hydraulic into electrical energy. A feasibility study and modeling of a hydraulic wind turbine based on the DOT concept is performed in (Diepeveen, 2013). This thesis considers the modeling, controller design, and in-field prototype tests of a wind turbine with a retrofitted 500 kW hydraulic drivetrain, based on the DOT concept.

1

Introduction

The introduction of this dissertation consists of two sections. The first section elaborates on major challenges in wind turbine control. Then, in the second section, the overall thesis goal is exposed, and is divided in subgoals. The approach in satisfying these goals is explained, and finally the outline presents a concise summary of the contents of each chapter.

Chapter contents

1.1. CHALLENGES IN WIND TURBINE CONTROL

Scaling the power of a wind turbine, while taking into account the mass increase as a function of rotor size, is described by the *square-cube law* (Burton et al., 2001). The *square* part indicates the relation between captured wind power and rotor diameter, and the *cube* part implies the relationship to mass. The law dictates that the expected turbine expenses per unit capacity rise linearly with its size, and consequently, the costs for multi-megawatt turbines are believed to rise (Jamieson and Hassan, 2011). Of course, the rule is too elementary to draw such conclusions, as it only valid when considering similar technologies. The amount of mass, and thus capital costs is dictated by the component design, which is in turn largely driven by the loads it must withstand.

As a result of the above stated, the importance of fatigue load reductions is becoming ever more prominent. For wind turbines with increased sizes and power ratings, taking the fatigue loads into consideration can be highly design driving towards effectuating net cost reductions. For taller turbines with larger rotors, the minimization of periodic blade

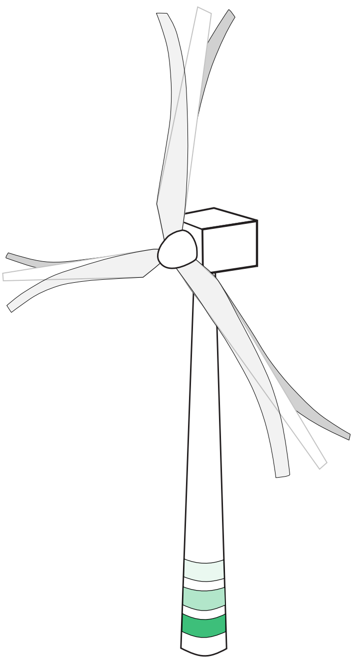

(a) Blade out-of-plane motion

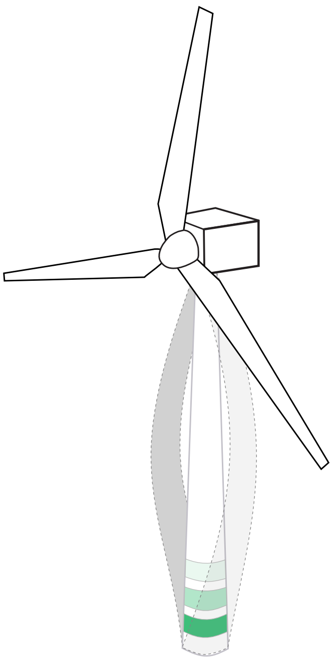

(b) Tower side-side oscillation

Figure 1.1: Wind turbine schematics indicating the types of vibrations targeted in this thesis. *(a)* Out-of-plane blade oscillations as a result of, amongst other things, the combined effects of wind shear, tower shadow, turbulence, and yaw misalignment. The blade moment is for each blade measured at the blade root, and fed to the IPC implementation, forming independent pitch contributions for load mitigations. *(b)* The tower side-side oscillations are lightly damped, in contrast to the fore-aft motion that has the benefits of aerodynamic damping. Active and passive control strategies exist for damping the side-side oscillations, by contributions to the generator torque signal. The schematics are adapted from (Burton et al., 2001).

and tower fatigue loads are of most concern (Dykes et al., 2018). Figure 1.1 shows the blade out-of-plane and structural side-side oscillations considered in this thesis. These vibrations contribute to accelerated and accumulative fatigue damage when left unconsidered during the (controller) design phase, and lead to early failure of structural parts. Control algorithms have already proven their contributing importance to fatigue load reductions (Menezes et al., 2018). Further control enhancements are very likely to facilitate the continued technological advancements of wind turbines.

Another approach of advancing state-of-the-art turbine technology, is by radically changing its energy harvesting mechanism. Turbines with a hydraulic drivetrain are an example of such a drastic design change. As concluded from the concepts discussed in the Prologue, optimizing the partial load efficiency is of major concern to make such turbines economically viable. Again, control algorithms play a key role in effectuating the optimal operational strategy.

This section illustrates several challenges in wind turbine control. First, the lack of a de facto standard baseline controller for the assessment of novel algorithms is discussed. Then, the status quo of control techniques for blade and tower fatigue load mitigations are described. Finally, state-of-the-art control methods for hydraulic wind turbine concepts are outlined. All sections discuss the currently available control strategies, informally explain their working principles, and give an overview of the relevant literature. The challenge tackled in this thesis is formulated at the end of each section.

1.1.1. ALIGNING THE BASELINE CONTROL ARCHITECTURE

A major challenge in wind turbine research is to align simulation software, reference models and baseline control strategies. Standardization of these components would have a major benefit in the reproducibility and evaluation of the actual benefits of proposed innovations. In the past decades, substantial effort has been put in the development of code for simulating wind turbines (National Renewable Energy Loboratory (NREL), 2019; DTU wind energy, 2019; DNV GL, 2019). Some of the referenced software packages are closed-source distributions, requiring a commercial license; others are open-source and publicly available. Nevertheless, these software packages are nowadays widely adopted in the research community.

Reference wind turbine models have been developed in the same period of standardizing simulation software. The most recent and frequently used multi-megawatt models are the NREL 5-MW (Jonkman et al., 2009) and DTU 10-MW (Bak et al., 2013) reference turbines. The former is developed by the National Renewable Energy Laboratory (NREL), and provides a reference for offshore wind turbine design specifications. The model is designed to closely match the properties of by the REpower 5M turbine (*REpower* 2004). Because the 5M's public specifications were only partially available at the time of developing the NREL 5-MW turbine, the best features of the DOWEC 6-MW (Kooijman et al., 2003), RECOFF 5-MW (Risoe National Laboratory, 2004), and WindPACT 5-MW (Malcolm and Hansen, 2006) conceptual models[1] are combined.

For development of the DTU 10-MW turbine model, DTU Wind Energy and Vestas

[1]The abbreviations respectively stand for: Dutch Offshore Wind Energy Converter (DOWEC), Recommendations for Design of Offshore Wind Turbines (RECOFF), and Wind Partnerships for Advanced Component Technology (WindPACT).

collaborated in the Light Rotor project (Bak et al., 2013). The project initially focused on the development of a low-weight 10 MW rotor and corresponding design methods. Later, for evaluation of the rotor performance, the DTU 10-MW reference turbine has been established, the design of which is inspired by the NREL 5-MW turbine. Remarkably, though, the new methods developed in the Light Rotor project for low-weight rotor design, are not used for upscaling the rotor of the DTU 10-MW turbine.

In contrast to the well-established simulation code and reference models, a go-to baseline wind turbine controller solution is lacking. Research groups frequently use in-house developed control solutions for the evaluation of proposed system level and controller innovations. As these self-developed implementations might be suboptimally tuned and/or publicly unavailable, there is no easy way to verify the often optimistic conclusions on performance enhancements. Fortunately, most simulation software packages have agreed on a common controller communication layer by means of the DISCON interface (Garrad Hassan & Partners Ltd, 2011). The interface – also referred to as the Bladed-style DISCON controller interface – provides access to a swap-array to read and write, controller actions and measured quantities. The interface, although abandoned in the latest versions of Bladed (*Bladed 4.50*), is widely used by other simulation software.

In the past, attempts have been made to provide a universal baseline wind turbine controller. With the development of the NREL 5-MW reference wind turbine, NREL supplied a corresponding controller (Jonkman et al., 2009). The controller uses the pitch angle and generator torque variables for effectuating the variable-speed variable-pitch (VS-VP) strategy. The implementation suffices for baseline turbine operation, but has not been extensively tuned. Furthermore, all parameters are hard-coded in the source file, and is therefore not easily applicable to other turbine models.

Another initiative is the *Basic DTU Wind Energy controller* (Hansen and Henriksen, 2013). The DTU baseline controller – developed as part of the earlier mentioned Light Rotor project – is more advanced. The controller provides proportional-integral strategies for below and above-rated operating regions, in conjunction with additional filters for other control objectives. The controller can be applied to various turbines, as it is configured by an external parameter file. However, at the time of writing, the controller repository does not seem to provide baseline parameter files for the NREL 5-MW and DTU 10-MW reference turbines (DTU Wind Energy, 2019). Also, the development is not driven by a large community and extensive documentation is lacking. For the reasons discussed, the following challenge is formulated.

Challenge I: Explore the possibilities for the development of a universal baseline wind turbine controller, to solve the lack of a de facto and go-to solution for the assessment of novel algorithms and innovations. The controller should be easy to use, well-documented, and widely applicable.

1.1.2. METHODS FOR BLADE FATIGUE LOAD REDUCTIONS

Larger turbine rotors experience spatial and temporal variations of turbulence over the rotor plane. Amongst other things, these variations induce out-of-plane blade oscillations causing fatigue damage to the blade, as illustrated in Figure 1.1a. Smaller and early

VS-VP turbines have the ability to collectively pitch the blades by a single actuator. In contrast, larger and more recent turbines have the ability to pitch the blades to distinct angles (Burton et al., 2001; Pao and Johnson, 2009). This system-level advancement has led to research interest for fatigue load reductions using individual pitch control (IPC).

In the past, measurement of the blade bending moments appeared to be a challenging task (Menezes et al., 2018). Therefore, simple implementations of IPC employ a feedforward approach, based on estimated loads as a function of the rotor azimuth position (Wright and Balas, 2004; Larsen et al., 2005). The feedforward method aims at the reduction of the more deterministic 1P (once-per-revolution) periodic load component, primarily caused by wind shear, tower shadow, and yaw-misalignment with the dominating wind direction (Hau, 2013; Jelavić et al., 2010). However, in realistic turbulent conditions, the combined effects are of a stochastic nature, which makes the loads variations to vary significantly with the prevailing operating conditions. Therefore, it is hard to show and quantify harmonic load reductions of the feedforward approach.

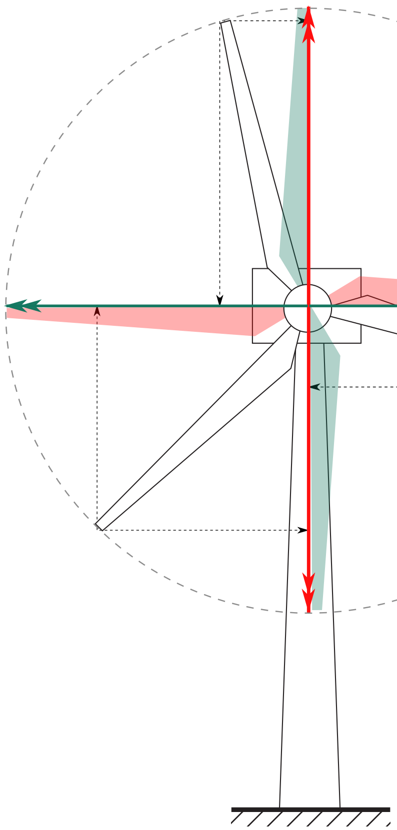

Figure 1.2: Based on the current azimuth position, the multiblade coordinate transformation projects the out-of-plane blade root bending moments in the rotating coordinate system on a fixed frame. The nonrotating orthogonal reference frame, consists of a yaw axis (red) and a tilt axis (green). The schematic is adapted from (Bianchi et al., 2006).

An intermediate solution is to deploy an estimator, estimating the out-of-plane blade harmonics (Jelavić et al., 2010). Such an implementation eliminates the need for blade load sensors, by only requiring a (filtered) wind direction measurement, and an estimate of the hub-height wind speed. Load reduction results show potential for idealized cases, however, for increased and more realistic turbulence levels, the performance gains diminish rapidly. Later in (Petrović et al., 2015), the same authors propose a method to retrieve higher harmonic structural load information, without the need for blade load measurements. Transformations on measurements from rotating or nonrotating coordinate systems are used to extract this data. The proposed control method aims at the reduction of structural loads caused by rotor asymmetries.

More recent turbines are nowadays – due to developments in sensor reliability – equipped with blade root load sensors. These sensors measure the blade flapping moments, and are used in a feedback IPC implementation (Bossanyi, 2003b; Geyler and Caselitz, 2007). This feedback approach often employs the multiblade coordinate (MBC) transformation (Bir, 2008b), also known as the Coleman transformation (Johnson, 2012). As shown in Figure 1.2, the MBC transformation decouples – or stated differently: *projects* – the blade loads in a nonrotating reference frame. The reference frame consists of a vertical yaw-axis, a horizontal tilt-axis, and a collective mode. At the same time, the rotor speed dependent n-times-per-revolution (nP) load harmonic is transferred to a steady-state contribution, simplifying controller design.

Figure 1.2 illustrates the working principles of the orthogonal projection. The transformation is however troubled by dynamic effects, often leading to coupling in the multivariable system. This phenomenon deteriorates the fatigue load mitigating performance, and increases actuator demands. To be able to analyze such control problems, the following challenge is posed.

Challenge II: Develop system analysis tools using well-developed methods from classical control theory. Subsequently, exploit the gathered insights to construct an optimal and practically implementable controller with conventional design methods.

1.1.3. Strategies for tower fatigue reduction and prevention

The urge towards increased turbine power ratings, requires the development and deployment of larger rotors and taller towers. Larger towers lead to increased material use and thus a higher weight of the overall support structure. As the capital investments are largely attributed to the turbine tower, it is crucial to minimize the material use, to which the tower costs are highly related.

Conventional towers are often carried out in soft-stiff configurations, and their design is subject to a lower-bound frequency constraint (Dykes et al., 2018). This constraint implies that the tower natural frequencies do not overlap with the speed dependent rotor rotational (1P) and blade passing (3P) frequencies, to avoid the excitation of resonances. Another, more practical hurdle, limiting the maximum outer diameter, are the per-country varying requirements for transport of oversize loads. Increasing the tower height, while keeping the diameter constant and holding on to the frequency constraint, leads to an exponential increase of the tower mass by the increased wall thickness.

For the above mentioned reasons, the application of soft-soft tower configurations is considered, alleviating the frequency constraint. Soft-soft designs are lighter, more flexible, and commonly have their fundamental frequency in the variable speed operating region. To enable the application of such towers, more advanced control techniques are needed to reduce or prevent resonance-induced loadings.

The tower fore-aft and side-side modes, the latter of which mentioned motion is illustrated in Figure 1.1b, are lightly damped (Burton et al., 2001), although the fore-aft direction has the benefit of aerodynamic damping. Two types of load reducing control strategies exist for both directions: mitigating already present vibrations, or preventing the excitation of resonances by rapidly skipping over speed regions. The techniques are respectively referred to as the *active* and *passive* control methods. The remainder of this section elaborates on the currently available methods for both control strategies.

Active tower vibration control: The control strategies aiming at the reduction of already present tower vibrations are categorized as active methods. Considering the tower dynamics as a second-order system, it is recognized that an additional external velocity related force can be added to increase the system's damping. The velocity signal is theoretically obtained by integrating the measured nacelle fore-aft and side-side acceleration, and added as a contribution to control signals.

For the fore-aft case, collective pitch action is used to provide the damping enhancements. By adding the scaled fore-aft velocity signal to the collective pitch signal, the forward oscillations and tower base loads can be reduced significantly (Bossanyi, 2000). For practical implementations, it is important to include additional filters preventing an accumulative offset causing signal drift, but also to exclude unintended frequency content in the pitch contribution (Bossanyi et al., 2010). Alternatively, to prevent the before mentioned complications, a Kalman filter can be used for the estimation of wind turbine structural states (Wright, 2004). Furthermore, it might be necessary to tune the phase of the control signal for optimal load reductions (Leithead and Dominguez, 2005). Side-side oscillations are reduced with a similar control scheme, by providing a contribution to the generator torque signal.

A more advanced approach using preview information of the wind field using a light detection and ranging (LIDAR) device, in conjunction with nonlinear model predictive control (NMPC) has been investigated in (Schlipf et al., 2013). While the attained performance advancements are promising, real time implementation remains impractical, and the results must be interpreted as the upper bound for other controllers.

Passive frequency skipping strategies: Passive methods prevent the excessive excitation of structural resonances, by restricting turbine operation in specific regions. This technique is often referred to as *frequency skipping* (van der Tempel and Molenaar, 2002), and is commonly implemented by adding logic to the generator torque controller (Bossanyi, 2000). While the implementation of *speed exclusion zones* is straightforward using logic and classical (PID) controller design techniques, it is inconvenient to tune and assess the (dynamic) optimality in terms of power maximization and fatigue load minimization. Predictive model-based control methods can play an important role in providing a convenient way of performing a trade-off between the earlier mentioned objectives. To this end, the following challenge is formulated.

Challenge III: Substitute traditional controller designs with advanced and practically feasible control techniques, solving prevalent control challenges to facilitate the development of next-generation wind turbines.

1.1.4. OPERATIONAL CONTROL STRATEGIES FOR HYDRAULIC DRIVETRAINS

Another approach for advancing wind turbine technology, with the aim of lowering the levelized cost of wind energy, is the application of hydraulic drivetrains. The main challenges in hydraulic system and controller design are associated with the component specific characteristics, varying with the current operating conditions. For individual hydraulic turbines, the control strategy mostly differs in the partial load region.

This section summarizes the control methods for different hydraulic turbines concepts. Hydraulic wind turbine concepts are divided in two categories: drivetrains with a variable transmission ratio, and configurations with a fixed volumetric displacement. This section makes the same distinction in the discussion of the related control methods.

Variable-displacement drivetrains: The possibility of adjusting the volumetric displacement of one or more components in a hydraulic drivetrain, is often referred to as a variable-displacement configuration. As shown in Figure 6 (Prologue), virtually all proposed concepts somehow implement the variable strategy. The variable displacement strategy facilitates the application of a synchronous generator, and can additionally provide efficiency benefits.

A study on the dynamics and controllability of a variable displacement drivetrain discloses some interesting properties (Schmitz et al., 2013). It is shown that the increased damping in the hydraulic drivetrain can partially compensate for the aerodynamic instability, imposed by the rotor torque gradient with respect to rotational speed. Moreover, nonminimum phase behavior is observed for operating conditions where the before mentioned torque gradient is positive. The findings are supported by experimental results using the IFAS hydraulic test bench (Vukovic and Murrenhoff, 2015).

Extensive modeling of a wind turbine employing a digital displacement component is described in (Pedersen et al., 2018). The digital aspect refers to the discrete way of switching between the number of active pressure chambers. A sophisticated model derivation is performed for the combined wind turbine, digital motor and auxiliary hardware. Subsequently, the system is linearized, to synthesize a linear-quadratic-Gaussian (LQG) optimal controller.

The controller design for a DOT-inspired open-circuit drivetrain, with a variable-displacement pump connected to the rotor, is described in (Buhagiar et al., 2016). For discharge line pressure regulation, the implemented feedforward-feedback control strategy uses a combination of pump displacement and variable-area orifice control inputs. Furthermore, hydraulic wind turbine networks employing variable-displacement components are modeled and simulated in (Jarquin Laguna, 2017).

Fixed-displacement drivetrains: A drivetrain consisting of fixed-displacement components ideally moves a fixed amount of volume per rotation. As a consequence, the applied torque at the driving axis determines the discharge pressure of a pump, or vice-versa for a motor.

Few control methods for fixed-displacement concepts have been described in the literature. An interesting passive torque control method for the DOT configuration is described and experimentally demonstrated in (Diepeveen and Jarquin-Laguna, 2014). Briefly summarized: rotor speed variations cause a varying flow through the exiting orifice, with a quadratic relation to the line pressure. A fixed orifice area relates to tracking a fixed tip-speed ratio, which is a necessity for maximum aerodynamic power extraction during below-rated operation. Laboratory scale tests, a feasibility study, and modeling of a turbine based on the DOT concept are described in (Schmitz et al., 2012; Diepeveen, 2013). In-field tests of the DOT500 wind turbine, with a 500 kW open-circuit and fixed-displacement hydraulic drivetrain, have been performed in the summer of 2016. Because of scarcely available information of similar turbines in the literature, a practical control implementation was lacking for the real-world demonstrator. To fill this gap in scientific knowledge and literature, the last challenge is given below.

Challenge IV: Develop the control system and corresponding operational strategy for the real-world DOT500 wind turbine with hydraulic drivetrain, and perform an effectiveness assessment by the analysis of test results.

1.2. Thesis goal, approach and outline

The previous section highlighted 4 control challenges. This section elaborates on how these challenges are addressed, and presents the overall thesis objective. To this end, first preliminary background information is given, which is used to substantiate the problem definition. Then, the thesis goal is presented, and is subdivided in subgoals to provide a contextual framework on the approach of satisfying the objectives. Finally, an outline of the thesis is given.

1.2.1. Background, problem definition and motivation

Concluding from the previous sections of this introduction, evolutions in wind turbine technology are prominently facilitated by advances in control methods. However, by the lack of a de facto standard wind turbine controller, the options for adequate evaluation of proposed system and controller innovations are limited. A universal baseline controller, additionally providing options to conveniently enable more advanced load-mitigating control strategies, helps the entire wind turbine research community, without the need for extensive knowledge on control theory and design. The development of such a controller is the first challenge of this thesis.

The ever increasing power ratings and sizes of present-day wind turbines, pose a challenge for the application of existing load mitigating control strategies. Without proper analysis tools and tunings, the algorithms show reduced or even adverse performance levels. Furthermore, traditional control methods start to become a limiting factor in solving design challenges for larger turbines. Therefore, advanced model predictive control techniques are key in enabling next-generation large-scale turbine designs. The creation of analysis tools, enabling improved and/or novel advanced controller designs, is therefore another thesis challenge.

Finally, wind turbines with radical design changes at system level, such as turbines with a hydraulic drivetrain, need an accompanying control system maximizing the operational efficiency. The last challenge is therefore to exploit the acquired knowledge gathered in the previously stated challenges, promoting the controller design process for a system with a fundamentally different drivetrain configuration.

1.2.2. THESIS GOALS AND APPROACH

Practical applicability of the innovations described in this thesis is an overarching theme, and is considered of utmost importance in accelerating the pace of technological evolutions. The approach is to deepen and improve on well-known control concepts discussed in the literature, that lack a careful analytical evaluation. It is shown that by understanding and thoroughly analyzing the control problem at hand, considerably simplified and more convenient controller designs are possible. Following this approach, enhanced performance levels are often attained.

Based on the previously stated, the goal of this thesis is formulated as follows:

Thesis goal: Develop analysis tools based on established control theory, providing optimal control solutions for stimulating advancements in wind turbine technology.

It is recognized that the presented thesis goal is somewhat broad and general. For this reason, the main goal is subdivided in different subgoals, which align with the previously introduced challenges. The corresponding text provides contextualization, and also sketches the approach in fulfilling the goals.

As the development of new controllers and system concepts evermore rely on numerical methods, a widely accepted and baseline wind turbine control strategy is key for the evaluation of improved or novel algorithms. Such a widely accepted control solution is – next to standardized simulation software and reference models – the last ingredient in unifying baseline load cases for the proper evaluation of innovations. Towards the development of such a controller, the following research question is formulated:

I: What are the prevalently applied operational and load mitigating wind turbine control methods, and is it possible to develop a universal baseline controller code, and improve on widely accepted ideas?

Fatigue load reducing control methods facilitate a path towards next-generation wind turbines, with higher power ratings, less material use, and thus increased cost effectiveness. Ideas on how such controllers should practically work are described in the literature. However, with the increasing sizes of turbines, these methods become more tedious to implement without expert knowledge, and are often times not suited for employment in modern predictive control methods. To this end, existing ideas and control schemes are further analyzed and improved, and novel algorithms have been developed. Two critical and design driving areas are targeted, namely: the mitigation periodic blade loads, and the prevention of tower resonance excitation.

For the blade load objective, it is of interest to evaluate the effect of the – in industry commonly applied – azimuth offset in the MBC transformation. The offset is often presumed to provide system decoupling advantages, however, this effect is never thoroughly analyzed. Therefore, the subgoal is formalized by the following research question:

> **II:** How do we develop analysis tools based on established control theory to disclose the effect(s) of the commonly applied azimuth offset for individual pitch control using the multiblade coordinate transformation? Can we subsequently use traditional controller design methods to improve (practical) load mitigating performance levels, towards the application of larger rotors?

The challenge in tower resonance excitation prevention, is the inability of existing frequency skipping controller designs – based on classical control techniques – to perform a dynamically optimal trade-off between produced energy and loads. This shortcoming is becoming ever more striking for wind turbines with higher power ratings and taller towers. Modern predictive control techniques might form a solution path, and the following subquestion is therefore formulated:

> **III:** Can we create a practically feasible model predictive control scheme, replacing existing implementations based on traditional control methods, for preventing the excitation of critical resonances, towards the application of taller and more cost/weight-effective towers?

Wind turbines with hydraulic drivetrains, approach wind energy cost reductions from a system design perspective. Conventional turbine drivetrains have been extensively developed in the past decades, and provide high levels of efficiency throughout in all operational regions. For hydraulic wind turbines to be commercially successful, a similar efficiency maximizing development has to take place. In the course of the PhD project, a real-world hydraulic wind turbine demonstrator was deployed. The turbine is subject to extensive testing, to find an answer to the somewhat exploratory question:

> **IV:** Are the analysis tools in subquestion/challenge **I** practically feasible to establish an operational strategy and controller design for a real-world wind turbine, with a fundamentally different hydraulic drivetrain configuration?

The six chapters in this thesis stand on their own, and can be read independently from each other. Because the chapters are not related in a mathematical sense, each has its own definition of symbols. An introduction is given at the start of each chapter. The final chapter of this thesis presents a summarizing conclusion.

1.2.3. OUTLINE

This section presents the outline of this thesis. Each paragraph gives a brief summary of the contents of each chapter.

Chapter 2 provides a description of the numerical software projects that lay out the foundation for the remaining chapters of this thesis. All software packages are open-source, publicly available, and (co-)developed by different research groups of the Delft University of Technology. A universal, baseline and community driven wind turbine controller is outlined. Complementary, a graphical controller design environment in MATLAB Simulink facilitates convenient and rapid development of control algorithms. Lastly, an educational graphical interface for NREL's simulation software FAST for graphical wind turbine and controller design is presented, aimed at the education of engineering talent formulating the technological innovations.

Chapter 3 presents an advancement in the widely applied IPC scheme using the MBC transformation, for the successful reduction of out-of-plane blade oscillations. The advancement encompasses the, up until recently, often undervalued azimuth offset tuning variable. Besides a thorough analysis, the importance of the offset is illustrated for turbines with larger and more flexible rotors, and/or with significant actuator phase delays. For such cases, the offset appears to be a crucial design variable towards successful load attenuations, and actuator duty cycle minimization.

Chapter 4 presents, in the wake of the previous chapter, an elegant solution for constraining persistent tower side-side resonance excitations. The proposed and more advanced control method uses a combination of techniques. A demodulation transformation, sharing properties with the MBC transformation, is employed to transfer frequency content to a steady-state contribution. The beneficial properties of the resulting quasi-LPV system are exploited in an efficient MPC scheme. The cutting edge strategy facilitates the development of next-generation turbines, enabling the application of cost-effective tall towers by reducing material use.

Chapter 5 shifts focus towards the (dynamic) modeling and controller design for a hydraulic wind turbine, in contrast to the previous chapters concentrating on advanced load mitigation strategies. In-field prototype tests are performed with a retrofitted 500 kW hydraulic drivetrain, based on the DOT concept. The concept aims at simplification of wind turbines and wind farms, minimizing the number of drivetrain components, and by collectively harvesting the power of multiple turbines at a centralized location.

2

Wind turbine control software

Standardized, easy to use, and preferably open-source research software is an important aspect in supporting and solidifying the wind turbine community. This chapter presents three open-source software projects that form the foundation for the work described in this thesis. First, a community-driven wind turbine baseline controller, the Delft Research Controller (DRC), is presented. The DRC is applicable to high-fidelity simulation software that uses the DISCON controller interface. The controller distinguishes itself by the variety of available control and estimation implementations, its ease of use, and the universal applicability to wind turbine models. Secondly, in the wake of the DRC, the SimulinkDRC graphical controller design and compilation environment has been developed. Users having access to Simulink can benefit from the convenient way of controller development the tool provides. Finally, the FASTTool has been established for educational purposes, by focusing on the graphical aspect of wind turbine (controller) design. The tool simplifies interaction with the advanced FAST simulation software, by comprehensive visualizations and analysis tools. This chapter demonstrates and describes the functionality of all three software projects.

Chapter contents

This chapter is based on the following publications:

S.P. Mulders and J.W. van Wingerden. Delft Research Controller: An open-source and community-driven wind turbine baseline controller. In *The Science of Making Torque from Wind (TORQUE)*, Milan, Italy, 2018

S.P. Mulders, M.B. Zaaijer, R. Bos and J.W. van Wingerden. Wind turbine control: open-source software for control education, standardization and compilation. In *NAWEA/WindTech*, Amherst, Massachusetts, USA, 2019

2.1. INTRODUCTION

Wind turbine control is a nontrivial task, and generally requires expert control knowledge and software skills for design, tuning and implementation. For this reason, wind energy research groups from the Delft University of Technology (TU Delft) develop and actively maintain various open-source, free, and publicly available wind turbine control oriented software projects. The following three open-source projects are outlined in this chapter:

Delft Research Controller (DRC). The DRC is an open-source and community-driven wind turbine baseline controller. The development of the controller is driven by the notion of wind energy research groups from various disciplines often using self-developed baseline implementations and tunings, complicating the evaluation and comparison of new control algorithms. To solve this problem, the DRC provides an open, modular and fully adaptable baseline wind turbine controller to the scientific community. New control implementations are easily added to the existing baseline controller, and in this way, convenient assessments of the proposed algorithms is possible. Because of the open character and modular set-up, scientists are able to collaborate and contribute in making continuous improvements to the code. The DRC is being developed in Fortran and uses the Bladed-style DISCON controller interface. The compiled controller is configured by a single control settings parameter file, and can work with any wind turbine model and simulation software using the DISCON interface. Baseline parameter files are supplied for the NREL 5-MW and DTU 10-MW reference wind turbines.

SimulinkDRC. In the wake of the DRC, a graphical controller design and compilation environment has been developed in Simulink, and is called SimulinkDRC. For engineers having access to Simulink, this tool provides an easy and convenient way of controller development.

FASTTool. The FASTTool has been developed for educational purposes in wind turbine design. FASTTool is a graphical user interface (GUI) for NREL's aeroelastic simulation code FAST (Fatigue, Aerodynamics, Structures, and Turbulence). The tool is centered around a three-dimensional animated wind turbine plot, which dynamically adapts to the defined design inputs. FASTTool provides users with convenient and insightful tools to tune controllers and assess the performance of the design.

All software is released under the MIT license – a free software license – at the following location:

`https://github.com/TUDelft-DataDrivenControl`

The organization of this chapter is as follows. Section 2.2 describes the philosophy, functionality and the working principles of the DRC baseline wind turbine controller. In Section 2.3, SimulinkDRC is presented, opening possibilities for graphical controller design in Simulink. Finally, Section 2.4 presents FASTTool: An educational and graphical interface for NREL's high-fidelity wind turbine simulation software FAST.

2.2. DRC: AN OPEN-SOURCE AND COMMUNITY-DRIVEN BASELINE CONTROLLER

The existence of reference models and baseline load cases is a crucial aspect in the scientific community, as it allows for convenient and fair evaluation of proposed innovations. In the wind turbine community, the National Renewable Energy Laboratory (NREL) 5-MW baseline wind turbine is a fictive, but fully defined reference wind turbine (RWT) model (Jonkman et al., 2009), and is actively used in the scientific field. To accommodate the next step in enlarging the size and rated power of offshore wind turbines, the Technical University of Denmark (DTU) provides a 10-MW RWT model (Bak et al., 2013). The DTU 10-MW model is developed in cooperation with Vestas Wind Systems. Its design is mainly focused on setting a reference for next generation rotors, with good aerodynamic performance at a relative low weight.

Besides reference models, wind turbine simulation software is also largely standardized. The industry standard, commercial and certified high-fidelity wind turbine simulation package is Bladed by DNV GL (DNV-GL, 2017). On the other hand, an open-source aeroelastic package for simulating horizontal-axis wind turbines is FAST, which was up until recently actively developed and maintained by NREL. However, a shift towards community-driven software development is seen in the scientific field, and OpenFAST is established with the FAST v8 code as its starting point (NWTC, 2019). The goal of OpenFAST is being a community model, with users and developers from research laboratories, academia and industry improving software quality and accelerating development.

In contrast to the previously mentioned reference models and simulation software, no clear choice of a baseline wind turbine controller currently exists that is easy to use, modular and extendable. Wind energy research groups from various disciplines generally use self-developed baseline control implementations and tunings, of which the source code is rarely available. This negatively impacts the ability to compare results from different research projects or groups. It has to be noted that NREL provides an open-source controller for its NREL 5-MW reference wind turbine (Jonkman et al., 2009). However, this controller is limited in functionality and inconvenient to extend or interchange between distinct wind turbine models as functionality, turbine parameters and controller tunings are hard-coded in a single source file. DTU also provides an internally developed controller for their DTU 10-MW RWT (Hansen and Henriksen, 2013) of which the source code is available, but the development is not driven by a broad community.

To this end, the Data Driven Control wind energy research group from Delft University of Technology started the initiative to develop an open-source and community-driven wind turbine baseline controller. A design specification was that the controller should be generally applicable to all turbine models defined in simulation software that uses the Bladed-style DISCON controller interface (Garrad Hassan & Partners Ltd, 2011), such as OpenFAST, Bladed or HAWC2. Also, a convenient way of configuring the controller should be present, without editing the source code and thus the need for recompilation. With these goals in mind, the foundations of a baseline wind turbine controller have recently been laid out, and is dubbed the Delft Research Controller (DRC). For consistency with OpenFAST, the DRC is being developed in the Fortran programming language (free-form) (Lahey and Ellis, 1994). The modular and open character allows scientists to collaborate and contribute in making continuous improvements to the code. The DRC is provided with a toolbox consisting of regularly used (control) functions and filters to allow for rapid development and implementation of new contributions. NREL recently acknowledged the potential of the DRC by adopting it as their baseline control solution of choice, and dubbed it as the Reference OpenSource Controller (ROSCO) (NREL, 2020).

The main contribution of this section is to provide a comprehensive description of the working principles and functionality of the DRC, and is organized as follows. In Section 2.2.1, an overview of the DRC is given, after which in Section 2.2.2 the built-in filter and function modules are described. A wind speed estimator, described in Section 2.2.3, is included to provide below-rated, closed-loop, tip-speed ratio tracking capabilities. The components in the before mentioned modules are used to make up the baseline torque, (individual) pitch and yaw controllers, described in Section 2.2.4. Section 2.2.5 describes fatigue load reduction control strategies, and Section 2.2.6 outlines the incorporated yaw control implementations.

2.2.1. Overview and description of the DRC

This section gives a general overview and description of the DRC controller architecture and philosophy. The overall DRC working principle is presented in Figure 2.1. The DRC is set up such that only a single parameter file `DISCON.IN` for each wind turbine model is required to define the complete control system. This feature removes the need for repetitive recompilation of the controller under a change in control settings. Baseline controller parameter configuration files are supplied for the NREL 5-MW and DTU 10-MW reference wind turbines, and the source code is publicly available under terms of the MIT License (Mulders and van Wingerden, 2019a).

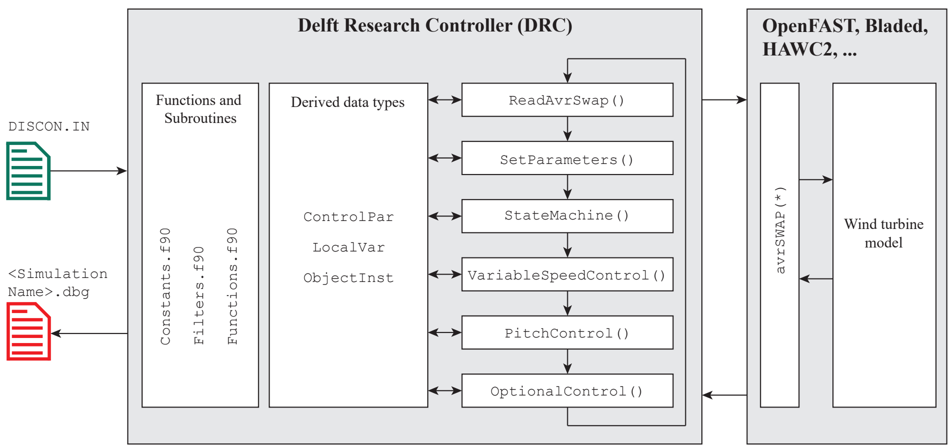

Figure 2.1: A schematic of the DRC architecture for wind turbine control. The controller exchanges data using the so-called the DISCON external controller interface via the `avrSWAP`-array. The DRC is completely parameterized by a single configuration file, and writes debug information to a log file when desired.

The DRC consists of multiple modules containing commonly used functions and subroutines, and uses derived data types to store parameters and variables in a centralized manner. Function calls are executed in a fixed sequence during each control iteration. The DRC reads the control in- and output `avrSWAP`-array (Garrad Hassan & Partners Ltd, 2011) and performs value assertions. Next, before calling any controller, the state-machine determines the state of the turbine, and this information is used by the controllers to perform corresponding control actions. To enable the Variable-Speed Variable-Pitch (VS-VP) control strategy, torque and pitch control subroutines are implemented. Optional controllers are executed after the two before-mentioned controllers.

2.2.2. Filters and functions modules

An overview of the included filters and functions are described in this section. The DRC comes with a collection of frequently used filters. The filters included are discretized using the bilinear transformation, also known as Tustin's method (Oppenheim, 1999). The filters are not bound to a predefined sampling time, as this variable is taken as an input from the simulation. All functions return a single real filtered output signal, with a default unity steady-state gain. The following filters are included:

- *First/second-order low-pass filter.* Pass signals with frequencies lower than the cross-over frequency, but attenuate signal components above this frequency.
- *First-order high-pass filter.* Passes signals with frequencies higher than the cut-in frequency, but attenuates signal components below this frequency.
- *Notch filter.* Passes most of the frequencies but attenuates in a very specific interval.
- *Inverted-notch filter with decreasing slopes.* Amplifies a very specific frequency region, and provides extra attenuation of frequencies outside this domain.

The DRC controller is supplied with the following frequently used functions:

- *Value/signal saturation.* Saturates a given input signal to a upper and lower value.
- *Signal rate limiter.* A signal rate limiter with respect to time.
- *Proportional-Integral (PI) controller.* An object-based PI-controller with integrator anti-wind up and signal saturation capabilities.
- *1D-interpolation.* A one dimensional interpolation function taking a one dimensional table. The x-data should be monotonically increasing.

2.2.3. Wind speed estimation

The wind speed measurement from the anemometer is influenced by induction, as it is often located downwind of the rotor at the back of the nacelle. Therefore, the measurements are often considered unreliable for use in control implementations (Østergaard et al., 2007), and only serve indication purposes. Moreover, the sensor only measures the wind speed at the center of the rotor swept area, while the wind speed varies spatially over the rotor surface (Bianchi et al., 2006). Although not perfect, to keep the rotor operating at maximum power coefficient tracking, torque control is often implemented as the optimal-mode gain, multiplied by the rotor or generator speed squared (Bossanyi, 2000). However, this control scheme assumes perfect model representation and knowledge about the rotor aerodynamic behavior. In real world scenarios, the model and actual rotor show increasing inconsistencies over time, as a result of wear, tear, fouling, icing and manufacturing imperfections (Hau, 2013). For this reason, often a wind speed estimator is employed to provide closed-loop tip-speed ratio tracking capabilities, eliminating the need for perfect a priori knowledge of aerodynamic characteristics.

Different types of wind speed estimators have been proposed (Soltani et al., 2013). While the wind field varies spatially and temporally over the rotor surface, for control purposes it often suffices to have an estimate of the rotor effective wind speed. The rotor effective wind speed is defined as the weighted wind speed average, taking into account the span-wise variation of power extraction. Popular estimator implementations include the power balance estimator (van der Hooft and van Engelen, 2004), and the (extended) Kalman filter (Østergaard et al., 2007; Knudsen et al., 2011). More advanced implementations are proposed for estimation of horizontal and vertical, misalignments and shears (Selvam et al., 2009; Bertelè et al., 2017).

Another rotor effective wind speed estimation technique, is the immersion and invariance (I&I) estimator (Ortega et al., 2013), inspired by the eponymous identification method described in (Liu et al., 2009). The technique assumes the rotor speed and applied generator torque being available as measured signals. The technique shows satisfactory estimation results, is conveniently implemented, and is therefore included as the rotor effective wind speed estimator in the DRC.

In the remainder of this section, only the main result of the I&I estimator derivation is given. The estimation algorithm relies on the following equations:

$$\dot{\hat{v}}_{\mathrm{w}}^{\mathrm{I}} = \frac{\gamma}{J}\left[\tau_{\mathrm{r}} - \Psi(\omega_{\mathrm{r}}, \hat{v}_{\mathrm{w}}^{\mathrm{I}} + \gamma\omega_{\mathrm{r}})\right], \tag{2.1}$$

$$\hat{v}_{\mathrm{w}} = \hat{v}_{\mathrm{w}}^{\mathrm{I}} + \gamma\omega_{\mathrm{r}}, \tag{2.2}$$

in which τ_{r} is the applied generator torque casted to the low-speed shaft (LSS), ω_{r} the rotor speed, Ψ the estimated aerodynamic torque, J the lumped drivetrain inertia casted to the low-speed shaft, γ the estimator adaption gain, and $\hat{v}_{\mathrm{w}}$ the estimated wind speed. When $\gamma > 0$ and other conditions are met, then

$$\lim_{t\to\infty} \hat{v}_{\mathrm{w}}(t) = v_{\mathrm{w}}. \tag{2.3}$$

For estimation of the aerodynamic torque

$$\Psi(\omega_{\mathrm{r}}, \hat{v}_{\mathrm{w}}^{\mathrm{I}} + \gamma\omega_{\mathrm{r}}) = \frac{1}{2}\rho_{\mathrm{a}}\pi R^2 \hat{v}_{\mathrm{w}}^3 C_{\mathrm{p}}(\lambda)/\omega_{\mathrm{r}}, \tag{2.4}$$

the power coefficient is analytically described by the parameterizable function

$$C_{\mathrm{p}}(\lambda) = \mathrm{e}^{-\theta_1/\lambda}(\theta_2/\lambda - \theta_3) + \theta_4\lambda, \tag{2.5}$$

in which $\boldsymbol{\theta} \in \mathbb{R}^4$ are chosen to fit the power coefficient mapping at the blade fine-pitch angle. Furthermore, ρ_{a} is the air density, λ the tip-speed ratio, R the blade length, and $\{N \geq 1\} \subset \mathbb{R}^+$ defines the gearbox ratio.

The I&I scheme relies on the approximation of the aerodynamic torque for rotor effective wind speed estimation. A balance between applied generator torque and the estimated aerodynamic torque is given by Eq. (2.1), in which frictional terms (e.g., from the main bearing and gearbox) are omitted. Consequently, these neglected effects are taken as part of the estimated aerodynamic torque. Therefore, if the additional frictional components are of significant magnitude, this leads to a biased wind speed estimate. One could include the frictional terms in the equation referred to, in order to obtain a more accurate wind speed estimate. However, this complexifies the implementation and requires knowledge on the (possibly varying) frictional characteristics. When implementing the presented method, one should trade-off simplicity and accuracy, based on the presence and quality of prior knowledge.

2.2.4. STATE-MACHINES, AND BASELINE PITCH AND TORQUE CONTROL

This section presents the concept of state-machines, and the pitch and torque control implementations included in the DRC. The purpose of the global state-machine is to determine the operational state of the wind turbine, and is included as a subroutine in the function module. Inside this function, separate state-machines are included for pitch and torque control. The operational state is determined by comparing measured turbine quantities and control signals to settings defined in the controller configuration file. Figure 2.2 gives an overview of the different wind turbine operating regions, indicating internal controller variables and configuration parameters.

The pitch and torque controllers use a common filtered generator speed measurement, to calculate the error from the reference set point. At the end and beginning of regions 1 and 2.5, two PI torque controllers are implemented to regulate the rotor speed towards the optimal below-rated torque path, and to above-rated operating conditions.

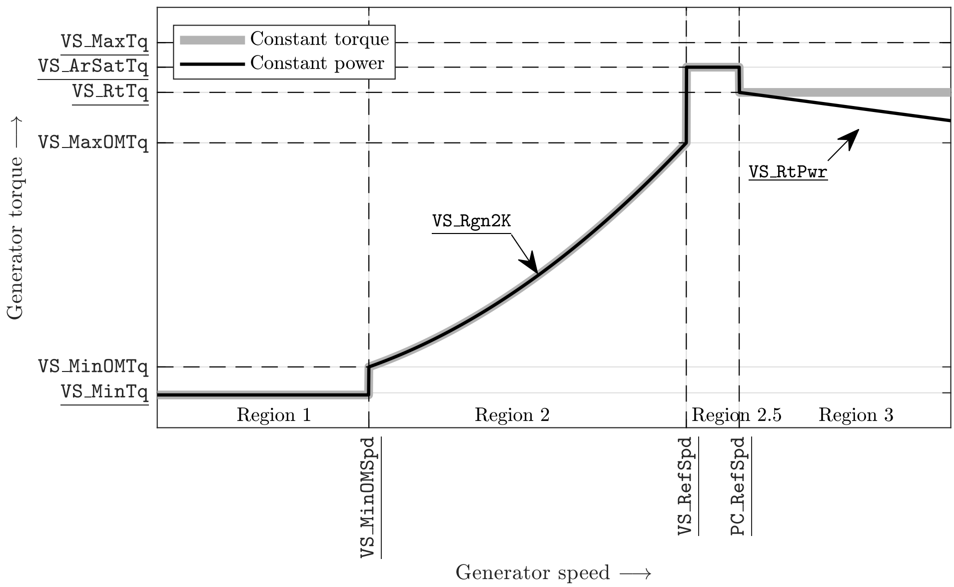

Figure 2.2: Torque control strategies implemented in the DRC. All variables regarding torque control are indicated by their respective names present in the control parameter file. For above-rated operation (Region 3), the control strategy can be configured to either constant torque of constant power.

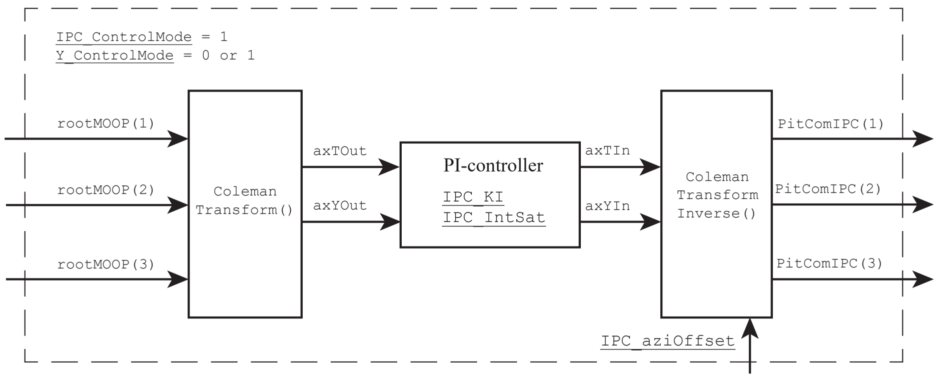

Figure 2.3: Individual pitch control for blade fatigue load reductions. The out-of-plane blade root moments are transformed in a tilt- and yaw-axis by a 1P Coleman transformation. After PI-control, the resulting pitch angles are transformed back by an inverse Coleman transformation to obtain IPC pitch signals to mitigate 1P fatigue loadings.

As shown in Figure 2.2, the maximum torque controller saturation can be set independently to facilitate less frequent switches between torque and pitch control. The cut-in speed for below-rated torque control (Region 2) can be defined, as well as the optimal mode-gain for tracking the maximum rotor power coefficient $C_{\mathrm{p,max}}$. The baseline pitch controller is implemented as a gain-scheduled PI-controller, and the gain information is defined in the parameter file as a function of pitch angles.

For power regulation during above-rated operation, the torque controller can be configured to either deliver a constant torque signal, or actively change the torque signal to obtain a constant power output. For constant power tracking, the torque signal varies subject to the measured generator speed and the electrical power set point.

2.2.5. FATIGUE LOAD CONTROL

Fatigue load reduction capabilities are available in the DRC, in the form of individual pitch control (IPC) for periodic blade load reductions, and active tower fore-aft damping. The two implementations are respectively described in this section.

Individual Pitch Control. IPC reduces out-of-plane blade oscillations causing fatigue, by adding contributions to the individual pitch control signals. A schematic IPC implementation overview is presented in Figure 2.3. The measured blade root out-of-plane moments, together with the rotor azimuth angle, are taken as input to the forward Coleman (or multiblade coordinate (MBC)) transformation (Bir, 2008b), resulting in nonrotating rotor tilt- and yaw-moments. The IPC implementation in the DRC allows for attenuation of the 1P blade load harmonic, or the combined 1P+2P periodic loads. A phase offset can be added to the azimuth angle in the reverse transformation, which turns out to be crucial for practical IPC implementations (Mulders et al., 2019a).

2

Tower fore-aft damping. Tower fore-aft oscillations are naturally lightly damped by aerodynamic damping (Burton et al., 2001). To further enhance damping of fore-aft oscillations, an active control strategy can be implemented. Active fore-aft damping uses an integrated nacelle acceleration signal, which is added to the collective pitch signal (Bossanyi, 2000). The acceleration signal is possibly additionally filtered by a notch filter to prevent unwanted actuation at, e.g., the blade passing frequency.

2.2.6. YAW CONTROL

To maximize energy extraction from the wind, the rotor axis of a wind turbine needs to be aligned with the dominating wind direction. Because the wind flow direction changes over time, a yaw system is required to keep the orientation of a wind turbine aligned with the wind direction to capture as much energy as possible (Manwell et al., 2010; Bianchi et al., 2006). Yawing the wind turbine nacelle and rotor on the support structure can be achieved in different ways, for example, by active yaw and free yaw-by-IPC implementations. Both implementations are included in the DRC, and are respectively described in this section.

Yaw-rate control. The yaw-rate control implementation does not provide continuous alignment, but intermittently aligns the turbine nacelle when a predefined threshold is exceeded. The implementation adapted from (Kragh and Fleming, 2012) and schematically depicted in Figure 2.4, is slightly adjusted to allow for yaw-angle offsets. The yaw-rate controller uses measurements from a wind vane located downwind, i.e., seen from upwind the vane is positioned behind the rotor and tower. The wind vane measures the nacelle yaw-misalignment with respect to the dominating wind direction, but does not give information on the absolute nacelle orientation. Yaw motors with a fixed yaw-rate are used for yaw movements.

Yaw-by-IPC. Besides of the common fatigue load reduction implementation, IPC can also be configured to act in a yaw-by-IPC set-up. Figure 2.5 shows a schematic overview

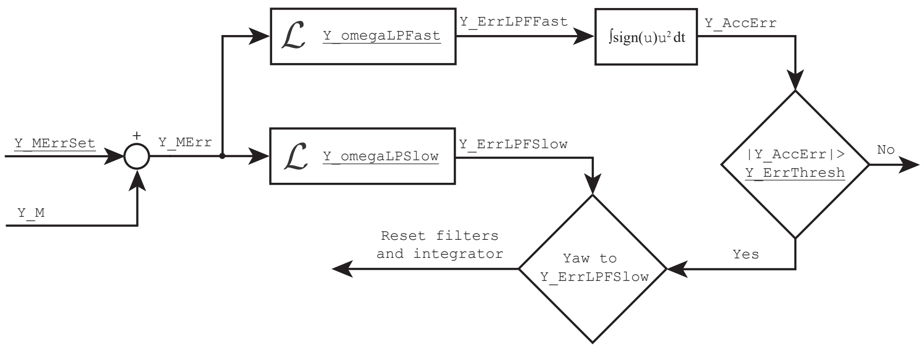

Figure 2.4: Yaw rate control uses the error between the misalignment set point and the measured misalignment with the dominating wind direction to intermittently perform yaw manoeuvres.

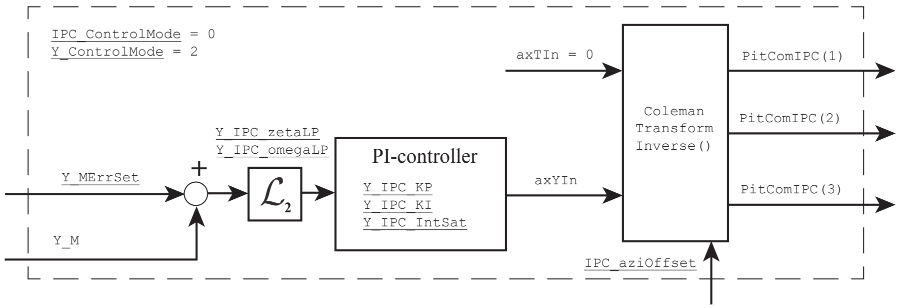

Figure 2.5: An IPC yaw control implementation for a wind turbine where the nacelle is mounted on the tower, in a free-damped fashion. The nonrotating tilt pitch angle is nullified, and the yaw angle is actively controlled by the error between the set point and measured yaw misalignment.

of the implementation. With yaw-by-IPC, a 1P contribution is added to the pitch signals resulting in a yaw moment over the entire rotor to actively regulate or track a yaw misalignment set point. Normally, this type of control is present in downwind wind turbines, where the nacelle is mounted in a free-damped fashion on the tower support structure (van Solingen et al., 2016a; Schorbach and Dalhoff, 2012). In the DRC, either the fatigue load reduction or the yaw-by-IPC controller is active. Simultaneous operation is possible by separating frequency activity, however, such an implementation requires in-depth knowledge and careful tuning (van Solingen et al., 2016a).

2.3. SIMULINKDRC: GRAPHICAL CONTROLLER DESIGN AND COMPILATION

The SimulinkDRC provides a more convenient and graphical controller design environment in MATLAB Simulink (MathWorks, 2019), as schematically depicted in Figure 2.6. All built-in Simulink objects and functions can be used, and compilation results into dynamic library files: *.dll* for Windows, and *.so* for Linux. The compiled controller uses the same DISCON controller interface as the DRC. The implementation includes custom code to compile a 32-bit dynamic library using a 64-bit version of MATLAB Simulink, which is helpful for use with older 32-bit versions of Bladed and FAST.

The tool has proven to be insightful in the development phase of new control algorithms. At the time of writing, a lightweight controller for the NREL 5-MW reference turbine is included. However, as not every engineer or scientist has access to Simulink, implementation of (novel) control algorithms is prioritized in the open-source DRC written in Fortran. The next development goal is to bring the controller functionality of SimulinkDRC on par with the Fortran-based DRC, sharing the functionality and support for external controller parameter files.

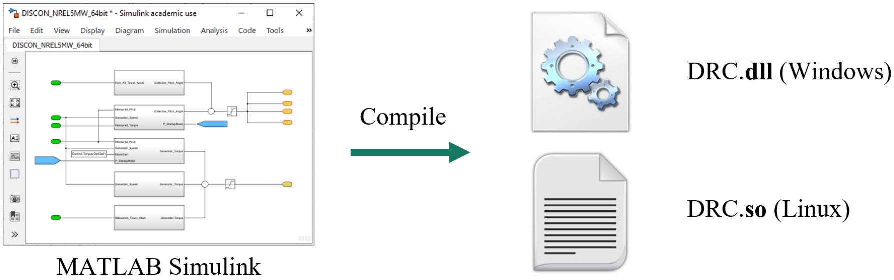

Figure 2.6: SimulinkDRC allows to graphically design a wind turbine controller in Simulink. Compilation results in a dynamic library with the DISCON controller interface, which is compatible with a wide variety of wind turbine simulation software.

2.4. FASTTool: An educational GUI for FAST

The FASTTool was developed in the wake of another educational project at Delft University of Technology (TU Delft), where the idea was to teach an online course through *gamification*. Students would play a game in which they can design and test their own wind turbine through various levels, each with a new challenge to overcome (e.g., wind shear, setting the right cut-out wind speed, etc.). There are plenty of examples of such games with a good educational value. For instance, playing SimCity teaches the essentials of urban planning, Poly Bridge teaches about statics and truss structures, and Kerbal Space Program teaches about rocketry and orbital mechanics. In fact, Kerbal Space Program was so successful in this that NASA began to actively contribute to the game as a means of public outreach and getting young people excited for spaceflight. The strength of these games, in terms of teaching a subject, lies in the fact that playing them does not feel as a chore and that there is good educational value in trying and failing a level. Although FASTTool was not developed with gamification in mind, the relatively simple user interface and many graphical elements were designed to lower the learning curve of the software and make it more enjoyable to use. This enables students to spend most of their time on substantive aspects of wind turbine design, while limiting distractions from the, often complex, capabilities of commercially available simulation and analysis software.

The strength of many wind turbine aeroelastic tools lies in the analysis and not in the user-friendliness per se, which hampers the usability in educational courses. This aspect results in students often losing themselves in the vast array of options. In FASTTool, this problem was solved by centering the graphical user interface (GUI) around an animated three-dimensional plot of the wind turbine. Changes to the geometry are immediately visible on screen, which provides students with an immediate sanity check, but also gives the feeling of creating something new. The performance of the turbine can be checked by a quick power curve calculation (e.g., to see the impact of rotor diameter), as well as through a full time series analysis by FAST, for which the input files are generated by the tool.

Summarizing, FASTTool is a wind turbine design, assessment and simulation tool. It is used in a master-level course on wind turbine design, in which students construct a turbine and assess its performance, dynamics and limit states. The design starts with a choice for system-level parameters and then focuses on the rotor, drivetrain, tower and controller design. As the name of the software already suggests, the simulation back-end is based on NREL's FAST v8.16 (Fatigue, Aerodynamics, Structures, and Turbulence), which is a high-fidelity open-source wind turbine simulation software package (NWTC Information Portal, 2019). The software is to date still under active development, and updated regularly based on new insights and feedback from students. The tool is publicly available at no cost as an open-source repository (Bos et al., 2019). This section gives a high-level overview of the FASTTool, and is organized as follows: Section 2.4.1 outlines the capabilities of the graphical user interface, and Section 2.4.2 demonstrates the back-end simulation and control environment.

2.4.1. MATLAB-BASED GRAPHICAL USER INTERFACE

The costs for industry standard wind turbine simulation software are often prohibitive for use in educational courses, considering the number of students involved. For this reason, FASTTool is developed in MATLAB/Simulink (MathWorks, 2019), in conjunction with the publicly available FAST simulation code. The choice of software is convenient for an academic environment, since no license fees are demanded for the use of FAST, while often students have access to and experience with MATLAB/Simulink. Although MATLAB and Simulink require a license, the employed environment provides flexibility and insight for both the end-user and developer. The MATLAB scripts and the Simulink model of the tool can be edited by more expert users to add or change functionality and to enable other inputs and outputs.

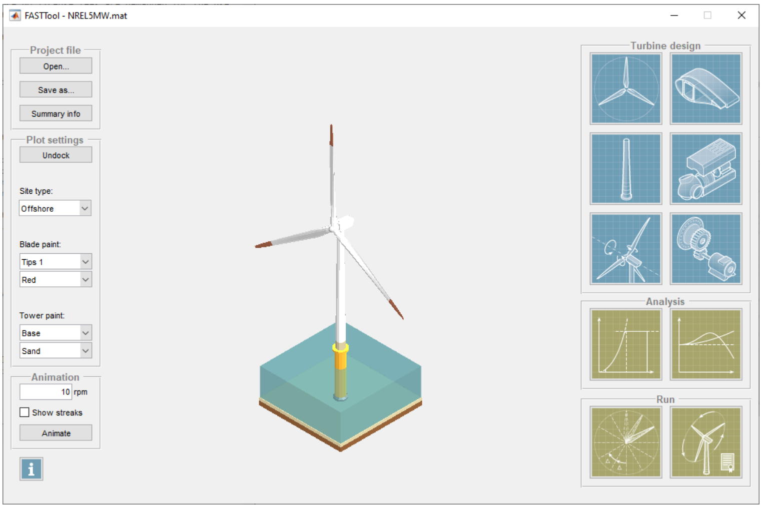

Figure 2.7: The main window of FASTTool. The wind turbine plotted in the center of the screen is animated and adapts to the current turbine design. The turbine's visual appearance can be changed by the options on the left-hand side of the screen. The design – in terms of blade, tower, nacelle, drivetrain, and controller – is altered by the blue-colored options on the right. Analysis and simulation functionality – steady-state operating curves, modal analysis, linearization and simulation – is included under the yellow-colored buttons.

Figure 2.7 presents the main window of the FASTTool, which gives access to the following functionality:

1. A three-dimensional animated wind turbine visualization, adapting to the current design defined by parameters in the graphical user interfaces for blade, tower, nacelle, drivetrain and controller design.
2. Determination of steady-state performance, calculation of turbine natural frequencies, and visualization in a Campbell diagram.
3. Linearization of the nonlinear turbine dynamics at the controller-defined operational path.
4. High-fidelity simulation of various load cases, by a wide variety of wind profiles.

Each item in the above-given enumeration is discussed in the remaining paragraphs of this section.

1. Structural, drivetrain and controller design. The various graphical interfaces for structural, drivetrain and controller design are presented in Figure 2.8. Because FASTTool is built for educational purposes, the software is supplied with the NREL 5-MW

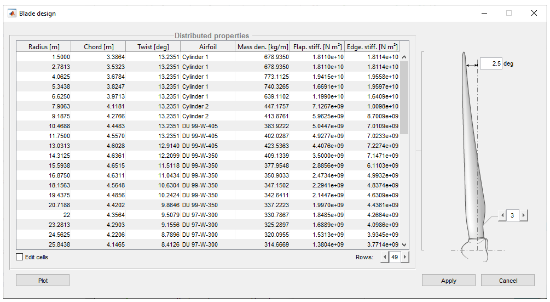

(a) Blade design

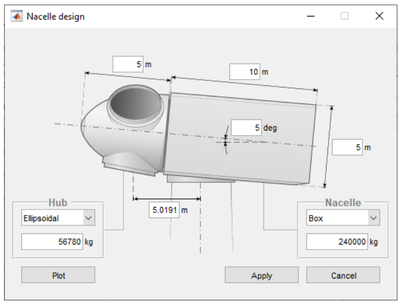

(b) Nacelle design

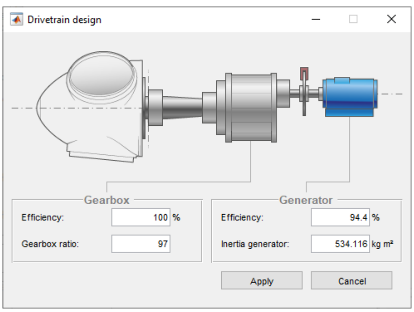

(c) Nacelle design

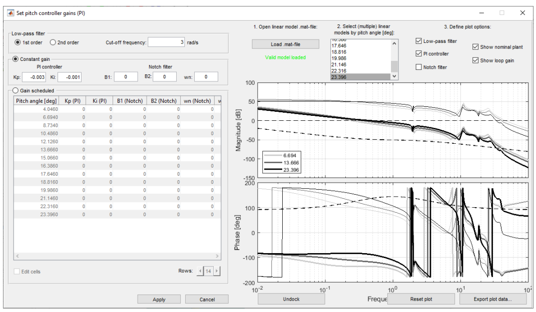

(d) Controller design

Figure 2.8: Different design modules of the FASTTool. The GUI provides a convenient way of changing the blade geometry, nacelle sizing, and drivetrain parameters. An extensive interface is available for controller design by loop-shaping techniques using standard filters.

reference wind turbine (Jonkman et al., 2009) as a MATLAB-style `.mat`-file, and student designs are based on scalings of this turbine. The blade design window in Figure 2.8a provides functionality to radially specify the blade geometry and structural properties by defining the chord, twist and airfoil for each node, as well as the mass density, flap- and edgewise stiffness. A similar interface is provided for tower design. The user can also edit airfoil properties or add new airfoils. Figures 2.8b and 2.8c respectively present the nacelle and drivetrain design options: Parameters size the nacelle, and define the drivetrain by efficiencies, the gearbox ratio, and the generator inertia. To easily check for mistakes in geometric data inputs, the blade, tower and turbine-nacelle configuration are assessed with graphical visualizations. Finally, the controller design component is shown in Figure 2.8d. The controller design section allows to visually tune the pitch controller by loop shaping the system's frequency responses. Loop-shaping is performed by tuning standard PI, low-pass and notch control modules. A comparison can be made between a fixed-gain, and a gain-scheduled controller, to advocate the performance advantages of a variable-gain control implementation. Several other control parameters, such as for the feed forward partial load torque control and for the braking action, can also be changed by the user.

2. Steady-state rotor performance and modal analysis. As a result of the structural geometry and mass properties, Figure 2.9a shows that a modal analysis can be performed on the tower fore-aft and side-side modes, along with the blade flap- and edgewise modes. The natural frequencies are determined with `BModes`, which is also developed by NREL as part of the FAST suite of tools (NWTC Information Portal, 2014). To analyze whether these structural modes interfere with the varying rotational nP harmonics, a Campbell diagram is plotted on the right hand side of the window. Figure 2.9b shows the configuration window for steady-state performance calculations. Steady-state mappings can be calculated at a predefined range of pitch angles, based on the blade and rotor configuration, and with use of included blade-element momentum (BEM) code. The overall turbine operational behavior as a function of wind speed is shown in Figure 2.9c, whereas Figure 2.9d shows the result of a the rotor power coefficient calculation as a function of pitch angle and tip-speed ratio (TSR). The figures are generally used to find the maximum power coefficient, rated wind speed and best pitch angle setting for partial load operation.

3. Linearization. A wide arsenal of powerful mathematical and frequency domain techniques is available for linear controller design. For this reason, high-fidelity non-linear models are generally linearized at operating points of interest. At the time of writing, FAST includes linearization functionality, however, unlike previous versions, it lacks the capability of finding operational trim conditions. The latter mentioned aspect is included in FASTTool. After finding the trim points for a predefined range of wind speeds, the input values are provided to an open-loop fixed-time FAST simulation that linearizes the model. The linear model is stored in a `.mat`-file, which is needed to support the controller design.

4. Wind load cases and simulation. When the wind turbine design is completed, FASTTool provides the opportunity to run certification simulations, as shown in Figure 2.10a. This means that as in Figure 2.10b, first a desired wind field is selected and dimensioned. The user can choose various wind conditions, such as steady wind, stepped wind speed changes, a normal or extreme turbulence model, an extreme operating gust. The more complex wind fields are generated by NREL's TurbSim (NWTC Information Portal, 2016). Wind profiles can be set for assessment of the behaviour of the design and the controller, or to run a load case according to the IEC 61400-1 standard (IEC, 2005). Various turbine conditions can be chosen, such as power production, grid loss, normal or emergency shutdown and idling, supporting IEC load case assessment. Then, when the output file-name is defined, a certification simulation is initiated. For this, FASTTool takes the user-defined turbine design parameters and generates the corresponding FAST input files,

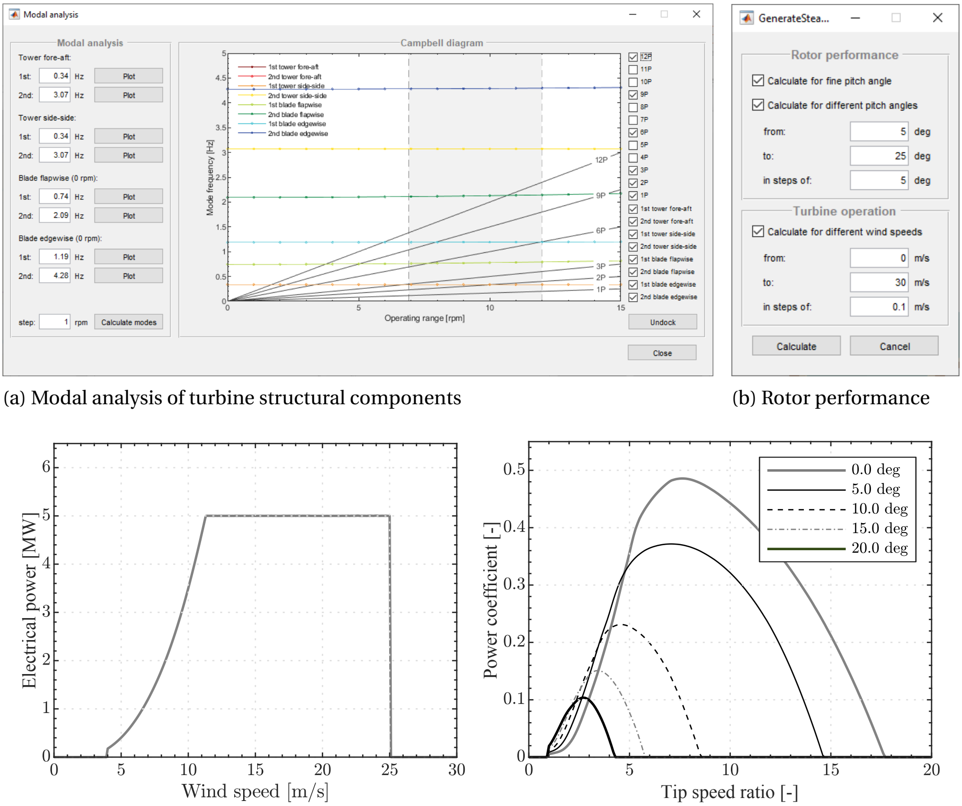

(a) Modal analysis of turbine structural components

(b) Rotor performance

(c) Operational power curve

(d) Steady-state rotor power coefficients

Figure 2.9: Modal analysis tools for calculating the tower and blade, first and second natural frequencies, and visualizing the results in a Campbell diagram. The diagram helps to identify problematic interactions with the variable turbine rotational frequency in the below-rated region. Furthermore, the operational path and steady-state rotor performance mappings are calculated based on the blade design, rotor configuration, and control strategy.

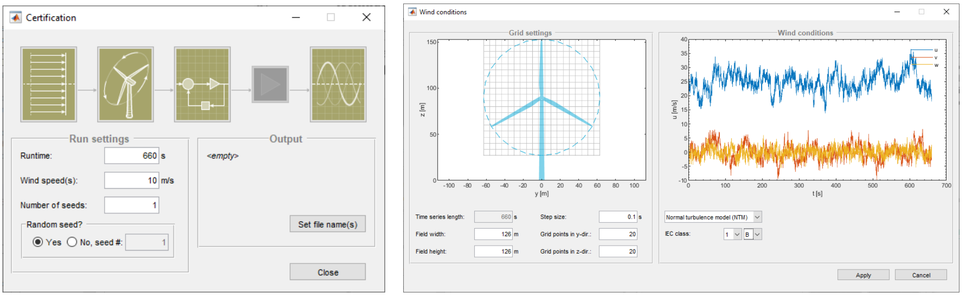

(a) Certification simulation (b) Wind profile design

Figure 2.10: Certification and wind field design windows. The certification section allows to define the total simulation time and mean wind speed of the high-fidelity FAST run. The wind field design window offers among others the selection of steady, stepped, or turbulent wind profiles. Turbulent wind files are generated using NREL's TurbSim (NWTC Information Portal, 2016).

after which it starts a high-fidelity nonlinear FAST simulation, implemented using an S-Function in Simulink. To avoid an overload of information, a small (but relevant) selection of the vast amount of signal outputs is made available to the user; an experienced user can extend the list of outputs. The next section outlines the FAST Simulink simulation and controller environment.

2.4.2. SIMULINK-BASED CONTROLLER AND SIMULATION ENVIRONMENT

FAST has the ability to either run as a compiled standalone application on Windows and Linux, or have the FAST dynamic library being called by a Simulink S-Function. The latter mentioned implementation is employed by FASTTool, as it provides a convenient and insightful development environment. During a simulation run, the built-in controller of FAST is disabled and the controller is provided by Simulink blocks, configured with information from the different interfaces. The Simulink implementation offers course participants, who want to gain a deeper understanding of wind turbine simulation and control, an accessible way of doing so. Experienced user can even change the controller and can for instance add active yaw control.

2.5. CONCLUSIONS

Three software projects are discussed in this chapter. First a community-driven wind turbine baseline controller is presented, applicable to high-fidelity simulation software that uses the DISCON controller interface. The controller aims in being the reference controller for evaluation of new control algorithms. The controller architecture is such that it can be used for any wind turbine model. A single parameter file configures the controller, which abandons the need for recompilation under a change in controller settings. Because of the modular set-up, the existing baseline control implementations are easily replaced, which enables for convenient comparison, reproducibility, and evaluation of new algorithms. Second, a Simulink tool for convenient graphical design and compilation of a turbine controller is demonstrated. Finally, FASTTool is showcased, which is a graphical user interface for NREL's aeroelastic simulation code FAST for educational purposes in wind turbine and controller design. FASTTool provides people new to the field with insights in the design process, by visualizing changes in a three-dimensional turbine visualization, adapting to the current design. The software has options for quick sanity checks, and can generate FAST input files to run high-fidelity simulations based on the turbine design.

With the aim of supporting, standardizing and solidifying the wind turbine (research) community, all software is open-source and publicly available at an online repository. The repositories are regularly updated, and users are invited to provide feedback and contribute to the projects.

3

Blade load reduction enhancements by the MBC azimuth offset

With the trend of increasing wind turbine rotor diameters, the mitigation of blade fatigue loadings is of special interest to extend the turbine lifetime. Fatigue load reductions can be partly accomplished using individual pitch control (IPC) facilitated by the so-called multiblade coordinate (MBC) transformation. This operation transforms and decouples the blade load signals in a yaw-axis and tilt-axis. However, in practical scenarios, the resulting transformed system still shows coupling between the axes, posing a need for more advanced multiple input multiple output (MIMO) control architectures. This chapter presents a novel analysis and design framework for decoupling of the nonrotating axes by the inclusion of an azimuth offset in the reverse MBC transformation, enabling the application of simple single input single output (SISO) controllers. A thorough analysis is given by including the azimuth offset in a frequency-domain representation. The result is evaluated on simplified blade models, as well as linearizations obtained from the NREL 5-MW reference wind turbine. A sensitivity and decoupling assessment justify the application of decentralized SISO control loops for IPC. Furthermore, closed-loop high-fidelity simulations show beneficial effects on pitch actuation and blade fatigue load reductions. Moreover, the importance of including the azimuth offset for higher harmonic (2P) mitigations are made evident: Excluding the offset results in worsened performance with respect to the baseline case without IPC.

Chapter contents

This chapter is based on the following publications:

S.P. Mulders, A.K. Pamososuryo, G.E. Disario and J.W. van Wingerden. Analysis and optimal individual pitch control decoupling by inclusion of an azimuth offset in the multiblade coordinate transformation. *Wind Energy*, 22(3), 2019

S.P. Mulders and J.W. van Wingerden. On the importance of the azimuth offset in a combined 1P and 2P SISO IPC implementation for wind turbine fatigue load reductions. In *American Control Conference (ACC)*, Philadelphia, Pennsylvania, USA, 2019

3.1. INTRODUCTION

As wind turbine blades are getting larger and more flexible with increased power ratings, the need for fatigue load reductions is getting ever stronger (Sieros et al., 2012). For a large Horizontal Axis Wind Turbine (HAWT), the wind varies spatially and temporally over the rotor surface because of the combined effect of turbulence, wind shear, yaw-misalignment and tower shadow (Fischer, 2006), and give rise to periodic blade loads. The blades itself mainly experience a once-per-revolution 1P cyclic load, whereas the tower primarily experiences a 3P cyclic load in the case of a three-bladed wind turbine.

To reduce fatigue loadings, the capability of wind turbines to individually pitch its blades is exploited by individual pitch control (IPC). The pitch contributions for fatigue load reductions are generally formed with use of the azimuth-dependent multiblade coordinate (MBC) transformation, acting on out-of-plane blade load measurements. The forward MBC transformation transforms the load signals from a rotating into a nonrotating reference frame, resulting in tilt and yaw rotor moments. After the obtained signals have been subject to control actions, the reverse MBC transformation is used to obtain implementable individual pitch contributions. The MBC transformation is also used in other fields such as in electrical engineering where it is often referred to as the Park or direct-quadrature-zero (dq0) transformation (O'Rourke et al., 2019), and in helicopter theory where it is called the Coleman transformation (Johnson, 2012).

IPC for wind turbine blade fatigue load reductions using the MBC transformation is widely discussed in the literature (Menezes et al., 2018). While high-fidelity simulation software shows promising results and field tests have been performed (Bossanyi et al., 2013; van Solingen et al., 2016b), publications on the in-field deployment of IPC is still scarce, likely because of the increased pitch actuator loading by continuous operation of IPC (Shan et al., 2013). Also, because of the complicated maintenance of blade load sensors, research has been conducted on load estimation using measurements from the turbine fixed tower support structure (Jelavić et al., 2010). In research, various IPC control methodologies have been proposed such as a comparison of more advanced linear-quadratic-Gaussian (LQG) and simple proportional-integral (PI) control (Bossanyi, 2003b), application of H_∞ techniques (Geyler and Caselitz, 2007), repetitive control (RC) (Navalkar et al., 2014) and model predictive control (MPC) using short-term wind field predictions (Spencer et al., 2013). The effect of pitch errors and rotor asymmetries and imbalances is also investigated (Petrović et al., 2015).

Common in industry is to apply an azimuth offset in the reverse MBC transformation, however, its interpretation, analysis, and effect is more than ambiguous. Bossanyi (Bossanyi, 2003b) states that a constant offset can be added to account for the remaining interaction between the two transformed axes. Later, the same author suggests (Bossanyi and Witcher, 2009) that a small offset in the reverse transformation can be used to account for the phase lag between the controller and pitch actuator. Houtzager et al. (Houtzager et al., 2013) states that the performance of IPC is reduced by a large phase delay between the controller and pitch actuator, but that also the total phase lag of the open-loop system at the 1P and 2P harmonics can be compensated for by including the offset. Mulders (Mulders, 2015) shows that the azimuth offset changes the dynamics of the IPC signal, and that an optimum is present in terms of damage equivalent load (DEL). During field tests on the three-bladed control advanced research turbine (CART3)

(Bossanyi et al., 2013), it is noted that for successful attenuation of the 1P and 2P harmonics, distinct offsets are needed for both frequencies: The offset values are found experimentally and are said to possibly reflect the frequency dependency of the pitch actuator. The same paper also reveals that the azimuth offset is required to compensate for cross-coupling between the fixed-frame axes. The work of Solingen et al. (van Solingen et al., 2016b) mentions that the MBC transformation can incorporate compensation for phase delays by including an azimuth offset in the reverse transformation.

All of the papers discussed above impose different claims on the effect of the azimuth offset in the reverse transformation, but in none of these papers, a thorough analysis is given. Coupling between the tilt and yaw axes is demonstrated (Lu et al., 2015) by a frequency-domain analysis of the MBC transformation with simplified control-oriented blade models. It is stated that this coupling should be taken into account during controller design and a $\mathscr{H}_\infty$ loop-shaping approach is therefore employed. However, the authors do not consider the effect of the azimuth offset in their derivation for decoupling of the nonrotating axes, and the resulting possible implementation of IPC with SISO controllers. The cross-coupling of the transformed system is taken into account in Ungurán et al. (Ungurán et al., 2019) by matrix multiplication with the steady state gain of the inverse plant. Doing so enables the application of an IPC controller with decoupled SISO control loops, however, requires evaluation of the low-frequent diagonal and off-diagonal frequency responses. The latter might be challenging from a numerical as well as a practical perspective.

This chapter uses the azimuth offset for decoupling of the transformed system, and gives a thorough analysis on the effect by providing the following contributions:

- Providing a formal frequency-domain framework for analysis of the azimuth offset;
- Describing a design methodology to find the optimal offset angles throughout the entire turbine operating envelope;
- Demonstrating the approach for rotor models of various fidelity, and thereby showing the implications on the accuracy of the found optimal offset;
- Showcasing the effects of the azimuth offset using simplified blade models;
- Performing an assessment on the degree of decoupling using the Gershgorin circle theorem and the consequences for controller synthesis by analysis of the sensitivity function;
- Using closed-loop high-fidelity simulations to show the offset implications on pitch actuation and blade load signals;
- Evaluating the effects of the azimuth offset in a combined 1P and 2P with multiple pitch actuator models.

This chapter is organized as follows. In Section 3.2, the time-domain MBC representation incorporating the azimuth offset is presented, and is used in an open-loop setting to formalize the problem by an illustrative example using the NREL 5-MW reference wind turbine. Next, in Section 3.3, a frequency-domain representation of the MBC transformation including the offset is derived. Two distinct rotor model structures are proposed, including and excluding blade dynamic coupling. The two beforementioned model structures are employed in Section 3.4 to show the effect of the offset on simplified blade models. Subsequently, in Section 3.5, the results are evaluated on linearizations of the NREL 5-MW turbine and validated to results presented in the first section. In Section 3.6, an assessment on a controller design with diagonal integrators and the effectiveness in terms of decoupling is given. In Section 3.7, high-fidelity simulations are performed to show the implications on pitch actuation and blade fatigue loading in 1P and 1P + 2P IPC configurations. Finally, conclusions are drawn in Section 3.8.

3.2. TIME DOMAIN MULTIBLADE COORDINATE TRANSFORMATION AND PROBLEM FORMALIZATION

This section starts with the time-domain formulation of the MBC transformation, including the option for an azimuth offset in the reverse transformation. Next, Section 3.2.2 shows high-fidelity simulation results of the NREL 5-MW turbine to showcase the effect of the offset. The results formalize the problem and are a basis for further analysis in subsequent sections.

3.2.1. TIME DOMAIN MBC REPRESENTATION

Conventional implementations of IPC use the MBC transformation for fatigue load reductions. The MBC transformation transforms measured blade moments from a rotating reference frame to a nonrotating frame, and decouples the signals for convenient analysis and controller design. A schematic diagram of the general IPC configuration for a three-bladed wind turbine is presented in Figure 3.1, where the generator torque

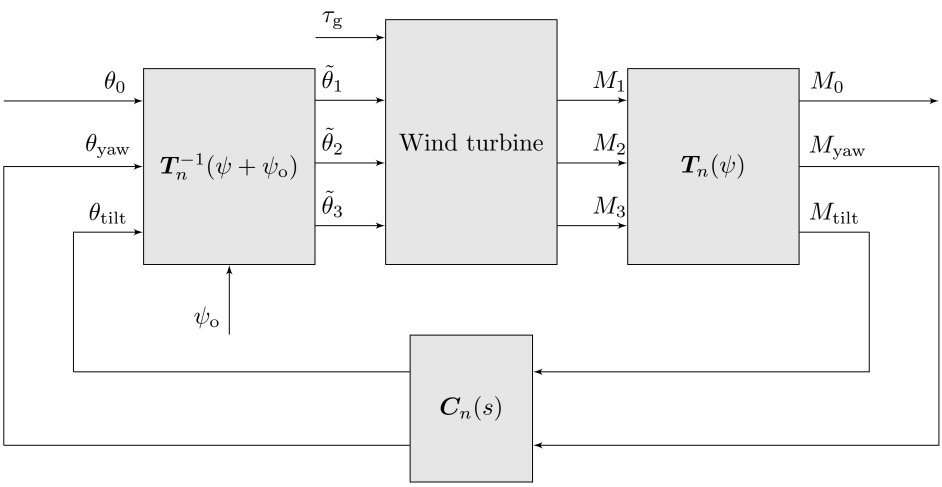

Figure 3.1: Typical implementation of IPC using azimuth-dependent forward and reverse MBC transformations $\boldsymbol{T}(\psi)$ and $\boldsymbol{T}^{-1}(\psi+\psi_o)$, decoupling and transforming blade load harmonics to a fixed reference frame. The IPC controller $\boldsymbol{C}(s)$ generates the fixed-frame pitch contributions by acting on the tilt and yaw moments. The nonrotating signals are transformed back to the rotating frame by the reverse transformation, resulting in pitch contributions $\tilde{\theta}_b$, made up of collective and individual pitch contributions θ_0 and θ_b, respectively. The generator torque control signal is indicated by τ_g. The collective pitch and generator torque control signals are generated by turbine controllers, omitted in this figure.

and collective pitch angle control signals are indicated by τ_g and θ_0, respectively. The relations transforming the rotating out-of-plane blade moments M_b, to their respective nonrotating degrees of freedom (Bir, 2008b) are defined by the forward MBC transformation

$$\begin{bmatrix} M_0(t) \\ M_{\text{tilt}}(t) \\ M_{\text{yaw}}(t) \end{bmatrix} = \underbrace{\frac{2}{B}\begin{bmatrix} 1/2 & 1/2 & 1/2 \\ \cos\left(n\psi_1(t)\right) & \cos\left(n\psi_2(t)\right) & \cos\left(n\psi_3(t)\right) \\ \sin\left(n\psi_1(t)\right) & \sin\left(n\psi_2(t)\right) & \sin\left(n\psi_3(t)\right) \end{bmatrix}}_{\boldsymbol{T}_n(\psi(t))} \begin{bmatrix} M_1(t) \\ M_2(t) \\ M_3(t) \end{bmatrix}, \tag{3.1}$$

where $n \in \mathbb{Z}^+$ is the harmonic number, $B = 3$ the total number of blades, and $\psi_b \subset \mathbb{R}$ is the azimuth position of blade $b \subset \mathbb{Z}^+$ with respect to the reference azimuth ψ, given by

$$\psi_b(t) = \psi(t) + (b-1)\frac{2\pi}{B}, \tag{3.2}$$

and the rotor azimuth coordinate system is defined as $\psi_b = 0$ when the blade is in the upright vertical position.

The obtained nonrotating (fixed-frame) degrees of freedom are called rotor coordinates because they represent the cumulative behavior of all rotor blades. The collective mode, M_0, represents the combined out-of-plane flapping moment of all blades. The cyclic modes, M_{tilt} and M_{yaw}, respectively represent the rotor fore-aft tilt (rotation around a horizontal axis and normal to the rotor shaft) and the rotor side-side coning (rotation around a vertical axis and normal to the rotor shaft) (Bir, 2008b). The cyclic modes are most important because of their fundamental role in the coupled motion of the rotor in the nonrotating system. For axial wind flows, the collective and cyclic modes of the rotor degrees of freedom couple with the fixed system.

After control action by the IPC controller $\boldsymbol{C}(s) \equiv \left\{C_{ij}(s)\right\}_{2\times 2}$, the reverse transformation converts the obtained nonrotating pitch angles θ_{tilt} and θ_{yaw} in the nonrotating frame back to the rotating frame

$$\begin{bmatrix} \tilde{\theta}_1(t) \\ \tilde{\theta}_2(t) \\ \tilde{\theta}_3(t) \end{bmatrix} = \begin{bmatrix} \theta_0 + \theta_1 \\ \theta_0 + \theta_2 \\ \theta_0 + \theta_3 \end{bmatrix} = \underbrace{\begin{bmatrix} 1 & \cos\left[n\left(\psi_1(t)+\psi_{\text{o}}\right)\right] & \sin\left[n\left(\psi_1(t)+\psi_{\text{o}}\right)\right] \\ 1 & \cos\left[n\left(\psi_2(t)+\psi_{\text{o}}\right)\right] & \sin\left[n\left(\psi_2(t)+\psi_{\text{o}}\right)\right] \\ 1 & \cos\left[n\left(\psi_3(t)+\psi_{\text{o}}\right)\right] & \sin\left[n\left(\psi_3(t)+\psi_{\text{o}}\right)\right] \end{bmatrix}}_{\boldsymbol{T}_n^{-1}(\psi(t)+\psi_{\text{o}})} \begin{bmatrix} \theta_0(t) \\ \theta_{\text{tilt}}(t) \\ \theta_{\text{yaw}}(t) \end{bmatrix},$$

where the resulting pitch angle $\tilde{\theta}_i$ consists of collective pitch and IPC contributions θ_0 and θ_i, respectively, and the azimuth offset is represented by $\psi_{\text{o}} \in \mathbb{R}$. The offset could have also been incorporated in the forward transformation and an extensive analysis on this aspect is given in the study of Disario (Disario, 2018).

The main topic of this chapter is to perform a thorough analysis on the effects of the offset and to provide a framework for derivation of the optimal phase offset throughout the complete turbine operating envelope. The analysis is performed on the 1P rotational frequency, however, the framework given is applicable to all nP harmonics.

3.2.2. PROBLEM FORMALIZATION BY AN ILLUSTRATIVE EXAMPLE

To showcase the effect of the azimuth offset, the implementation depicted in Figure 3.2 is used to identify nonparametric spectral models of the system indicated by the dashed

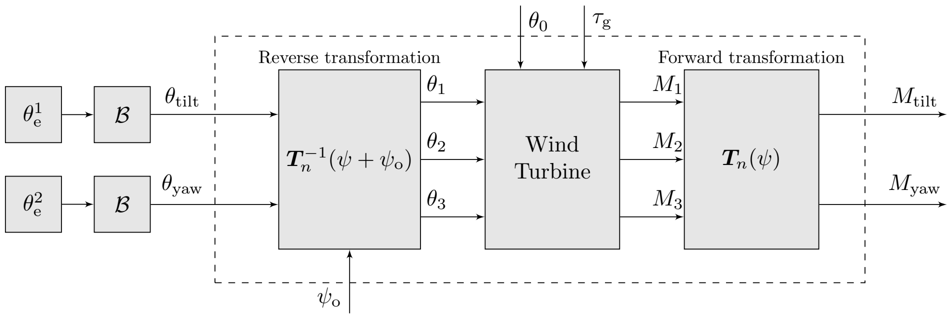

Figure 3.2: Set-up for identification of a nonparametric spectral model $\boldsymbol{P}_s(j\omega)$ of the dashed system. The wind turbine is a nonlinear model and is subject to a steady-state collective pitch angle θ_0 and generator torque τ_g. The nonrotating pitch excitation signals θ_e are filtered by a band-pass filters $\mathscr{B}$, and the wind turbine includes a pitch actuator model. The identification is performed for distinct azimuth offsets ψ_o.

box for different offsets and wind speeds. To this end, the NREL 5-MW reference turbine is subject to the previously introduced MBC transformation, implemented in an open-loop set-up using fatigue, aerodynamics, structures, and turbulence (FAST): A high-fidelity open-source wind turbine simulation software package (NWTC Information Portal, 2019). The nonlinear wind turbine is commanded with fixed collective pitch and generator torque demands, corresponding to a constant wind speed in the range $U = 5 - 25$ m s^{-1}. The forward and reverse transformations are employed at the $n = 1$ (1P) harmonic, and the reverse transformation is configured with different offsets values. The wind turbine includes first-order pitch actuator dynamics with a bandwidth of $\omega_a = 2.5$ rad s^{-1}, which results in an additional open-loop frequency-dependent phase loss.

For identification purposes, the excitation signals θ_e^i are taken as random binary signals (RBS) of different seeds with an amplitude of 1 deg and a clock period (Ljung, 1999) of $N_c = 1$, resulting in flat signal spectra. A bandpass filter $\mathscr{B}$ is included to limit the low and high the frequency content entering the (pitch) system. The cut-in and cut-off frequencies of the bandpass filter are specified at 10^{-3} and 10^2 rad s^{-1}, respectively, as results will be evaluated in the frequency range from 10^{-1} to 10^1 rad s^{-1}. The sampling frequency is set to $\omega_s = 125$ Hz, and the total simulation time is 2200 seconds, where the first 200 seconds are discarded to exclude transient effects from the data set. A frequency-domain estimate of the nonrotating system transfer function $\boldsymbol{P}_s \in \mathbb{C}^{2\times 2}$ is obtained from the tilt and yaw pitch to blade moment signals by spectral analysis[1].

Figure 3.3 presents a spectral analysis of the nonrotating system subject to a wind speed of 25 m s^{-1} for different offset values. Because the MBC transformation moves the 1P harmonic to a 0P DC contribution, the aim is to minimize the off-diagonal low-frequency content. It is shown that ψ_o primarily influences the low-frequency magnitude from the off-diagonal terms of the 2×2 system. From now on, the *optimal offset* is defined as the value for which the main-diagonal terms have a maximized, and off-diagonal terms have a minimized low-frequency gain. This is further formalized using the relative gain array (RGA) (Skogestad and Postlethwaite, 2007), which is defined as the

[1] For spectral analysis, the `spa_avf` routine of the Predictor-Based-Subspace-IDentification (PBSID) toolbox (van Wingerden, 2018) is used.

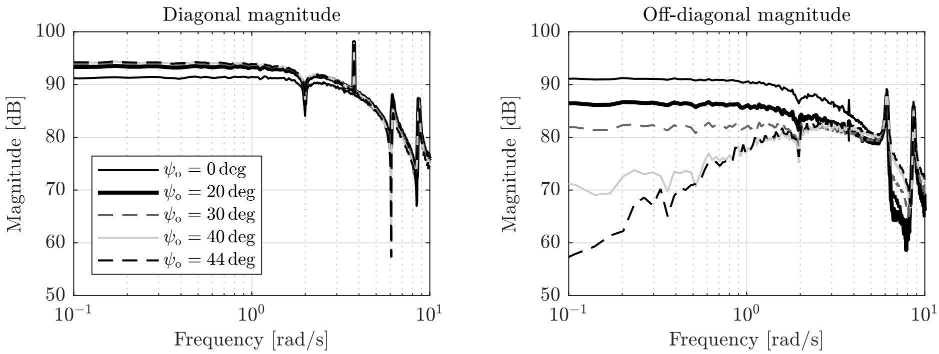

Figure 3.3: Diagonal and off-diagonal magnitudes of $\boldsymbol{P}_\mathrm{s}$ for the input-output pairs $(\theta_\mathrm{tilt}, M_\mathrm{tilt})$ and $(\theta_\mathrm{yaw}, M_\mathrm{yaw})$, obtained from nonlinear wind turbine model simulations with $U = 25\ \mathrm{m\,s^{-1}}$. The reverse MBC transformation is supplied with different azimuth offset values. It is shown that the offset primarily influences the low-frequency off-diagonal magnitude.

element-wise product (the Hadamard or Schur product, indicated by ($\circ$)) of the nonrotating system frequency response and its inverse-transpose

$$\boldsymbol{R}(j\omega) = \boldsymbol{P}(j\omega) \circ \big(\boldsymbol{P}(j\omega)\big)^{-\mathrm{T}}. \tag{3.3}$$

Subsequently, the level of system interaction over a frequency range is quantified by a single off-diagonal element of the RGA, defined by

$$R_{\#} = \frac{1}{L}\sum_{i=1}^{L} \left|R_{12}(j\omega_{\mathrm{s},i})\right|, \tag{3.4}$$

where $\omega_{\mathrm{s},i} \in \mathbb{R}$ for $i \in \{1, 2, \ldots, \mathrm{L}\}$ specifies the frequency range of interest. In Figure 3.4, the optimal offset is evaluated by minimization of $R_{\#}$ for the low-frequency range from

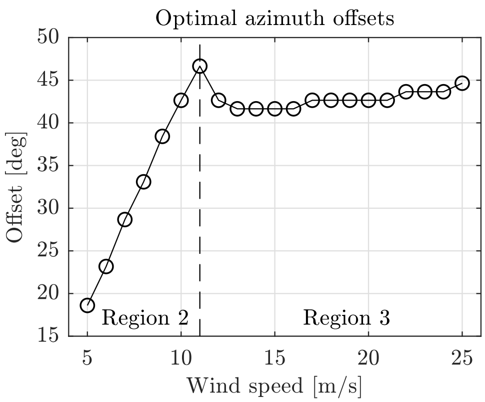

Figure 3.4: The optimal azimuth offset as function of wind speed, both with an accuracy up to the nearest integer value. The optimal offset minimizes $R_{\#}$ of the frequency-domain estimate of the system transfer function. It is shown that the operating condition of the turbine has a high influence on the optimal offset value.

$\omega_{s,1} = 0.1$ to $\omega_{s,L} = 1\ \mathrm{rad\,s^{-1}}$. It is shown that the optimal offset value changes for each wind speed and is thus highly dependent on the turbine operating conditions. An elaborate analysis on the establishment of the optimal azimuth offset is given in the remainder of this chapter.

3.3. FREQUENCY DOMAIN MULTIBLADE COORDINATE REPRESENTATION

In the work of Lu et al.(Lu et al., 2015), a three-bladed wind turbine incorporating the MBC forward and reverse transformations is expressed in the frequency domain using a transfer function representation. By doing so, it was found that while the assumed simplified rotor model – consisting out of three identical linear blade models – did not include cross-terms, coupling between the tilt-axis and yaw-axis was present. This chapter extends the derivation for different rotor model structures, by also including the azimuth offset.

In Sections 3.3.1 to 3.3.3, the derivation of a frequency-domain representation of the MBC transformation is presented. Sections 3.3.4 and 3.3.5 combine the obtained results by assuming rotor model structures excluding and including cross-terms. Finally, Section 3.3.6 incorporates the azimuth offset in the framework.

3.3.1. PRELIMINARIES

For analysis of the considered system in the frequency domain, the rotor speed denoted by ω_r is taken constant such that the azimuth is expressed as $\psi(t) = \omega_r t$. The following Laplace transformations (Oppenheim et al., 2013) are defined first as they are used subsequently in the derivation

$$
\begin{aligned}
\mathscr{L}\{\cos(n\omega_r t)x(t)\} &= \mathscr{L}\left\{\frac{e^{jn\omega_r t}+e^{-jn\omega_r t}}{2}x(t)\right\} = \frac{1}{2}\big(X(s-jn\omega_r)-X(s+jn\omega_r)\big),\\
\mathscr{L}\{\sin(n\omega_r t)x(t)\} &= \mathscr{L}\left\{\frac{\left(e^{jn\omega_r t}-e^{-jn\omega_r t}\right)}{2j}x(t)\right\} = \frac{1}{2j}\big(X(s-jn\omega_r)-X(s+jn\omega_r)\big),
\end{aligned}
$$

where $x(t)$ is an arbitrary signal, and $X(s)$ is its Laplace transform. With a slight abuse of notation, the frequency-shifted Laplace operators are defined as follows:

$$
\begin{aligned}
s_- &= s - jn\omega_r,\\
s_+ &= s + jn\omega_r,
\end{aligned}
$$

where $n \in \mathbb{Z}^+$ is the harmonic number and $j = \sqrt{-1}$ is the imaginary unit.

3

3.3.2. FORWARD MBC TRANSFORMATION

The time-domain representation of the forward MBC transformation in Equation (3.1), is now rewritten using trigonometric identities (Stewart, 2009) as follows:

$$M_{\text{tilt}}(t) = \frac{2}{3}\sum_{b=1}^{3} M_b(t)\left[\cos(n\omega_{\text{r}}t)\cos\left(\frac{2\pi n(b-1)}{3}\right) - \sin(n\omega_{\text{r}}t)\sin\left(\frac{2\pi n(b-1)}{3}\right)\right],$$
$$M_{\text{yaw}}(t) = \frac{2}{3}\sum_{b=1}^{3} M_b(t)\left[\sin(n\omega_{\text{r}}t)\cos\left(\frac{2\pi n(b-1)}{3}\right) + \cos(n\omega_{\text{r}}t)\sin\left(\frac{2\pi n(b-1)}{3}\right)\right].$$

Now the cyclic modes are transformed to their frequency-domain representation as follows:

$$\begin{aligned}\begin{bmatrix} M_{\text{tilt}}(s) \\ M_{\text{yaw}}(s)\end{bmatrix} &= \underbrace{\frac{2}{3}\frac{1}{2}\begin{bmatrix} 1 & j \\ -j & 1\end{bmatrix}\begin{bmatrix}\cos(0) & \cos(2\pi n/3) & \cos(4\pi n/3) \\ \sin(0) & \sin(2\pi n/3) & \sin(4\pi n/3)\end{bmatrix}}_{C_{\text{L},n}}\begin{bmatrix} M_1(s_-) \\ M_2(s_-) \\ M_3(s_-)\end{bmatrix} \\ &+ \underbrace{\frac{2}{3}\frac{1}{2}\begin{bmatrix} 1 & -j \\ j & 1\end{bmatrix}\begin{bmatrix}\cos(0) & \cos(2\pi n/3) & \cos(4\pi n/3) \\ \sin(0) & \sin(2\pi n/3) & \sin(4\pi n/3)\end{bmatrix}}_{C_{\text{H},n}}\begin{bmatrix} M_1(s_+) \\ M_2(s_+) \\ M_3(s_+)\end{bmatrix},\end{aligned} \tag{3.5}$$

where $\boldsymbol{C}_{\text{L},n}$ and $\boldsymbol{C}_{\text{H},n}$ are referred to as the *low* and *high* partial transformation matrices, respectively, because of their association with signals of lower and higher frequencies. By inspection of Equation (3.5) it is already shown that the rotor speed dependent nP harmonic is transferred to a DC-component.

3.3.3. REVERSE MBC TRANSFORMATION

Next, the time-domain expression of the reverse MBC transformation is rewritten as follows:

$$\begin{aligned}\theta_b(t) = \theta_{\text{tilt}}(t)&\left[\cos(n\omega_{\text{r}}t)\cos\left(\frac{2\pi n(b-1)}{3}\right) - \sin(n\omega_{\text{r}}t)\sin\left(\frac{2\pi n(b-1)}{3}\right)\right] \\ +\theta_{\text{yaw}}(t)&\left[\sin(n\omega_{\text{r}}t)\cos\left(\frac{2\pi n(b-1)}{3}\right) + \cos(n\omega_{\text{r}}t)\sin\left(\frac{2\pi n(b-1)}{3}\right)\right],\end{aligned} \tag{3.6}$$

and is transformed to its frequency-domain representation by

$$\begin{aligned}\begin{bmatrix}\theta_1(s) \\ \theta_2(s) \\ \theta_3(s)\end{bmatrix} &= \underbrace{\frac{1}{2}\begin{bmatrix}\cos(0) & \sin(0) \\ \cos(2\pi n/3) & \sin(2\pi n/3) \\ \cos(4\pi n/3) & \sin(4\pi n/3)\end{bmatrix}\begin{bmatrix} 1 & -j \\ j & 1\end{bmatrix}}_{C^T_{\text{L},n}}\begin{bmatrix}\theta_{\text{tilt}}(s_-) \\ \theta_{\text{yaw}}(s_-)\end{bmatrix} \\ &+ \underbrace{\frac{1}{2}\begin{bmatrix}\cos(0) & \sin(0) \\ \cos(2\pi n/3) & \sin(2\pi n/3) \\ \cos(4\pi n/3) & \sin(4\pi n/3)\end{bmatrix}\begin{bmatrix} 1 & j \\ -j & 1\end{bmatrix}}_{C^T_{\text{H},n}}\begin{bmatrix}\theta_{\text{tilt}}(s_+) \\ \theta_{\text{yaw}}(s_+)\end{bmatrix},\end{aligned} \tag{3.7}$$

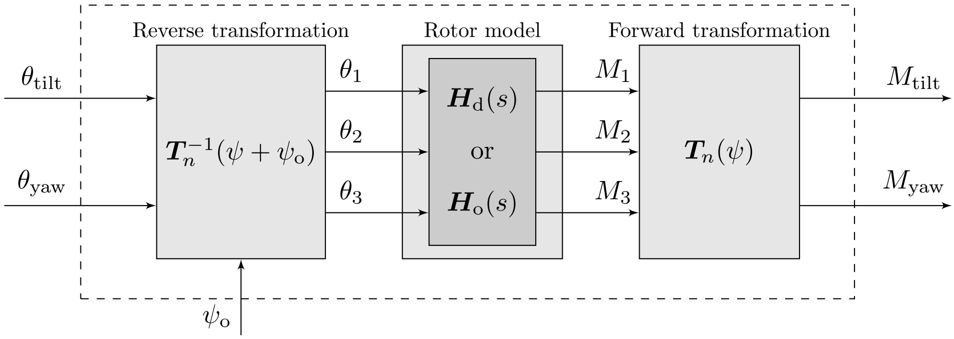

Figure 3.5: Open-loop nonrotating wind turbine system with fixed-frame input pitch angles θ_{tilt} and θ_{yaw}, and output blade moments M_{tilt} and M_{yaw}. For linear analysis purposes, either the diagonal $\boldsymbol{H}_{\mathrm{d}}(s)$ rotor model including, or the coupled $\boldsymbol{H}_{\mathrm{o}}(s)$ rotor model excluding cross-terms is considered.

where it is seen that the *low* and *high* partial transformation matrices reoccur in a transposed manner. The partial transformation matrices have the remarkable property that $\boldsymbol{C}_{\mathrm{L},n}\boldsymbol{C}_{\mathrm{L},n}^T = 0$ and $\boldsymbol{C}_{\mathrm{H},n}\boldsymbol{C}_{\mathrm{H},n}^T = 0$, which appears to be useful later on.

3.3.4. COMBINING THE RESULTS: DECOUPLED BLADE DYNAMICS

Now that the frequency-domain representations of the MBC transformations are defined, the rotor model structure is chosen to be diagonal in this section. In Figure 3.5, the open-loop system with nonrotating pitch angles as input and nonrotating blade moments as output is presented. The diagonal rotor model in the rotating frame is defined as follows:

$$\begin{bmatrix} M_1(s) \\ M_2(s) \\ M_3(s) \end{bmatrix} = \underbrace{\begin{bmatrix} H_1(s) & 0 & 0 \\ 0 & H_1(s) & 0 \\ 0 & 0 & H_1(s) \end{bmatrix}}_{\boldsymbol{H}_{\mathrm{d}}(s)} \begin{bmatrix} \theta_1(s) \\ \theta_2(s) \\ \theta_3(s) \end{bmatrix}, \tag{3.8}$$

such that pitch angle $\theta_i(s)$ and blade moment $M_j(s)$ are only related for $i = j$. As will be shown later, the assumption of a diagonal rotor model structure is convenient for analysis purposes, but nonrealistic for actual turbines. By substitution of the rotor model from Equation (3.8) into the forward MBC frequency-domain relation in Equation (3.5), and subsequently substituting Equation (3.7), the following transformed frequency-domain representation is obtained:

$$\begin{aligned} \begin{bmatrix} M_{\mathrm{tilt}}(s) \\ M_{\mathrm{yaw}}(s) \end{bmatrix} = {} & \frac{2}{3}\boldsymbol{C}_{\mathrm{L},n}\, H_1(s_-)\, \boldsymbol{I}_3 \left(\boldsymbol{C}_{\mathrm{L},n}^T \begin{bmatrix} \theta_{\mathrm{tilt}}(s-2jn\omega_{\mathrm{r}}) \\ \theta_{\mathrm{yaw}}(s-2jn\omega_{\mathrm{r}}) \end{bmatrix} + \boldsymbol{C}_{\mathrm{H},n}^T \begin{bmatrix} \theta_{\mathrm{tilt}}(s) \\ \theta_{\mathrm{yaw}}(s) \end{bmatrix} \right) \\ & + \frac{2}{3}\boldsymbol{C}_{\mathrm{H},n}\, H_1(s_+)\, \boldsymbol{I}_3 \left(\boldsymbol{C}_{\mathrm{L},n}^T \begin{bmatrix} \theta_{\mathrm{tilt}}(s) \\ \theta_{\mathrm{yaw}}(s) \end{bmatrix} + \boldsymbol{C}_{\mathrm{H},n}^T \begin{bmatrix} \theta_{\mathrm{tilt}}(s+2jn\omega_{\mathrm{r}}) \\ \theta_{\mathrm{yaw}}(s+2jn\omega_{\mathrm{r}}) \end{bmatrix} \right). \end{aligned} \tag{3.9}$$

Since $\boldsymbol{C}_{\mathrm{L},n}\boldsymbol{C}_{\mathrm{L},n}^T = \boldsymbol{C}_{\mathrm{H},n}\boldsymbol{C}_{\mathrm{H},n}^T = 0$, the expression simplifies into

$$\begin{bmatrix} M_{\mathrm{tilt}}(s) \\ M_{\mathrm{yaw}}(s) \end{bmatrix} = \frac{1}{2}\left(H_1(s_-)\, \boldsymbol{I}_2 \begin{bmatrix} 1 & j \\ -j & 1 \end{bmatrix} + H_1(s_+)\, \boldsymbol{I}_2 \begin{bmatrix} 1 & -j \\ j & 1 \end{bmatrix} \right) \begin{bmatrix} \theta_{\mathrm{tilt}}(s) \\ \theta_{\mathrm{yaw}}(s) \end{bmatrix}, \tag{3.10}$$

where $\boldsymbol{I}_2 \in \mathbb{R}^{2\times 2}$ is an identity matrix, and is rewritten as the transfer function matrix

$$\begin{bmatrix} M_{\text{tilt}}(s) \\ M_{\text{yaw}}(s) \end{bmatrix} = \underbrace{\frac{1}{2}\begin{bmatrix} H_1(s_-)+H_1(s_+) & jH_1(s_-)-jH_1(s_+) \\ -jH_1(s_-)+jH_1(s_+) & H_1(s_-)+H_1(s_+) \end{bmatrix}}_{\boldsymbol{P}_{\text{d}}(s,\omega_{\text{r}})} \begin{bmatrix} \theta_{\text{tilt}}(s) \\ \theta_{\text{yaw}}(s) \end{bmatrix}. \tag{3.11}$$

Although the wind turbine blade models $H_1(s)$ in Equation (3.8) are implemented in a decoupled way, it is seen that the off-diagonal terms are nonzero when the response of $H(s)$ is frequency dependent (nonconstant). Thus, the presumably decoupled tilt and yaw-axes show cross-coupling in $\boldsymbol{P}_{\text{d}}(s,\omega_{\text{r}})$ when a diagonal and dynamic rotor model is considered. This conclusion was drawn earlier (Lu et al., 2015). However, in the next section, the assumption of a diagonal rotor model is alleviated by the introduction of cross-terms.

3.3.5. COMBINING THE RESULTS: COUPLED BLADE DYNAMICS

In the previous section, the rotor model was assumed to consist of decoupled blade models. Now, this assumption is alleviated by incorporating off-diagonal blade models

$$\begin{bmatrix} M_1(s) \\ M_2(s) \\ M_3(s) \end{bmatrix} = \underbrace{\begin{bmatrix} H_1(s) & H_2(s) & H_2(s) \\ H_2(s) & H_1(s) & H_2(s) \\ H_2(s) & H_2(s) & H_1(s) \end{bmatrix}}_{\boldsymbol{H}_{\text{o}}(s)} \begin{bmatrix} \theta_1(s) \\ \theta_2(s) \\ \theta_3(s) \end{bmatrix}, \tag{3.12}$$

such that coupling is also present between pitch angle $\theta_i(s)$ and blade moment $M_j(s)$ for $i \neq j$ by $H_2(s)$: In Section 3.5.1 it is shown that this model structure represents the interactions of high-fidelity model linearizations. The derivation to arrive at the transfer function matrix $\boldsymbol{P}_{\text{o}}(s,\omega_{\text{r}})$ is omitted in this section, as it follows a similar procedure given in the previous section. The resulting matrix is given by

$$\begin{bmatrix} M_{\text{tilt}}(s) \\ M_{\text{yaw}}(s) \end{bmatrix} = \underbrace{\frac{1}{2}\begin{bmatrix} H_{12}(s_-)+H_{12}(s_+) & jH_{12}(s_-)-jH_{12}(s_+) \\ -jH_{12}(s_-)+jH_{12}(s_+) & H_{12}(s_-)+H_{12}(s_+) \end{bmatrix}}_{\boldsymbol{P}_{\text{o}}(s,\omega_{\text{r}})} \begin{bmatrix} \theta_{\text{tilt}}(s) \\ \theta_{\text{yaw}}(s) \end{bmatrix}, \tag{3.13}$$

with

$$H_{12}(s) = H_1(s) - H_2(s). \tag{3.14}$$

As will be shown later, the obtained model structure is better able to identify the optimal azimuth offset opposed to the result from Section 3.3.4, for operating conditions with increased dynamic blade coupling. The following section incorporates the azimuth offset in the framework for both the decoupled and coupled rotor model structures.

3.3.6. INCLUSION OF THE AZIMUTH OFFSET

In this section, the effect on the main and off-diagonal terms by incorporating an azimuth offset $\psi_{\text{o}} \in \mathbb{R}$ in the reverse transformation is considered: Variables subject to the effect of the offset are denoted with a tilde $\tilde{(\cdot)}$. Multiplication of the transformation matrices $\boldsymbol{T}(\psi)\tilde{\boldsymbol{T}}^{-1}(\psi+\psi_{\text{o}})$ for $\psi_{\text{o}} \neq 0$ does not result in an identity matrix, and influences the diagonal and off-diagonal terms in the transfer function matrix $\tilde{\boldsymbol{P}}$. For evaluation of this effect, Equation (3.7) is expanded by adding the azimuth offset to the nominal azimuth such that the following expression is obtained:

$$\begin{aligned}\begin{bmatrix}\theta_1(s)\\ \theta_2(s)\\ \theta_3(s)\end{bmatrix} &= \underbrace{\frac{1}{2}\begin{bmatrix}\cos(n\psi_o) & \sin(n\psi_o)\\ \cos(n(2\pi/3+\psi_o)) & \sin(n(2\pi/3+\psi_o))\\ \cos(n(4\pi/3+\psi_o)) & \sin(n(4\pi/3+\psi_o))\end{bmatrix}\begin{bmatrix}1 & -j\\ j & 1\end{bmatrix}}_{\tilde{\boldsymbol{C}}^T_{\mathrm{L},n}(\psi_o)}\begin{bmatrix}\theta_{\mathrm{tilt}}(s_-)\\ \theta_{\mathrm{yaw}}(s_-)\end{bmatrix}\\ &+\underbrace{\frac{1}{2}\begin{bmatrix}\cos(n\psi_o) & \sin(n\psi_o)\\ \cos(n(2\pi/3+\psi_o)) & \sin(n(2\pi/3+\psi_o))\\ \cos(n(4\pi/3+\psi_o)) & \sin(n(4\pi/3+\psi_o))\end{bmatrix}\begin{bmatrix}1 & j\\ -j & 1\end{bmatrix}}_{\tilde{\boldsymbol{C}}^T_{\mathrm{H},n}(\psi_o)}\begin{bmatrix}\theta_{\mathrm{tilt}}(s_+)\\ \theta_{\mathrm{yaw}}(s_+)\end{bmatrix}.\end{aligned} \tag{3.15}$$

where the partial transformation matrices now include the azimuth offset and are redefined using trigonometric identities as follows:

$$\tilde{\boldsymbol{C}}^T_{\mathrm{L},n}(\psi_o) = \frac{1}{2}\begin{bmatrix}\cos(0) & \sin(0)\\ \cos(2\pi n/3) & \sin(2\pi n/3)\\ \cos(4\pi n/3) & \sin(4\pi n/3)\end{bmatrix}\begin{bmatrix}\cos(n\psi_o) & \sin(n\psi_o)\\ -\sin(n\psi_o) & \cos(n\psi_o)\end{bmatrix}\begin{bmatrix}1 & -j\\ j & 1\end{bmatrix}, \tag{3.16}$$

$$\tilde{\boldsymbol{C}}^T_{\mathrm{H},n}(\psi_o) = \frac{1}{2}\begin{bmatrix}\cos(0) & \sin(0)\\ \cos(2\pi n/3) & \sin(2\pi n/3)\\ \cos(4\pi n/3) & \sin(4\pi n/3)\end{bmatrix}\begin{bmatrix}\cos(n\psi_o) & \sin(n\psi_o)\\ -\sin(n\psi_o) & \cos(n\psi_o)\end{bmatrix}\begin{bmatrix}1 & j\\ -j & 1\end{bmatrix}. \tag{3.17}$$

Comparing the partial transformation matrices to the with results obtained earlier in Equations (3.5) and (3.7) shows the addition of a rotation matrix. By applying the correct (optimal) phase offset, the rotation matrix corrects for the phase losses in the rotating frame, and lets the transformed axes coincide with the horizontal tilt and vertical yaw

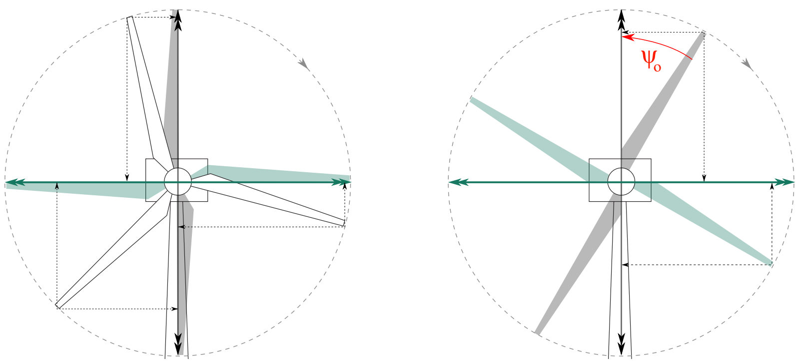

Figure 3.6: ***Left:*** In the ideal case, the MBC transformation transforms the blade bending moments from a rotating to a nonrotating orthogonal reference frame, aligning with the horizontal tilt and vertical yaw axes. ***Right:*** However, when system phase losses are involved, the orthogonal projection is twisted. As a result, the transformed system has off-diagonal contributions to both the tilt and yaw axes, which results in multivariable coupling. The azimuth offset serves as a correction to realign the twisted projection with the tilt and yaw axes.

axes in the nonrotating frame. Figure 3.6 further illustrates and explains this effect. Furthermore, the matrix is a normalized version of the steady-state gain matrix of the inverse plant (Ungurán et al., 2019), and can alternatively be taken as part of the controller outside the transformed system.

By deriving the transformation matrix for the decoupled rotor model structure, now including the azimuth offset, results in

$$\begin{bmatrix} M_{\text{tilt}}(s) \\ M_{\text{yaw}}(s) \end{bmatrix} = \tilde{\boldsymbol{P}}_{\text{d}}(s, \omega_{\text{r}}, \psi_{\text{o}}) \begin{bmatrix} \theta_{\text{tilt}}(s) \\ \theta_{\text{yaw}}(s) \end{bmatrix}, \tag{3.18}$$

whereas the matrix is defined for the coupled case as follows:

$$\begin{bmatrix} M_{\text{tilt}}(s) \\ M_{\text{yaw}}(s) \end{bmatrix} = \tilde{\boldsymbol{P}}_{\text{o}}(s, \omega_{\text{r}}, \psi_{\text{o}}) \begin{bmatrix} \theta_{\text{tilt}}(s) \\ \theta_{\text{yaw}}(s) \end{bmatrix}, \tag{3.19}$$

in which

$$\tilde{\boldsymbol{P}}_{\text{d}} = \frac{1}{2} \begin{bmatrix} H(s_-)\tilde{p}(\psi_{\text{o}}) + H(s_+)\tilde{q}(\psi_{\text{o}}) & jH(s_-)\tilde{p}(\psi_{\text{o}}) - jH(s_+)\tilde{q}(\psi_{\text{o}}) \\ -jH(s_-)\tilde{p}(\psi_{\text{o}}) + jH(s_+)\tilde{q}(\psi_{\text{o}}) & H(s_-)\tilde{p}(\psi_{\text{o}}) + H(s_+)\tilde{q}(\psi_{\text{o}}) \end{bmatrix},$$

$$\tilde{\boldsymbol{P}}_{\text{o}} = \frac{1}{2} \begin{bmatrix} H_{12}(s_-)\tilde{p}(\psi_{\text{o}}) + H_{12}(s_+)\tilde{q}(\psi_{\text{o}}) & jH_{12}(s_-)\tilde{p}(\psi_{\text{o}}) - jH_{12}(s_+)\tilde{q}(\psi_{\text{o}}) \\ -jH_{12}(s_-)\tilde{p}(\psi_{\text{o}}) + jH_{12}(s_+)\tilde{q}(\psi_{\text{o}}) & H_{12}(s_-)\tilde{p}(\psi_{\text{o}}) + H_{12}(s_+)\tilde{q}(\psi_{\text{o}}) \end{bmatrix},$$

and where $\tilde{p}(\psi_{\text{o}})$ and $\tilde{q}(\psi_{\text{o}})$ are

$$\tilde{p}(\psi_{\text{o}}) = \cos(n\psi_{\text{o}}) - j\sin(n\psi_{\text{o}}),$$
$$\tilde{q}(\psi_{\text{o}}) = \cos(n\psi_{\text{o}}) + j\sin(n\psi_{\text{o}}).$$

From the above derived result, it is concluded that the azimuth offset influences the main and off-diagonal terms for both the coupled and decoupled cases. By comparing Equations 3.18 and 3.19, it is observed that both are similar, but the latter mentioned differs in a way that cross-coupling between the blade models influences the nonrotating dynamics. As a result, the optimal offset value will be different for both cases. An analysis using simplified blade models is given in the next section.

3.4. ANALYSIS ON SIMPLIFIED ROTOR MODELS

This section showcases the effect and implications of the azimuth offset using simplified models, for both decoupled and coupled rotor model structures in Sections 3.4.1 and 3.4.2, respectively. First-order linear dynamic blade models are taken, as this allows for a convenient assessment of the offset effects: Application of higher-order models would result in a similar analysis.

3.4.1. DECOUPLED BLADE DYNAMICS

The decoupled rotor model is made up of first-order blade models of the form

$$H_1(s) = \frac{M_b}{\theta_b} = K_1 \frac{1}{\tau_1 s + 1}, \tag{3.20}$$

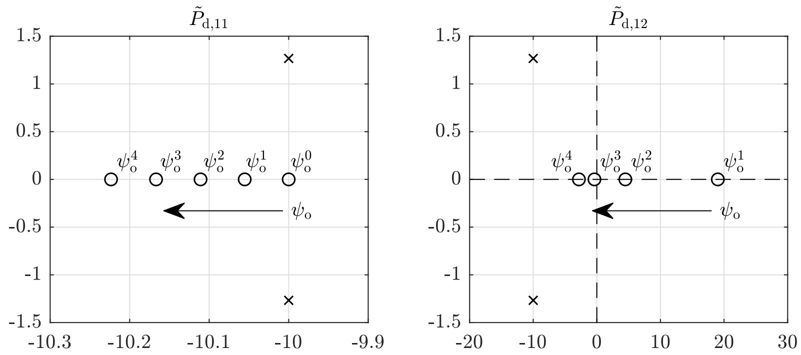

Figure 3.7: Pole-zero map for the main- and off-diagonal transfer functions in $\tilde{P}_{11}$ and $\tilde{P}_{12}$, respectively. It is shown that for the assumed model $H_1(s)$ with $K_1 = 1$ and $\tau_1 = 0.1$, the azimuth offset influences the location of the open-loop zeros (∘) in both cases; the pole (×) locations remain unchanged. The magnitude of the cross-terms is minimized by choosing the optimal offset value ψ_o^*.

where K_1 is the steady-state gain, and τ_1 the time constant of the transfer function. As the main-diagonal elements of $\tilde{\boldsymbol{P}}_d$ are equal and the off-diagonal elements are the same up to a sign-change, only the transfer functions in the matrix upper row are considered. By substitution of $s = j\omega$, the frequency response function of the diagonal elements is given by

$$\begin{aligned}\tilde{P}_{d,11}(j\omega,\omega_r,\psi_o) = \tilde{P}_{d,22}(j\omega,\omega_r,\psi_o) = \\ K_1 \frac{\tau_1\omega\cos(\psi_o) - (\tau_1\omega_r\sin(\psi_o) + \cos(\psi_o))\,j}{2\tau_1\omega + (\tau_1^2\omega^2 - \tau_1^2\omega_r^2 - 1)\,j},\end{aligned} \tag{3.21}$$

and the frequency response functions of the off-diagonal terms are represented by

$$\begin{aligned}\tilde{P}_{d,12}(j\omega,\omega_r,\psi_o) = -\tilde{P}_{d,21}(j\omega,\omega_r,\psi_o) = \\ K_1 \frac{-\tau_1\omega\sin(\psi_o) - \big(\tau_1\omega_r\cos(\psi_o) - \sin(\psi_o)\big)\,j}{2\tau_1\omega + (\tau_1^2\omega^2 - \tau_1^2\omega_r^2 - 1)\,j}.\end{aligned} \tag{3.22}$$

In both expressions the azimuth offset only occurs in the numerator. For the off-diagonal expression in Equation (3.22), the low-frequency magnitude ($\omega \to 0$) can be attenuated using the offset. In effect, the complex term in the frequency response function of Equation (3.22) cancels out, and minimizes the low-frequency gain.

For illustration purposes, the transfer function $H_1(s)$ is taken with a steady-state gain $K_1 = 1$, a time constant $\tau_1 = 0.1$ s and a rotor speed $\omega_r = 1.27$ rad s^{-1}, which is the rated speed of the NREL 5-MW reference turbine. In Figure 3.7, pole-zero diagrams are given for the transfer function elements $\tilde{P}_{d,11}$ and $\tilde{P}_{d,12}$. For the latter mentioned transfer function, the offset introduces a zero, which is nonpresent in the case of $\psi_o = 0$. The offset is used to actively influence the zero location, and does not affect the pole locations. The zero attains a lower real value for increasing offsets. The optimal offset moves the introduced off-diagonal zero to the imaginary axis to form a pure differentiator, of which the effect is shown in Figure 3.8. For the same optimal offset, the steady-state gain of the diagonal term is maximized. The influence of the offset on the main diagonal steady-state low-frequency gain should be taken into account during controller design. That is, including the optimal offset increases the bandwidth of the open-loop gain.

For a decoupled rotor model consisting of first-order blade dynamics, the optimal offset is analytically computed by

$$\psi^*_{\mathrm{o,d}} = \tan^{-1}(\tau_1 \omega_{\mathrm{r}}). \tag{3.23}$$

Calculation of the optimal offset results in $\psi^*_{\mathrm{o,d}} = 7.22$ deg, which is in accordance to the near-optimal result found in Figure 3.8. Figure 3.9 presents the RGA of $\tilde{P}_{\mathrm{d},12}$ over a range of first-order model time constants and azimuth offsets. It is shown that a clear optimal offset path is present, which is predicted using the analytic expression given above. It is furthermore concluded that for the decoupled blade model case, the optimal offset is equal to the phase loss of the blade pitch to blade moment system at the considered nP harmonic. Equation (3.23) also shows that the optimal offset is dependent on the rotor speed, which is of importance when IPC is applied in the below-rated operating region.

3.4.2. COUPLED BLADE DYNAMICS

The derivation is now performed for the rotor model with coupled blade dynamics, $\tilde{\boldsymbol{P}}_{\mathrm{o}}$. The main-diagonal transfer function $H_1(s)$ is taken as in Equation (3.20), whereas two distinct cases for the off-diagonal model $H_2(s)$ are examined. The first case is a reduced magnitude version of $H_1(s)$ with $K_2 = \delta K_1$ where $\{\delta \subset \mathbb{R} \mid 0 < \delta < 1\}$, and the second case additionally has a time constant $\tau_2 \neq \tau_1$. The transfer function is given by

$$H_2(s) = \frac{M_i}{\theta_j} = K_2 \frac{1}{\tau_2 s + 1} \quad \text{with} \quad i \neq j, \tag{3.24}$$

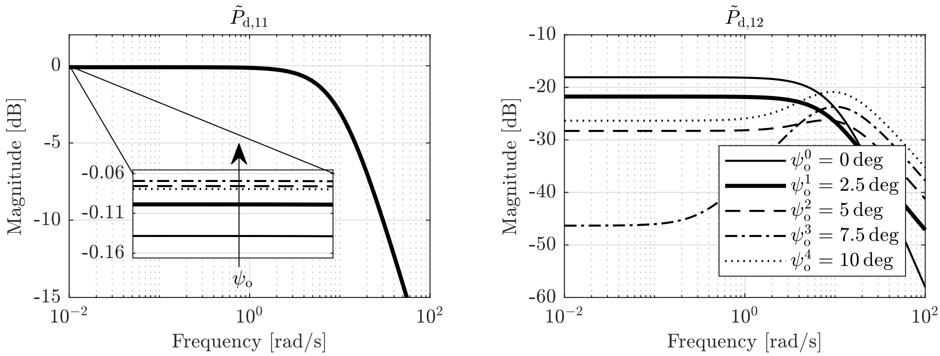

Figure 3.8: Bode diagrams of $\tilde{P}_{\mathrm{d},11}$ and $\tilde{P}_{\mathrm{d},12}$ for different ψ_{o}. The steady-state gain of the diagonal term increases, whereas the gain of the off-diagonal term decreases up to a certain offset value.

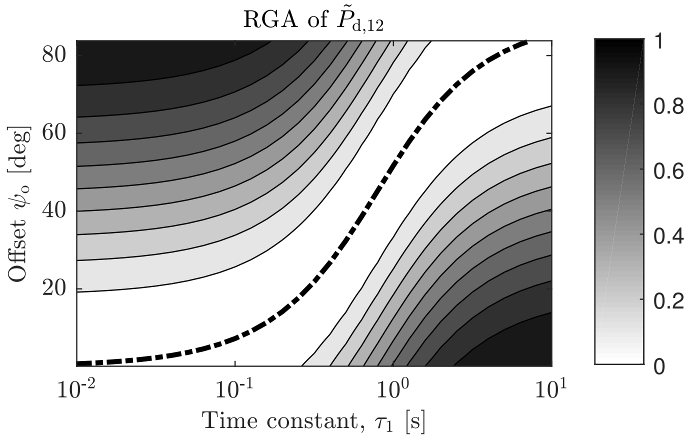

Figure 3.9: RGA of $\tilde{P}_{\mathrm{d},12}$ evaluated at $\omega = 0$ for the decoupled rotor model structure. The dash-dotted line represents the optimal offset found by the analytical expression. It is shown that the optimal offset is highly dependent on the model dynamics.

and according to Equation (3.14), the resulting expressions of the combined transfer functions become

$$\textbf{Case 1: } K_2 = \delta K_1,\ \tau_1 = \tau_2 \qquad H_{12}^1(s) = K_1(1-\delta)\frac{1}{\tau_1 s + 1}, \tag{3.25}$$

$$\textbf{Case 2: } K_2 = \delta K_1,\ \tau_1 \neq \tau_2 \qquad H_{12}^2(s) = \frac{K_1(\tau_2 s + 1) - K_2(\tau_1 s + 1)}{(\tau_1 s + 1)(\tau_2 s + 1)}. \tag{3.26}$$

By comparing Equation (3.20) and (3.25) it is immediately recognized that for the first case, the result is only scaled by a factor δ and does not influence the optimal offset. However, for the second case, the resulting transfer function changes significantly for which the derivation is performed. The resulting elements of the matrix upper row of $\tilde{\boldsymbol{P}}_\mathrm{o}$ are as follows:

$$\begin{aligned}\tilde{P}_{\mathrm{o},11}(j\omega,\omega_\mathrm{r},\psi_\mathrm{o}) &= \tilde{P}_{\mathrm{o},22}(j\omega,\omega_\mathrm{r},\psi_\mathrm{o})\\ &= \frac{\tilde{p}(\psi_\mathrm{o})}{2}\left(\frac{K_1}{\tau_1(\omega-\omega_\mathrm{r})j+1} - \frac{K_2}{\tau_2(\omega-\omega_\mathrm{r})j+1}\right)\\ &+ \frac{\tilde{q}(\psi_\mathrm{o})}{2}\left(\frac{K_1}{\tau_1(\omega+\omega_\mathrm{r})j+1} - \frac{K_2}{\tau_2(\omega+\omega_\mathrm{r})j+1}\right),\end{aligned} \tag{3.27}$$

$$\begin{aligned}\tilde{P}_{\mathrm{o},12}(j\omega,\omega_\mathrm{r},\psi_\mathrm{o}) &= -\tilde{P}_{\mathrm{o},21}(j\omega,\omega_\mathrm{r},\psi_\mathrm{o})\\ &= \frac{\tilde{p}(\psi_\mathrm{o})j}{2}\left(\frac{K_1}{\tau_1(\omega-\omega_\mathrm{r})j+1} - \frac{K_2}{\tau_2(\omega-\omega_\mathrm{r})j+1}\right)\\ &- \frac{\tilde{q}(\psi_\mathrm{o})j}{2}\left(\frac{K_1}{\tau_1(\omega+\omega_\mathrm{r})j+1} - \frac{K_2}{\tau_2(\omega+\omega_\mathrm{r})j+1}\right).\end{aligned} \tag{3.28}$$

Further substitution and manipulations of the above given relations lead to cumbersome expressions. However, also in this case, it is possible to nullify the numerator using the

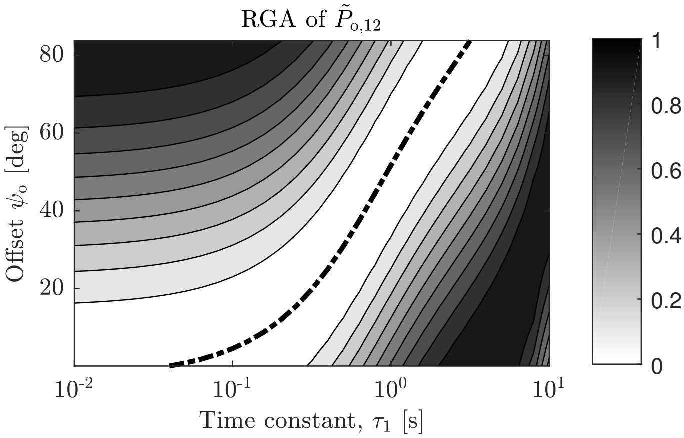

Figure 3.10: RGA of $\tilde{P}_{o,12}$ evaluated at $\omega = 0$ for the coupled rotor model structure. The dash-dotted line represents the optimal offset found by the analytical expression. It is shown that the optimal offset is highly dependent on the combined diagonal and off-diagonal dynamic model characteristics and differs significantly from the characteristics found for the decoupled case.

optimal azimuth offset given by the analytic expression

$$\psi^*_{o,o} = \tan^{-1}\left(\frac{K_1\tau_1(1+\tau_2^2\omega_r^2) - K_2\tau_2(1+\tau_1^2\omega_r^2)}{K_1(1+\tau_2^2\omega_r^2) - K_2(1+\tau_1^2\omega_r^2)}\omega_r\right), \tag{3.29}$$

where for the case $K_2 = 0$ (no coupling), the relation reduces to the expression given by Equation (3.23).

For illustration purposes, the constants K_1, τ_1 and ω_r are taken as in Section 3.4.1, and $K_2 = 0.1$ and $\tau_2 = 1$ s. Using these values, the optimal offset is calculated being $\psi^*_{o,o} = 4.60$ deg, which differs from the result found in the previous section. Furthermore, Figure 3.10 shows the off-diagonal RGA for the coupled rotor case. It is shown that the decoupling characteristics differ significantly from the results obtained in Figure 3.9, especially for higher time constants (slower blade dynamics). The main conclusion of this section is that the chosen rotor model structure, including or excluding blade dynamic coupling, has a high influence on the analysis for finding the optimal offset value.

3.5. RESULTS ON THE NREL 5-MW REFERENCE WIND TURBINE

The previous section shows significant improvements on the decoupling of transformed model structures using simplified blade models. This section is devoted to the validation of the described theory on linearizations of the NREL 5-MW reference wind turbine. In Section 3.5.1, linearizations of the NREL 5-MW reference turbine are obtained and used in Section 3.5.2 to compute the optimal offset. The results are subsequently validated against the nonparametric spectral models presented in the problem formalization (Section 3.2.2).

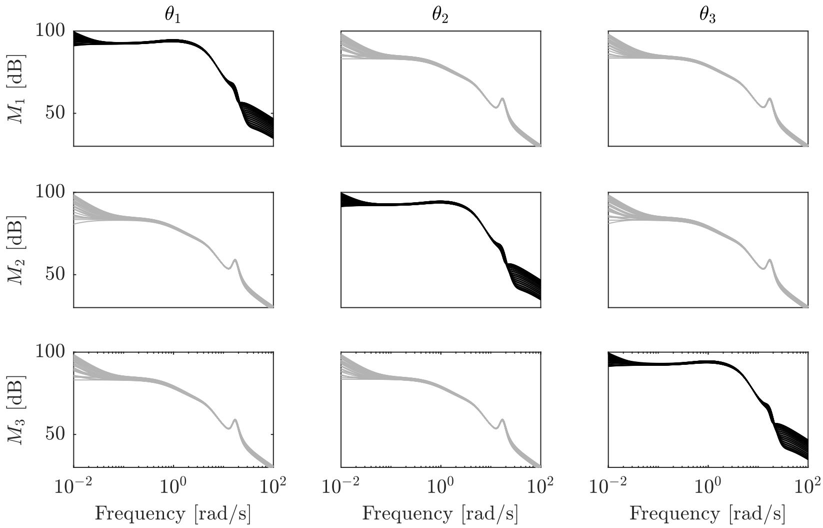

Figure 3.11: Main- and off-diagonal linear models of the NREL 5-MW blade dynamics in black and gray, respectively, showing the dynamics from blade pitch θ_i to out-of-plane blade root moment M_j in the rotating frame. It is shown that the off-diagonal dynamics have an overall reduced, but nonnegligible magnitude compared to the main-diagonal elements.

3.5.1. Obtaining linearizations in the rotating frame

Linearizations of the NREL 5-MW turbine are obtained using an extension (Bos et al., 2019) for NREL's FAST v8.16. The extension program includes a graphical user interface (GUI) and functionality for determining trim conditions prior to the open-loop simulations for linearization. Linear models are obtained for wind speeds $U = 5 - 25$ m s^{-1}.

The resulting state-space model for each wind speed consists of the system $A \in \mathbb{R}^{r\times r\times k}$, input $B \in \mathbb{R}^{r\times p\times k}$, output $C \in \mathbb{R}^{q\times r\times k}$ and direct feedthrough $D \in \mathbb{R}^{q\times p\times k}$ matrices. Over a full rotor rotation, $k = 36$ evenly spaced models are obtained with a model order $r = 14$ and $p = q = 3$ inputs and outputs. Figure 3.11 presents the linearization results by means of Bode magnitude plots from blade pitch to blade moment for a wind speed of $U = 25$ m s^{-1}. This wind speed is chosen as an exemplary case, as the effect of dynamic blade coupling becomes more apparent for higher wind speed conditions. As the models are defined in a rotating reference frame, the dynamics vary with the rotor position. However, it can be seen that the dynamics from θ_i to M_j show similar dynamics for both $i = j$ and $i \neq j$. The linearizations include first-order pitch actuator dynamics with a bandwidth of $\omega_{\mathrm{a}} = 2.5$ rad s^{-1}. The next sections elaborate on the effect of including and excluding the cross terms in the analysis.

3.5.2. Transforming linear models and evaluating decoupling

As recognized previously by inspection of Figure 3.11, the set of diagonal and off-diagonal models show similar dynamics. The effect of this coupling on the optimal azimuth offset is investigated in this section using linearizations of the NREL 5-MW turbine.

Up to this point, the analysis of the effect of the azimuth offset is illustrated us-

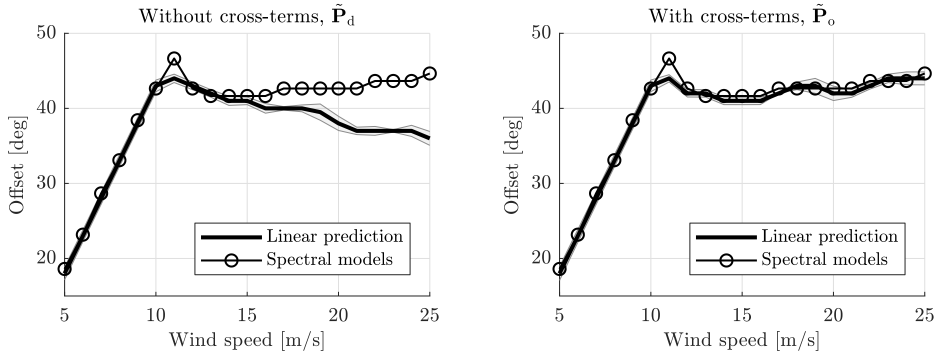

Figure 3.12: Linear prediction of the optimal azimuth offset over k linearizations, where the median per wind speed is taken as the optimal offset value. The transformation is applied for the cases of decoupled (left) and coupled (right) blade dynamics. It is shown that the inclusion of blade coupling is able to better explain the results obtained from spectral analysis.

ing a multiple input multiple output (MIMO) transfer function representation. However, transforming higher-order models (e.g., linearizations obtained from FAST) in this representation can become numerically challenging. Therefore, Appendix A includes a derivation of the MBC transformation including the offset in the state-space system representation. Because this approach only requires subsequent matrix multiplications, the implementation is faster and numerically more stable. However, in the remainder of this chapter, the transfer function representation is used to highlight insights for various problem aspects.

In this section, by using the transfer function representation, the off-diagonal elements are easily included and excluded from the analysis. Therefore, the obtained linear state-space systems are converted to transfer functions and transformed to symbolic expressions for substitution of the Laplace operators s by s_- and s_+. The expressions are prevented to become ill-defined by ensuring minimal realizations using a default tolerance of $\sqrt{\epsilon} = 1.5 \cdot 10^{-8}$.

The obtained models are substituted in Equations (3.18) and (3.19). The system interconnection measure $R_\#$ is evaluated at $\omega = 10^{-2}$ rad s^{-1} for each linear model at a range of azimuth offsets. Because k models are obtained, the optimal offset is defined as the median of computed optimal offsets for each set of linear models. In Figure 3.12, the results of the two distinct transformations are presented and compared with the results from spectral analysis in Figure 3.4. The linear prediction of the optimal azimuth offset including the rotor model cross terms clearly outperforms the case excluding the terms. The provided frequency-domain analysis framework, taking into account blade dynamic coupling, is able to provide a concise estimate of the actual optimal azimuth offset.

3.6. ASSESSMENT ON DECOUPLING AND SISO CONTROLLER DESIGN

This section investigates the potential application of single-gain and decoupled SISO control loops for IPC by incorporating the optimal azimuth offset. The former aspect is explored using a sensitivity analysis in Section 3.6.1, whereas the latter aspect is investigated using the Gershgorin circle theorem in Section 3.6.2.

3.6.1. SENSITIVITY ANALYSIS USING SINGULAR VALUES PLOTS

In this section, the effect of the azimuth offset to the sensitivity function is assessed. The sensitivity function using negative feedback is defined as follows:

$$\boldsymbol{S}(j\omega) = \left(\boldsymbol{I}_2 + \boldsymbol{L}(j\omega)\right)^{-1}, \tag{3.30}$$

where $\boldsymbol{L} \in \mathbb{R}^{2\times 2}$ is the open-loop gain, which is defined as the multiplication of the multivariable system and the diagonal controller

$$\boldsymbol{L}(s) = \tilde{\boldsymbol{P}}(s, \omega_\mathrm{r}, \psi_\mathrm{o})\boldsymbol{C}(s), \tag{3.31}$$

where $\boldsymbol{C}(s) = \mathrm{diag}\left(c_1(s),\ c_2(s)\right)$ consists of the pure integrators $c_1(s) = c_2(s) = c_\mathrm{I}/s$. For MIMO systems, the sensitivity function gives information on the effectiveness of control through the bounded ratio

$$\underset{\sim}{\sigma}\left(S(j\omega)\right) \leq \frac{||y(\omega)||_2}{||v(\omega)||_2} \leq \bar{\sigma}(S(j\omega)), \tag{3.32}$$

where $\underset{\sim}{\sigma}\left(S(j\omega)\right)$ indicates the smallest, and $\bar{\sigma}\left(S(j\omega)\right)$ the highest singular value of $S(j\omega)$, determined by the direction of the output and measurement disturbance signals y and v, respectively. For evaluation of the considered MIMO system sensitivity, the singular values of the system frequency response are computed. This is done by performing a singular value decomposition (SVD) on the frequency response of the dynamic system (Skogestad and Postlethwaite, 2007).

The sensitivity is evaluated in the fixed frame for the cases without and with the optimal offset. As the offset influences the steady-state gain of the main-diagonal elements, an integral gain correction is applied when implementing an azimuth offset, which is summarized in Table 3.1. In this way, a consistent open-loop baseline control bandwidth of $2.2 \cdot 10^{-2} \times 2\pi$ rad s^{-1} is attained. It is concluded that the absolute steady-state gain of the main-diagonal terms after transformation with the optimal azimuth offset is increased by 37 %.

Figure 3.13 shows the evaluation of the multivariable sensitivity. The results presented are obtained from high-fidelity simulations (spectral estimate) and from analytical results using the framework presented in this chapter. The trajectories show good

Table 3.1: The integrator gains c_I are corrected for the influence of the azimuth offset in the steady-state gain to obtain a consistent control bandwidth.

$\boldsymbol{\psi}_\mathrm{o}$	0	30	44^*	58	deg
$c_\mathrm{I} \times 10^{-6}$	3.65	2.66	2.65	2.66	rad (Nm s)$^{-1}$

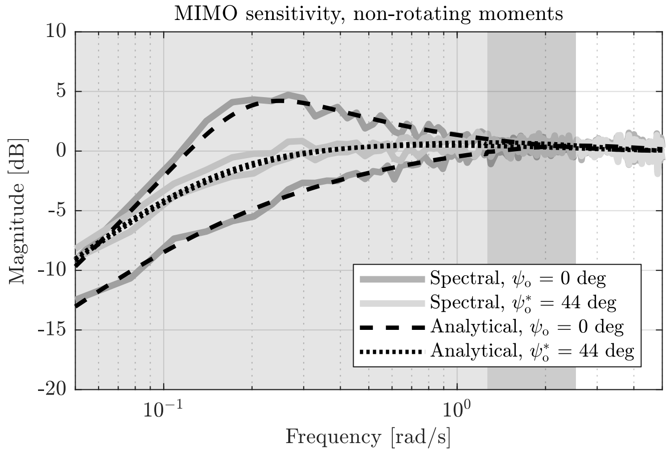

Figure 3.13: Analysis of azimuth offset on the closed-loop sensitivity in the nonrotating frame, including the diagonal gain-corrected controller $\boldsymbol{C}(s)$. The optimal offset reduces the sensitivity peak and compensates for the gain difference between the trajectories.

resemblance for both cases. For the case without an azimuth offset, the peak of the sensitivity function $M_s = \max_{0\le\omega<\infty} |S(j\omega)|$ is the highest, and a significant gain difference between the minimum and maximum sensitivity trajectory is observed. On the contrary, the optimal offset results in a smoothened trajectory and an attenuated sensitivity peak, resulting in a more robust IPC implementation. Furthermore, the minimized gain difference reduces directionality and advocates the applicability of decoupled SISO control loops. The gray-shaded regions $\{0, \omega_r\}$ and $\{\omega_r, 2\omega_r\}$ are used in Section 3.7 for comparison with the rotating blade moments.

3.6.2. DECOUPLING AND STABILITY ANALYSIS USING GERSHGORIN BANDS

Up to this point, a quantification and visualization of the system's degree of decoupling has only been given on simplified linear models using the RGA. For a decoupling and stability analysis of the obtained higher order linearizations, in this section, the Gershgorin circle theorem is employed. The theorem provides both qualitative and quantitative measures of the beforementioned criteria by graphical interpretations and scalar stability margins.

The Gershgorin circle theorem makes use of the Nyquist array containing Nyquist curves of its frequency dependent elements (Maciejowski, 1989). Here, the Nyquist array $\boldsymbol{L}(s) \in \mathbb{R}^{m\times m}$ consists of open loop-transfer elements $l_{ij}(s)$ with $\{i, j\} \subset \mathbb{Z}^m = \{1, 2\}$. Furthermore, a Gershgorin band consists of frequency dependent Gershgorin circles with a radius $\mathscr{R}_i(j\omega)$ drawn on the diagonal Nyquist curves $l_{ii}(j\omega)$, defined by

$$\mathscr{R}_i(j\omega) = \sum_{i,\, i\neq j}^{m} \left|l_{ij}(j\omega)\right|. \tag{3.33}$$

Put differently, these bands show the cumulative gains of the row-wise off-diagonal elements of $\boldsymbol{L}(s)$ projected on the main-diagonal Nyquist curves. In general, the off-diagonal

Nyquist curves are disregarded for convenient presentation. The closed-loop stability is determined by the direct Nyquist array (DNA) stability theorem (Rosenbrock, 1970; Rosenbrock and Owens, 1976). If the Gershgorin bands do not include the critical -1 point, the system is said to be diagonally dominant. The smaller the bands, the higher the diagonal dominance degree, and the system may be treated as m individual SISO systems with negligible interactions. For this reason, the Gershgorin bands can be used as a measure of MIMO (de)coupling (Maciejowski, 1989).

Furthermore, Gershgorin bands can be used to shape the earlier defined loop-transfer matrix $\boldsymbol{L}(s)$ according to gain, phase, and modulus margins specifications established for SISO controller design. However, because of the presence of the Gershgorin bands over the Nyquist loci, the introduced margins need to be redefined into their *extended* forms (Ho et al., 1997; Garcia et al., 2005), denoted by $(\cdot)'$. Figure 3.14 visualizes the presented notions, and the adapted definitions for gain margin A_m, phase margin ϕ_m and modulus margin M_m are defined as follows:

$$A'_\mathrm{m} = \frac{A_\mathrm{m}}{\left(1 + \frac{\sum_{i=1,i\neq j}^{m} |l_{ji}(j\omega_\mathrm{p})|}{|l_{ii}(j\omega_\mathrm{p})|}\right)}, \tag{3.34}$$

$$\phi'_\mathrm{m} = \phi_\mathrm{m} - 2\arcsin\left(\frac{\sum_{i=1,i\neq j}^{m} |l_{ji}(j\omega_\mathrm{g})|}{2\,|l_{ii}(j\omega_\mathrm{g})|}\right), \tag{3.35}$$

$$M'_\mathrm{m} = \left|1 + l_{ii}(j\omega_\mathrm{m})\right| - \sum_{i,i\neq j}^{m} \left|l_{ji}(j\omega_\mathrm{m})\right|, \tag{3.36}$$

where ω_p, ω_g and ω_m indicate the frequencies at which the margins are defined. The modulus margin quantifies the sensitivity of the closed-loop system to variations of the considered loop-gain, and thus serves as a measure for robustness. The modulus margin is in general considered as a combined measure of the gain and phase margins, as it represents the minimal distance of the Nyquist locus to the critical -1 point by a single value. Consequently, the modulus margin is taken as the main performance indicator in the next section.

DECOUPLING ASSESSMENT BY GERSHGORIN BANDS

This section assesses and quantifies the degree of decoupling and stability of the IPC implementation for high-order linear models. For this purpose, the Gershgorin circle

Table 3.2: The extended gain, phase, and modulus margins of the system of different ψ_o's. The margins higher than the benchmark ($\psi_\mathrm{o} = 0°$) are underlined. The tilt and yaw loops are denoted by $l_{11}(s)$ and $l_{22}(s)$, respectively.

ψ_o (°)	A'_m (–)		ϕ'_m (°)		M'_m (–)	
	$l_{11}(s)$	$l_{22}(s)$	$l_{11}(s)$	$l_{22}(s)$	$l_{11}(s)$	$l_{22}(s)$
0	–	–	–	–	–	–
30	$\underline{23.540}$	$\underline{23.540}$	71.339	71.339	0.897	0.897
44	21.167	21.167	$\underline{84.195}$	$\underline{84.195}$	$\underline{0.912}$	$\underline{0.912}$
58	18.194	18.194	71.215	71.215	0.883	0.883

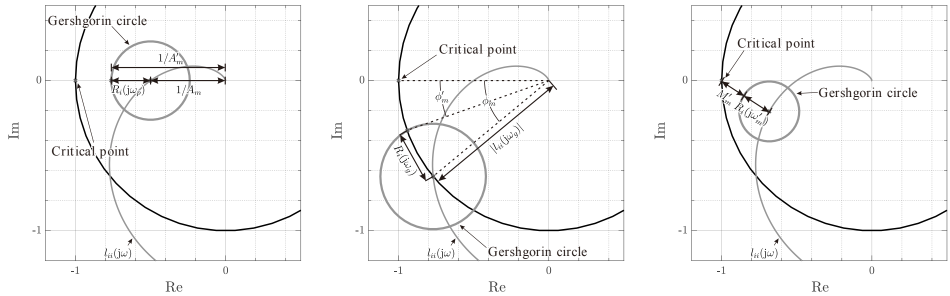

Figure 3.14: Graphical interpretations of the extended gain margin A'_{m} (left), phase margin ϕ'_{m} (middle) and modulus margin M'_{m} (right), adapted from (Ho et al., 1997; Garcia et al., 2005). The presence of the Gershgorin circles over the Nyquist locus alters the definition of the conventional margins.

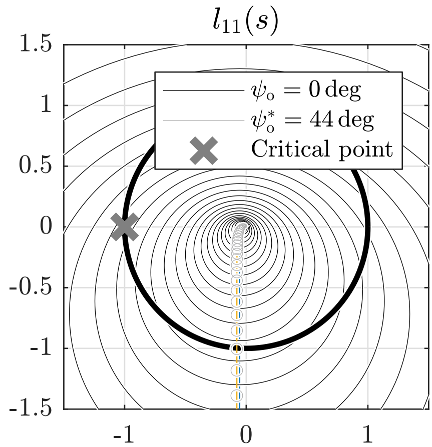

Figure 3.15: Nyquist loci with Gershorin bands of $l_{11}(s)$. The amount of coupling is greatly reduced and the open-loop system becomes diagonally dominant by incorporating the optimal azimuth offset.

theorem is used in conjunction with the previously introduced extended margins. The cases considering and disregarding the optimal azimuth offset are examined.

The first step is to design a compensator that decouples the MIMO system to some extent (Ho et al., 1997). For this purpose, the azimuth offset is used, whereafter an actual diagonal controller $\boldsymbol{C}(s)$ is implemented that shapes the loop-gain to attain closed-loop performance and stability specifications.

Figure 3.15 shows the Nyquist locus of the first diagonal elements $l_{11}(s)$ using a pure integrator controller, with and without optimal azimuth offset. The no-offset case has no diagonal dominance, whereas by inclusion of the optimal offset the open-loop system becomes diagonally dominant, shown by the decreased circle radii. In Table 3.2 the effect is further quantified by evaluation of the extended stability margins. Two additional (but suboptimal) cases of 30 and 58 deg offset are evaluated, and the resulting best

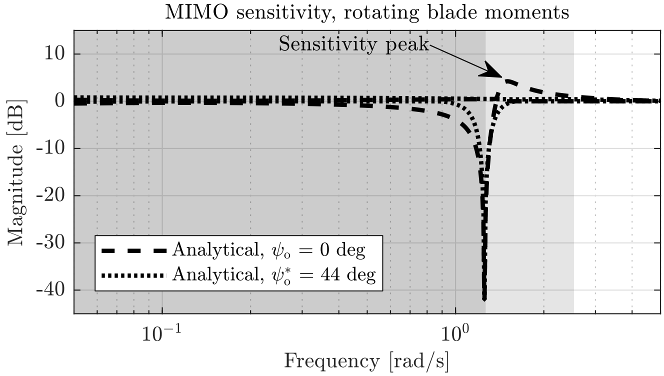

Figure 3.16: Multivariable sensitivity of the rotating blade moments with and without optimal azimuth offset. The maximum sensitivity peak in the light-gray area is attenuated. The gray-shaded regions relate the sensitivities in the (non)rotating frames.

margins are underlined. It is shown that the suboptimal case of 30 deg gives the highest extended gain margins, whereas the optimal offset of 44 deg results in significantly improved extended phase and modulus margins compared with the baseline case. As the latter mentioned margin is inversely proportional to the sensitivity peak and serves as a main performance indicator, it is concluded that the offset of 44 deg results in optimal decoupling and robustness.

3.7. HIGH-FIDELITY EVALUATIONS ON BLADE LOAD AND PITCH SIGNALS

In this final section, high-fidelity simulations are performed to evaluate the effect of the azimuth offset on pitch actuation and the blade loads in the rotating frame. This section is divided in two subsections. In Section 3.7.1, a 1P-only implementation is evaluated according to the set-up depicted in Figure 3.1. Then, in Section 3.7.2, the effect is assessed for a combined 1P and 2P implementation.

For examining the performance of the two cases, the blade load signal M_1 is recorded. A total simulation time of 2200 s is taken, of which the first 200 s are discarded to exclude transient effects from the data set. Furthermore, a wind profile with a mean wind speed of 25 m s^{-1}, a Kaimal IEC 61400-1 Ed.3 turbulence model, class A characteristic turbulence (TI = 18 %), and a wind shear exponent of $\alpha = 0.14$ is used (NWTC Information Portal, 2016). For the 1P case, a diagonal integral controller $\boldsymbol{C}(s)$ with gains c_I according to Table 3.1 is used; the controller tunings for the combined 1P and 2P case are given in the related section. For the *No IPC* simulations, the integral gain is set to zero.

3.7.1. A 1P-ONLY IPC IMPLEMENTATION

Figure 3.16 presents the multivariable sensitivity of the rotating blade moments for the 1P-only IPC implementation, including and excluding the offset. By inclusion of the optimal offset, it is shown that the maximum sensitivity peak around 1.5 rad s^{-1} is attenu-

3

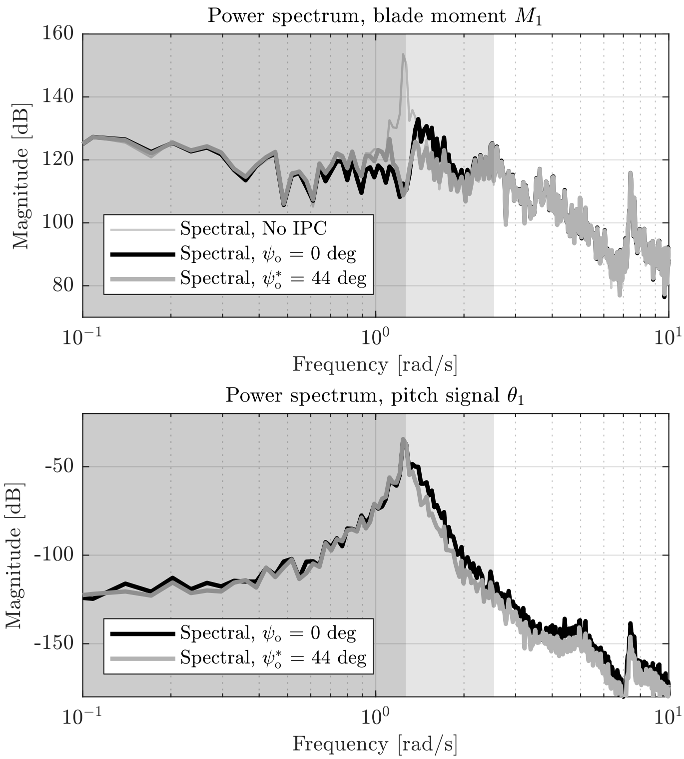

Figure 3.17: Power spectra of the out-of-plane blade loads, compared for the cases of No IPC, without and with optimal azimuth offset. A significant difference is observed in the light-gray shaded region, where the frequency content significantly drops by inclusion of the offset. For the dark-shaded lower frequency region, the frequency content is slightly increased, however, a more consistent reduction around 1P is attained. For the IPC pitch signal θ_1, a significant overall decrease of high frequency content is seen.

ated, while the low frequent sensitivity is overall slightly amplified. The same results are observed for the blade moment M_1 spectra in Figure 3.17, resulting in a more consistent reduction of the 1P load region. By evaluation of the IPC pitch contribution signal θ_1 in the same figure, it is concluded that the high-frequency actuation content is overall significantly reduced.

Furthermore, the gray-shaded regions of Figure 3.13 and the figures included in this section are interchanged and indicate the relation between the frequency content in the nonrotating and rotating domains. Referring back to Equation (3.7), the operators s_+ and s_- show that the frequency content in the rotating domain is mapped from the nonrotating domain by a 1P shift. Figures 3.13 and 3.16 are used for illustration: The peak in the rotating domain at $\omega = 1.5\ \mathrm{rad\,s^{-1}}$ (light-gray) is shifted frequency content from the nonrotating domain at $\omega = 1.5 - 1\mathrm{P} \approx 0.25\ \mathrm{rad\,s^{-1}}$.

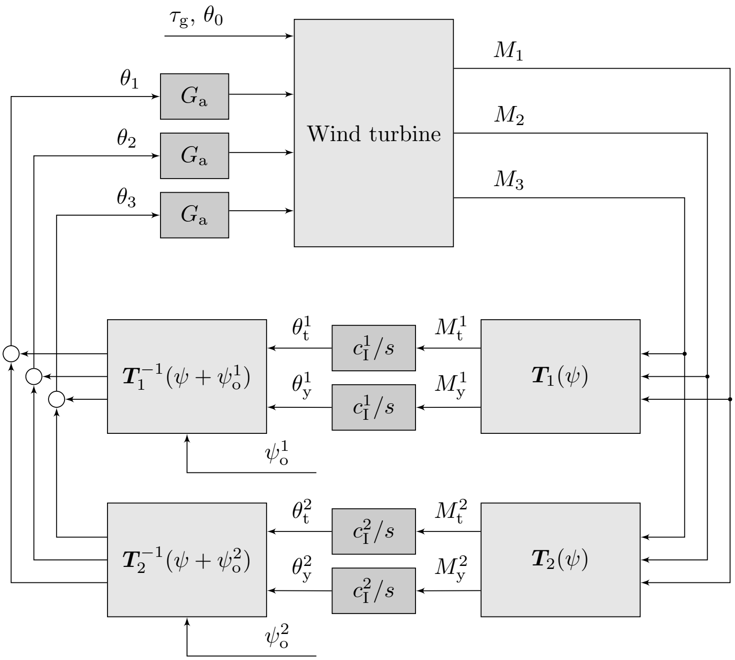

Figure 3.18: A combined 1P and 2P implementation of IPC. For both 1P and 2P loops in the fixed frame, the tilt- and yaw-axis loads signals are subjected to integral controllers using equal gains on both axes. After the reverse transformation including separate azimuth offsets ψ_o^n, the 1P and 2P contributions are summed to form the implementable IPC signals θ_i for attenuation of the respective blade out-of-plane harmonic loads. A pitch actuator model G_a is included. The collective pitch and generator torque control signals, θ_0 and τ_g, are generated by turbine controllers, which are omitted in this figure.

Table 3.3: Parameters and design specification of the IPC control loops, including and excluding the optimal azimuth offset.

$\psi_o = 0$	$\omega_a = 2.5$ rad s^{-1}		$\omega_a = 5.0$ rad s^{-1}	
	1P	2P	1P	2P
c_I^n [rad Nm^{-1} s^{-1}]	3.64e−6	7.1e−6	3.0e−6	1.75e−6
ω_c^n [rad s^{-1}]	0.14	0.038	0.14	0.038
ψ_o^n [deg]	0	0	0	0
$\psi_o = \psi_o^*$	$\omega_a = 2.5$ rad s^{-1}		$\omega_a = 5.0$ rad s^{-1}	
	1P	2P	1P	2P
c_I^n [rad Nm^{-1} s^{-1}]	2.65e−6	9.7e−7	2.55e−6	7.75e−7
ω_c^n [rad s^{-1}]	0.14	0.038	0.14	0.038
ψ_o^n [deg]	44	41	31	32

3.7.2. A COMBINED 1P AND 2P IPC IMPLEMENTATION

This last result section presents the case for a combined 1P and 2P IPC implementation, of which a new schematic diagram is given in Figure 3.18. Only for this section, some symbols are redefined: the pitch signals θ_i are now only made up of IPC contri-

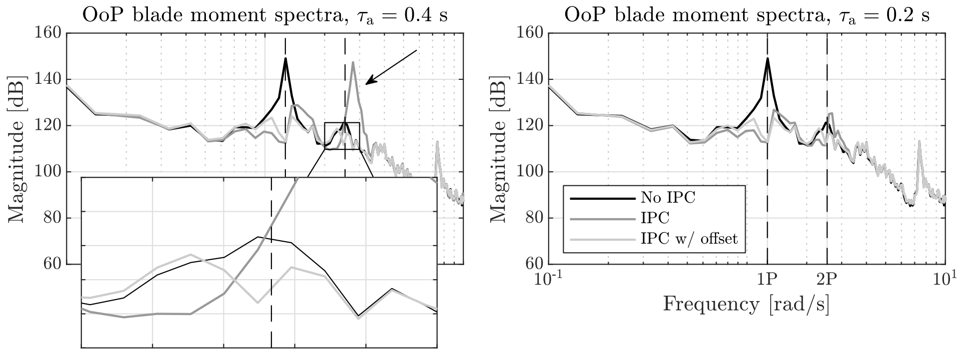

Figure 3.19: Out-of-plane blade load moment spectra for *No IPC*, *IPC* and *IPC with the optimal azimuth offset*. It is shown that for a pitch actuator with slow dynamics, the IPC implementation without offset significantly amplifies the 2P load harmonic (indicated by the arrow). The same conclusion holds for faster pitch actuators, however, the effect is less prominent. The IPC implementation with optimal offset successfully attenuates the 2P load, as shown in zoomed inset graph. Mean wind speed 25 m s^{-1}, TI = 16 %.

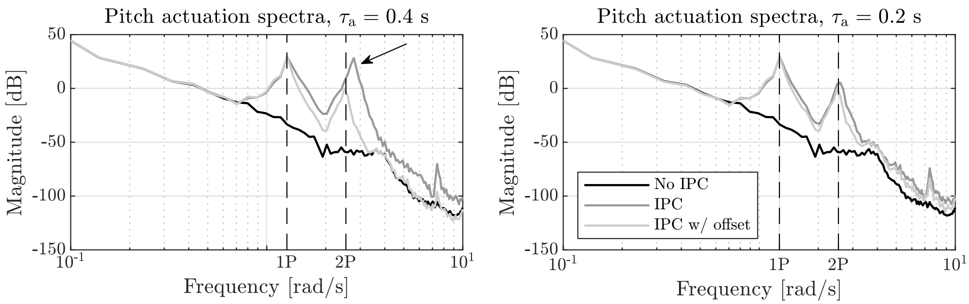

Figure 3.20: Pitch actuation signals with combined CPC and IPC contributions. Omitting the azimuth offset results in an increased 2P pitch contribution at an erroneous frequency (indicated by the arrow), resulting in fatigue load amplifications. The effect is most prominent for slower pitch actuators. Furthermore, the optimal azimuth offset reduces the overall high-frequency pitch content. Mean wind speed 25 m s^{-1}, TI = 16 %.

butions, the azimuth offset ψ_o^n is indicated with the corresponding nP harmonic in the superscript, and the first-order pitch actuator models G_a are now pulled out from the wind turbine plant. This separation is done because two different actuator models are applied, with bandwidths of $\omega_a = 2.5$ and 5.0 rad s^{-1}.

In the following, the obtained time-domain data sets are used to perform a frequency-domain analysis on the blade bending moments and pitch signal contributions. Also, the level of fatigue loading is quantified by the scalar DEL. The relevant (design) parameters are summarized in Table 3.3, where the control bandwidth is defined at the open-loop unity-gain cross-over frequency ω_c^n.

A frequency domain analysis is performed on the out-of-plane blade bending moments and combined CPC and IPC pitch signal of the first blade in Figures 3.19 and 3.20, respectively. The cases

1. *No IPC*,

2. *IPC,*
3. *IPC with optimal offset,*

are evaluated for both actuator models in distinct graphs. For all cases IPC is able to attenuate the 1P disturbance, whereas differences are observed regarding the frequency content on both sides of the harmonic for cases 2 and 3. The former mentioned case shows non-uniform magnitude response (respectively lower and higher, left and right of 1P), whereas the latter mentioned case does show uniform behavior. The effect is more drastic in the region around the 2P frequency. Case 2 with $\omega_a = 2.5\ \mathrm{rad\,s^{-1}}$, results in excessive pitch actuation at an erroneous frequency in the rotating frame, right of the 2P harmonic. This effect is caused by a high-amplitude sensitivity peak right of 2P, similar to the effect shown earlier in Figure 3.16. The blade load, as well as pitch actuation signal, show deteriorated performance compared to the first baseline case. By including the optimal azimuth offset for both actuator models shows attenuation of the 2P periodic load.

Lastly, the load measurements are converted into DELs as a measure of fatigue loading, and represent the amplitude of a certain harmonic load variation that would cause the same damage level when it is repeated for a given number of cycles (Freebury and Musial, 2000; Bossanyi et al., 2013). Figure 3.21 shows the out-of-plane blade bending moment DEL for the three introduced cases. It is shown that the inclusion of the optimal azimuth offset is crucial from a fatigue perspective: including IPC in a system with high phase loss results in a significant deterioration of fatigue loadings, respectively causing premature damage and excessive actuation to the structural parts and pitch actuators. The effect becomes less severe for faster systems, however, incorporation of the optimal offset is still beneficial from a fatigue load perspective.

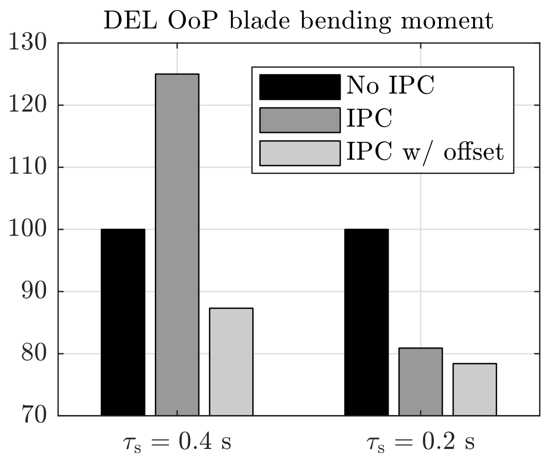

Figure 3.21: Normalized DELs with respect to the baseline *No IPC* case for different actuator models. From a fatigue loading perspective, incorporation of the azimuth offset is crucial for slow systems (higher phase losses). The positive effect is less prominent but still present for faster systems.

3.8. CONCLUSIONS

Although the inclusion of an azimuth offset in the reverse MBC transformation is widely applied in literature, up until now, no profound analysis of its implications has been performed. The analysis has shown that the application of an azimuth offset further decouples the system in the nonrotating reference frame. The offset for optimal decoupling heavily depends on the changing blade dynamics throughout the entire turbine operating window. The dynamic transfer from pitch angle to the out-of-plane blade bending moment – by also including the off-diagonal components – determines the optimal offset value, and a detailed study is conducted on this aspect. By evaluation of the multivariable system singular values, it is shown that the optimal offset reduces the directionality. Moreover, also the degree of coupling is minimized and the system is made diagonally dominant, as shown using Gershgorin circle theorem. In effect, the application of decoupled and single-gain SISO IPC control loops is justified. Reduction of the sensitivity peak in the nonrotating frame results in attenuation of the maximum sensitivity peak for the rotating blade load sensitivity. Furthermore, because of higher phase losses, it is shown that the offset is even more crucial for higher harmonic IPC implementations: omittance may result in excessive actuator duty cycle and load amplification, opposing the scheme's intent and accelerating structural damage. Likewise, for larger rotors with more flexible blades, the inclusion of the azimuth offset in SISO IPC implementations is of increased importance.

4

Preventing tower resonance by a quasi-LPV MPC framework

With the ever increasing power rates of wind turbines, more advanced control techniques are needed to facilitate tall towers that are low in weight and cost-effective but in effect more flexible. Such soft-soft tower configurations generally have their fundamental side-side frequency in the below-rated operational domain. Because the turbine rotor practically has or develops a mass imbalance over time, a periodic and rotor-speed dependent side-side excitation is present during below-rated operation. Persistent operation at the coinciding tower and rotational frequency degrades the expected structural life span. To reduce this effect, earlier work has shown the effectiveness of active tower damping control strategies using collective pitch control. A more passive approach is frequency skipping by inclusion of speed exclusion zones, which avoids prolonged operation near the critical frequency. However, neither of the methods incorporates a convenient way of performing a trade-off between energy maximization and fatigue load minimization. Therefore, this chapter introduces a quasi-linear parameter varying model predictive control (qLPV-MPC) scheme, exploiting the beneficial (convex) properties of a qLPV system description. The qLPV model is obtained by a demodulation transformation, and is subsequently augmented with a simple wind turbine model. Results show the effectiveness of the algorithm in synthetic and realistic simulations using the NREL 5-MW reference wind turbine in high-fidelity simulation code. Prolonged rotor speed operation at the tower side-side natural frequency is prevented, whereas when the trade-off is in favor of energy production, the algorithm decides to rapidly pass over the natural frequency to attain higher rotor speeds and power productions.

Chapter contents

This chapter is based on the following publication:

S.P. Mulders, T.G. Hovgaard, J.D. Grunnet and J.W. van Wingerden. Preventing wind turbine tower natural frequency excitation with a quasi-LPV model predictive control scheme. Accepted to: *Wind Energy*

4.1. INTRODUCTION

The tower makes up a substantial part of the total turbine capital costs, and therefore finding an optimum between its mass and manufacturing expenses is a critical trade-off (Dykes et al., 2018). For conventional towers, diameters are limited because of land-based transportation constraints. This aspect dictates the increase of wall thickness for the production of taller towers, and consequently leads to increased weight and costs. Conventional tower designs are soft-stiff to locate the tower fundamental frequency outside the turbine variable-speed operational range, and thereby eliminate the possibility of exciting a tower resonance by the rotor rotational or blade-passing frequency. However, with the ever increasing wind turbine power rates, a combination of technical solutions should enable future, low-cost, tall towers, by relaxing this frequency constraint. Soft-soft tower configurations form an opportunity for tall towers by their smaller tower diameters and reduced wall thickness. As a result, soft-soft towers are less stiff, and have their natural frequency in the turbine operational range. Therefore, more advanced control solutions will be key in avoiding the excitation of these frequencies for extended periods of time.

In practical scenarios, the center of mass of the wind turbine rotor assembly does not coincide with the actual rotor center as a result of, eg, manufacturing imperfections, wear and tear, fouling, and icing (Hau, 2013). Moreover, vibrations are also induced by rotor aerodynamic imbalances caused by pitch errors and damage to the blade surface (Germanischer Lloyd, 2012). Consequently, during variable-speed below-rated operation, the rotor rotational or blade-passing frequency may excite the structural side-side natural frequency. Small perturbations can lead to load fluctuations comparable to fore-aft stresses, because the turbine rotor provides negligible aerodynamic side-side damping, at an order of magnitude smaller than the fore-aft damping ratio (Burton et al., 2001). As a result, excitation of the side-side mode possibly results in accelerated and accumulative fatigue damage.

Straightforward control implementations are available for reducing and mitigating the excitation of the tower fore-aft and side-side modes. An active method for reducing tower motion is the use of an integrated nacelle acceleration signal in a proportional feedback structure. Depending on the measured acceleration direction, the resulting signals form an addition to the collective pitch (Bossanyi, 2003a; Bossanyi et al., 2012) or generator torque (Wright et al., 2011) control signal, for respective damping of fore-aft and side-side vibrations. Another more passive method entails the prevention of structural mode excitation by manipulating the generator torque when the rotor speed approaches the excitation frequency (Bossanyi, 2000). This method is often referred to as *frequency skipping* by inclusion of *speed exclusion zones*.

All of the active and passive methods described above complicate the controller design, by requiring extra proportional-integral-derivative (PID) feedback control loops with additional logic and speed set-points. Also, the methods do not incorporate convenient and inherent tuning capabilities for a trade-off between produced energy and fatigue loading. Therefore, more advanced control algorithms might form a solution by providing a more integrated way of controller synthesis, incorporating power, and load objectives. While an abundance of publications on advanced wind turbine control algorithms outlines the possible benefits (Bianchi et al., 2006), to the authors' knowledge, more sophisticated control methods do not yet see a wide-spread adoption in industrial-grade wind turbine control systems; PID control structures (Mulders and van Wingerden, 2018) provide ease of implementation while resulting in a sufficient performance level.

An advanced control method that has seen a substantial gain of interest from industry in the past decades is model predictive control (MPC) (Rawlings and Mayne, 2009; Hovgaard et al., 2015). The most evident benefits of MPC over PID control (Holkar and Waghmare, 2010) are (1) the ability of including constraints, (2) coping with the complexity of nonminimum phase systems, (3) robustness against deviations of the control model to the actual process, and (4) the convenient application to multivariable control problems. MPC has been considered in the literature for wind turbine load mitigations. A nonlinear MPC (NMPC) method is applied by assuming future wind speed knowledge using a light-detection and ranging (LIDAR) system (Schlipf et al., 2013). Simulation results shows promising load reductions without affecting the energy production. Furthermore, a robust MPC (RMPC) implementation is compared with a nominal MPC control structure for the purpose of active tower fore-aft damping (Evans et al., 2015). In numerical simulations, the former outperforms the latter mentioned, as particularly around rated operating conditions, physical actuations constraints form a limiting factor. The benefits of NMPC using a future wind speed prediction are once again emphasized for similar operating conditions (Tofighi et al., 2015).

All of the described MPC implementations above focus on the active mitigation of structural loads. A more passive MPC implementation, providing frequency skipping capabilities, and thereby making an *optimal* trade-off between loads and energy production over the prediction horizon, does not seem to have been backed up by literature in the past. For tall soft-soft tower configurations, the complexity lies in the fact that fatigue loads are minimized by preventing operation at the natural frequency, while it is essential to cross the same frequency for attaining higher rotational speeds and power productions. The conflicting objectives form a burden for describing the objective as a convex optimization problem. Moreover, NMPC for solving nonconvex problems is – because of its computational complexity – often considered ineligible for real-time applications.

Imposing spectral constraints might form a possible solution path, by employing the short-time Fourier transform (STFT) on the system output signal in a nonlinear MPC setting (Hours et al., 2015). A similar methodology (Jain et al., 2015) uses the selective discrete Fourier transform (SDFT) in an MPC approach to dampen oscillation modes in power system stabilizers (PSS). However, from an implementation and tuning perspective, a frequency domain approach seems to be unintuitive and nontrivial. Therefore, in this chapter, another approach is considered. The method involves a model demodulation transformation described for application and control in the field of tapping mode-atomic force microscopy (TM-AFM) (Keyvani et al., 2019). The model transformation is applied to the turbine tower model and transfers frequency-dependent magnitude and phase content to a quasi steady-state contribution. This is accomplished by converting a linear-time invariant (LTI) system description into a linear-parameter varying (LPV) model, scheduled on the excitation frequency. The technique shows similarities with the multiblade coordinate (MBC) transformation (Mulders et al., 2019a), often used in individual pitch control (IPC) implementations for blade fatigue load reductions (Bossanyi, 2003b; Geyler and Caselitz, 2007; Mulders and van Wingerden, 2019b).

An LPV system representation is frequently used for capturing nonlinear dynamics into a system description with a linear input-output mapping (Hanema, 2018). An external scheduling variable varies the dynamics of the linear model. Now, consider the combination of an LPV model with MPC. The model-based control method uses a mathematical system description to compute an optimal control signal over the prediction horizon. Unfortunately, for LPV systems, the considered model is subject to changes over time, described by the yet unknown scheduling trajectory. However, when the system is scheduled on state variables and/or input signals, the model is referred to as a quasi-LPV (qLPV) system. Recently, an efficient MPC scheme for such qLPV systems is proposed by solving subsequent quadratic programs (QPs) (Cisneros et al., 2016).

This chapter subjects a tower model to the earlier introduced demodulation transformation and augments it with a simplified wind turbine model, such that a qLPV model is obtained. The result is combined with the efficient MPC method, exploiting the beneficial properties of qLPV systems (Cisneros et al., 2016). The proposed qLPV-MPC framework provides a methodology for performing an optimal trade-off between produced energy and tower loads is presented, and thereby presents the following contributions:

- Providing the derivation results of a model demodulation transformation, for moving the magnitude and phase content at the excitation frequency to a quasi steady-state contribution.
- Applying the transformation to a second-order tower model and showcasing its working principles by an illustrative example.
- Combining the transformed tower model with a simplified wind turbine model and linearizing at below-rated operating points, for obtaining a qLPV state-space system description.
- Discretizing and converting the qLPV model to its affine form.
- Formally deriving the efficient MPC approach for affine qLPV model structures.
- Showcasing the proposed approach in closed-loop high-fidelity simulations with different wind profiles, to clearly show its effectiveness and practical applicability.

The chapter is organized as follows. Section 4.2 describes a methodology for transforming a nominal tower model into a demodulated LPV system description. In Section 4.3, the obtained system is combined with a simplified wind turbine model, resulting in a qLPV system description after linearization. Next, in Section 4.4, the efficient MPC scheme is combined with the qLPV model to make an optimal and user-defined trade-off between tower loads and energy production for the prevailing environmental conditions. In Section 4.5, the qLPV-MPC framework is evaluated with high-fidelity simulations using the NREL 5-MW reference wind turbine, subject to synthetic and realistic wind profiles. Finally, conclusions are drawn in Section 4.6.

4.2. PROBLEM FORMALIZATION AND TOWER MODEL DEMODULATION TRANSFORMATION

For performing a produced energy versus tower fatigue load trade-off, a wind turbine model needs to be combined with a structural tower model. Section 4.2.1 describes the tower side-side dynamics by a second-order mass-damper-spring system. Section 4.2.2 formalizes the problem statement and explains why straightforward combination of wind turbine and tower models results in nonconvexity. Therefore, in Section 4.2.3, the nominal tower model is subject to a demodulation transformation to facilitate convexification. The effects and implications of the transformation are analyzed and clarified by an illustrative example in Section 4.2.4.

4.2.1. MODELING THE TOWER DYNAMICS AS A SECOND-ORDER SYSTEM

In practical scenarios, the center of mass of a wind turbine rotor is likely to be unaligned with the rotor center. In effect, as large-scale state-of-the-art wind turbines are operated with a variable-speed control strategy for below-rated conditions, the support structure is excited by a periodic and frequency-varying centripetal force, as illustrated in Figure 4.1. The tower dynamics, excited by a rotor-speed dependent once-per-revolution

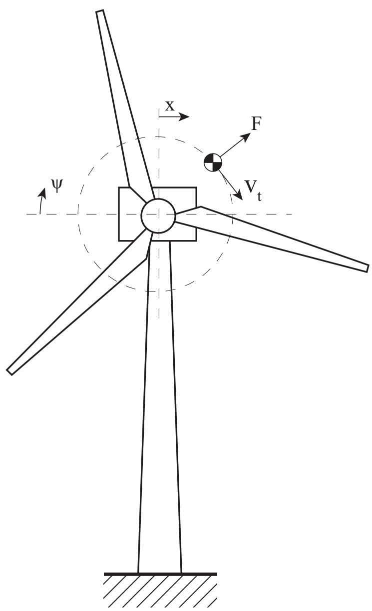

Figure 4.1: A rotor imbalance excites the turbine support structure because of the centripetal force $F = a_{\mathrm{u}} \cos(\psi(t))$ at the once-per-revolution and rotor-speed dependent (1P) frequency. The tangential speed of the imbalance is denoted as v_{t}, and the side-side tower-top displacement x is given in the hub coordinate system.

(1P) periodic force, are modeled by a second-order mass-damper-spring system

$$m\ddot{x}(t) + \zeta\dot{x}(t) + kx(t) = a_{\mathrm{u}}\cos(\psi(t)), \tag{4.1}$$

in which $\{m, \zeta, k\} \in \mathbb{R}^+$ are respectively the constant first mode modal mass, modal damping and modal stiffness, $\psi(t) \in [0, 2\pi)$ is the rotor azimuth angle, $a_{\mathrm{u}} \in \mathbb{R}^+$ quantifies the periodic force amplitude, and $\{x, \dot{x}, \ddot{x}\} \in \mathbb{R}$ respectively represent the side-side tower-top displacement, velocity and acceleration in the hub coordinate system, illustrated in Figure 4.1. A second-order system is taken to represent the tower first mode using the well known modal-decomposition model reduction technique (Hansen, 2004; Dahleh et al., 2011), and allows for a convenient assessment and derivation of the demodulation transformation in the next section. Application of the transformation to higher-order models is also possible and would result in a similar analysis. Furthermore, the force amplitude a_{u} is assumed to be constant for all rotational speeds; however, as will be shown later, this assumption can be relaxed for mildly varying amplitude changes.

4

The system in Eq. (4.1) is split in a set of first-order differential equations by defining $x_1 = \dot{x}(t)$ and $x_2 = x(t)$, respectively, representing the tower-top velocity and displacement, such that it is rewritten in the standard state-space $\dot{\boldsymbol{x}} = \mathbf{A}_{\mathrm{g}}\boldsymbol{x} + \mathbf{B}_{\mathrm{g}}\boldsymbol{u}$ representation

$$\begin{bmatrix} \dot{x}_1 \\ \dot{x}_2 \end{bmatrix} = \begin{bmatrix} -\zeta/\mathrm{m} & -\omega_{\mathrm{n}}^2 \\ 1 & 0 \end{bmatrix} \begin{bmatrix} x_1 \\ x_2 \end{bmatrix} + \begin{bmatrix} \mathrm{a_u} \\ 0 \end{bmatrix} \cos(\psi(t)) \qquad \text{and} \qquad G(s) \overset{s}{=} \left[\begin{array}{c|c} \mathbf{A}_{\mathrm{g}} & \mathbf{B}_{\mathrm{g}} \\ \hline \mathbf{C}_{\mathrm{g}} & \mathbf{0} \end{array}\right], \tag{4.2}$$

in which $\mathbf{A}_{\mathrm{g}} \in \mathbb{R}^{n_{\mathrm{g}} \times n_{\mathrm{g}}}$, $\mathbf{B}_{\mathrm{g}} \in \mathbb{R}^{n_{\mathrm{g}}}$, and $\omega_{\mathrm{n}} = \sqrt{k/m}$ is the structural natural frequency. All states are assumed to be measured, thus $\mathbf{C}_{\mathrm{g}} = I_{n_{\mathrm{g}}}$. Using the operator $\overset{s}{=}$ to equate the state-space system description to the transfer function with Laplace variable s, is a notation taken from Skogestad *et. al* (Skogestad and Postlethwaite, 2007). The notation means that the transfer function $G(s)$ has a state-space realization given by the quadruple $(\mathbf{A}_{\mathrm{g}}, \mathbf{B}_{\mathrm{g}}, \mathbf{C}_{\mathrm{g}}, \mathbf{0})$. An explicit definition of the transfer function is omitted in this work, since the notation is only used as a convenient way of parameterizing and referring to the state-space system.

4.2.2. PROBLEM FORMALIZATION

This section formalizes the problem considered in this chapter. The aim is to provide a trade-off between energy production efficiency and tower fatigue load reductions, by preventing rotor speed operation near the tower natural frequency. The considered nominal framework is graphically presented in Figure 4.2. The wind turbine model has a wind disturbance and a generator torque control input, the latter of which is subject to optimization. A cosine function acts on the azimuth position output from the wind turbine model, which results in a periodic input to the tower model.

The load and energy outputs of the respective tower and wind turbine models, together with the torque input signal are included in the following cost function to optimize the energy-load trade-off

$$\underset{\text{Torque}}{\arg\min} \quad -\lambda_1(\text{Energy}) + \lambda_2(\text{Loads}) + \lambda_3(\text{Torque}), \tag{4.3}$$

in which λ_i and $i = \{1, 2, 3\}$ are positive weighting constants determining the objective trade-offs. The above given relation presents the optimization objective in an informal

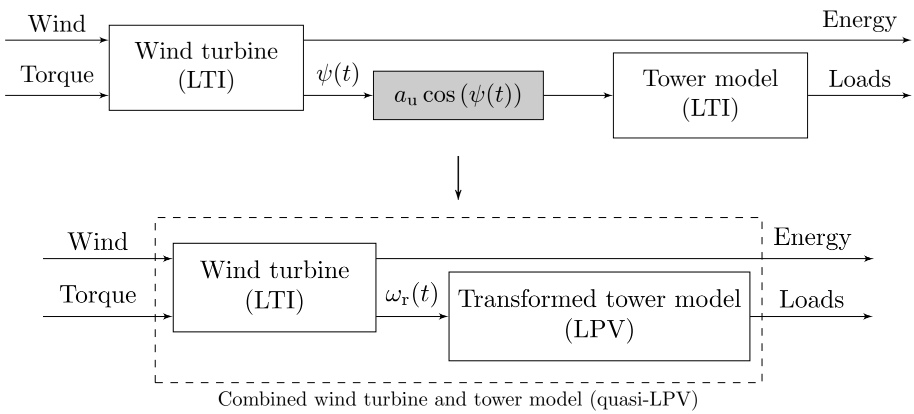

Figure 4.2: In the *upper diagram*, a wind turbine model is driven by wind disturbance and torque control inputs and has energy production and azimuth position as outputs. The latter mentioned output is taken by a cosine function and serves as an input to the tower model, resulting in a fatigue load signal. The presence of the trigonometric function forms a barrier for describing the energy-load trade-off as a convex optimization problem. Therefore, in the *lower diagram*, the trigonometric function is combined with the tower model by a model demodulation transformation, resulting in an LPV system description. Joining the wind turbine model with the transformed tower model results in a quasi-LPV system description, in which the rotor speed state serves as the scheduling variable.

fashion for illustration purposes; later sections define the problem in a mathematical correct way. The load signal is a periodic and rotor-speed dependent measure for tower fatigue loading, caused by the presence of the trigonometric function. This forms a burden for describing the objective as a convex optimization problem.

The solution path employed in this chapter is to subject the combined nonlinear trigonometric function and LTI tower model by a demodulation transformation. The transformed tower model results in an LPV system description. The subsequent aggregation with a wind turbine model results in a quasi-LPV model, as the internal rotor speed state serves as the scheduling variable. The next section provides theory for derivation of the demodulation transformation, whereas later sections elaborate on an efficient MPC method exploiting the beneficial properties of qLPV model structures. The process of obtaining a demodulated version of a periodically excited LTI model, is referred to as the demodulation transformation in the remainder of this chapter.

4.2.3. THEORY ON THE TOWER MODEL DEMODULATION TRANSFORMATION WITH PERIODIC EXCITATION TOWARDS AN LPV REPRESENTATION

In signal analysis, *modulation* is the process of imposing an information-bearing signal onto a second signal, often referred to as the carrier, carrier signal, or carrier wave (Oppenheim et al., 2013). Subsequently, the procedure of recovering the signal of interest from the modulated signal is called *demodulation*. The modulation-demodulation scheme is in communication systems mostly performed using dedicated hardware. A second method for performing the operation is the derivation of a mathematical framework for obtaining a demodulated model, which can be applied when the dominant dynamics of the nominal process are known. The latter mentioned approach is employed in this work, as it will appear useful for analysis, controller design, and forward propagation in MPC.

The aim of the demodulation transformation is to obtain a linear (but parameter varying) system description, which provides the frequency dependent dynamical behavior as a steady-state signal. The demodulated signal is used in a later section to form a convex quadratic optimization problem in an MPC setting for computing the optimal control signal over the prediction horizon. The demodulation transformation is applied to the assumed tower model, introduced in Section 4.2.1.

4

The model demodulation transformation is inspired by the work of Keyvani et al. (Keyvani et al., 2019), and only the main results are given in this section. The derivation is performed and validated with symbolic manipulation software for algebraic expressions (MathWorks, 2019), and the code is made publicly available (Mulders et al., 2019b). The transformation relies on the assumption that the changes in system response amplitude $a_{\mathrm{y}}(\tau)$ and phase change $\phi(\tau)$ are much slower than that of the driving excitation frequency ω_{r}. For this reason, the slower time scale is indicated by τ as a substitute for the normal time scale t. Variables that are a function of the slow-varying time scale are assumed to be constant over a single period $T_{\mathrm{r}} = 2\pi/\omega_{\mathrm{r}}$ of the excitation:

$$\int_0^{T_{\mathrm{r}}} f(\tau)g(t)dt = f(\tau)\int_0^{T_{\mathrm{r}}} g(t)dt. \tag{4.4}$$

Driving a linear system with a periodic input results in a periodic response with the same frequency, however, with a certain phase shift and magnitude relative to that of the input, which is characterized by:

$$x_i(t) = a_i(\tau)\cos(\omega_{\mathrm{r}} t + \phi(\tau)), \tag{4.5}$$

in which $\phi \in \mathbb{R}$ is the phase shift, $a_i \in \mathbb{R}^+$ is the amplitude, and the subscript $i \in \mathbb{Z}^+$ is a counter variable. By taking into account the introduced time-scales, and using Euler's formula $e^{\mathrm{j}\phi} = \cos(\phi) + \mathrm{j}\sin(\phi)$, the state variables are rewritten as

$$x_i(t) = \Re\{a_i(\tau)e^{\mathrm{j}(\omega_{\mathrm{r}} t+\phi(\tau))}\}, \tag{4.6}$$

with $\mathrm{j} = \sqrt{-1}$ being the imaginary unit, and $i = \{1,2\}$, where $i = 1$ relates to velocity and $i = 2$ to displacement. The symbol $\Re\{\cdot\}$ indicates the real part of a given expression, whereas $\Im\{\cdot\}$ is used to represent the imaginary part. The slow varying term $X_i \in \mathbb{C}$ is now written as a product with the fast harmonic function, with a fixed phase and amplitude:

$$x_i(t) = \Re\{a_i(\tau)e^{\mathrm{j}\phi(\tau)}e^{\mathrm{j}\omega_{\mathrm{r}} t}\} = \Re\{X_i(\tau)e^{\mathrm{j}\omega_{\mathrm{r}} t}\}, \tag{4.7}$$

and taking the first time derivative gives

$$\dot{x}_i(t) = \Re\{\left(\dot{X}_i(\tau) + \mathrm{j}\omega_{\mathrm{r}} X_i(\tau)\right)e^{\mathrm{j}\omega_{\mathrm{r}} t}\}. \tag{4.8}$$

By substitution of Eqs. (4.7) and (4.8) in the nominal state space representation of Eq. (4.2), the following expressions are obtained

$$\Re\left\{\left(\dot{X}_1(\tau) + j\omega_{\mathrm{r}} X_1(\tau) + (\zeta/m)X_1(\tau) + \omega_{\mathrm{n}}^2 X_2(\tau)\right)e^{j\omega_{\mathrm{r}} t} - a_{\mathrm{u}} e^{j\omega_{\mathrm{r}} t}\right\} = 0, \tag{4.9}$$

$$\Re\left\{\left(\dot{X}_2(\tau) + j\omega_{\mathrm{r}} X_2(\tau) - X_1(\tau)\right)e^{j\omega_{\mathrm{r}} t}\right\} = 0. \tag{4.10}$$

Furthermore, the following property of orthogonality is used, where

$$\int_0^{T_r} \Re\left\{Ce^{j\theta}\right\}e^{j\theta}\,d\theta = 0, \tag{4.11}$$

if and only if $\{C \in \mathbb{C}\} = 0$. Thus, Eqs. (4.9) and (4.10) are multiplied with $e^{j\omega_r t}$ as follows:

$$\int_0^{T_r} \Re\left\{\left(\dot{X}_1(\tau) + j\omega_r X_1(\tau) + (\zeta/m)X_1(\tau) + \omega_n^2 X_2(\tau)\right)e^{j\omega_r t} - a_u e^{j\omega_r t}\right\}e^{j\omega_r t}\,dt = 0, \tag{4.12}$$

$$\int_0^{T_r} \Re\left\{\left(\dot{X}_2(\tau) + j\omega_r X_2(\tau) - X_1(\tau)\right)e^{j\omega_r t}\right\}e^{j\omega_r t}\,dt = 0. \tag{4.13}$$

Term-by-term integration of the integrals in Eq. (4.13) using the mathematical property in Eq. (4.4), gives the following result

$$\begin{bmatrix}\dot{X}_1\\ \dot{X}_2\end{bmatrix} = \begin{bmatrix} j\omega_r X_1 - (\zeta/\mathrm{m})X_1 - \omega_n^2 X_2 + a_u \\ j\omega_r X_2 + X_1\end{bmatrix}. \tag{4.14}$$

Now, by defining $\boldsymbol{q} = [q_1, q_2, q_3, q_4]^{\mathrm{T}} = [\Re\{X_1\}, \Im\{X_1\}, \Re\{X_2\}, \Im\{X_2\}]^{\mathrm{T}}$ as a new state sequence, the system is rewritten as $\dot{\boldsymbol{q}}(\omega_r) = \mathbf{A}_h(\omega_r)\boldsymbol{q} + \mathbf{B}_h$, such that the following expression is obtained:

$$\begin{bmatrix}\dot{q}_1\\ \dot{q}_2\\ \dot{q}_3\\ \dot{q}_4\end{bmatrix} = \begin{bmatrix} -\zeta/\mathrm{m} & \omega_r & -\omega_n^2 & 0\\ -\omega_r & -\zeta/\mathrm{m} & 0 & -\omega_n^2\\ 1 & 0 & 0 & \omega_r\\ 0 & 1 & -\omega_r & 0\end{bmatrix}\begin{bmatrix}q_1\\ q_2\\ q_3\\ q_4\end{bmatrix} + \begin{bmatrix}a_u\\ 0\\ 0\\ 0\end{bmatrix}$$
$$\text{and} \qquad H(s,\omega_r) \overset{s}{=} \left[\begin{array}{c|c}\mathbf{A}_h & \mathbf{B}_h\\ \hline \mathbf{C}_h & \mathbf{0}\end{array}\right], \tag{4.15}$$

in which $\mathbf{A}_h \in \mathbb{R}^{n_h \times n_h}$, $\mathbf{B}_h \in \mathbb{R}^{n_h}$ and $n_h = 2n_g$. Again, all states are measured, thus $\mathbf{C}_h = I_{n_h}$. The system $H(s,\omega_r)$ has a state-space realization, which is given by the quadruple $(\mathbf{A}_h, \mathbf{B}_h, \mathbf{C}_h, \mathbf{0})$ (Skogestad and Postlethwaite, 2007). The instantaneous amplitude and phase of the dynamic system response at frequency ω_r are given by

$$a_y(\tau) = \sqrt{q_3^2 + q_4^2}, \tag{4.16}$$

$$\phi(\tau) = \tan^{-1}(q_4/q_3). \tag{4.17}$$

It is also possible to write the result of the derivation using a summation of Kronecker products

$$H(s,\omega_r) \overset{s}{=} \dot{\boldsymbol{q}} = \left(\mathbf{A}_g \otimes I_{n_g} + I_{n_g} \otimes \begin{bmatrix}0 & \omega_r\\ -\omega_r & 0\end{bmatrix}\right)\boldsymbol{q} + \left(\mathbf{B}_g \otimes \begin{bmatrix}1\\ 0\end{bmatrix}\right). \tag{4.18}$$

The nominal and transformed model representations $G(s)$ and $H(s,\omega_r)$ are interchangeable: Figure 4.3 graphically summarizes the transformation of the nominal periodically excited second-order tower model (Eq. (4.2)) into an LPV model structure (Eq. (4.15)). The amplitude a_u of the periodic input is in the demodulated model a direct input to the system. The outputs are the amplitude a_y and phase shift ϕ with respect to the input frequency. Note that the frequency ω_r is in the transformed case a scheduling variable to the LPV system, changing the system dynamics. The following section demonstrates and further explains the effects of the presented transformation by an illustrative analysis.

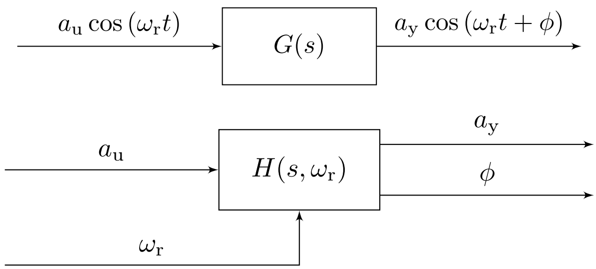

Figure 4.3: *Top:* The nominal tower model is periodically excited at a certain frequency and amplitude. For the linear case, the response is scaled and phase-shifted with respect to the driving input signal. *Bottom:* After the demodulation transformation, the input amplitude is a direct input to the system, whereas its frequency changes the system dynamics. The resulting outputs give the response amplitude and phase shift as a quasi-steady state signal.

4.2.4. ILLUSTRATING THE EFFECTS OF THE TRANSFORMATION

This section adds context to the rather abstract derivation of the demodulation transformation in Section 4.2.3. Therefore, the first part of this section presents a frequency domain analysis of the transformation properties. Then, in an illustrative time domain simulation case, a frequency sweep is applied to the nominal and transformed models. The analysis and exemplary simulation clarify the characteristics and applicability of the transformation for the considered objective in this chapter.

The nominal and transformed tower models from Eqs. (4.2) and (4.16) are parameterized by the following quantities: A modal mass of $m = 1000$ kg, a modal damping coefficient of $\zeta = 100$ kg s^{-1}, and a modal spring constant of $k = 500$ kg s^{-2}. Resulting from the somewhat arbitrarily selected parameters, the first tower mode is located at

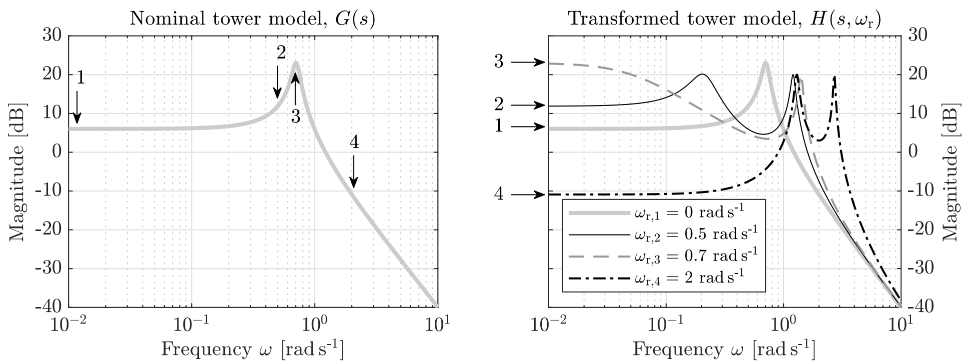

Figure 4.4: ***Left:*** Frequency response of the nominal tower model $G(j\omega)$. A clear tower resonance peak is observed at $\omega_n \approx 0.71$ rad s^{-1}, and a −40 dB/decade roll-off at higher frequencies. A set of 4 comparison points $\omega_{r,i} \in \mathbf{\Omega}_r = \{0, 0.5, 0.7, 2.0\}$ rad s^{-1} is chosen for evaluation of the nominal and demodulated model. ***Right:*** Frequency responses of the transformed model $H(j\omega, \omega_{r,i})$ for the set of comparison points. The magnitude content at the indicated frequencies in the left plot is transferred to a steady-state contribution in the transformed case. When the input signal a_u to the transformed model is considered constant or slowly varying, the additional resonances at higher frequencies do not contribute to the output.

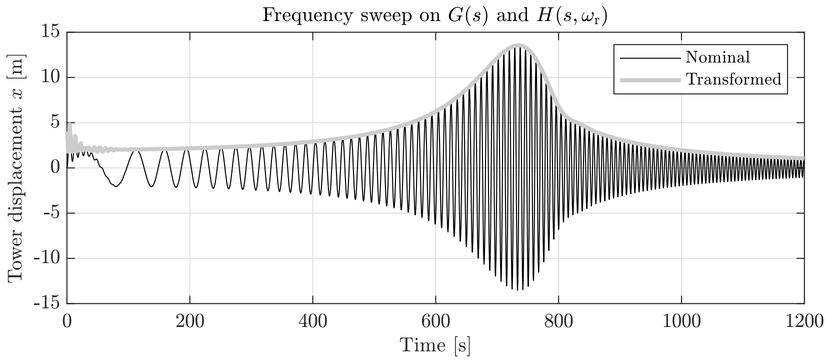

Figure 4.5: Frequency sweep applied to the nominal and transformed model, from $\omega_r = 0$ to 1.2 rad s^{-1} with a constant acceleration in 1200 s. The transformed model shows a very close amplitude tracking of the nominal model magnitude response.

$\omega_n \approx 0.71$ rad s^{-1}, with a clearly present resonance peak at the same frequency. Section 4.5 modifies the NREL 5-MW reference turbine tower to move its side-side fundamental frequency to the same location. Figure 4.4 shows Bode magnitude plots of the nominal plant and its demodulated counterpart in the frequency range:

$$\mathbf{\Omega} = \left\{\omega \mid \omega \subset \mathbb{R},\ 10^{-2} \leq \omega \leq 10^{1} \text{ rad s}^{-1}\right\}.$$

To obtain the amplitude output a_y of the demodulated model, the Euclidean norm of the frequency responses of q_3 and q_4 at each frequency point is taken.

Figure 4.4 showcases the frequency domain effects of the transformation. The frequency responses are evaluated for 4 rotor speeds $\omega_{r,i} \in \mathbf{\Omega}_r$, $i = \{1, 2, 3, 4\}$, defined by the set $\mathbf{\Omega}_r = \{0, 0.5, 0.7, 2.0\}$ rad s^{-1}. The rotor speed elements parameterize the transformed model $H(s, \omega_r)$. The plots in Figure 4.4 show arrows, indicating that frequency dependent magnitude information (left) is transferred to a steady-state contribution (right). Note that for $\omega_{r,1} = 0$ rad s^{-1} the transformed model reduces to the nominal case. Moreover, the right plot shows that the nominal resonance peak at ω_n is for each frequency response split into two peaks with a 3 dB magnitude reduction. In effect, when the input amplitude a_u of the transformed model is constant or varied slowly, the magnitude at specific nominal model frequency points is mapped to a DC contribution in the transformed case; rapid variations will result in contributions from the resonances at higher frequencies. However, in this chapter, additional measures to reduce these effects, such as low-pass or notch filters, are dispensable, because a_u is assumed to be constant.

Figure 4.5 shows the time-domain characteristics of the transformation. For this, a frequency sweep is applied to the nominal and transformed models. For the total simulation time of 1200 seconds, the signal has a linearly increasing frequency, with a constant increase rate of $\dot{\omega}_r = 10^{-3}$ rad s^{-2}, starting from $\omega_r = 0$ to 1.2 rad s^{-1}. This frequency range is chosen as modern large-scale variable-speed wind turbines are controlled in this operating region. The transformed model shows a very close amplitude tracking of the nominal model dynamics. The earlier imposed assumption on the change in amplitude and phase by a slow time scale τ, does not seem to limit the proposed method for applicability to the considered wind turbine control objective.

4.3. WIND TURBINE MODEL AUGMENTATION AND LINEARIZATION

This section considers the derivation of a simple (linear) NREL 5-MW model, for augmentation to the demodulated tower model such that a quasi-LPV model is obtained. Section 4.3.1 provides the simple first-order wind turbine model. Next, in Section 4.3.2, the model is symbolically linearized and augmented with the transformed tower model in a qLPV representation. Section 4.3.3 provides linearization parameters over the complete below-rated operating region based on the properties of the NREL 5-MW reference wind turbine (Jonkman et al., 2009). Finally, Section 4.3.4 validates the first-order and affine linear models to simulation results of their nonlinear equivalent.

4.3.1. SIMPLIFIED WIND TURBINE SYSTEM DESCRIPTION

Because the dynamics of the transformed tower model $H(s,\omega_{\mathrm{r}})$ are scheduled by the input excitation frequency, which is in this case the (1P) rotor speed, it is a logical step to augment a wind turbine model adding this state to the overall system description. A system of which the scheduling variable is part of the state vector is known as a qLPV system description. The considered first-order wind turbine model is

$$J_{\mathrm{r}}\dot{\omega}_{\mathrm{r}} = \tau_{\mathrm{a}} - \underbrace{N(\tau_{\mathrm{g}} + \Delta\tau_{\mathrm{g}})}_{\tau_{\mathrm{s}}}, \tag{4.19}$$

in which $J_{\mathrm{r}} \in \mathbb{R}^+$ is the total rotor inertia consisting out of the hub and 3 times the blade inertia, $\{N \geq 1\} \subset \mathbb{R}^+$ is the gearbox ratio, and τ_{a} is the aerodynamic rotor torque defined as

$$\tau_{\mathrm{a}} = \frac{1}{2}\rho_{\mathrm{a}}\pi R^3 U^2 C_\tau(\lambda,\beta), \tag{4.20}$$

in which $\rho_{\mathrm{a}} \in \mathbb{R}^+$ is the air density, $R \in \mathbb{R}^+$ the rotor radius, $U \in \mathbb{R}^+$ the rotor effective wind speed, and $C_\tau \in \mathbb{R}$ the torque coefficient as a function of the blade pitch angle β and the dimensionless tip-speed ratio $\lambda = \omega_{\mathrm{r}}R/U$. The system torque $\tau_{\mathrm{s}} \in \mathbb{R}^+$ is a summation of the generator torque $\tau_{\mathrm{g}} \in \mathbb{R}^+$ resulting from a standard *K-omega-squared* torque control strategy (Bossanyi, 2000), and $\Delta\tau_{\mathrm{g}} \in \mathbb{R}$ is an additional torque contribution resulting from the MPC framework described later in this chapter. The *K-omega-squared* torque control law is taken as an integral part of the model, and is defined as

$$\tau_{\mathrm{g}} = K\omega_{\mathrm{r}}^2/N, \tag{4.21}$$

in which $K \in \mathbb{R}^+$ is the optimal mode gain

$$K = \frac{\pi\rho_{\mathrm{a}}R^5 C_{\mathrm{p}}(\lambda,\beta)}{2\lambda^3}, \tag{4.22}$$

calculated for the low-speed shaft (LSS) side.

4.3.2. LINEARIZING THE AUGMENTED TURBINE AND TOWER MODEL

This section augments the wind turbine model from Section 4.3.1 to the demodulated tower model $H(s,\omega_\mathrm{r})$, such that the following system is obtained:

$$\begin{bmatrix}\dot{q}_1\\ \dot{q}_2\\ \dot{q}_3\\ \dot{q}_4\\ \dot{\omega}_\mathrm{r}\end{bmatrix} = \begin{bmatrix}-\zeta/\mathrm{m} & \omega_\mathrm{r} & -\omega_\mathrm{n}^2 & 0 & 0\\ -\omega_\mathrm{r} & -\zeta/\mathrm{m} & 0 & -\omega_\mathrm{n}^2 & 0\\ 1 & 0 & 0 & \omega_\mathrm{r} & 0\\ 0 & 1 & -\omega_\mathrm{r} & 0 & 0\\ 0 & 0 & 0 & 0 & 0\end{bmatrix}\begin{bmatrix}q_1\\ q_2\\ q_3\\ q_4\\ \omega_\mathrm{r}\end{bmatrix} + \begin{bmatrix}a_\mathrm{u}\\ 0\\ 0\\ 0\\ \left(\tau_\mathrm{a} - N\left(\tau_\mathrm{g} + \Delta\tau_\mathrm{g}\right)\right)/J_\mathrm{r}\end{bmatrix}, \tag{4.23}$$

$$a_\mathrm{y} = \sqrt{q_3^2 + q_4^2}. \tag{4.24}$$

The above-given system description contains the nonlinear aerodynamic and generator torque input defined previously by Eqs. (4.20) and (4.21). Furthermore, the output a_y is a nonlinear combination of state vector elements. The system is subject to linearization, where the desired linear state, input, and output vectors are defined as

$$\hat{\boldsymbol{q}}(t) = \left[\hat{q}_1, \hat{q}_2, \hat{q}_3, \hat{q}_4, \hat{\omega}_\mathrm{r}\right]^\mathrm{T}, \tag{4.25}$$

$$\hat{\boldsymbol{u}}(t) = \left[\hat{U}, \Delta\hat{\tau}_\mathrm{g}\right]^\mathrm{T}, \tag{4.26}$$

$$\hat{\boldsymbol{y}}(t) = \hat{A}_\mathrm{y}, \tag{4.27}$$

and the $\hat{(\cdot)}$-notation indicates the deviation with respect to the considered linearization point. Now, the system is linearized by taking the partial derivatives of Eqs. (4.23) and (4.24) with respect to the state and inputs vectors, such that a linear state-space system is obtained

$$\begin{aligned}\dot{\hat{\boldsymbol{q}}}(t) &= \mathbf{A}(\boldsymbol{p})\hat{\boldsymbol{q}}(t) + \mathbf{B}(\boldsymbol{p})\hat{\boldsymbol{u}}(t)\\ \hat{\boldsymbol{y}}(t) &= \mathbf{C}(\boldsymbol{p})\hat{\boldsymbol{q}}(t),\end{aligned} \tag{4.28}$$

in which the state, input and output matrices are defined as

$$\mathbf{A}(\boldsymbol{p}) = \begin{bmatrix}-\zeta/\mathrm{m} & \bar{\omega}_\mathrm{r} & -\omega_\mathrm{n}^2 & 0 & \bar{q}_2\\ -\bar{\omega}_\mathrm{r} & -\zeta/\mathrm{m} & 0 & -\omega_\mathrm{n}^2 & -\bar{q}_1\\ 1 & 0 & 0 & \bar{\omega}_\mathrm{r} & \bar{q}_4\\ 0 & 1 & -\bar{\omega}_\mathrm{r} & 0 & -\bar{q}_3\\ 0 & 0 & 0 & 0 & (\bar{k}_{\omega_\mathrm{r}} - N\bar{k}_{\tau_\mathrm{g}})/J_\mathrm{r}\end{bmatrix}, \quad \mathbf{B}(\boldsymbol{p}) = \begin{bmatrix}0 & 0\\ 0 & 0\\ 0 & 0\\ 0 & 0\\ \bar{k}_\mathrm{U}/J & -N/J\end{bmatrix},$$

$$\mathbf{C}(\boldsymbol{p}) = \begin{bmatrix}0 & 0 & 0.5\bar{q}_3(\bar{q}_3^2 + \bar{q}_4^2)^{-1/2} & 0.5\bar{q}_4(\bar{q}_3^2 + \bar{q}_4^2)^{-1/2} & 0\end{bmatrix}. \tag{4.29}$$

The aerodynamic rotor torque is linearized with respect to the rotor speed and wind speed

$$\hat{\tau}_\mathrm{a} = \frac{\partial\tau_\mathrm{a}}{\partial\omega_\mathrm{r}}\hat{\omega}_\mathrm{r} + \frac{\partial\tau_\mathrm{a}}{\partial U}\hat{U} = \bar{k}_{\omega_\mathrm{r}}(\omega_\mathrm{r},\ \beta,\ U)\hat{\omega}_\mathrm{r} + \bar{k}_\mathrm{U}(\omega_\mathrm{r}, \beta, U)\hat{U}, \tag{4.30}$$

with

$$\bar{k}_{\omega_\mathrm{r}}(\omega_\mathrm{r}, \beta, U) = c_\mathrm{r} R U \frac{\partial C_\tau(\lambda,\beta)}{\partial\lambda}\bigg|_{\omega_\mathrm{r}=\bar{\omega}_\mathrm{r},\, \beta=\bar{\beta},\, U=\bar{U}}, \tag{4.31}$$

$$\bar{k}_\mathrm{U}(\omega_\mathrm{r}, \beta, U) = 2c_\mathrm{r} C_\tau(\lambda,\beta) U - c_\mathrm{r}\omega_\mathrm{r} R \frac{\partial C_\tau(\lambda,\beta)}{\partial\lambda}\bigg|_{\omega_\mathrm{r}=\bar{\omega}_\mathrm{r},\, \beta=\bar{\beta},\, U=\bar{U}}, \tag{4.32}$$

and $c_\mathrm{r} = 0.5\rho\pi R^3$ is a constant factor. Finally, the *K-omega-squared* torque controller is linearized as

$$\hat{\tau}_\mathrm{g}(\omega_\mathrm{r}) = \frac{\partial \tau_\mathrm{g}}{\partial \omega_\mathrm{r}}\hat{\omega}_\mathrm{r} = \bar{k}_{\tau_\mathrm{g}}(\omega_\mathrm{r})\hat{\omega}_\mathrm{r} = 2K\omega_\mathrm{r}/N\bigg|_{\omega_\mathrm{r}=\bar{\omega}_\mathrm{r}}\hat{\omega}_\mathrm{r}. \tag{4.33}$$

The $\bar{(\cdot)}$-notation indicates the steady-state values of the corresponding operating points. The advantage of this approach is that for each operating point, corresponding steady-state values are substituted in the state-space matrices. This is done by a function $\boldsymbol{p} = f(\omega_\mathrm{r}(t)) : \mathbb{R} \to \mathbb{R}^{n_\mathrm{p}}$, which schedules the system $\mathbf{A}(\boldsymbol{p}) : \mathbb{R}^{n_\mathrm{p}} \to \mathbb{R}^{n\times n}$, input $\mathbf{B}(\boldsymbol{p}) : \mathbb{R}^{n_\mathrm{p}} \to \mathbb{R}^{n\times m}$ and output $\mathbf{C}(\boldsymbol{p}) : \mathbb{R}^{n_\mathrm{p}} \to \mathbb{R}^{q\times n}$ matrices. This leads to the description of nonlinear dynamics by a set of linear models, varying the system according to the operating point parameterized by $\boldsymbol{p} \in \mathscr{P}$. For the qLPV case, the scheduling variable is part of the state, which makes the system self-scheduling at each time step. In this chapter, a finite number of linearizations is considered for operating conditions along the optimal power coefficient $C_{\mathrm{p,max}}(\lambda^*) = C_\tau(\lambda^*)\lambda^*$ corresponding to the set $\mathscr{U}$ of below-rated wind speeds.

The current form of the linear model in Eq. (4.28) only describes deviations from the current operating point. To approach the actual states and outputs of the nonlinear model with a qLPV model structure, offsets for the state, input, and output should be incorporated in the system description. The process of incorporating these operating point offsets, converting the LPV model to its affine form, is described in Appendix B.1. The same appendix also describes the employed fourth order Runge-Kutta state-space discretization method. When in the remainder of this chapter is referred to the qLPV model, the system in its affine form is intended.

4.3.3. COMPLETING THE LINEARIZATION FOR THE NREL 5-MW REFERENCE TURBINE

This section provides the data for linearization of the NREL 5-MW turbine and performs a validation of the resulting affine qLPV system to the nonlinear turbine model in high-fidelity simulation code. All linearization parameters are summarized in Table 4.1.

First, an analytical fit is made to the NREL 5-MW torque coefficient data as a function of the tip-speed ratio. This is needed as $\bar{k}_{\omega_\mathrm{r}}$ and $\bar{k}_\mathrm{U}$ are a function of the operational rotor and wind speed. The torque coefficient data are obtained using a graphical extension (Bos et al., 2019) to NREL's high-fidelity wind turbine simulation software FAST v8.16 (NWTC Information Portal, 2019), which includes blade element momentum (BEM) code (Burton et al., 2001) for obtaining rotor characteristic data. As the framework being derived in this chapter focuses on the below-rated region, and conventional wind turbine controllers keep the pitch angle fixed at fine-pitch angle β_0 during partial load (Pao and Johnson, 2011), the dependency of the torque coefficient on β is omitted. An often used parameterizable torque coefficient function is defined by

$$C_\tau(\lambda) = \mathrm{e}^{-\theta_1/\lambda}(\theta_2/\lambda - \theta_3)/\lambda + \theta_4, \tag{4.34}$$

which is fitted by optimizing the values θ_i using a nonlinear least-squares routine, minimizing the sum-of-squares between the fit and the data-points. Figure 4.6 shows the

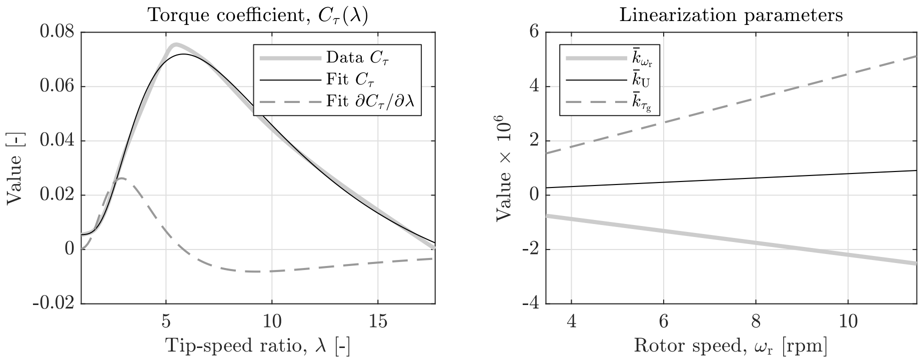

Figure 4.6: ***Left:*** torque coefficient curve of the NREL 5-MW reference wind turbine as a function of the dimensionless tip-speed ratio. The fit according to the model structure proposed by Eq. (4.34) shows a close fit to the data points. The fit allows the derivation and evaluation of the partial gradient. ***Right:*** the linearization parameters defining the LPV model at each scheduling instant.

torque coefficient trajectory as a function of the tip-speed ratio for $\beta = \beta_0$, and the fit to this data. Also, an evaluation of the analytically computed partial gradient with respect to the tip-speed ratio is given. Furthermore, the same figure shows the linearization parameters $\bar{k}_{\omega_r}$, $\bar{k}_U$ and $\bar{k}_{\tau_g}$. The evaluation is performed for all below-rated rotor speed conditions along the maximum power coefficient $C_{p,max}$ at an optimal tip-speed ratio of $\lambda^* = 7.7$. The trajectories show smooth and linear behavior for all operating points.

Table 4.1: Parameters for linearization and simulation of the qLPV model in the below-rated operating region.

Description	**Symbol**	**Value**	**Unit**
Blade inertia	J_b	$11.776 \cdot 10^6$	$kg\,m^2$
Hub inertia	J_h	115 926	$kg\,m^2$
Total rotor inertia	J_h	$35.444 \cdot 10^6$	$kg\,m^2$
Torque coefficient fit (1/2)	$\theta_{1,2}$	14.5924, 42.7653	-
Torque coefficient fit (2/2)	$\theta_{3,4}$	2.4604, 0.0036	-
Gearbox ratio	N	97	-
Air density	ρ_a	1.225	$kg\,m^{-3}$
Fine pitch angle	β_0	$1.9 \cdot 10^{-3}$	rad
Rotor radius	R	63	m
Optimal mode gain (LSS)	K	$2.1286 \cdot 10^6$	$Nm\,(rad\,s^{-1})^{-2}$
Optimal tip-speed ratio	λ^*	7.7	-
Input excitation amplitude	a_u	1	-
Tower mass	m	1000	kg
Tower damping	ζ	100	$kg\,s^{-1}$
Tower stiffness	k	500	$kg\,s^{-2}$
Tower natural frequency	ω_n	0.7071	$rad\,s^{-1}$

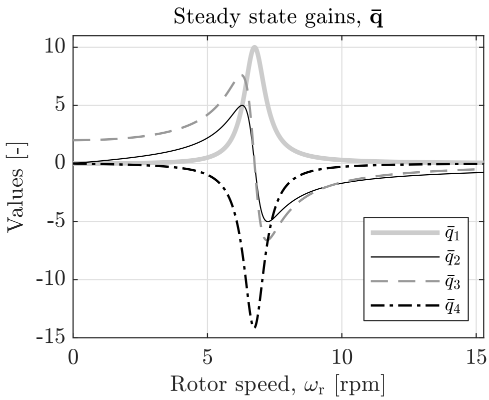

Figure 4.7: State-state gains $\bar{q}_1$ to $\bar{q}_4$ as a function of the rotor speed scheduling variable. Around the natural tower frequency, the gains show a higher sensitivity to the x-coordinate, raising the need for an LPV model set on a fine scheduling grid.

4

In Figure 4.7, the steady-state values for $\bar{q}_1$, $\bar{q}_2$, $\bar{q}_3$, and $\bar{q}_4$ are given as a function of rotor speed for the optimal power coefficient operating conditions. Compared to the previously presented linearization parameters, these trajectories show a more volatile behavior: At the tower natural frequency, two of the trajectories change signs, while the other two reach their extrema. This, as will be shown later, results in some erratic behavior when the qLPV model self-schedules itself around the natural frequency. Therefore, a fine grid of linear models should be taken in the LPV scheduling space, to minimize artifacts and to properly describe the nonlinear dynamics.

4.3.4. THE QLPV MODEL SUBJECT TO A TURBULENT WIND

The main advantage of a qLPV model, is that the scheduling parameter is part of the state vector. In this way, the scheduling signal is not exogenous, and the model is consequently self-scheduling according to its state evolution. To verify the validity of the derived affine qLPV model during below-rated operation, a uniform turbulent wind signal with a mean wind speed and turbulence intensity of respectively, $\bar{U} = 6.5\ \mathrm{m\,s^{-1}}$ and $\mathrm{TI} = 25\ \%$ is applied to:

1. A nonlinear NREL 5-MW aerodynamic model simulated in the high-fidelity **FAST** code. A second-order, first mode tower model $G(s)$ is excited by a unity amplitude cosine as a function of the azimuth position.
2. The **first-order** linearized NREL 5-MW wind turbine model with $C_\tau(\lambda)$ look-up table, driving the **transformed** tower model $H(s,\omega_r)$ by the rotor speed output.
3. The **qLPV** model, incorporating the linear wind turbine rotor and **transformed** tower dynamics, self-scheduled by its rotor speed state.

The simulation results, based on the parameters in Table (4.1), are presented in Figure 4.8. The left plot shows the rotor speed simulation, which demonstrates that the first-order and qLPV models accurately follow the FAST output. Subsequently, the right plot compares the tower-top side-side displacement responses, as a result of the rotor

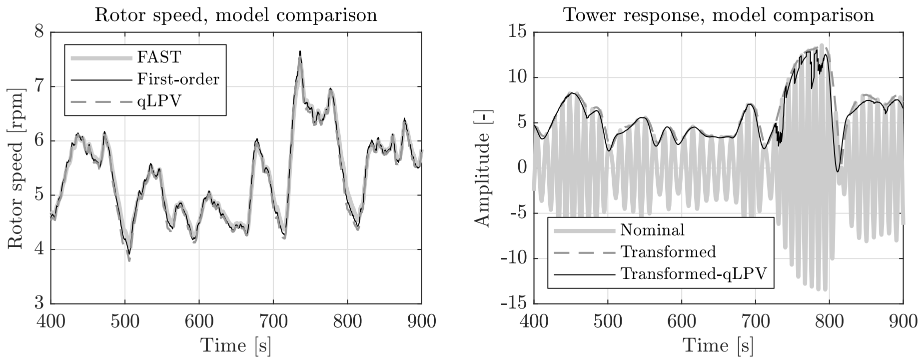

Figure 4.8: Simulation results showing the rotor speed and tower-top displacement amplitude for different models driven by a turbulent wind disturbance input signal. The FAST model excites the nominal tower model and serves as a baseline simulation case. The first-order wind turbine model is combined with the nonlinearized transformed tower model. The qLPV system is a single scheduled system description for the rotor and tower dynamics, and shows – apart from minor artifacts around the tower natural frequency – a close resemblance to its nonlinear companion.

imbalance excitation. As concluded earlier by the frequency sweep in Figure 4.5, the nominal and transformed tower models show a good match. The additional qLPV response in Figure 4.8 shows a similar trajectory as the transformed model, apart from some minor artifacts between 700 – 800 s, when the rotor speeds approaches the tower natural frequency. These anomalies are a result of the steady-state gains $\bar{q}_{1-4}$ being more sensitive in the region of ω_n (Figure 4.7), and the switching between the linear models by the scheduling parameter. However, as the response serves as a load indication, and the exact value is of less importance, the qLPV method is concluded being suitable for its intended purpose in the qLPV-MPC framework, described in the next section.

4.4. QUASI-LPV MODEL PREDICTIVE CONTROL

Nonlinear MPC is – because of its computational complexity – often considered as an unsuitable control method for application in fast real-time systems. Therefore, in this chapter, an approach towards an efficient method for nonlinear MPC is employed, exploiting the inherent self-scheduling property of a qLPV system. This section describes the qLPV-MPC framework, with the aim to provide a convex QP, defining a trade-off between maximizing power production efficiency, and minimizing tower natural frequency excitation. Practically, this means that the rotor deviates from the maximum power extraction trajectory when it approaches the rotor speed coinciding with the structural resonance frequency.

An economic MPC approach is used to directly optimize for the economic performance of the process (Rawlings et al., 2012). For the considered case, a predefined quadratic performance criterion specifies the trade-off between energy production maximization and resonance excitation minimization, and the optimizer finds the optimal corresponding control signal in the prediction horizon. However, as for each time step, the scheduling sequence over the prediction horizon is unknown, the nonlinear MPC control problem is solved by an iterative method (Cisneros et al., 2016). The method solves subsequent QPs minimizing the predefined cost and uses the resulting predicted scheduling sequence as a warm-start for the next iteration. Each iteration uses a single QP solve. A norm on the consecutive output differences is used to determine whether the algorithm has converged.

By manipulation of the affine system representation defined by Eqs. (B.6) and (B.7), an expression is derived for forward propagation of the qLPV model output, only requiring the initial state at time instant k and the scheduling sequence over the prediction horizon:

$$\begin{aligned} \boldsymbol{Y}_{k+1} = &\mathbf{H}(\mathbf{P}_k)\left(x_k - \check{x}(p_{\mathrm{k}})\right) + \mathbf{S}(\mathbf{P}_k)\Delta\boldsymbol{U}_k(\mathbf{P}_k) \\ &+ \left(\check{\boldsymbol{Y}}_{k+1}(\mathbf{P}_k) + \mathbf{L}(\mathbf{P}_k)\Delta\check{\boldsymbol{X}}_k(\mathbf{P}_k) + \mathbf{D}(\mathbf{P}_k)\Delta\boldsymbol{U}_{k+1}(\mathbf{P}_k)\right), \end{aligned} \tag{4.35}$$

in which the matrices $\{\boldsymbol{H}, \boldsymbol{S}, \Delta\boldsymbol{U}_k, \check{\boldsymbol{Y}}_{k+1}, \mathbf{L}, \Delta\check{\boldsymbol{X}}_k, \mathbf{D}, \Delta\boldsymbol{U}_{k+1}\}$ are defined in Appendix B.2, and $\mathbf{P}_{\mathrm{k}} = \left[\boldsymbol{p}_k, \boldsymbol{p}_{k+1} \cdots \boldsymbol{p}_{k+\mathrm{N_p}}\right] \in \mathbb{R}^{n_{\mathrm{p}} \times N_{\mathrm{p}}}$ is the collection of scheduling variables at each time instant over the prediction horizon $N_{\mathrm{p}} \in \mathbb{Z}^+$. The $\check{(\cdot)}$-notation indicates steady-state offsets from the current operating point for the the states, in- and outputs (Appendix B.1). The opportunity for defining a control horizon $N_{\mathrm{c}} \in \mathbb{Z}$ is disregarded in this chapter and is chosen to equal N_{p}. For sake of completeness, the above given propagation expression includes a direct feedthrough matrix $\mathbf{D}$, although it is not used for the considered problem.

At time instant $k = 0$, only the initial state is assumed to be known, and the scheduling parameters are chosen constant over the prediction horizon, such that:

$$\boldsymbol{P}_0 = \mathbf{1}_{\mathrm{N_p}} \otimes \boldsymbol{p}_0, \tag{4.36}$$

in which $\mathbf{1}_{\mathrm{N_p}} \in \mathbb{R}^{N_{\mathrm{p}}}$ is a one-dimensional vector of ones. By assuming the initialization vector, the convex QP is solved with $\Delta\boldsymbol{\Theta}_{\mathrm{g},k+1} = \left[\Delta\tau_{\mathrm{g},k+1} \cdots \Delta\tau_{\mathrm{g},k+N_{\mathrm{p}}}\right] \in \mathbb{R}^{N_{\mathrm{p}}}$ as the decision variable vector, minimizing the cost

$$\begin{aligned} \underset{\Delta\boldsymbol{\Theta}_{\mathrm{g},k+1}}{\arg\min} \quad & \boldsymbol{Y}_{k+1}^T \mathbf{Q} \boldsymbol{Y}_{k+1} + \Delta\boldsymbol{\Theta}_{\mathrm{g},k+1}^T \mathbf{R} \Delta\boldsymbol{\Theta}_{\mathrm{g},k+1} \\ \text{subject to} \quad & \text{Dynamical system in Eq. (4.35)}, \end{aligned} \tag{4.37}$$

in which $\mathbf{Q} = \mathtt{diag}(Q, Q \cdots Q) \in \mathbb{R}^{\mathrm{N_p} \times \mathrm{N_p}}$ and $\mathbf{R} = \mathtt{diag}(R, R \cdots R) \in \mathbb{R}^{\mathrm{N_p} \times \mathrm{N_p}}$ are, respectively, weight matrices acting on the predicted tower-top displacement amplitude and deviation from the optimal torque control signal. The latter term of the cost requires the assumption of optimal power production efficiency using the *K-omega-squared* torque control strategy. Now, compare the above given minimization objective with the one introduced in the problem formalization by Eq. (4.3). The first term of Eq. (4.37) aims on fatigue load minimization, whereas the latter term is a combination of energy production maximization and penalization on the control input. Formulating the objective in this way, results in a convenient trade-off between power production and load reductions by varying the weight ratio of Q and R.

After the first solve with the initial scheduling sequence of Eq. (4.36), the inherent qLPV property is exploited by using the predicted evolution of the state to form a warm-start initialization of $\mathbf{P}_k^{j+1}$ in the next iteration. This iterative process is repeated until

Algorithm 1 - Pseudocode for iteratively finding the scheduling vector $\mathbf{P}_\mathrm{k}$ in the first time step, and warm-starting for subsequent time instants.

$k \leftarrow 0, \quad j \leftarrow 1, \quad j_\mathrm{n} \leftarrow 5$
Define Q, R, N_p
Initialize matrices $\mathbf{Q}$, $\mathbf{R}$
Initialize state $\mathbf{X}$, output $\mathbf{Y}$, and scheduling $\boldsymbol{P}$ matrices as empty $\mathbf{0}$-matrices
$\mathbf{P}_k^j \leftarrow 1_{\mathrm{N_p}} \otimes f(\boldsymbol{x}_0), \quad \mathbf{X}(:,k) = \boldsymbol{x}_0$
for time instant k **do**
  while $j \leq j_\mathrm{n}$ **do**
    Construct matrices $\mathbf{H}(\mathbf{P}_k^j)$, $\mathbf{S}(\mathbf{P}_k^j)$, $\mathbf{L}(\mathbf{P}_k^j)$, $\Delta\boldsymbol{U}(\mathbf{P}_k^j)$, $\check{\boldsymbol{Y}}_{k+1}(\mathbf{P}_k^j)$, $\Delta\check{\boldsymbol{X}}_{k+1}(\mathbf{P}_k^j)$
    Solve for $\Delta\boldsymbol{\Theta}_\mathrm{g}$ as in Eq. (4.37) with $\mathbf{X}(:,k)$ as initial state
    Simulate the qLPV model with $\Delta\boldsymbol{\Theta}_\mathrm{g}$ for N_p samples to find the state evolution $\mathscr{X}^j$
    Define $\mathbf{P}_k^{j+1} = f(\mathscr{X}^j)$
    $j \leftarrow j+1$
  end while
  $j \leftarrow 1, \quad j_\mathrm{n} \leftarrow 1$
  Take the first sample of $\Delta\boldsymbol{\Theta}_\mathrm{g}$ to apply in high-fidelity code and simulate for $t_{\mathrm{s,FAST}}$
  Save resulting state and output data: $\mathbf{X}(:,k+1) \leftarrow \boldsymbol{x}_k, \quad \mathbf{Y}(:,k) \leftarrow \boldsymbol{y}_k$
  Define $\mathbf{P}_{k+1}^j = f(\mathscr{X}^{\mathrm{end}})$ as a warm start for the next time instant
  $k \leftarrow k+1$
end for

$\left|\left|\boldsymbol{Y}_k^{j+1} - \boldsymbol{Y}_k^j\right|\right|_2 < \epsilon$, or for a maximum number of iterations j_n, with ϵ being a predefined error threshold. The algorithm is summarized using pseudocode in Algorithm 1.

An evaluation has shown that after convergence during initialization, warm-starting the scheduling sequence for the subsequent time-steps shows excellent results. That is, performing multiple iterations for time instants $k > 0$ shows no significant performance enhancements for the considered problem. Therefore, the described process is only performed in the initial time step $k = 0$. The need for only a single QP in each step, makes the approach for solving the nonlinear MPC problem computationally efficient and tractable for real-world implementations.

4.5. HIGH-FIDELITY SIMULATION SETUP AND RESULTS

This section implements the proposed qLPV-MPC framework in conjunction with the NREL 5-MW reference wind turbine model in the high-fidelity FAST code. The software implementation is made publicly available (Mulders et al., 2019b). As the side-side natural frequency of the NREL 5-MW turbine is located outside the rotor speed operating region, the tower properties are modified. The tower wall thickness is scaled down by a factor 7.5 to mimic the characteristics of a tall, more flexible, soft-soft tower configuration. As a result of the reduced thickness, an effective turbine side-side resonance frequency of approximately 0.71 rad s^{-1} is attained, equal to ω_n defined in Section 4.2.4. Also, two of the three blades are configured to have an overall mass increase and de-

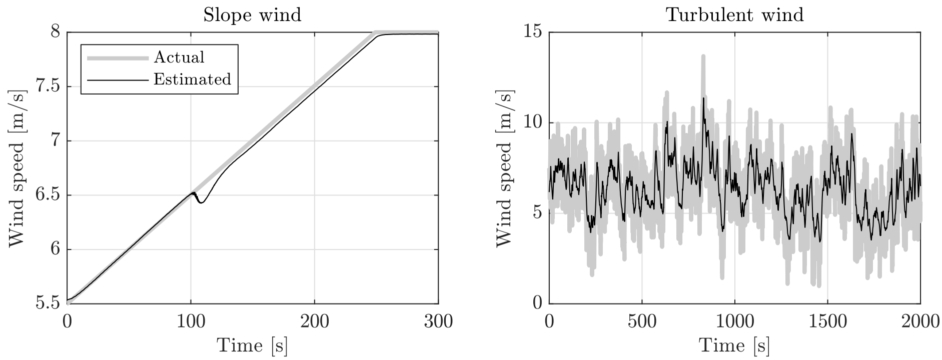

Figure 4.9: A linearly increasing slope and turbulent wind profile employed for the two simulation cases. The rotor effective wind speed is estimated by a wind speed estimator. A discrepancy of the estimated sloped wind speed is observed after 100 seconds, which is a result of sudden changes in applied generator torque and measured rotor speed.

crease of 2 % with respect to the reference blade. This mass imbalance induces a rotor eccentricity, exacerbating the excitation of the turbine side-side mode.

Furthermore, the simulation environment incorporates the demodulated second-order tower model from Eq. (4.15). The transformed tower model is scheduled by the simulated rotor speed, and the resulting integrator states are, together with the rotor speed, used in each time-step to form the initial state. The initial state is, as shown in Algorithm 1, at each time instant used for forward propagation of the qLPV model by Eq. (4.35).

The aim is now to showcase the framework capabilities of successfully preventing prolonged rotor speed operation near the tower resonance frequency. This is done by defining two separate simulation cases:

- **Case 1:** Initializing the wind turbine for operating conditions corresponding to a constant uniform wind speed of U = 5.5 m s^{-1}, followed by a linearly increasing trajectory to a maximum wind speed of U = 8.0 m s^{-1} in approximately 250 s.
- **Case 2:** Operating the wind turbine in uniform turbulent wind conditions with a mean wind speed and turbulence intensity of respectively, $\bar{U}$ = 6.5 m s^{-1} and TI = 25 % for 2000 s. The chosen mean wind speed results in operation at the tower side-side resonance frequency.

For both cases, the behavior of the qLPV-MPC implementation is compared with standard *K-omega-squared* torque control.

The employed wind signals are presented in Figure 4.9. Because the wind speed cannot assumed to be measurable in real-world scenarios, an effective immersion and invariance (I&I) rotor effective wind speed estimator is used (Ortega et al., 2013; Soltani et al., 2013), which is also plotted in the same figure. Because the future wind speed is unknown at time instant k, the wind speed evolution is chosen to be constant and equal to the current estimated value over the prediction horizon. Also, the smoothened course of the estimated signal aids the qLPV-MPC algorithm to prevent from overreacting to rapid

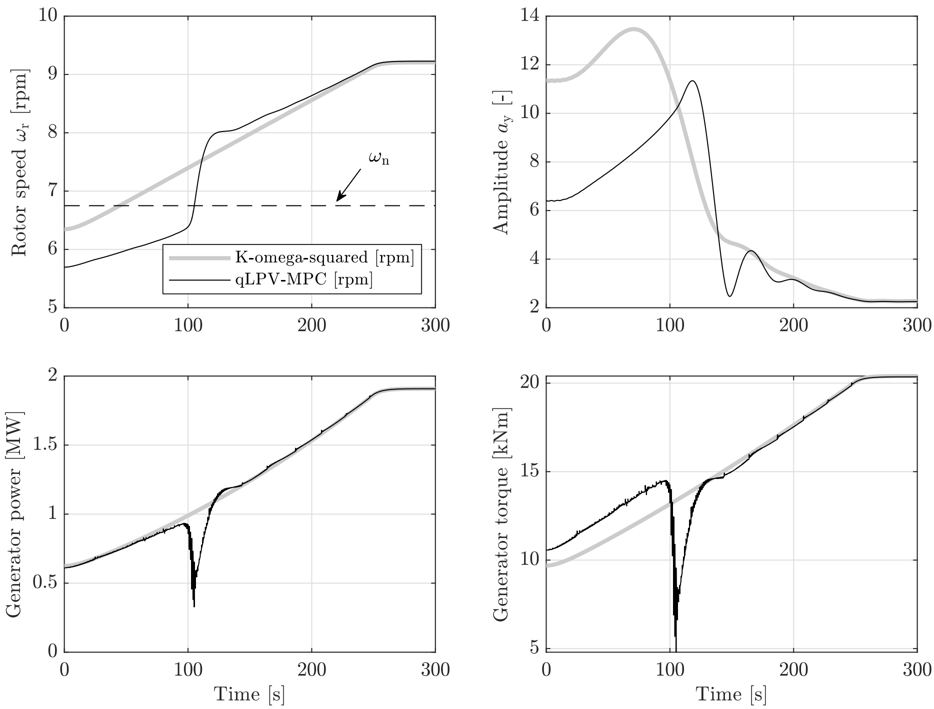

Figure 4.10: Simulation **Case 1** shows a comparison with conventional torque control subject to a linearly increasing wind speed. The proposed algorithm prevents the rotor speed from prolonged operation at the tower's natural frequency by imposing an additional generator torque demand. Then, when the wind speed is sufficient for operation at a higher rotor speed, the additional generator torque is rapidly reduced to facilitate a swift crossing of the critical frequency. The strategy is beneficial for reducing periodic tower loading at a specific frequency, at the expense of generated power.

variations. As the wind speed estimator takes the applied generator torque and measured rotor speed as inputs, and a rapid rotor speed and generator torque change occurs after 100 seconds, a discrepancy is seen at this time instant. Nonetheless, the estimator shows a quick recovery in consequent time steps.

Distinct sampling intervals are used for the simulation environment and MPC update actions. Simulation of the NREL 5-MW reference turbine in FAST requires a sampling time of $t_{\mathrm{s,FAST}} = 0.01$ second to prevent numerical issues. The MPC sampling time is set to $t_{\mathrm{s,MPC}} = 1.0$ s. Note that this rather low sampling interval is possible because the demodulation transformation moves the load signal to a quasi-steady state contribution. As a result of this transformation, the algorithm's goal is to find the optimal operating trajectory, and not to actively mitigate a specific frequency. The low sampling interval is especially convenient for real-world applications, as this allows solving the QP less frequently, reducing the need for powerful control hardware.

The FAST simulation environment, implemented in MATLAB Simulink (MathWorks, 2019), simulates for $t_{\mathrm{s,MPC}}$, after which is simulation is paused, and essential informa-

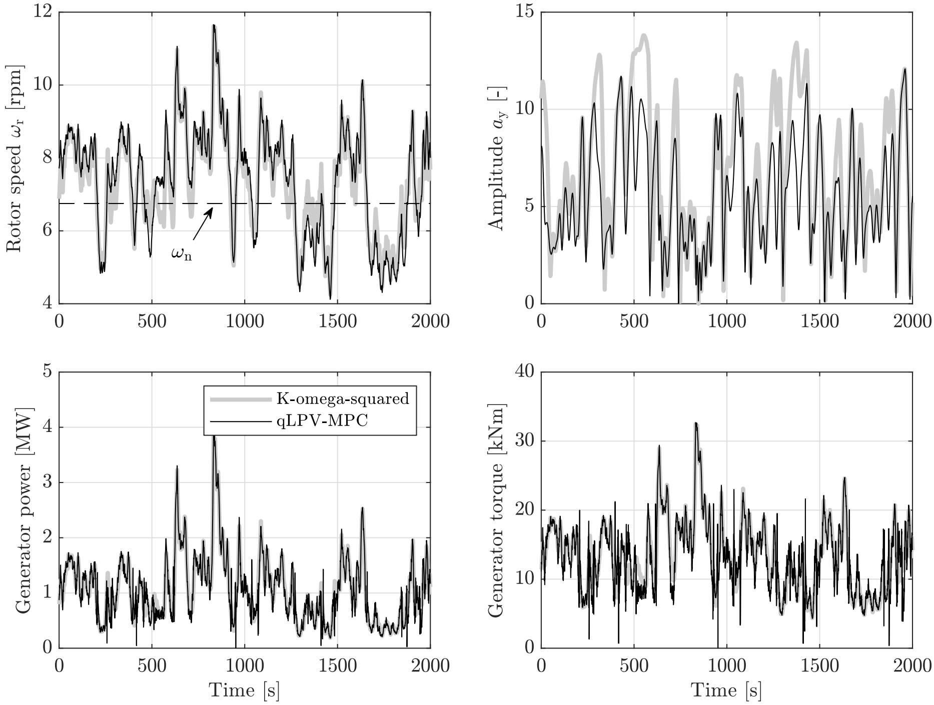

Figure 4.11: Simulation **Case 2** shows a comparison with conventional torque control subject to a realistic turbulent wind profile. The tower loading extremes are significantly reduced by preventing prolonged operation at the critical rotor speed. The algorithm shows to have minimal impact on the generated power.

tion is extracted. The simulation data are provided to the MPC algorithm in MATLAB using CVX: A package for specifying and solving convex programs (Grant and Boyd, 2014; Grant and Boyd, 2008). After solving the optimization problem, the first input sample of the decision variable vector is updated in the simulation environment. The simulation is resumed and the input is held constant for the next $t_{s,MPC}$ seconds, after which it is paused again.

Figure 4.10, presents the results for simulation **Case 1**. For this case, the in- and output weighing factors are chosen as $Q = 0.1$, $R = 25$, and the prediction horizon is set to $N_p = 25$. The simulation results show the ability of the algorithm to withhold the turbine from operating at a rotational speed exciting the tower natural frequency by increasing $\Delta\tau_g$. Then, around 100 seconds, the wind speed is sufficient for the load and power trade-off to be in favor of the latter mentioned. This is reflected by a swift reduction of the generator torque resulting in a rapid crossing of the critical rotor speed at $\omega_r = \omega_n = 6.75$ RPM. The tower-top displacement shows a reduction in amplitude by excitation of the natural frequency for a shorter period of time. Obviously, this comes at the expense of produced energy.

The simulation results for **Case 2** are given in Figure 4.11. By inspection of the rotor speed around the resonance frequency, it shows that the qLPV-MPC implementation

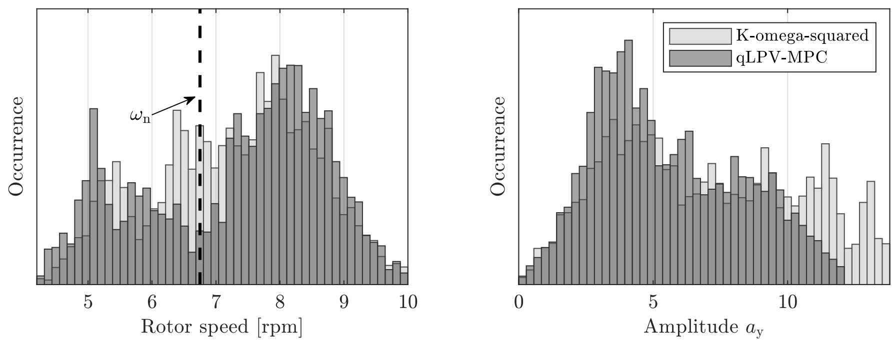

Figure 4.12: Histograms of the rotor speed and displacement amplitude occurrence for simulation **Case 2**. The rotor speed histogram (*left*) clearly shows that the qLPV-MPC algorithm prevents operation at the critical speed. Consequently, the amplitude histogram (*right*) shows a reduced maximum occurrence, whereas smaller amplitudes happen more frequently, which is beneficial from a fatigue loading viewpoint.

prevents operation at this speed for extended time periods. This operational strategy results in a significant decrease of tower-top displacement amplitudes. To further clarify this effect, Figure 4.12 shows histograms of the rotor speed and displacement amplitude signals. Furthermore, Figures 4.13a and 4.13b show the sidewards displacement spectra of the two control strategies. A significant reduction of 18 dB is attained at the turbine side-side natural frequency.

Finally, a fatigue assessment is performed on the tower base side-side moment by evaluating the damage equivalent loads (DEL) from the corresponding time-domain signals using `MLife` (NWTC Information Portal, 2015). The DEL measure quantifies the amplitude of a certain harmonic load variation that would cause the same damage level when repeated for a given number of cycles (Freebury and Musial, 2000; Bossanyi et al., 2013). In this fatigue analysis, a Wöhler-exponent of 4 is chosen, which is a typical value for steel (Germanischer Lloyd, 2012). With respect to the baseline case, a significant 52 % DEL reduction is attained. Since the analysis is based on the single load case performed in this section, the short-term DELs are calculated using the 1 Hz equivalent load (Burton et al., 2001). This implies that the number of cycles is equal to the simulation time, and consequently makes the analysis independent of the simulation runtime.

The generator power and torque trajectories of the control strategies show a high degree of similarity, which indicates a minimal penalty on the overall energy production. The observation is confirmed by evaluation of the produced energy over the total simulation time, resulting in 603.34 kWh and 601.19 kWh for the respective baseline and qLPV-MPC cases, which turns out in a produced energy reduction of 0.36 %. The trade-off is conveniently tuned by varying the weight ratio between Q and R.

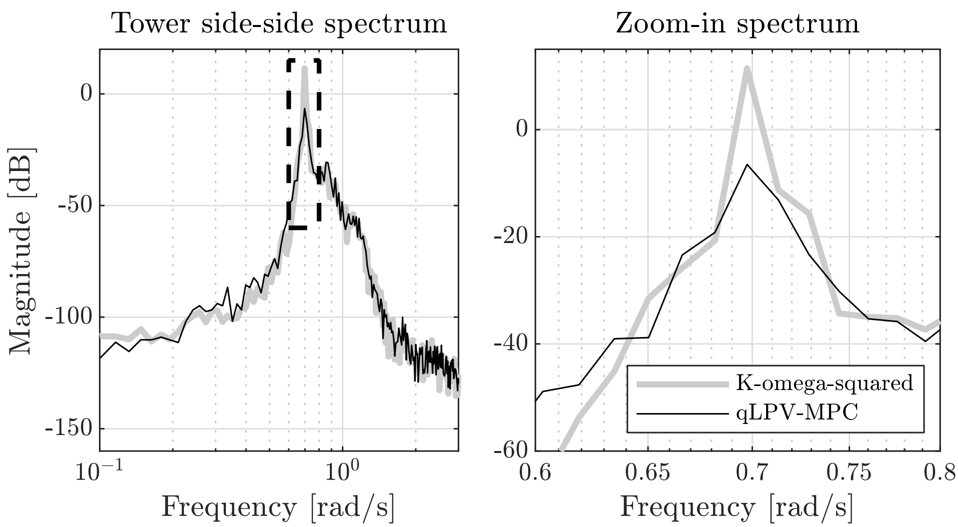

(a) (b)

Figure 4.13: **(a)** Side-side displacement spectra of the NREL 5-MW turbine subject to high-fidelity turbulent wind simulations. The tower wall thickness is modified, such that a turbine side-side natural frequency of approximately 0.71 rad s^{-1} is obtained. The blades are given a dissimilar mass to induce rotor eccentricity. Spectra for the *K-omega-squared* and qLPV-MPC implementations show a significant reduction of the dominant resonance. **(b)** The content in the dashed box is enlarged and shows a peak reduction of 18 dB.

4.6. CONCLUSIONS

In practical scenarios, wind turbine rotors possess a mass and/or aerodynamic imbalance, which cause a periodic side-side excitation. For future turbines with higher power ratings and taller towers to be weight and cost effective, soft-soft tower configurations are being considered. Such towers are more flexible and have their side-side natural frequency in the variable-speed domain, possibly coinciding with the rotor rotational or blade passing frequencies.

To date, no efficient and intuitive MPC framework is available for preventing rotor speed operation at this frequency. In this chapter, the dynamics of a wind turbine tower are subject to a demodulation transformation and thereby transformed into a quasi-LPV system description. The resulting qLPV model, by aggregation with a wind turbine model, is reconciled with an MPC scheme. The combination exploits the inherent properties of the qLPV model, leading to an efficient method of solving a convex optimization problem. The qLPV-MPC approach involves finding the qLPV scheduling sequence by performing multiple iterative QP solves for the first time step. Subsequent time steps only require a single QP solve using a scheduling sequence warm start originating from the previous time step. By imposing an additional torque contribution, the rotor speed is prevented from operating near the tower natural frequency at the expense of reduced aerodynamic efficiency. Simulation results with artificial sloped and realistic turbulent wind profiles show that the algorithm prevents persistent excitation of the tower fundamental frequency, by sacrificing an insignificant amount of produced energy. The current work only considers the exclusion of a single excitation frequency, however, the presented framework can be extended towards the exclusion of multiple resonances.

5

Delft Offshore Turbine with hydraulic drivetrain

Hydraulic transmissions are generally employed in high-load systems, because of their robustness, compactness, and high power density. As offshore wind turbines are getting larger in terms of size and power output, the business case for multi-megawatt compact hydraulic wind turbine drivetrains is becoming ever stronger. The Delft Offshore Turbine (DOT) is a hydraulic wind turbine concept replacing conventional drivetrain components with a single seawater pump. This chapter presents the research that has been performed on the DOT500 prototype and in-field hydraulic wind turbine. It is shown that the overall drivetrain efficiency and controllability are increased by operating the rotor at maximum rotor torque in the below-rated region using a passive torque control strategy. An active valve control scheme is employed and evaluated in near-rated conditions.

Chapter contents

This chapter is based on the following publications:

S.P. Mulders, N.F.B. Diepeveen and J.W. van Wingerden. Control design, implementation, and evaluation for an in-field 500 kW wind turbine with a fixed-displacement hydraulic drivetrain. *Wind Energy Science*, 3(2), 2018

S.P. Mulders, N.F.B. Diepeveen and J.W. van Wingerden. Control design and validation for the hydraulic DOT500 wind turbine. In *International Fluid Power Conference (IFK)*, Aachen, Germany, 2018

S.P. Mulders, N.F.B. Diepeveen and J.W. van Wingerden. Extremum Seeking Control for optimization of a feed-forward Pelton turbine speed controller in a fixed-displacement hydraulic wind turbine concept. In *WindEurope*, Bilbao, Spain, 2019

5.1. Introduction

The drivetrain of horizontal-axis wind turbines (HAWTs) generally consists of a rotor-gearbox-generator configuration in the nacelle, which enables each wind turbine to produce and deliver electrical energy independent of other wind turbines. While the HAWT is a proven concept, the turbine rotation speed decreases asymptotically and torque increases exponentially with increasing blade length and power ratings (Burton et al., 2001). As offshore wind turbines are getting ever larger, this results in a lower rotation speed and higher torque at the rotor axis. This inevitably leads to design challenges when scaling up conventional turbine drivetrains for the high-load subsystems (Kotzalas and Doll, 2010). The increased loads primarily affect high-weight components in the turbine, such as the generator, bearings, and gearbox, and makes repair and replacement a costly and challenging task (Spinato et al., 2009; Ragheb and Ragheb, 2010). Furthermore, due to the contribution of all nacelle components to the total nacelle mass, the complete wind turbine support structure and foundation are designed to carry this weight for the entire expected lifetime, which in turn leads to extra material, weight, and thus total cost of the wind turbine (EWEA, 2009; Fingersh et al., 2006).

In an effort to reduce turbine weight, maintenance requirements, complexity, and thus the levelized cost of energy (LCOE) for offshore wind, hydraulic drivetrain concepts have been considered in the past (Piña Rodriguez, 2012). Integration of hydraulic transmission systems in offshore wind turbines seems to be an interesting opportunity, as they are generally employed in high-load applications and have the advantage of a high power-to-weight ratio (Merritt, 1967). It is concluded in (Silva et al., 2014) that hydrostatic transmissions could lower drivetrain costs, improve system reliability, and reduce the nacelle mass.

The Delft Offshore Turbine (DOT) is an open-circuit seawater hydraulic wind turbine concept. The pump, directly connected to the low-speed shaft, replaces conventional drivetrain components with high maintenance requirements in the nacelle, which reduces the weight, support structure requirements, and turbine maintenance frequency. This effect is clearly visualized in Figure 5.1. Pressurized seawater is directed to a combined Pelton turbine connected to an electrical generator on a central multi-megawatt electricity generation platform.

This chapter presents the first steps in realizing the integrated hydraulic wind turbine concept by full-scale prototype tests with a retrofitted Vestas V44 600 kW wind turbine, the conventional drivetrain of which is replaced by a 500 kW hydraulic configuration. A spear valve is used to control the nozzle outlet area, which in effect influences the fluid pressure in the hydraulic discharge line of the water pump and forms an alternative way of controlling the reaction torque to the rotor. Preliminary results of the in-field tests were presented earlier in (Mulders et al., 2018a).

The main contribution of this chapter is to elaborate on mathematical modeling and controller design for a hydraulic drivetrain with fixed-displacement components, subject to efficiency and controllability maximization of the system. The controller design is based on steady-state and dynamic turbine models, which are subsequently evaluated on the actual in-field retrofitted 500 kW wind turbine. Furthermore, a framework for the modeling of fluid dynamics is provided, a parameter study on how different design variables influence the controllability is given, and future improvements to the system and

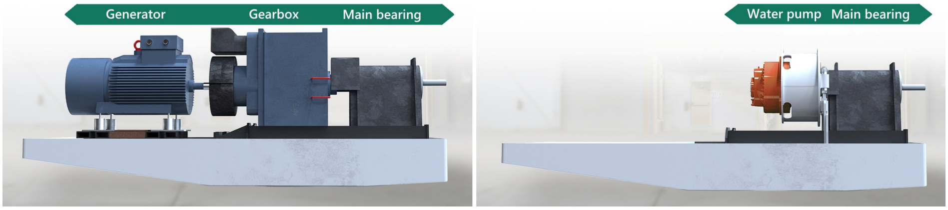

Figure 5.1: The high power-to-weight ratio of hydraulic components and the possibility to abandon power electronics from the nacelle, make the advantages of mass and space reductions in the nacelle self-evident.

controller design are proposed.

The organization of this chapter is as follows. In Section 5.2, the DOT configuration used during the in-field tests is explained, and drivetrain components are specified. Section 5.3, which involves drivetrain modeling, is divided into two parts: A steady-state drivetrain model is derived in 5.3.1, and a drivetrain model including fluid dynamics is presented in Section 5.3.2. Controller design is presented in Section 5.4, and the steady-state model is used in Section 5.4.1 for the design of a passive control strategy for below-rated operation. In Section 5.4.2 the dynamic model is used to derive an active control strategy for the region between below- and above-rated operation (near-rated region). Because the in-field tests are performed prior to theoretical model derivation and controller design, preliminary conclusions from these tests are incorporated. In Section 5.5, in-field test results are presented for the evaluation of the overall controller design. Finally, in Section 5.6, conclusions are drawn and an outlook for the DOT concept is given.

5.2. The DOT500 – prototype turbine with off-the-shelf components

In this section, the intermediate prototype DOT turbine on which in-field tests are performed is described in Section 5.2.1. Subsequently, the drivetrain components used for the intermediate concept are discussed in Section 5.2.2.

5.2.1. The intermediate DOT500 prototype

At the time of writing, a low-speed high-torque seawater pump required for the ideal DOT concept is not commercially available. This pump is being developed by DOT, enabling the ideal concept in later stages of the project (Nijssen et al., 2018). An intermediate setup using off-the-shelf components is proposed to speed up development and test the practical feasibility. A visualization of the DOT500 setup is given in Figure 5.2.

A Vestas V44 600 kW turbine is used and its drivetrain is retrofitted into a 500 kW hydraulic configuration. The original Vestas V44 turbine is equipped with a conventional drivetrain consisting of the main bearing, a gearbox, and a 600 kW three-phase asynchronous generator. The blades are pitched collectively by means of a hydraulic cylinder driven by a HPU (hydraulic power unit) with a safety pressure accumulator. The drivetrain of the Vestas turbine is replaced by a hydraulic drivetrain. This means that the gearbox and generator are removed from the nacelle and replaced by a single oil pump coupled to the rotor via the main bearing.

In the retrofitted hydraulic configuration, a low-speed oil pump is coupled to the rotor and its flow hydraulically drives a high-speed oil-motor–water-pump combination at the bottom of the turbine tower. The oil circuit acts as a hydraulic gearbox between the rotor and the water pump. The water circuit, including the Pelton generator combination, is depicted in Figure 8 (see Prologue) as an ideal setup. It is known and taken into account that the additional components and energy conversions result in a reduced overall efficiency: The in-field tests show a below-rated efficiency in the range of 30–45 %, whereas in the above-rated region a drivetrain efficiency of 45 % is attained. However, the DOT500 allows for prototyping and provides a proof of concept for faster development towards the ideal DOT concept.

From this point onwards, all discussions and calculations will refer to the intermediate DOT500 setup, including the described oil circuit (Diepeveen et al., 2018). A prototype was erected in June 2016 at Rotterdam Maasvlakte II, the Netherlands.

5.2.2. DRIVETRAIN COMPONENT SPECIFICATION

The drivetrain component specifications are summarized in Table 5.1 and a schematic overview and photograph of the DOT500 setup is presented in Figure 5.2. An exhaustive description of the component matching process for the DOT500 is described in (Diepeveen, 2013). The components are described according to the enumerated labels in the figure.

1. *Oil pump.* The rotor drives a Hägglunds CB840, which is a fixed-displacement radial piston motor. The motor is used here as pump and is referred to as the oil pump in the remainder of this chapter. The pump is supplied with sufficient flow and constant feed pressure of 21 bar to keep the piston bearings in continuous contact with the cam ring (Hägglunds, 2015). Load pins are integrated into the

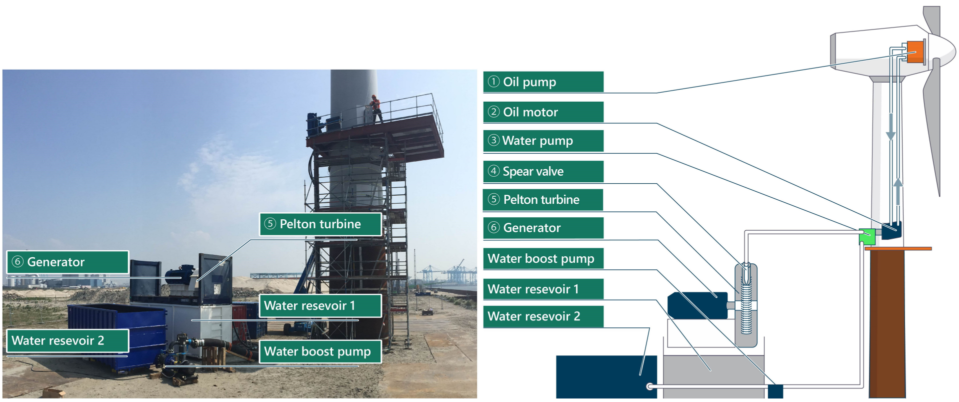

Figure 5.2: Overview of the intermediate DOT500 hydraulic wind turbine configuration. An oil pump is coupled to the rotor low-speed shaft in the nacelle and hydraulically drives an oil motor in the bottom of the tower. This closed oil circuit serves as a hydraulic gearbox between the rotor and water pump. The motor is mechanically coupled to a water pump which produces a pressurized water flow. The flow is converted to high-velocity water jets by spear valves and a Pelton turbine-generator configuration harvests the hydraulic into electric energy.

Table 5.1: Hydraulic oil pump, oil motor and water pump specifications (Hägglunds, 2015; Bosch-Rexroth, 2012; KAMAT, 2016)

Description	**Oil pump**	**Oil motor**	**Water pump**
Brand	Hägglunds	Bosch-Rexroth	Kamat
Model number	CB840	A6VLM	K80120G-5M
Volumetric displacement	52.8 $\mathrm{l\,rev^{-1}}$	1.0 $\mathrm{l\,rev^{-1}}$	2.3 $\mathrm{l\,rev^{-1}}$
Nominal speed	32 $\mathrm{rev\,min^{-1}}$	1600 $\mathrm{rev\,min^{-1}}$	1500 $\mathrm{rev\,min^{-1}}$
Torque range available	0 - 280 kNm	0 - 5571 Nm	0 - 5093 Nm
Pressure range available	0 - 350 bar	0 - 350 bar	0 - 125 bar
Power range available	0 - 870 kW	0 - 933 kW	0 - 800 kW
Torque range applied	0 - 210 kNm	0 - 3000 Nm	0 - 3000 Nm
Pressure range applied	0 - 230 bar	0 - 230 bar	0 - 70 bar

suspension of the pump in the nacelle to measure the pump torque.

2. *Oil motor.* The high-pressure hydraulic discharge line of the oil pump drives a Bosch-Rexroth A6VLM variable displacement axial piston oil motor (Bosch-Rexroth, 2012), configured here with a (maximum) fixed displacement.
3. *Water pump.* The oil motor is mechanically coupled to a Kamat K80120-5G fixed-displacement water plunger pump (KAMAT, 2016). An external centrifugal pump supplies the water pump with sufficient flow and feed pressure of around 2.6 bar.
4. *Spear valve.* The pressure in the water pump discharge line is controlled by variable-area orifices in the form of two spear valves. The valves are used to control the system torque and rotor speed in below- and near-rated operating conditions and form high-speed water jets towards the Pelton turbine. A schematic visualization of this system is shown in Figure 5.3. The spear positions are measured and individually actuated by DC motors. The spear valves are actuated in such a way that only full on–off spear position actuation is possible. This means that either the spear moves forwards–backwards at full speed or the spear valve position remains at its current position. A deadband logic controller is implemented to enable position control of the valve within a predefined band around the set point.
5. *Pelton turbine.* When the water flow exits the spear valves, the hydrostatic energy in the high-pressure line is converted to a hydrodynamic high-velocity water jet. The momentum of the jet exerts a force on the Pelton turbine buckets (Zhang, 2007). Pelton turbines are highly specialized pieces of equipment and are designed to meet specific conditional requirements (Brekke, 2001). The Sy Sima 315 MW turbine in Norway, for 88.5 bar of head pressure, is to date the largest known (Cabrera et al., 2015). The custom-manufactured Pelton turbine employed in the DOT500 setup is designed for the nominal pressure and the optimal speed conditions of the connected electrical generator. The pitch circle diameter (PCD) of the custom-manufactured wheel is 0.85 m and the nominal speed of the turbine is in the range of 1230–1420 RPM. According to the manufacturer, the optimal operational pressure is in the range of 60–80 bar for a nominal flow of approximately

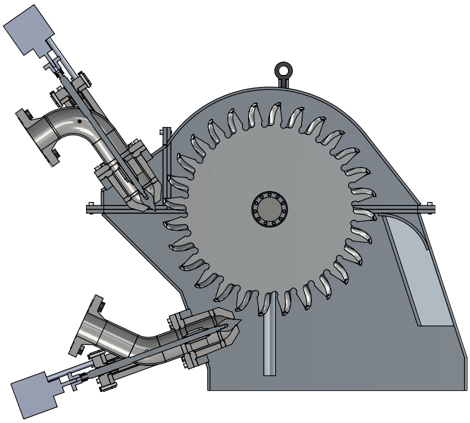

Figure 5.3: The pressurized hydrostatic water flow is converted to a hydrodynamic water jet using spear valves. The high-speed jets exert a force on the buckets of the Pelton turbine.

58 $\mathrm{L\,min^{-1}}$ using two spear valves. The optimal ratio between the tangential Pelton and water jet speed is approximately 1/2 (Thake, 2000) and is maintained by speed control of the asynchronous generator using a filtered pressure measurement. Further considerations on optimal Pelton operation under varying conditions are given below.

6. *Generator.* The mechanical rotational energy of the Pelton turbine is harvested by a mechanically coupled generator. As a grid connection was unavailable at the test location, the electrical energy excess is dissipated by a brake resistor.

In addition to the components described in the above-given enumeration, auxiliary hardware is present and required for operation of the turbine. A more detailed description is presented in (Diepeveen et al., 2018); however, a short summary of the relevant components and remarks is given.

- *Cooling system.* Because of the significant mechanical losses, the working medium needs to be cooled to enable long-term operation of the turbine. The pump and motor in the oil circuit are equipped with flushing lines, which lead to the oil reservoir. A parallel forced-convection cooling circuit regulates the oil temperature.
- *Water circuit.* After the high-velocity water jet has hit the Pelton buckets, it falls back into the first water reservoir. A second water reservoir is connected to the first by a high-volume line to prevent a disturbed flow to the water pump. From the second reservoir the water is fed to the water pump by a centrifugal pump. The high-pressure circuit includes a pressure relief valve.

Furthermore, a remark has to be made on the operational strategy of the Pelton turbine. It is concluded from earlier tests and manufacturer data sheets that Pelton efficiency characteristics are mainly a function of flow and to a lesser extend of line pressure. The flow to the Pelton turbine is proportional to the wind turbine rotor speed, which results in suboptimal operation of the Pelton. The Pelton speed control strategy described above aims to extract the maximum amount of energy given the conditions it is subjected to. For now, this is a design choice, and further research needs to be conducted to elaborate on Pelton design and efficiency maximization given the varying operational conditions.

5.3. THEORY AND MODEL DERIVATION OF THE HYDRAULIC DRIVETRAIN

The theory for model derivation of the DOT500 hydraulic drivetrain is presented in this section. As control actions influence the turbine operating behavior to the point at which the hydrodynamic water jet exits the spear valve, modeling of the turbine drivetrain is performed up to that point. After the water flow exits the spear valve, the aim of operating the Pelton turbine–generator combination at maximum efficiency is a decoupled control objective from the rest of the drivetrain. Considerations on this aspect are given in Section 5.2.2.

A simplified hydraulic diagram of the setup is given in Figure 5.4. The components considered in the model derivation are shown in black, whereas auxiliary systems are presented in gray. The symbols in this figure are specified throughout the different parts of this section. In this section, pressures are generally given as a pressure difference Δp over a component, but when the pressure with respect to the atmospheric pressure p_0 is intended, the Δ indication is omitted.

The organization is divided into two parts. First, a steady-state drivetrain model is derived in Section 5.3.1. This model is used later for the derivation of a passive torque control strategy. Secondly, in Section 5.3.2, a drivetrain model including oil line dynamics is derived and is used for the design of an active spear valve control strategy.

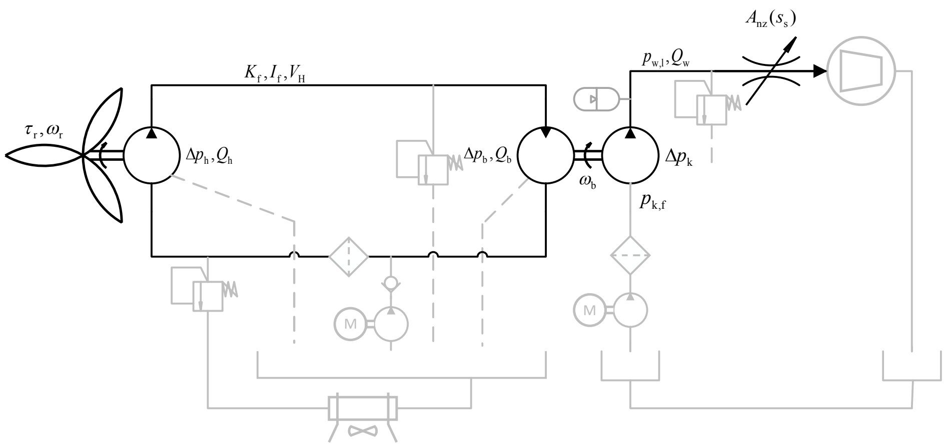

Figure 5.4: Schematic overview of the DOT500 hydraulic wind turbine drivetrain. All pumps and motors have a fixed volume displacement. Charge pressure pumps and filters are included on the low-pressure sides of both the oil and water circuits. Pressure relief valves are incorporated in both circuits. A parallel circuit around the oil reservoir is present for cooling purposes.

5.3.1. STEADY-STATE DRIVETRAIN MODELING

A steady-state model of the drivetrain is derived for hydraulic torque control design in below-rated operating conditions. Mathematical models of hydraulic wind turbines have been established, but mostly incorporate a drivetrain with variable-displacement components (Buhagiar et al., 2016; Jarquin Laguna, 2017). In (Skaare et al., 2011; Skaare et al., 2013) a more simple, robust, and efficient drivetrain with a discrete hydraulic gear ratio is proposed by enabling and disabling hydraulic motors. Recently, a feedback control strategy for wind turbines with digital fluid power transmission was described in (Pedersen et al., 2018). However, only fixed-displacement components are considered and modeling such a DOT drivetrain is described in (Diepeveen, 2013).

The model derivation in this section incorporates the components employed in the actual DOT500 setup. First, a simplified wind turbine model is introduced. Secondly, the derived model is complemented in by analytic models of drivetrain components.

SIMPLIFIED WIND TURBINE MODEL

The Newton law for rotational motion is employed as a basis for modeling the wind turbine rotor speed dynamics:

$$J_{\mathrm{r}}\dot{\omega}_{\mathrm{r}} = \tau_{\mathrm{r}} - \tau_{\mathrm{sys}}, \tag{5.1}$$

where J_{r} is the rotor inertia, ω_{r} the rotor rotational speed, τ_{r} the mechanical torque supplied by the rotor to the low-speed shaft, and τ_{sys} the system torque supplied by the hydraulic oil pump to the shaft. The rotor inertia J_{r} of the rotor is not publicly available. However, an estimation of the rotor inertia is obtained using an empiric relation on blade length given in (Rodriguez et al., 2007), resulting in a value of $6.6\cdot10^5$ kg m^2. Moreover, experiments were performed on the actual turbine and confirm this theoretical result (Jager, 2017). The torque supplied by the rotor (Bianchi et al., 2006) is given by

$$\tau_{\mathrm{r}} = \frac{1}{2}\rho_{\mathrm{air}}\pi R^3 U^2 C_{\mathrm{p}}(\lambda,\beta)/\lambda, \tag{5.2}$$

where the density of air ρ_{air} is taken as a constant value of 1.225 kg m^{-3}, U is the velocity of the upstream wind, and R is the blade length of 22 m. The power coefficient C_{p} represents the fraction between the captured rotor power P_{r} and the available wind power Pwind and is a function of the blade pitch angle β and the dimensionless tip-speed ratio λ given by

$$\lambda = \omega_{\mathrm{r}} R/U. \tag{5.3}$$

The power coefficient C_{p} is related to the torque coefficient by $C_\tau(\lambda,\beta) = C_{\mathrm{p}}(\lambda,\beta)/\lambda$ such that Equation (5.2) can be rewritten as

$$\tau_{\mathrm{r}} = \frac{1}{2}\rho_{\mathrm{air}}\pi R^3 U^2 C_\tau(\lambda,\beta). \tag{5.4}$$

The rotor power and torque extraction capabilities from the wind are characterized in respective power and torque coefficient curves. These curves of the actual DOT500

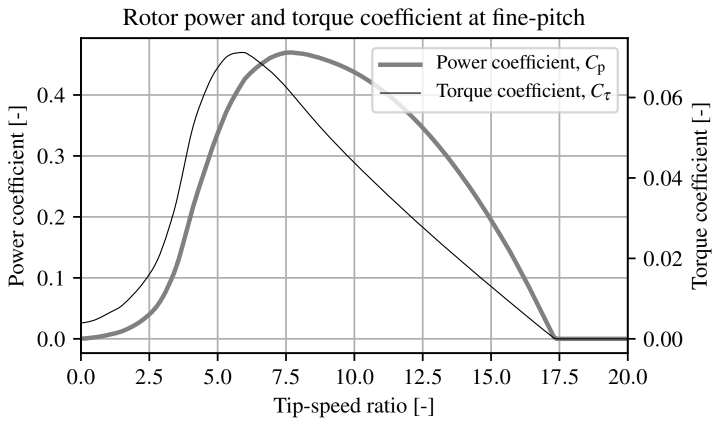

Figure 5.5: Rotor power and torque coefficient curve of the rotor, obtained from a BEM analysis performed on measured blade-geometry data. The maximum power coefficient $C_{\mathrm{p,max}}$ of 0.48 is attained at a tip-speed ratio of 7.8. The maximum torque coefficient of $C_{\tau,\mathrm{max}}$ is given by $7.2 \cdot 10^{-2}$ at a lower tip-speed ratio of 5.9.

rotor are generated by mapping the actual blade airfoils and applying blade element momentum (BEM) theory (Burton et al., 2001); they are given in Figure 5.5 at the blade fine-pitch angle. The fine-pitch angle β_0 indicates the blade angle resulting in maximum rotor power extraction in the below-rated operating region (Bossanyi, 2000). The theoretical maximum rotor power and torque coefficients equal $C_{\mathrm{p,max}} = 0.48$ and $C_{\tau,\mathrm{max}} = 7.2 \cdot 10^{-2}$ at tip-speed ratios of 7.8 and 5.9, respectively. The complete power, torque, and thrust coefficient data set is available as an external supplement under (Mulders et al., 2018b).

The system torque τ_{sys} is supplied by the hydraulic drivetrain to the rotor low-speed shaft. This torque is influenced by the components in the drivetrain, which all have their own energy conversion characteristics expressed in efficiency curves. All components are off the shelf and their combined efficiency characteristics influence the operating behavior of the turbine.

Hydraulic components are known for their high torque-to-inertia ratio and have high acceleration capabilities as a result (Merritt, 1967). In typical applications of a hydraulic transmission, the fairly low rotational inertia of pumps and motors is still relevant. However, the considered wind turbine drivetrain is driven by a rotor with a large inertia J_{r} compared to the drivetrain components. Referring to the specification sheet of the oil motor (Bosch-Rexroth, 2012), it is stated that the unit has a moment of inertia of $J_{\mathrm{b}} = 0.55\,\mathrm{kg\,m^2}$. The resulting reflected inertia to the rotor of $J_{\mathrm{b}\to\mathrm{r}} = 0.55/G^2 = 1533.312\,\mathrm{kg\,m^2}$ is still negligible, where G^{-1} represents the *hydraulic gear ratio* of 52.8. Furthermore, a particular study on this aspect has been carried out in (Kempenaar, 2012), in which it is concluded that the inclusion of component dynamics does not result in significantly improved model accuracy. For the reasons mentioned, the pumps and motor included in the drivetrain are assumed to have negligible dynamics, and the power conversion (flow speed, torque pressure) is given by static relations.

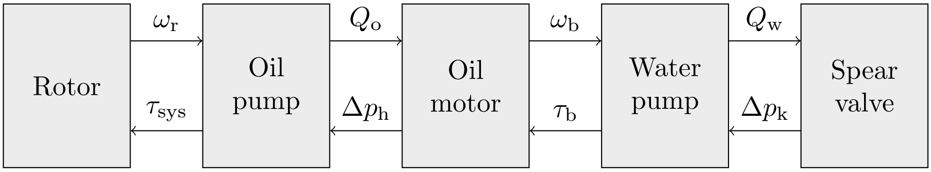

Figure 5.6: Flow diagram of the DOT500 hydraulic drivetrain. For steady-state modeling purposes, first the flow path is calculated up to the spear valve. The effective nozzle area and the water flow through the spear valve determine the hydraulic feed line pressure, which influences the system torque τ_{sys} to the rotor.

ANALYTIC DRIVETRAIN COMPONENTS DESCRIPTION

A flow diagram of the modeling strategy is presented in Figure 5.6. To obtain an expression for the system torque τ_{sys}, the complete hydraulic flow path with its volumetric losses is modeled first. When the flow path reaches the spear valve at the water discharge to the Pelton turbine, the simulation path is reversed to calculate the effect of all component characteristics to the line pressures. The spear valve allows for control of the water discharge pressure, the effect of which propagates back to the system torque τ_{sys}. The high-pressure oil flow by the oil pump is proportional to the rotor speed,

$$Q_{\mathrm{o}} = V_{\mathrm{p,h}}\omega_{\mathrm{r}}\eta_{\mathrm{v,h}}, \tag{5.5}$$

where $V_{\mathrm{p,h}}$ is the pump volumetric displacement, and $\eta_{\mathrm{v,h}}$ the volumetric efficiency. The volumetric efficiency indicates the volume loss as a fraction of the total displaced flow as a function of the component operating conditions. However, as volumetric efficiency data are unavailable for most of the components and the aim is to provide a simplified model of the hydraulic drivetrain, volumetric losses are considered as a constant factor of the displaced flow. The resulting oil flow Q_{o} drives the oil motor, which results in a rotational speed of the motor shaft subject to volumetric losses:

$$\omega_{\mathrm{b}} = \frac{Q_{\mathrm{o}}}{V_{\mathrm{p,b}}}\eta_{\mathrm{v,b}}, \tag{5.6}$$

where $V_{\mathrm{p,b}}$ is the oil motor volumetric displacement, and $\eta_{\mathrm{v,b}}$ the volumetric efficiency of the oil motor. As the water pump is mechanically coupled to the oil motor axis, its rotational speed is equal to ω_{b}. The expression relating the rotational speed to the water pump discharge water flow Q_{w} is given by

$$Q_{\mathrm{w}} = V_{\mathrm{p,k}}\omega_{\mathrm{b}}\eta_{\mathrm{v,k}}, \tag{5.7}$$

where $V_{\mathrm{p,k}}$ is the volumetric displacement of the water pump, and $\eta_{\mathrm{v,k}}$ the volumetric efficiency of the water pump. The pressure in the water discharge line is controlled by a spear valve of which a visualization is given in Figure 5.7 with the spear position coordinate system. The effective nozzle area is variable according to the relation

$$A_{\mathrm{nz}}(s) = N_{\mathrm{s}}\pi\left(D_{\mathrm{nz}}^2/4 - (s_{\max} - s)^2 \tan^2(\alpha/2)\right), \tag{5.8}$$

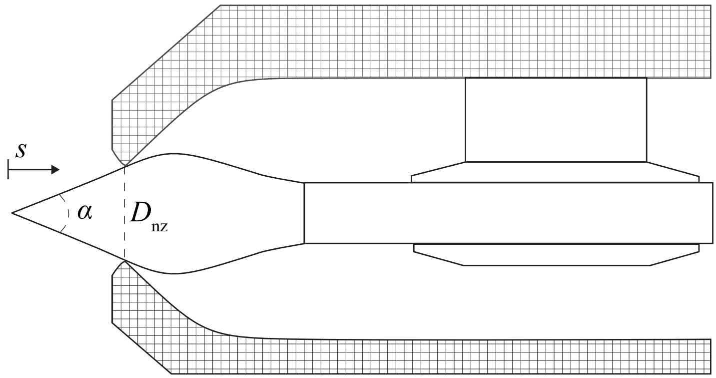

Figure 5.7: Cross-section of the spear valve used. The coning angle of the spear is given by α, the nozzle diameter by D_{nz}, and the position of the spear tip in the nozzle by s. The nozzle heads are adjustable for adjustment of the outlet area.

where $\{s \subset \mathbb{R} \mid 0 \leq s \leq s_{max}\}$ represents the position of the spear in the circular nozzle cross section, D_{nz} is the nominal nozzle diameter, α the spear coning angle, and N_s indicates the number of spear valves on the same line. Modeling multiple spear valves by N_s assumes equal effective nozzle areas for all valves. The maximum spear position (fully open) is given by

$$s_{max} = \frac{D_{nz}}{2\tan(\alpha/2)}. \tag{5.9}$$

and a mapping for spear position to effective nozzle area for different nozzle diameters D_{nz} is given in Figure 5.8. The spear valve is closed for all cases at position $s = 0$ mm. The spear valve converts the hydrostatic water flow into a high-speed hydrodynamic water jet that exerts a thrust force on the buckets of the Pelton turbine (Zhang, 2007). Using the Bernoulli equation for incompressible flows (White, 2011), an expression for the discharge water pressure is obtained:

$$p_{w,1}(s) = \frac{\rho_w}{2}\left(\frac{Q_w}{C_d A_{nz}(s)}\right)^2, \tag{5.10}$$

with the flow and effective nozzle area $\left\{Q_w, A_{nz}\right\} \subset \mathbb{R}^+$. As observed in the above given relation, the pressure can be controlled by varying the feed flow and spear position, as the latter influences the effective nozzle area A_{nz}. The discharge coefficient C_d is introduced to account for pressure losses due to the geometry and flow regime at the nozzle exit (Al'tshul' and Margolin, 1968). The discharge coefficient of an orifice is defined as the ratio between the vena contracta area and the orifice area (Bragg, 1960). The vena contracta is the point at which the streamlines become parallel, which usually occurs downstream of the orifice at which the streamlines are still converging. The pressure in the water discharge line propagates back into the system and is used as a substitute for

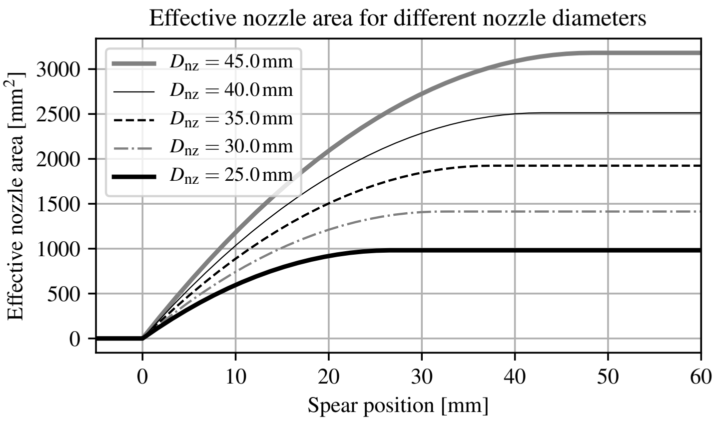

Figure 5.8: Effective nozzle area as a function of the spear position in the circular nozzle cross-section. The spear valve is fully closed at $s = 0$ mm and fully opened at $s = s_{\max}$, the latter of which is variable according to the nozzle head diameter.

conventional wind turbine torque control. A relation for the mechanical torque at the axis between the water pump and oil motor is given by

$$\tau_{\mathrm{b}} = \frac{V_{\mathrm{p,k}} \Delta p_{\mathrm{k}}}{\eta_{\mathrm{m,k}}(\omega_{\mathrm{b}}, \Delta p_{\mathrm{k}})}, \tag{5.11}$$

where $\eta_{\mathrm{m,k}}$ is the mechanical efficiency of the water pump as a function of the rotational speed and pressure difference over the pump:

$$\Delta p_{\mathrm{k}} = p_{\mathrm{w,l}} - p_{\mathrm{k,f}}, \tag{5.12}$$

where $p_{\mathrm{k,f}}$ is a known and constant feed pressure. The torque τ_{b} is used to calculate the pressure difference over the oil motor and pump by

$$\Delta p_{\mathrm{b}} = \Delta p_{\mathrm{h}} = \frac{\tau_{\mathrm{b}}}{V_{\mathrm{p,b}} \eta_{\mathrm{m,b}}(\omega_{\mathrm{b}}, \tau_{\mathrm{b}})}, \tag{5.13}$$

where $\eta_{\mathrm{m,b}}$ is the mechanical efficiency of the oil motor. It is assumed that the pressure at the discharge outlet of the oil motor Δp_{b} is constant as the feed pressure to the oil pump is regulated. Finally, the system torque supplied to the rotor low-speed shaft is given by

$$\tau_{\mathrm{sys}} = \frac{V_{\mathrm{p,h}} \Delta p_{\mathrm{h}}}{\eta_{\mathrm{m,h}}(\omega_{\mathrm{r}}, \Delta p_{\mathrm{h}})}. \tag{5.14}$$

Using the relations derived, a passive strategy for below-rated turbine control is presented in Section 5.4.1.

5.3.2. DYNAMIC DRIVETRAIN MODELING

In contrast to the steady-state model presented previously, this section elaborates on the derivation of a drivetrain model including fluid dynamics for validation of the controller design in the near-rated region. First, preliminary knowledge on fluid dynamics is given, whereafter a dynamic DOT500 drivetrain model is presented.

ANALYSIS OF FLUID DYNAMICS IN A HYDRAULIC LINE

The dynamics of a volume in a hydraulic line are modeled in this section. For this, analogies between mechanical and hydraulic systems are employed for modeling convenience. A full derivation is given in Appendix C.2, and only the results are given in this section. The system considered, representing the high-pressure discharge oil line, is a cylindrical control volume $V_{\mathrm{H}} = AL_{\mathrm{l}} = \pi r_{\mathrm{l}}^2 L_{\mathrm{l}}$ with radius r_{l} and length L_{l} excited by a pressure $\Delta p = p_{\mathrm{in}} - p_{\mathrm{out}}$. The net flow into the control volume is defined as $Q = Q_{\mathrm{in}} - Q_{\mathrm{out}}$. For a hydraulic expression with pressure Δp as the external excitation input and the flow Q as output, one obtains

$$\Delta p = L_{\mathrm{H}}\dot{Q} + R_{\mathrm{H}}Q + \frac{1}{C_{\mathrm{H}}}\int Q dt, \tag{5.15}$$

where L_{H}, R_{H} and C_{H} are the hydraulic induction, resistance, and capacitance (Esposito, 1969), respectively, and are defined in Appendix C.1. The inverse result of Equation (5.15) is obtained (Murrenhoff, 2012) with flow Q as the external excitation and Δp as output:

$$Q = C_{\mathrm{H}}\Delta\dot{p} + \frac{1}{R_{\mathrm{H}}}\Delta p + \frac{1}{L_{\mathrm{H}}}\int \Delta p dt. \tag{5.16}$$

Finally, the differential equation defined by Equation (5.15) is expressed as a transfer function,

$$G_{\mathrm{Q}/\Delta\mathrm{p}}(s) = \frac{s/L_{\mathrm{H}}}{s^2 + (R_{\mathrm{H}}/L_{\mathrm{H}})s + 1/(C_{\mathrm{H}}L_{\mathrm{H}})}, \tag{5.17}$$

and the same is done for Equation (5.16):

$$G_{\Delta\mathrm{p}/\mathrm{Q}}(s) = \frac{s/C_{\mathrm{H}}}{s^2 + 1/(R_{\mathrm{H}}C_{\mathrm{H}})s + 1/(C_{\mathrm{H}}L_{\mathrm{H}})}. \tag{5.18}$$

The transfer functions defined in Equations (5.17) and (5.18) show the characteristics of an inverted notch with +1 and −1 slopes on the left and right side of the natural frequency, respectively. This physically means that exciting the system pressure results in a volume velocity change predominantly at the system natural frequency for the former case. An illustrative Bode plot is given in Section 5.4.2. Exciting the flow results in amplification and transmission to pressure in a wider frequency region. This effect is a result of the inverse proportionality between the damping coefficients ζ_{Q} and ζ_{p} (see Appendix C.2).

DRIVETRAIN MODEL DERIVATION

A dynamic model of the DOT500 drivetrain is derived by application of the theory presented in the previous section. The drivetrain is defined from the rotor up to the spear valve, and the following assumptions are made.

- Because of the high torque-to-inertia ratio of hydraulic components (Merritt, 1967), the dynamics of oil pumps and motors are disregarded and taken as analytic relations.
- Because of the longer line length and higher compressibility of oil compared to the shorter water column, the high-pressure oil line is more critical for controller design, and a dynamic model is implemented for this column only.
- The fluids have a constant temperature.

The dynamic system is governed by the following differential equations:

$$\mathcal{V} = \mathcal{V}_{\text{in}} - \mathcal{V}_{\text{out}}, \qquad \dot{\mathcal{V}} = Q = Q_{\text{in}} - Q_{\text{out}}, \tag{5.19}$$

$$\begin{aligned}\Delta p_{\text{h}} &= \underbrace{\left(\frac{J_{\text{r}}\eta_{\text{m,h}}}{V_{\text{p,h}}^2\eta_{\text{v,h}}} + L_{\text{H}}\right)}_{L_{\text{R}}^*}\dot{Q}_{\text{in}} + R_{\text{H}}(Q_{\text{in}} - Q_{\text{out}}) + \frac{K_{\text{e}}}{V_{\text{H}}}(\mathcal{V}_{\text{in}} - \mathcal{V}_{\text{out}}) \\ &= L_{\text{R}}^*\dot{Q}_{\text{in}} + R_{\text{H}}(Q_{\text{in}} - Q_{\text{out}}) + \frac{1}{C_{\text{H}}}\mathcal{V},\end{aligned} \tag{5.20}$$

$$\begin{aligned}\Delta p_{\text{b}} &= L_{\text{H}}\dot{Q}_{\text{out}} + R_{\text{H}}(Q_{\text{out}} - Q_{\text{in}}) + \frac{K_{\text{e}}}{V_{\text{H}}}(\mathcal{V}_{\text{out}} - \mathcal{V}_{\text{in}}) \\ &= L_{\text{H}}\dot{Q}_{\text{out}} + R_{\text{H}}(Q_{\text{out}} - Q_{\text{in}}) - \frac{1}{C_{\text{H}}}\mathcal{V},\end{aligned} \tag{5.21}$$

where K_{e} is the equivalent bulk modulus, including the fluid and line compressibility defined in Equation (C.5), and $\mathcal{V}$ is the net volume inflow to the considered oil line between the oil pump discharge and oil motor feed port. For convenience, mechanical model quantities are expressed hydraulically in terms of fluid flows and pressure differences over the components. Therefore, the rotor inertia J_{r} is expressed in terms of fluid induction and is combined with the hydraulic induction term into L_{R}^*.

Both the spear position and pitch angle are modeled by a first-order actuator model:

$$\dot{s} = \frac{1}{t_{\text{s}}}(s_{\text{ref}} - s), \tag{5.22}$$

$$\dot{\beta} = \frac{1}{t_\beta}(\beta_{\text{ref}} - \beta), \tag{5.23}$$

where t_{s} and t_β are the time constant for the spear valve and pitch actuators, respectively, and the phase loss at the actuator bandwidth is assumed to account for actuation delay effects.

The above-given dynamic equations are written in a state-space representation as

$$\begin{bmatrix} \dot{\mathcal{V}} \\ \dot{Q}_{\text{in}} \\ \dot{Q}_{\text{out}} \\ \dot{s} \\ \dot{\beta} \end{bmatrix} = \begin{bmatrix} 0 & 1 & -1 & 0 & 0 \\ -\frac{1}{C_{\text{H}}L_{\text{R}}^*} & -\frac{R_{\text{H}}}{L_{\text{R}}^*} & \frac{R_{\text{H}}}{L_{\text{R}}^*} & 0 & 0 \\ \frac{1}{C_{\text{H}}L_{\text{H}}} & \frac{R_{\text{H}}}{L_{\text{H}}} & -\frac{R_{\text{H}}}{L_{\text{H}}} & 0 & 0 \\ 0 & 0 & 0 & -\frac{1}{t_{\text{s}}} & 0 \\ 0 & 0 & 0 & 0 & -\frac{1}{t_\beta} \end{bmatrix} \begin{bmatrix} \mathcal{V} \\ Q_{\text{in}} \\ Q_{\text{out}} \\ s \\ \beta \end{bmatrix} + \begin{bmatrix} 0 \\ \frac{1}{L_{\text{R}}^*}\Delta p_{\text{h}} \\ -\frac{1}{L_{\text{H}}}\Delta p_{\text{b}} \\ \frac{1}{t_{\text{s}}}s_{\text{ref}} \\ \frac{1}{t_\beta}\beta_{\text{ref}} \end{bmatrix}. \tag{5.24}$$

It is seen that the pressure difference over the oil pump and motor appear as inputs, but these quantities cannot be controlled directly. For this reason, linear expressions of the rotor torque and spear valves are defined next. The rotor torque is linearized with respect to the tip-speed ratio, pitch angle, and wind speed:

$$\hat{\tau}_{\mathrm{r}}(\bar{\omega}_{\mathrm{r}}, \bar{\beta}, \bar{U}) = k_{\omega_{\mathrm{r}}}(\bar{\omega}_{\mathrm{r}}, \bar{\beta}, \bar{U})\hat{\omega}_{\mathrm{r}} + k_{\beta}(\bar{\omega}_{\mathrm{r}}, \bar{\beta}, \bar{U})\hat{\beta} + k_{\mathrm{U}}(\bar{\omega}_{\mathrm{r}}, \bar{\beta}, \bar{U})\hat{U}, \tag{5.25}$$

where $\hat{(\cdot)}$ indicates a value deviation from the operating point, and $\bar{(\cdot)}$ is the value at the operating point (Bianchi et al., 2006). Furthermore,

$$k_{\omega_{\mathrm{r}}}(\omega_{\mathrm{r}}, \beta, U) = \frac{\partial \tau_{\mathrm{r}}}{\partial \omega_{\mathrm{r}}} = c_{\mathrm{r}} R U \frac{\partial C_{\tau}(\omega_{\mathrm{r}} R/U, \beta)}{\partial \lambda}, \tag{5.26}$$

$$k_{\beta}(\omega_{\mathrm{r}}, \beta, U) = \frac{\partial \tau_{\mathrm{r}}}{\partial \beta} = c_{\mathrm{r}} U^2 \frac{\partial C_{\tau}(\omega_{\mathrm{r}} R/U, \beta)}{\partial \beta}, \tag{5.27}$$

$$\begin{aligned} k_{\mathrm{U}}(\omega_{\mathrm{r}}, \beta, U) = \frac{\partial \tau_{\mathrm{r}}}{\partial U} &= 2 c_{\mathrm{r}} U C_{\tau}(\omega_{\mathrm{r}} R/U, \beta) + c_{\mathrm{r}} U^2 \frac{\partial C_{\tau}(\omega_{\mathrm{r}} R/U, \beta)}{\partial \lambda} \frac{\partial \lambda}{\partial U} \\ &= 2 c_{\mathrm{r}} U C_{\tau}(\omega_{\mathrm{r}} R/U, \beta) - c_{\mathrm{r}} \omega_{\mathrm{r}} R \frac{\partial C_{\tau}(\omega_{\mathrm{r}} R/U, \beta)}{\partial \lambda}, \end{aligned} \tag{5.28}$$

$$c_{\mathrm{r}} = \frac{1}{2} \rho \pi R^3, \tag{5.29}$$

where the quantities $k_{\omega_{\mathrm{r}}}$, k_{β} and k_{U} represent the intrinsic speed feedback gain, the linear pitch gain, and the linear wind speed gain, respectively. The intrinsic speed feedback gain can also be expressed as a function of the tip-speed ratio by

$$k_{\lambda}(\lambda, \beta, U) = k_{\omega_{\mathrm{r}}}(\omega_{\mathrm{r}}, \beta, U) \frac{U}{R}. \tag{5.30}$$

For aerodynamic rotor stability, the value of k_{λ} needs to be negative. In Figure 5.9 the intrinsic speed feedback gain $k_{\lambda}(\lambda, \bar{\beta}, \bar{U})$ is evaluated as a function of the tip-speed ratio at the fine-pitch angle β_0. For incorporation of the linearized rotor torque in the drivetrain model, Equation (5.25) is expressed in the pressure difference over the oil pump:

$$\Delta \hat{p}_{\mathrm{h}}(\bar{\omega}_{\mathrm{r}}, \bar{\beta}, \bar{U}) = k^{*}_{\mathrm{Q_{in}}}(\bar{\omega}_{\mathrm{r}}, \bar{\beta}, \bar{U}) \hat{Q}_{\mathrm{in}} + k^{*}_{\beta}(\bar{\omega}_{\mathrm{r}}, \bar{\beta}, \bar{U})\hat{\beta} + k^{*}_{\mathrm{U}}(\bar{\omega}_{\mathrm{r}}, \bar{\beta}, \bar{U})\hat{U}, \tag{5.31}$$

where the conversions of the required quantities are given by

$$k^{*}_{\mathrm{Q_{in}}} = k_{\omega_{\mathrm{r}}} \frac{\eta_{\mathrm{m,h}}}{V_{\mathrm{p,h}}^2 \eta_{\mathrm{v,h}}}, \qquad k^{*}_{\beta} = k_{\beta} \frac{\eta_{\mathrm{m,h}}}{V_{\mathrm{p,h}}}, \qquad k^{*}_{\mathrm{U}} = k_{\mathrm{U}} \frac{\eta_{\mathrm{m,h}}}{V_{\mathrm{p,h}}}. \tag{5.32}$$

Similarly, the water line pressure as defined in Equation (5.10) is linearized with respect to the spear position and flow through the valve:

$$\hat{p}_{\mathrm{w,l}}(\hat{Q}_{\mathrm{w}}, \hat{s}) = k_{\mathrm{s,s}}(\bar{Q}_{\mathrm{w}}, \bar{s})\hat{s} + k_{\mathrm{s,Q_w}}(\bar{Q}_{\mathrm{w}}, \bar{s})\hat{Q}_{\mathrm{w}}, \tag{5.33}$$

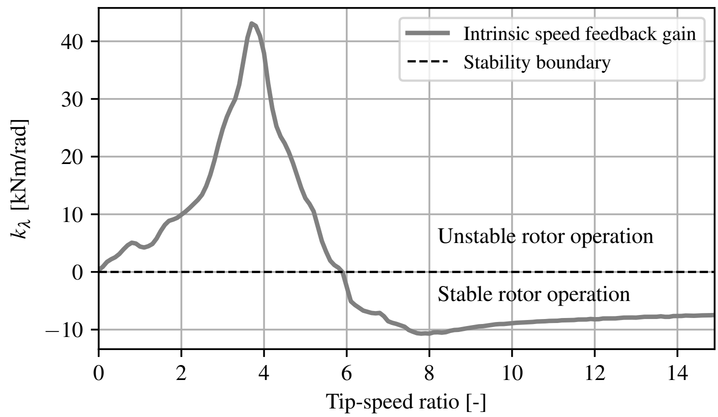

Figure 5.9: The intrinsic speed feedback gain $k_\lambda(\lambda, \bar{\beta}, \bar{U})$ as a function of tip-speed ratio λ, at a fixed pitch angle and wind speed of −2 deg and 8 m s^{-1}. Stable turbine operation is attained for nonpositive values of k_λ.

where

$$k_{\mathrm{s,s}}(\bar{Q}_\mathrm{w}, \bar{s}) = \left. \frac{2Q_\mathrm{w}^2 \rho_\mathrm{w}(s - s_\mathrm{max}) \tan^2(\alpha/2)}{C_\mathrm{d}^2 N_\mathrm{s}^2 \pi^2 \left(D_\mathrm{nz}^2/4 - (s_\mathrm{max} - s)^2 \tan^2(\alpha/2)\right)^3} \right|_{\bar{Q}_\mathrm{w}, \bar{s}}, \tag{5.34}$$

$$k_{\mathrm{s,Q_w}}(\bar{Q}_\mathrm{w}, \bar{s}) = \left. \frac{Q_\mathrm{w} \rho_\mathrm{w}}{C_\mathrm{d}^2 N_\mathrm{s}^2 \pi^2 \left(D_\mathrm{nz}^2/4 - (s_\mathrm{max} - s)^2 \tan^2(\alpha/2)\right)^2} \right|_{\bar{Q}_\mathrm{w}, \bar{s}}. \tag{5.35}$$

The pressure difference over the oil motor is defined in terms of the water line pressure, which is a function of the spear position:

$$\Delta \hat{p}_\mathrm{b} = \frac{1}{c_\mathrm{m,bk}} \Delta \hat{p}_\mathrm{k} \approx \frac{1}{c_\mathrm{m,bk}} \hat{p}_\mathrm{w,l}(s) = \frac{1}{c_\mathrm{m,bk}} \left(k_\mathrm{s,s}(\bar{Q}_\mathrm{w}, \bar{s})\hat{s} + k_{\mathrm{s,Q_w}}(\bar{Q}_\mathrm{w}, \bar{s})\hat{Q}_\mathrm{w}\right), \tag{5.36}$$

where the mechanical and volumetric conversion factors from oil to water pressure and flow are defined as

$$c_\mathrm{m,bk} = \frac{V_\mathrm{p,b}}{V_\mathrm{p,k}} \eta_\mathrm{m,k} \eta_\mathrm{m,b}, \qquad c_\mathrm{v,bk} = \frac{V_\mathrm{p,k}}{V_\mathrm{p,b}} \eta_\mathrm{v,k} \eta_\mathrm{v,b} \tag{5.37}$$

The system defined in Equation (5.24) is now presented as a linear state-space system of the form

$$\begin{aligned} \dot{x} &= \mathbf{A}\boldsymbol{x} + \mathbf{B}\boldsymbol{u} + \boldsymbol{B}_\mathrm{U}\hat{U} \\ y &= \mathbf{C}\boldsymbol{x}. \end{aligned} \tag{5.38}$$

With substitution of the rotor torque and water pressure approximations defined by Equations (5.31) and (5.36) in Equation (5.24), the state **A**, input **B**, wind disturbance

$\boldsymbol{B}_{\mathrm{U}}$, and output $\mathbf{C}$ matrices are given by

$$\mathbf{A}=\begin{bmatrix} 0 & 1 & -1 & 0 & 0 \\ -\frac{1}{C_{\mathrm{H}}L_{\mathrm{R}}^{*}} & -\frac{\tilde{R}_{\mathrm{H,Q_{in}}}}{L_{\mathrm{R}}^{*}} & \frac{R_{\mathrm{H}}}{L_{\mathrm{R}}^{*}} & 0 & \frac{k_{\beta}^{*}}{L_{\mathrm{R}}^{*}} \\ \frac{1}{C_{\mathrm{H}}L_{\mathrm{H}}} & \frac{R_{\mathrm{H}}}{L_{\mathrm{H}}} & -\frac{\tilde{R}_{\mathrm{H,Q_{w}}}}{L_{\mathrm{H}}} & -\frac{k_{\mathrm{s,s}}}{c_{\mathrm{m,bk}}L_{\mathrm{H}}} & 0 \\ 0 & 0 & 0 & -\frac{1}{t_{\mathrm{s}}} & 0 \\ 0 & 0 & 0 & 0 & -\frac{1}{t_{\beta}} \end{bmatrix}, \quad \mathbf{B}=\begin{bmatrix} 0 & 0 & 0 & \frac{1}{t_{\mathrm{s}}} & 0 \\ 0 & 0 & 0 & 0 & \frac{1}{t_{\beta}} \end{bmatrix}^{\mathrm{T}},$$

$$\boldsymbol{B}_{\mathrm{U}}=\begin{bmatrix} 0 & \frac{k_{\mathrm{U}}^{*}}{L_{\mathrm{R}}^{*}} & 0 & 0 & 0 \end{bmatrix}^{\mathrm{T}}, \qquad \mathbf{C}=\begin{bmatrix} 1 & 0 & 0 & 0 & 0 \\ 0 & \frac{1}{V_{\mathrm{p,h}}\eta_{\mathrm{v,h}}} & 0 & 0 & 0 \\ 0 & 0 & 0 & 1 & 0 \\ 0 & 0 & 0 & 0 & 1 \end{bmatrix}, \tag{5.39}$$

with the state, input, and output matrices

$$\begin{aligned} \boldsymbol{x} &= \begin{bmatrix} \hat{V} & \hat{Q}_{\mathrm{in}} & \hat{Q}_{\mathrm{out}} & \hat{s} & \hat{\beta} \end{bmatrix}^{T}, \\ \boldsymbol{u} &= \begin{bmatrix} \hat{s}_{\mathrm{ref}} & \hat{\beta}_{\mathrm{ref}} \end{bmatrix}^{T}, \\ \boldsymbol{y} &= \begin{bmatrix} \hat{V} & \hat{\omega}_{\mathrm{r}} & \hat{s} & \hat{\beta} \end{bmatrix}^{T}, \end{aligned} \tag{5.40}$$

and

$$\tilde{R}_{\mathrm{H,Q_{in}}} = R_{\mathrm{H}} - k_{\mathrm{Q_{in}}}^{*}, \tag{5.41}$$

$$\tilde{R}_{\mathrm{H,Q_{w}}} = \left(R_{\mathrm{H}} + \frac{c_{\mathrm{v,bk}}}{c_{\mathrm{m,bk}}} k_{\mathrm{s,Q_{w}}} \right). \tag{5.42}$$

The dynamic model derived in this section is used in Section 5.4.2 to create an active spear valve torque control strategy in the near-rated region.

5.4. CONTROLLER DESIGN

In this section designs are presented for control in the below- and near-rated operating region. A schematic diagram of the overall control system is given in Figure 5.10. It is seen that the turbine is controlled by two distinct proportional–integral (PI) controllers, a spear valve torque, and blade pitch controller acting on individual rotor speed set point errors e_{s} and e_{β}, respectively. As both controllers have a common control objective of regulating the rotor speed and are implemented in a decentralized way, it is ensured that they are not active simultaneously. The gain-scheduled pitch controller is designed and implemented in a similar way as in conventional wind turbines (Jonkman et al., 2009) and is therefore not further elaborated in this chapter. The spear valve torque controller, however, is nonconventional and its controller design is outlined in this section.

For the below-rated controller design a passive torque control strategy is employed, a description of which is given in Section 5.4.1. Subsequently, in Section 5.4.2, the in-field active spear valve control implementation is evaluated using the dynamic drive-train model.

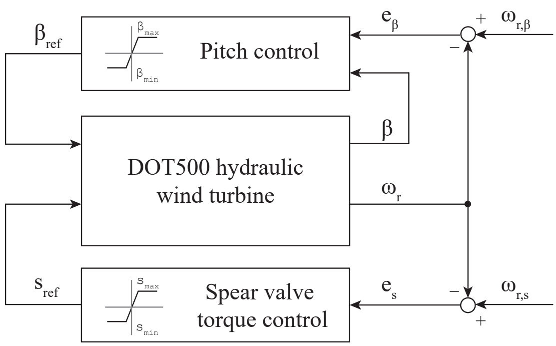

Figure 5.10: Schematic diagram of the DOT500 control strategy. When the control error e is negative, the controllers saturate at their minimum or maximum setting. In the near-rated operating region, the rotor speed is actively regulated to $\omega_{\mathrm{r,s}}$,s by generating the spear position control signal s_{ref}, influencing the fluid pressure and the system torque. When the spear valve is at its rated minimum position, the gain-scheduled pitch controller generates a pitch angle set point β_{ref} to regulate the rotor speed at its nominal value $\omega_{\mathrm{r},\beta}$.

5

5.4.1. PASSIVE BELOW-RATED TORQUE CONTROL

The passive control strategy for below-rated operation is described in this section. Conventionally, in below-rated operating conditions, the power coefficient is maximized by regulating the tip-speed ratio at λ_0 using generator torque control. Generally, the maximum power coefficient tracking objective is attained by implementing the feed-forward torque control law

$$\tau_{\mathrm{sys}} = \frac{\rho_{\mathrm{air}}\pi R^5 C_{\mathrm{p,max}}}{2\lambda^3}\omega_{\mathrm{r}}^2 = K_{\mathrm{r}}\omega_{\mathrm{r}}^2, \tag{5.43}$$

where K_{r} is the optimal mode gain in Nm (rad/s)$^{-2}$.

As the DOT500 drivetrain lacks the option to directly influence the system torque, hydraulic torque control is employed using spear valves. An expression for the system torque for the hydraulic drivetrain is derived by substitution of Equations (5.11) and (5.13) in Equation (5.14)

$$\tau_{\mathrm{sys}} = \frac{V_{\mathrm{p,h}}V_{\mathrm{p,k}}}{V_{\mathrm{p,b}}}\frac{1}{\eta_{\mathrm{m,h}}(\omega_{\mathrm{r}},\Delta p_{\mathrm{h}})\eta_{\mathrm{m,b}}(\omega_{\mathrm{b}},\tau_{\mathrm{b}})\eta_{\mathrm{m,k}}(\omega_{\mathrm{b}},\Delta p_{\mathrm{k}})}\Delta p_{\mathrm{k}}, \tag{5.44}$$

and by substituting Equations (5.10) and (5.12) an expression as a function of the spear position is obtained:

$$\tau_{\mathrm{sys}} = \frac{V_{\mathrm{p,h}}V_{\mathrm{p,k}}}{V_{\mathrm{p,b}}}\frac{1}{\eta_{\mathrm{m,h}}(\omega_{\mathrm{r}},\Delta p_{\mathrm{h}})\eta_{\mathrm{m,b}}(\omega_{\mathrm{b}},\tau_{\mathrm{b}})\eta_{\mathrm{m,k}}(\omega_{\mathrm{b}},\Delta p_{\mathrm{k}})}\left(\frac{\rho_{\mathrm{w}}}{2}\left(\frac{Q_{\mathrm{w}}}{C_{\mathrm{d}}A_{\mathrm{nz}}(s)}\right)^2 - p_{\mathrm{k,f}}\right). \tag{5.45}$$

Now substituting Equations (5.5) and (5.6) in Equation (5.7) results in an expression relating the water flow to the rotor speed:

$$Q_{\mathrm{w}} = \frac{V_{\mathrm{p,h}}V_{\mathrm{p,k}}}{V_{\mathrm{p,b}}}\frac{\eta_{\mathrm{v,k}}\eta_{\mathrm{v,b}}\eta_{\mathrm{v,h}}}{1}\omega_{\mathrm{r}}. \tag{5.46}$$

Combining Equations (5.45) and (5.46) and disregarding the water pump feed pressure $p_{\mathrm{k,f}}$ gives

$$\tau_{\mathrm{sys}} = \frac{\rho_{\mathrm{w}}}{2C_{\mathrm{d}}^2 A_{\mathrm{nz}}^2(s)} \left(\frac{V_{\mathrm{p,h}} V_{\mathrm{p,k}}}{V_{\mathrm{p,b}}}\right)^3 \frac{\left(\eta_{\mathrm{v,h}}\eta_{\mathrm{v,b}}\eta_{\mathrm{v,k}}\right)^2}{\eta_{\mathrm{m,h}}(\omega_{\mathrm{r}},\Delta p_{\mathrm{h}})\eta_{\mathrm{m,b}}(\omega_{\mathrm{b}},\tau_{\mathrm{b}})\eta_{\mathrm{m,k}}(\omega_{\mathrm{b}},\Delta p_{\mathrm{k}})} \omega_{\mathrm{r}}^2 = K_{\mathrm{s}}\omega_{\mathrm{r}}^2. \quad (5.47)$$

Rotor speed variations cause a varying flow through the spear valve, which results in a varying system pressure and thus system torque, regulating the tip-speed ratio of the rotor. The above-obtained result shows that when K_{s} is constant, the tip-speed ratio can be regulated in the below-rated region by a fixed nozzle area A_{nz}. Under ideal circumstances, it is shown in (Diepeveen and Jarquin-Laguna, 2014) that a constant nozzle area lets the rotor follow the optimal power coefficient trajectory and is called passive torque control. This means that no active control is needed up to the near-rated operating region. For this purpose, the optimal mode gain K_{s} of the system side needs to equal that of the rotor K_{r} in the below-rated region.

However, for the passive strategy to work, the combined drivetrain efficiency needs to be consistent in the below-rated operating region. As seen in Equation (5.47), the combined efficiency term is a product of the consequent volumetric divided by the mechanical efficiencies of all components as a function of their current operating point. To assess the consistency of the overall drivetrain efficiency, different operating strategies are examined. Subsequently, a component efficiency analysis is given.

OPERATIONAL STRATEGIES

Because hydraulic components are in general more efficient in high-load operating conditions (Trostmann, 1995), it might be advantageous for a hydraulic wind turbine drivetrain to operate the rotor at a lower tip-speed ratio. Operating at a lower tip-speed ratio

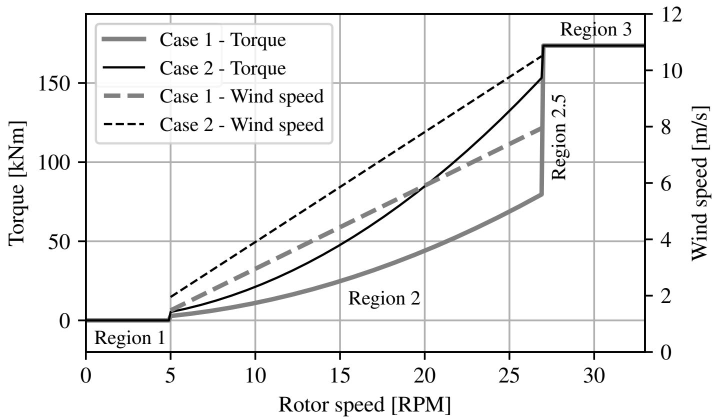

Figure 5.11: Torque control strategies for maintaining a fixed tip-speed ratio λ, tracking the optimal power coefficient $C_{\mathrm{p,max}}$ (case 1) and the maximum torque coefficient $C_{\tau,\mathrm{max}}$ (case 2). The dashed lines show the wind speed corresponding to the distinct strategies (right y axis).

results in a lower rotational rotor speed and a higher torque for equal wind speeds, but at the same time decreases the rotor power coefficient C_p. By sacrificing rotor efficiency, the resulting higher operational pressures might lead to maximization of the total drive-train efficiency. For these reasons, an analysis of this trade-off is divided into two cases.

- Case 1: Operating the rotor at its maximum power coefficient $C_{\text{p,max}}$.
- Case 2: Operation at the maximum torque coefficient $C_{\tau,\text{max}}$.

Referring back to the rotor power–torque curve in Figure 5.5 and substituting the values for operation at $C_{\text{p,max}}$ and $C_{\tau,\text{max}}$ in Equation (5.43), optimal mode gain values of $K_{\text{r,p}} = 1.00 \cdot 10^4$ Nm (rad/s)$^{-2}$ and $K_{\text{r},\tau} = 2.05 \cdot 10^4$ Nm (rad/s)$^{-2}$ are found for cases 1 and 2, respectively. The result of evaluating the rotor torque path in the below-rated region for the two cases is presented in Figure 5.11. Because of the lower tip-speed ratio in case 2, the rotor speed is lower for equal wind speeds or a higher wind speed is required for operation at the same rotor speed, resulting in a higher torque. An efficiency evaluation of the proposed operational cases using actual component efficiency data is given in the next section.

DRIVETRAIN EFFICIENCY AND STABILITY ANALYSIS

This section presents the available component efficiency data and evaluates steady-state drivetrain operation characteristics for the two previously introduced operating cases. The component efficiency characteristics primarily influence the steady-state response of the wind turbine, as shown in Equation (5.47). To perform a fair comparison between the two operating cases, the rotor efficiency is normalized with respect to case 1, resulting in a constant efficiency factor of 0.85 for operating case 2. Detailed efficiency data are available for the oil pump and motor; however, as no data for the efficiency characteristics of the water pump are available, a constant mechanical and volumetric efficiency of$\eta_{\text{m,k}} = 0.83$ and $\eta_{\text{m,k}} = 0.93$ are assumed, respectively. The oil pump is supplied with total efficiency data $\eta_{\text{t,h}}$ as a function of the (rotor) speed ω_r and the supplied torque

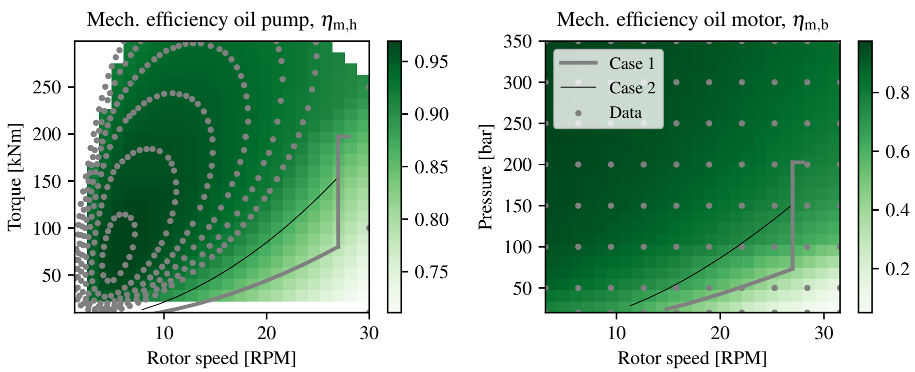

Figure 5.12: Mechanical efficiency mapping of the oil pump and oil motor. Manufacturer-supplied data (gray dots) are evaluated using an interpolation function. Operating cases 1 and 2 are indicated by the solid gray and black lines, respectively.

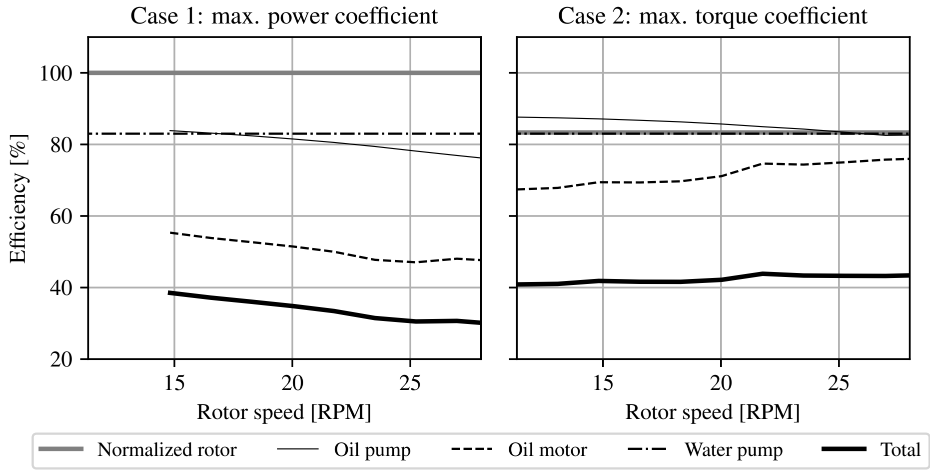

Figure 5.13: Comparison of the total drivetrain efficiency for operating cases 1 and 2. It is observed that the total efficiency is higher in the complete below-rated region for case 2. The efficiency over all rotor speeds is also more consistent, enabling passive torque control using a constant nozzle area A_{nz}.

τ_{sys} (Hägglunds, 2015). An expression relating the mechanical, volumetric, and total efficiency is given by

$$\eta_{\mathrm{m,h}}(\omega_{\mathrm{r}}, \tau_{\mathrm{sys}}) = \frac{\eta_{\mathrm{t,h}}(\omega_{\mathrm{r}}, \tau_{\mathrm{sys}})}{\eta_{\mathrm{v,h}}}, \tag{5.48}$$

where $\eta_{\mathrm{v,h}}$ is taken as 0.98, and the result is presented in Figure 5.12 (left). The plotted data points (dots) are interpolated on a mesh grid using a regular grid linear interpolation method from the Python SciPy interpolation toolbox (SciPy.org, 2017). Operating cases 1 and 2 are indicated by the solid lines. The same procedure is performed for the data supplied with the oil motor, the result of which is presented in Figure 5.12 (right), in which $\eta_{\mathrm{v,b}}$ is taken as 0.98. As concluded from the efficiency curves, hydraulic components are generally more efficient in the low-speed, high-torque, and/or high-pressure region. It is immediately clear that for both the oil pump and the motor, operating the rotor at a lower tip-speed ratio (case 2) is beneficial from a component efficiency perspective.

The drivetrain efficiency analysis for both operating cases is given in Figure 5.13. The lack of efficiency data at lower rotor speeds in the left plot of Figure 5.13 (case 1) is because of the unavailability of data at lower pressures. From the resulting plot it is concluded that the overall drivetrain efficiency for case 2 is higher and more consistent compared to case 1. The consistency of the total drivetrain efficiency is advantageous for control, as this enables passive torque control to maintain a constant tip-speed ratio. As a result of this observation, the focus is henceforth shifted to the implementation of a torque control strategy tracking the maximum torque coefficient (case 2).

It should be stressed that this operational strategy is beneficial for the considered drivetrain, but can by no means be generalized for other wind turbines with hydraulic drivetrains. As the overall efficiency of hydraulic components is a product of mechanical and volumetric efficiency, a more rigorous approach would be to optimize the ideal below-rated operational trajectory subject to all component characteristics. However, to perform a more concise analysis, only the two given trajectories are evaluated.

A stability concern for operation at the maximum torque coefficient needs to be highlighted. For stable operation, the value of k_λ needs to be negative. As shown in Figure 5.9, the stability boundary is located at a tip-speed ratio of 5.9. Operation at a lower tip-speed ratio results in unstable turbine operation and deceleration of the rotor speed to standstill. However, as concluded in (Schmitz et al., 2013), hydraulic drivetrains can compensate for this theoretical instability, allowing for operation at lower tip-speed ratios. Therefore, the case 2 torque control strategy is designed for the theoretical calculated minimum tip-speed ratio of 5.9, and in-field test results need to confirm the practical feasibility of the implementation.

5.4.2. ACTIVE NEAR-RATED TORQUE CONTROL

A feedback hydraulic torque control is derived for near-rated operation in this section. To this end, active spear position control is employed to regulate the rotor speed. The effect on fluid resonances is analyzed, as these are possibly excited by an increased rotor speed control bandwidth. The in-field tests with corresponding control implementations are performed prior to the theoretical dynamic analysis of the drivetrain. For this reason, the controller design and tunings used in-field are evaluated and possible improvements are highlighted. In the following, the modeling parameters of the oil col-

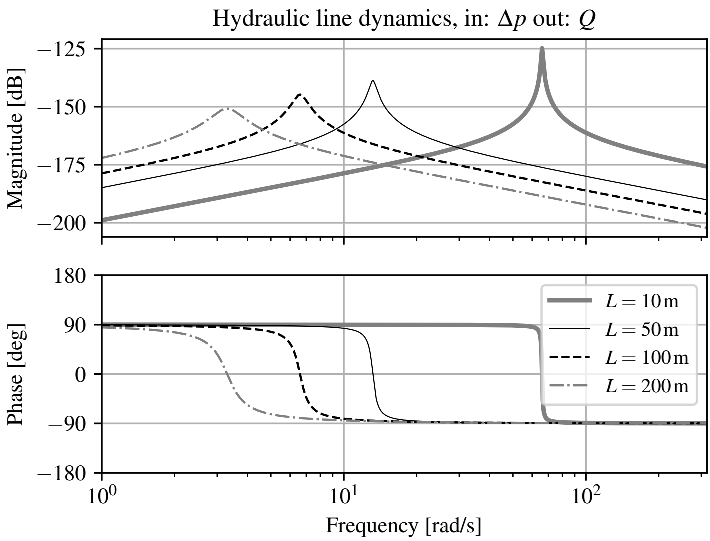

Figure 5.14: Bode plot of a hydraulic control volume modeled as a harmonic oscillator with pressure change Δp as input and flow Q as output. The length of the hydraulic line has a great influence on the location of the natural frequency and magnitude of the damping coefficient.

umn and spear valve actuator are defined. The parameters are subsequently used for spear valve torque controller design.

DEFINING THE HYDRAULIC MODEL PARAMETERS

The high-pressure oil line in the DOT500 drivetrain is considered to contain SAE30 oil, with a density of $\rho_o = 900\ \mathrm{kg\,m^{-3}}$ and an effective bulk modulus of $K_{f,o} = 1.5$ GPa. The hydraulic line is cylindrical with a length of $L_l = 50$ m, a radius of $r_l = 43.3$ mm, and a bulk modulus of $K_l = 0.80$ GPa (Hružík et al., 2013). According to Equation C.5, the equivalent bulk modulus becomes $K_e = 0.52$ GPa. The dynamic viscosity of SAE30 oil is taken at a fixed temperature of 20 °C, at which it reads a value of $\mu = 240$ mPa s. With these data the hydraulic inductance, resistance, and capacitance have calculated values of $L_H = 7.64 \cdot 10^6\ \mathrm{kg\,m^{-4}}$, $R_H = 8.69 \cdot 10^6\ \mathrm{kg\,m^{-4}\,s^{-1}}$ and $1/C_H = 1.77 \cdot 10^9\ \mathrm{kg\,m^{-4}\,s^{-2}}$, respectively. Using Equation (C.10), the flow is calculated to be laminar as $Re = 1244$ with oil flow at a nominal rotor speed of $1478\ \mathrm{l\,min^{-1}}$, and thus a correction factor $f_c = 4/3$ is applied to the hydraulic inductance.

By substitution of the calculated values in Equation (5.17), a visualization of the transfer function frequency response is given in Figure 5.14 at a range of hydraulic line lengths. In this Bode plot, it is shown that the line length has a great influence on the location of the natural frequency and damping coefficient. A longer line shifts the frequency to lower values and increases the damping coefficient.

MODELING SPEAR VALVE CHARACTERISTICS

For determining the time constant ts of the spear valve actuator model defined in Equation (5.22), a generalized (pseudo-random) binary noise (GBN) identification signal (Godfrey, 1993) is supplied to one of the spear valve actuators. From this test it is seen that the

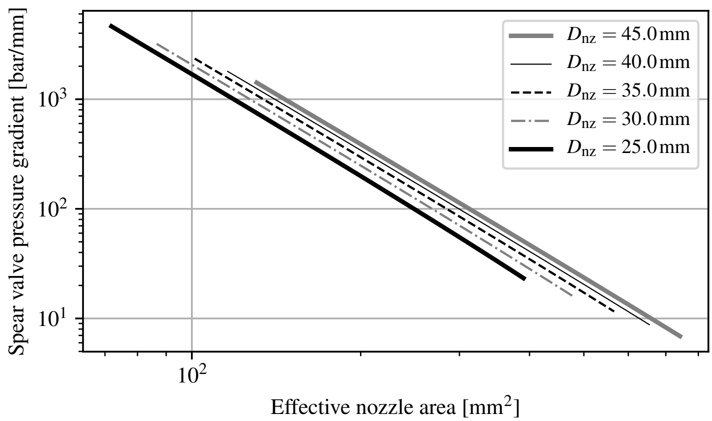

Figure 5.15: Spear valve position pressure gradient evaluated for different nozzle head diameters at a range of effective nozzle areas. The pressure sensitivity is higher for larger nozzle diameters at equal effective areas. Results are presented in a double logarithmic plot.

actuator has a fixed and rate-limited positioning speed of $\dot{s}_{\max} = 0.44\ \mathrm{mm\,s^{-1}}$ and shows no observable transient response.

Because of the nonlinear rate-limited response, an actuator model is parameterized for the worst-case scenario. This is done by evaluating the response at maximum actuation amplitude and determining the corresponding bandwidth such that closed-loop reference position tracking is ensured. As concluded from in-field experiments, the spear position control range in the near-rated operating region is 1.5 mm, and the corresponding time constant for reference tracking is given by $t_\mathrm{s} = 1.69$ s.

The spear position relates in a nonlinear fashion to the applied system torque as a consequence of the spear valve geometry presented in Figures 5.7 and 5.8. Therefore, in Figure 5.15, an evaluation of the spear valve pressure gradient with respect to the spear position $k_{\mathrm{s,s}}$ is given. This is done for distinct nozzle head diameters at a range of effective nozzle areas. It is shown that the spear pressure gradient with respect to the position is higher for larger nozzle head diameters at equal effective areas.

TORQUE CONTROL DESIGN AND EVALUATION

The active spear valve torque control strategy employed during the in-field tests is now evaluated. A fixed-gain controller was implemented for rotor speed control in the near-rated region. As the goal is to make a fair comparison and evaluation of the in-field controller design, the same PI controller is used in this analysis.

The dynamic drivetrain model presented in Section 5.3.2 is further analyzed. The linear state-space system in Equation (5.39) is evaluated at different operating points in the near-rated region. The operating point is chosen at a rotor speed of $\omega_{\mathrm{r,s}} = 27$ RPM, which results in a water pump discharge flow of $\bar{Q}_\mathrm{w} = 2965\ \mathrm{l\,min^{-1}}$, taking into account the volumetric losses. For the entire near-rated region, a range of wind speeds and corresponding model parameters are computed and listed in Table 5.2. An analysis is performed on the single-input single-output (SISO) open-loop transfer system with the speed error e_s as input and rotor speed as output, including the spear valve PI torque controller used during field tests. The gains of the PI controller were $K_\mathrm{p} = 3.8 \cdot 10^{-3}\ \mathrm{m\,(rad/s)^{-1}}$, and $K_\mathrm{i} = 6.6845 \cdot 10^{-4}\ \mathrm{m\,rad^{-1}}$.

By inspection of the state **A** matrix, various preliminary remarks can be made regarding system stability and drivetrain damping. First it is seen that for the (2, 2) element, the hydraulic resistance R_H influences the intrinsic speed feedback gain $k^*_{Q_\mathrm{in}}$. It was concluded in Section 5.4.1 that the rotor operation is stable for negative values of k_{ω_r} and thus $k^*_{Q_\mathrm{in}}$. Thus, the higher the hydraulic resistance, the longer the (2, 2) element stays negative for decreasing tip-speed ratios, resulting in increased operational stability. This effect has been observed earlier in (Schmitz et al., 2012; Schmitz et al., 2013), in which it was shown that turbines with a hydraulic drivetrain are able to attain lower tip-speed ratios. This is in accordance with Equations (C.13) and (C.14), in which it is shown that the resistance term only influences the damping. Furthermore, the spear valve pressure feedback gain $k_{\mathrm{s},Q_\mathrm{w}}$ provides additional system torque when the rotor has a speed increase or overshoot, resulting in additional damping to the (3, 3) element in the state matrix.

During analysis, an important result is noticed and is shown by discarding and including the spear valve pressure feedback gain $k_{\mathrm{s},Q_\mathrm{w}}$ in the linearized state-space system.

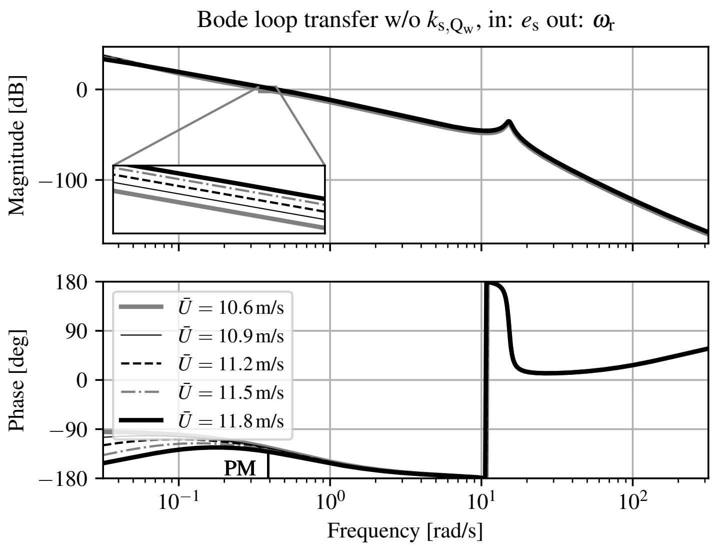

Figure 5.16: Bode plot of open-loop transfer, including controller from spear valve position reference to the rotor speed, *without* spear valve pressure feedback gain k_{s,Q_w}. The phase margin (PM) at magnitude crossover is indicated.

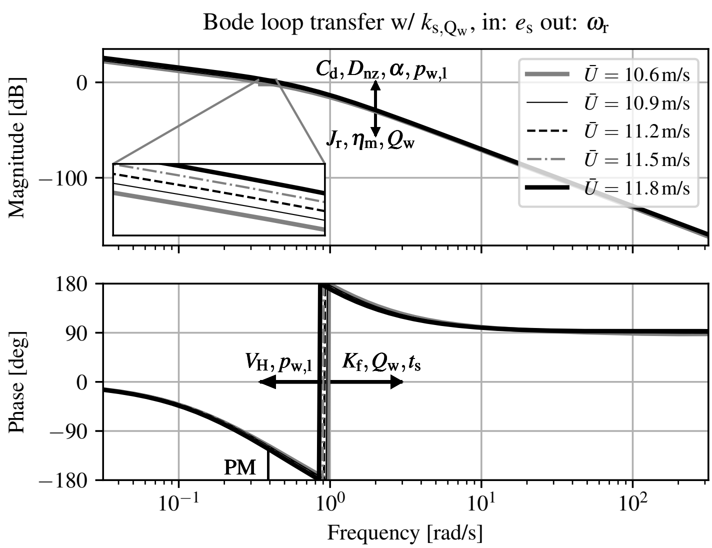

Figure 5.17: Bode plot of the plant for transfer from spear valve position reference to the rotor speed, *with* spear valve pressure feedback gain k_{s,Q_w}. The effect of increasing important model parameters on the frequency response is indicated, together with the phase margin (PM) at the magnitude crossover frequency.

Table 5.2: Parameters for linearization of the model in the near-rated operating region.

Description	**Symbol**	**Value**	**Unit**
Wind speed	$\bar{U}$	10.6 – 11.8	m s^{-1}
Rotor speed set point	$\bar{\omega}_{\mathrm{r}}$	27.0	RPM
Water flow	$\bar{Q}_{\mathrm{w}}$	2965	l min^{-1}
Water pressure	$\bar{p}_{\mathrm{w,l}}$	51.4 – 62.4	bar
Oil flow	$\bar{Q}_{\mathrm{o}}$	1354	l min^{-1}
Oil pressure	$\Delta\bar{p}_{\mathrm{h}}$	166 – 201	bar
Rotor torque	$\bar{\tau}_{\mathrm{r}}$	163.8 – 198.7	kNm
Rotor inertia	J_{r}	$6.6\cdot10^{5}$	kg m^{2}
Nozzle diameter	D_{nz}	38	mm
Spear coning angle	α	50	deg
Number of spear valves	N_{s}	2	-
Discharge coefficient	C_{d}	1.0	-
Effective nozzle area	A_{nz}	486.9 – 442	mm^{2}
Spear position	$\bar{s}$	4.64 – 4.18	mm
Density of air	ρ_{a}	1.225	kg m^{-3}
Density of oil	ρ_{o}	900	kg m^{-3}
Density of water	ρ_{w}	998	kg m^{-3}
Component mechanical efficiency	$\eta_{\mathrm{m,x}}$	0.85	-
Component volumetric efficiency	$\eta_{\mathrm{v,x}}$	0.95	-
Hydraulic line radius	r_{l}	43.3	mm
Hydraulic line length	L_{l}	50.0	m
Hydraulic line volume	V_{H}	295	l
Hydraulic induction, oil	L_{H}	$7.64\cdot10^{6}$	kg m^{-4}
Hydraulic resistance, oil	R_{H}	$8.69\cdot10^{6}$	kg m^{-4}s^{-1}
Equivalent bulk modulus, oil and line	K_{e}	0.52	GPa
Dynamic viscosity, oil	μ_{o}	0.240	Pa s
Spear valve actuator time constant	t_{s}	1.69	s
Pitch actuator time constant	t_{β}	0.5	s

The open-loop Bode plot of the system excluding the term is presented in Figure 5.16 and including the term in Figure 5.17. It is noted that the damping term completely damps the hydraulic resonance peak in the oil column as a result of the intrinsic flow pressure feedback effect. At the same time, the attainable bandwidth of the hydraulic torque control implementation is limited. This bandwidth-limiting effect becomes more severe by applying longer line lengths and thus larger volumes in the discharge line, as it increases the hydraulic induction. Fortunately, various solutions are possible to mitigate this effect and are discussed next.

The effect of increasing different model parameters is depicted in Figure 5.17. In the DOT500 setup an intermediate oil circuit is used, which is omitted in the ideal DOT concept. Seawater has a higher effective bulk modulus compared to oil and this has

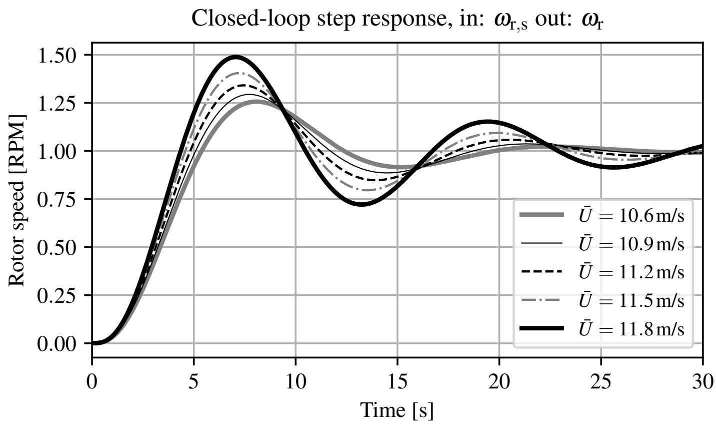

Figure 5.18: Closed-loop step responses of the spear valve torque control implementation. It is shown that the feedback loop is stabilized, but that the dynamics vary with increasing wind speeds. A control implementation that takes care of the varying spear valve position pressure gradient would lead to a more consistent response.

a positive effect on the maximum attainable torque control bandwidth for equal line lengths. Moreover, a faster spear valve actuator has a positive influence on the attainable control bandwidth.

From both figures it is also observed that the system dynamics change according to the operating point. At higher wind speeds, the magnitude of response results is higher. The effect was seen earlier in Figure 5.15, in which the pressure gradient with respect to the spear valve position is higher for smaller effective nozzle areas. It is concluded that the sizing of the nozzle diameter is a trade-off between the minimal achievable pressure and its controllability with respect to the resolution of the spear positioning and actuation speed.

The loop-shaped frequency responses attain a minimum and maximum bandwidth of 0.35 and 0.43 rad s^{-1} with phase margins (PM) of 64 and 58°, respectively. For later controller designs a more consistent control bandwidth can be attained by gain-scheduling the controller gains on a measurement of the water pressure or spear position. Closed-loop step responses throughout the near-rated region (for different wind speeds) are shown in Figure 5.18. It is seen that the controller stabilizes the system, and the control bandwidth increases for higher wind speeds.

5.5. IMPLEMENTATION OF CONTROL STRATEGY AND IN-FIELD RESULTS

This section covers the implementation and evaluation of the derived control strategies on the real-world in-field DOT500 turbine. In accordance with the previous section, a distinction is made between passive and active regulation for below- and near-rated wind turbine control, respectively. To illustrate the overall control strategy from in-field gathered test data, operational visualizations are given in Section 5.5.1. Evaluation of the effectiveness of the passive below-rated and active near-rated torque control strategy is presented in Section 5.5.2.

5.5.1. TURBINE PERFORMANCE CHARACTERISTICS AND CONTROL STRATEGY

To illustrate the overall control strategy, three-dimensional rotor torque and rotor speed plots are shown as a function of spear position and wind speed in Figure 5.19. By fixing the valve position at a range of positions, making sure that sufficient data are collected throughout all wind speeds and binning the data accordingly, a steady-state drivetrain performance mapping is derived. Both figures show the data binned in predefined spear valve positions and wind speeds. This is done on a normalized scale, on which 0 % is the maximum spear position (larger nozzle area) and 100 % the minimum spear position (smaller nozzle area). The absolute difference between the minimum and maximum spear position is 1.5 mm. The spear position is the only control input in the below-rated region and is independent from other system variables. During data collection, the pitch system regulates the rotor speed up to its nominal set point value when an overspeed occurs.

In both figures the control strategy is indicated by colored lines. For below-rated operation (black), the spear valve position is kept constant: Flow fluctuations influence the water discharge pressure and thus the system torque. In near-rated conditions (gray), the spear position is actively controlled by a PI controller. Under conditions of a constant regulated water flow corresponding to $\omega_{r,s} = 27$ RPM, the controller continuously adjusts the spear position and thus water discharge pressure to regulate the rotor speed. Once the turbine reaches its nominal power output, the rotor limits wind energy power capture using gain-scheduled PI pitch control (white), maintaining the rotor speed at $\omega_{r,\beta} = 28$ RPM.

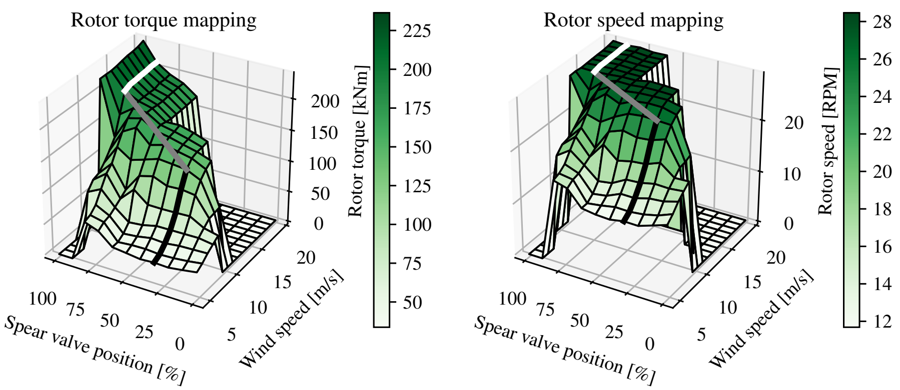

Figure 5.19: Steady-state rotor torque and speed at predefined spear valve positions (nozzle areas) and wind speed conditions. The black line indicates the operation strategy at fixed spear valve position in the below-rated region, whereas the gray trajectory indicates active spear valve position control towards rated conditions. The effect of blade pitching is indicated in white.

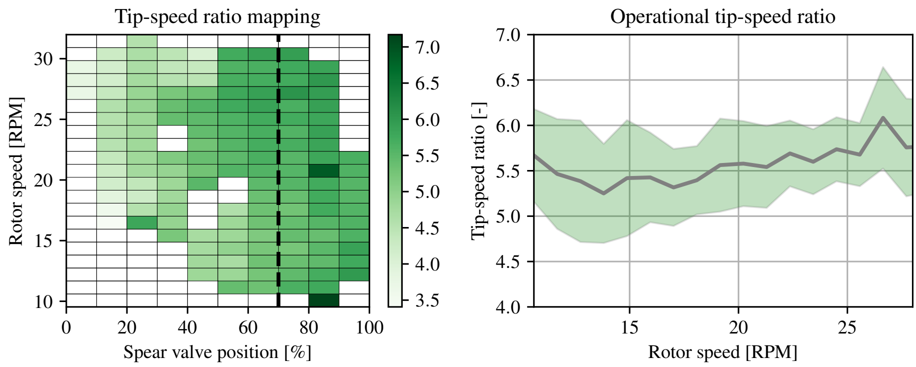

5

Figure 5.20: Tip-speed ratio mapping as a function of spear valve position and rotor speed (a). The dashed line indicates the fixed spear position selected for below-rated passive torque control. Panel (b) shows the corresponding evaluation of the tip-speed ratios along this path with 1σ standard deviation bands.

5.5.2. EVALUATION OF THE CONTROL STRATEGY

Previously, in Section 5.4.1, drivetrain characteristics are deduced from prior component information throughout the wind turbine operating region. Characteristic data from the rotor, the oil pump, and the oil motor are evaluated to generate a hydraulic torque control strategy. Due to the predicted consistent mechanical efficiency of the hydraulic drivetrain, the nozzle area can be fixed and no active torque control is needed in the below-rated region. This results from the rotor speed being proportional to water flow and relates to system torque according to Equation (5.47). From the analysis it is also concluded that operating at a lower tip-speed ratio results in a higher and more consistent overall efficiency for this particular drivetrain.

As concluded in Section 5.4.1, stable turbine operation is attained when the rotor operates at a tip-speed ratio such that k_λ is negative, and Figure 5.9 shows that the predicted stability boundary is located at a tip-speed ratio of $\lambda = 5.9$. Using the data obtained from in-field tests, a mapping of the attained tip-speed ratios as a function of the spear valve position and rotor speed is given in Figure 5.20. An anemometer on the nacelle and behind the rotor measures the wind speed. As turbine wind speed measurements are generally considered less reliable (Østergaard et al., 2007) and the effect of induction is not included in this analysis, the obtained results serve as an indication of the turbine behavior. The dashed line indicates the fixed spear position of 70 % and is chosen as the position for passive torque control in the below-rated region. The attained tip-speed ratio averages are presented in Figure 5.20 (left), and Figure 5.20 (right) shows a two-dimensional visualization of the data indicated by the dashed line, including 1 standard deviation. Closing the spear valve further for operation at an even lower tip-speed ratio and higher water pressures resulted in a slowly decreasing rotor speed and thus unstable operation.

In Figure 5.20, it is shown that the calculated tip-speed ratio is regulated around a mean of 5.5 for below-rated conditions. Although the attained value is lower than the theoretical calculated minimum tip-speed ratio of 5.9, stable turbine operation is at-

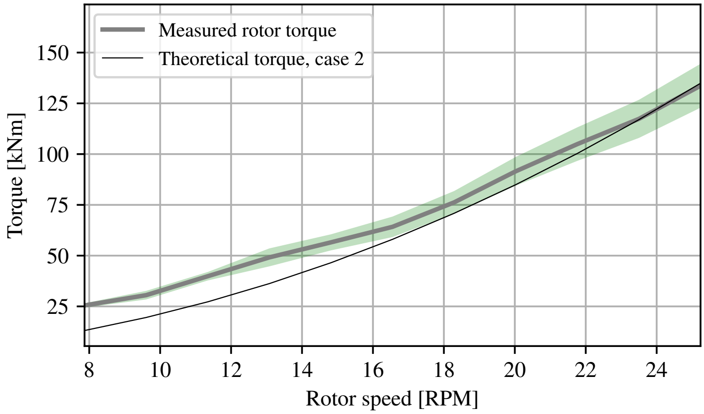

Figure 5.21: Evaluation of the passive torque control strategy by comparison of the theoretical torque for case 2 to the torque measured by load pins in the oil pump suspension. For higher speeds, the passive torque control strategy succeeds in near-ideal tracking of the desired case 2 path. At lower rotor speeds, the torque is higher than the aimed theoretical line as a result of the lower combined drivetrain efficiency in this operating region.

tained during in-field tests. A plausible explanation is that the damping characteristics of hydraulic components compensate for instability as predicted in Section 5.4.2.

Figure 5.21 shows reaction torque measurements by the load pins in the suspension of the oil pump to estimate the attained rotor torque during below-rated operation. From the tip-speed ratio heat map and the rotor torque measurements it is concluded that the case 2 (maximum rotor torque coefficient) strategy works on the actual turbine, and the passive strategy regulates the torque close to the desired predefined path. However, as seen in both figures for lower rotor speeds, the tip-speed ratio attains lower values and the rotor torque increases. An explanation for this effect is the decreased mechanical water pump efficiency, the efficiency characteristics of which, as stated earlier, are unknown. An analysis of the water pump efficiency is performed using measurement data and shows nonconstant mechanical efficiency characteristics: The efficiency drops rapidly when the rotor speeds is below 15 RPM.

Finally, the active spear valve torque control strategy is evaluated. The aim is to regulate the rotor speed to a constant reference speed in the near-rated operating region. In-field test results are given in Figure 5.22, in which the environmental conditions were such that the turbine operated around the near-rated region. All values are normalized for convenient presentation. It is shown that active spear valve control combined with pitch control regulates the wind turbine for (near-)rated conditions in a decentralized way. Small excursions to the below-rated region are observed when the spear valve position saturates at is minimal normalized value. The spear position tracks the control signal reference and shows that the strategy has sufficient bandwidth to act as a substitute for conventional torque control.

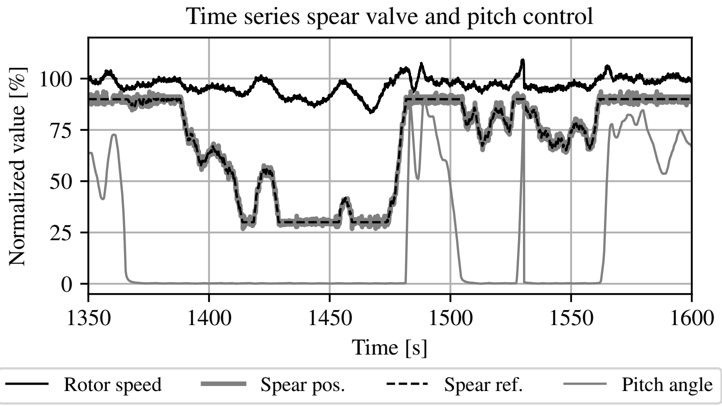

Figure 5.22: A time series showing the hydraulic control strategy for the DOT500 turbine. The spear valve position actively regulates the rotor speed as a substitute for conventional turbine torque control. In the above-rated region, pitch control is employed to keep the rotor at its nominal speed. All signals in this plot are normalized.

5.6. CONCLUSIONS

This chapter presents the controller design for the intermediate DOT500 hydraulic wind turbine. This turbine with a 500 kW hydraulic drivetrain is deployed in-field and served as a proof of concept. The drivetrain included a hydraulic transmission in the form of an oil circuit, as at the time of writing a low-speed high-torque seawater pump was not commercially available and is being developed by DOT.

First it is concluded that for the employed drivetrain, operating at maximum rotor torque, instead of maximum rotor power, is beneficial for drivetrain efficiency maximization. This results not only in an increased overall efficiency, but comes with an additional advantage of the efficiency characteristics being consistent for the considered drivetrain. From a control perspective, a consistent overall drivetrain efficiency is required for successful application of the below-rated passive torque control strategy. Another benefit of the hydraulic drivetrain is the added damping, enabling operation at lower tip-speed ratios. It is shown using in-field measurement data that the passive strategy succeeds in tracking the torque path corresponding to maximum rotor torque for a large envelope in the below-rated region. For a smaller portion, the combined drivetrain mechanical efficiency drops, which results in deviation from the desired trajectory.

Secondly, a drivetrain model including the oil dynamics is derived for spear valve controller design in the near-rated region. It is shown that by including a spear valve as a control input, the hydraulic resonance is damped by the flow-induced spear valve pressure feedback. This intrinsic pressure feedback effect also limits the attainable torque control bandwidth. However, this limiting effect can be coped with by using a stiffer fluid, a decreased hydraulic line volume, or a faster spear valve actuator. The sizing of the nozzle head diameter influences the pressure sensitivity with respect to the spear position and affects the attainable control bandwidth by spear valve actuation speed constraints and positioning accuracy. In-field test results show the practical feasibility of the strategy including spear valve and pitch control inputs to actively regulate the wind turbine in the (near-)rated operating region. Future controller designs will be improved by including a control implementation taking into account the varying spear valve pressure gradient. This will result in a higher and more consistent system response.

The ideal DOT concept discards the oil circuit and only uses water hydraulics with an internally developed seawater pump. As a result, the controller design process is simplified and the overall drivetrain efficiency should be greatly improved. Future research will focus on the design of a centralized control implementation for DOT wind turbines acting in a hydraulic network.

Data availability. The data set and code used in this chapter are available under: https://doi.org/10.5281/zenodo.1405387 (Mulders et al., 2018b).

6

Conclusions and recommendations

6.1. CONCLUSIONS

Advances in control algorithms are of key importance for the sustained growth of wind turbine power capacities. While an abundance of research has been conducted to such algorithms, a spectrum of problems remains relatively understated by the absence of a careful analysis, and consequent controller designs. For this reason, the following thesis goal was posed in the Introduction of this dissertation:

> **Thesis goal:** Develop analysis tools based on established control theory, providing optimal control solutions for stimulating advancements in wind turbine technology.

To fulfill this goal, well-known control concepts that lack a thorough analysis were further explored in this thesis. As a result, established control implementations from the literature, aiming for tower and blade fatigue load reductions, are taken to a next level. The higher load reducing capabilities enable the more economical use of materials, resulting in turbines with higher specific powers. Also, by including the advancements in a publicly available and universal wind turbine controller, disciplines are supported in the proper assessment of innovations. Finally, the overall gathered insights, have led to the synthesis of a successful control system for a wind turbine with a hydraulic drivetrain configuration. The combined contributions of this thesis stimulate advancements in wind turbine technology, and facilitate the development of next-generation wind turbines, ultimately lowering the cost of wind energy.

According to the subgoals stated in the Introduction, the conclusions on the different parts of this thesis are presented next. The main conclusions are divided in three sections, following the structure of this thesis. First, finalizing comments on the open-source and publicly available control software packages are given. Then, conclusions are drawn on the control methodological advances for blade and tower fatigue load reductions. The last section presents the conclusions on the controller design for a real-world hydraulic wind turbine, based on the Delft Offshore Turbine (DOT) concept.

OPEN-SOURCE AND PUBLICLY AVAILABLE CONTROL SOFTWARE

The proper assessments of novel algorithms and innovations heavily relies on decent (baseline) controller performance. However, broadly available and convenient controller design software packages were still lacking. For this reason, the first research question posed in this thesis was:

> **I:** What are the prevalently applied operational and load mitigating wind turbine control methods, and is it possible to develop a universal baseline controller code, and improve on widely accepted ideas?

To answer this research question, three control-oriented packages for wind turbines were developed. First, for the purpose of providing a de facto standard and baseline wind turbine control solution, the Delft Research Controller (DRC) has been developed. The controller achieves this goal by providing extensive documentation, and baseline

6

tunings for celebrated reference models, in an easy to use and modular framework. Furthermore, the controller is being adopted by the National Renewable Energy Laboratory (NREL) and is dubbed as the Reference OpenSource Controller (ROSCO) (NREL, 2020), stimulating its wide acceptance.

Secondly, besides the DRC – that is written in a high-level programming language – a MATLAB Simulink tool is developed for convenient graphical controller design and compilation. The main benefits of this tool are the insightful development environment, and the possibilities for utilization of built-in Simulink objects and functions.

Finally, a graphical user interface for NREL's aeroelastic simulation code FAST has been developed. The tool is dubbed as FASTTool, and is intended for educational purposes in wind turbine (controller) design. By reflecting parameter changes in a three-dimensional animated turbine visualization, FASTTool provides people new to the field with insights in the design process. The software is aimed at the education of engineering talent formulating future technological innovations.

The software packages have been established with the aim of control software standardization, and supporting the wind turbine community in doing sound evaluations of proposed innovations. With these incentives in mind, and to improve on transparency and stimulating collaborations, all code is open-source and publicly available.

BLADE AND TOWER FATIGUE LOAD REDUCING CONTROL METHODS

Control methods for fatigue load reductions facilitate a path towards next-generation wind turbines, with higher power ratings, a more economical use of materials, and thus increased cost effectiveness. In this thesis, two approaches for algorithmic advancements are employed to solve prevailing load mitigating design problems.

The first approach entailed the further analysis and improvements to existing ideas and control schemes, by exploiting well-developed methods from classical control theory. This method is applied to the mitigation of periodic blade loads using individual pitch control (IPC). For IPC implementations, the azimuth offset is a frequently employed design variable in the literature. However, up until recently, different claims on the effects of the offset were reported, and no profound analysis was performed of its implications. Therefore, the following research question was formulated:

> **II:** How do we develop analysis tools based on established control theory to disclose the effect(s) of the commonly applied azimuth offset for individual pitch control using the multiblade coordinate transformation? Can we subsequently use traditional controller design methods to improve (practical) load mitigating performance levels, towards the application of larger rotors?

The investigation in this thesis has shown that the azimuth offset improves the decoupling of the nonrotating yaw and tilt rotor moment axes. The optimal offset is highly related to the current operating point, and the system dynamics in the rotating frame, with special attention to off-diagonal interactions and phase delays. Furthermore, the offset reduces directionality and makes the system diagonally dominant, allowing for the application of single-input single-output (SISO) control loops. In an evaluation of a combined 1P + 2P IPC implementation, omittance of the correct offset value results in an increased actuator duty cycle and fatigue load amplification, accelerating structural damage. The inclusion of the offset is of increased importance for larger rotors with more flexible blades, because of higher phase losses and possibly increased blade load cross-coupling in the rotating frame.

The second approach employed the application of advanced control methods, to provide extended capabilities and to reach performance levels that are unattainable for schemes based on classical control techniques. This methodology is applied to the problem of tower resonance excitation prevention for the side-side direction. Preventing such excitation is attained by skipping over a predefined resonance inducing frequency, and facilitates the application of tall, light-weight, and more flexible soft-soft tower configurations. Therefore, upon the creation of a resonance frequency skipping algorithm, the third research question introduced in this thesis was:

III: Can we create a practically feasible model predictive control scheme, replacing existing implementations based on traditional control methods, for preventing the excitation of critical resonances, towards the application of taller and more cost/weight-effective towers?

The proposed frequency skipping strategy performs a dynamically optimal trade-off between produced energy and loads for the prevention of tower resonance excitation. For the effectuation of this strategy, a combination of control techniques is used in an intuitive and efficient model predictive control (MPC) framework. First, for convexification of the optimization problem, a demodulation transformation is applied to the dynamics of a wind turbine tower. After augmentation of the result with an aerodynamic wind turbine model, a quasi-linear parameter varying (LPV) system description is obtained. The beneficial properties of the quasi-LPV model are exploited in an efficient MPC scheme. The qLPV-MPC framework converges towards the LPV scheduling sequence by performing multiple iterative QP solves in the first time step. Subsequent time steps only require a single QP solve by using a scheduling sequence warm start from the previous time step. Results show a significant reduction in the excitation of the tower fundamental frequency by sacrificing produced energy: The trade-off between power production and load reductions is conveniently tuned by weighting matrices.

MODELING AND CONTROLLER DESIGN FOR HYDRAULIC DRIVETRAINS

Wind turbine hydraulic drivetrains, approach wind energy cost reductions from a system design perspective. Using hydraulics might form an opportunity for reducing turbine weight, maintenance requirements, complexity, and thus the cost of wind energy. However, for hydraulic wind turbines to be commercially successful, an energy efficiency maximizing development has to take place. The first steps in realizing this goal, have been laid out by real-world and full-scale prototype tests with a retrofitted hydraulic drivetrain turbine. For the development of an effective control strategy for the in-field wind turbine, the last research question posed in this thesis is:

IV: Are the analysis tools in subquestion/challenge **I** practically feasible to establish an operational strategy and controller design for a real-world wind turbine, with a fundamentally different hydraulic drivetrain configuration?

To fulfill this goal, first a model of the 500 kW hydraulic drivetrain configuration has been established. Consequently, based on this model, a controller design and strategy was derived. The main conclusion from the in-field experiment is that the overall drivetrain efficiency is maximized by operating the rotor away from its optimal aerodynamic efficiency at lower tip-speed ratios. This strategy resulted in higher torques and line pressures, operating the hydraulic components in more favorable efficiency regimes. The added hydraulic damping aided the operation at lower tip-speed ratios.

Furthermore, successful application of the passive torque control strategy for below-rated operation has been demonstrated. From a control perspective, a consistent overall drivetrain efficiency is required for successful application of this passive strategy. The practical feasibility of an active (near-)rated region control scheme, using spear valve and pitch actuation, has also been proven during the in-field tests. However, the intrinsic pressure feedback induced by the spear valve also limits the attainable torque control bandwidth. Methods have been proposed on how to cope with this limitation.

The in-field tests were performed on an intermediate version of the ideal DOT concept, including an oil circuit. The ideal DOT concept discards the oil circuit and only uses water hydraulics with an internally developed seawater pump. As a result, the control design process is simplified and the overall drivetrain efficiency should be greatly improved.

6.2. RECOMMENDATIONS

This work has presented advances for controller standardization, improvements for load mitigation strategies, and a strategic analysis for optimally operating turbines with a hydraulic drivetrain. In the course of the research, potential interesting opportunities for further investigation were identified. These recommendations are summarized in this section.

1. The presented DRC baseline wind turbine controller, consists of more conventional control elements. While such control architectures provide ease of implementation, and result in sufficient performance levels, the industry recognizes the potential of predictive control methods such as model predictive control. MPC has the ability of handling constraints, and offers straightforward integration with more complex multivariable and nonminimum phase systems. The development of a publicly available and open-source MPC-based controller, is therefore the first recommendation. The development should be performed in a modern and easy accessible programming language, such as Python. As in the DRC, the practical feasibility of implementations should be kept in mind. Wide acceptance of a more advanced controller could bring the scientific community on par with control performance levels seen in the industry.

2. As shown in this thesis, IPC implementations employing the MBC transformation – optimally tuned by the azimuth offset – can use basic control elements for attaining high performance levels. However, the downside of such an architecture is that without applying logic, the controller is always active. That is, even by the presence of an insignificant amount of fatigue blade loading, the pitch system is continuously active. This increases the actuator duty cycle and possibly reduces lifetime expectancies. Predictive control methods could form an elegant solution for this problem. These control techniques naturally have the ability of incorporating constraints on the control signal, and therefore form an interesting opportunity for IPC. With MPC, it should be possible to permit fatigue stresses up to some predefined limit (no control), and only activate control when the threshold is exceeded.

3. Perform a practical evaluation of the proposed blade and tower fatigue load minimization techniques in laboratory wind tunnel, or full-scale turbine experiments. While the innovations proposed in the corresponding chapters are evaluated in high-fidelity simulations, it would be interesting to explore the practical hurdles, and see the real-world benefits.

4. A distinction can be made between control strategies for above-rated regulation: Either the generator torque or generator power is held constant. When employing a power regulating implementation, the rated power of the turbine is mathematically divided by the low-pass filtered measured rotational speed, resulting in the generator torque demand. In case over an overspeed, the torque demand is lowered to keep the power constant. However, this control action results in an even higher speed excursion, for which the pitch controller has to correct. A proper analysis of this phenomenon could lead to a more effective controller tuning, and enhanced performance levels.

5. For the tower resonance excitation prevention scheme, a demodulation transformation is employed, convexifying the control optimization problem. By further manipulations, a quasi-LPV system is obtained, which has the advantage of its scheduling variable being part of the state vector. The proposed combination with an efficient MPC scheme, only requires a single quadratic program (QP) solve in each time step, and shows to be very effective and tractable for practical application. The combination of techniques is interesting and poses opportunities for further research. Example might be to explore the ability of excluding the operation at multiple, distinct frequencies, or the possibilities for more insightful blade fatigue load reduction implementations.

6. Although the work on Bayesian optimization (BO) is not included in this thesis, it was found that the optimization routine is tractable for fixed-structure controller tuning. Bayesian optimization is an efficient algorithm for the optimization of black box functions or systems, of which the evaluation is (computationally) expensive. Often, the damage equivalent load (DEL) is a design driver for controller tunings, however, the quantity can only be computed offline from time-series data. The application of BO acting on a multiobjective cost function, includ-

ing the DEL, yields an efficient setup for controller tuning. Frameworks for the tuning of a fixed-structure 1P + 2P IPC implementation, and a Kalman filter-based wind speed estimator have already been developed, and show promising results. Application to other, more complex, possibly nonlinear fixed-structure controller implementations might be an interesting opportunity for exploration.

Appendix

A

INCLUDING THE AZIMUTH OFFSET IN A STATE-SPACE REPRESENTATION

The state-space system representation with inclusion of the azimuth offset is presented here. The derivation is based on the work by (Bir, 2008b) and the corresponding `MBC3` code (Bir, 2008a). The `MBC3` implementation assumes that the dynamics from individual blade pitch angles to blade root out-of-plane bending moments are described as second-order models. This is in accordance with linear systems obtained from the high-fidelity wind turbine simulation software package FAST (NWTC Information Portal, 2019).

The rotating system is related to the nonrotating system by

$$X = \tilde{\mathscr{T}}_n^{-1} X_{\mathrm{NR}} \tag{A.1}$$

and

$$\tilde{\mathscr{T}}_n^{-1}(\psi + \psi_o) = \begin{bmatrix} \boldsymbol{I}_{F\times F} & 0 \\ 0 & \tilde{\boldsymbol{T}}_n^{-1}(\psi + \psi_o) \end{bmatrix}, \tag{A.2}$$

where F represents the number of fixed-frame degrees of freedom and $\tilde{\mathscr{T}}^{-1}(\psi + \psi_o) \in \mathbb{R}^{(F+Bm)\times(F+Bm)}$ is a diagonal matrix, where m is the number of rotating degrees of freedom. The forward transformation, transforming the rotating out-of-plane blade moments into their nonrotating counterparts, is defined by $\boldsymbol{T}(\psi)$. Now, combining the results, the following relations transform the periodic matrices to a nonrotating reference frame by applying a state-coordinate change

$$
\begin{aligned}
A = &\begin{bmatrix} \mathcal{T}_n(\psi) & 0 \\ 0 & \mathcal{T}_n(\psi) \end{bmatrix} A^*(\psi) \left(\begin{bmatrix} \tilde{\mathcal{T}}_n^{-1}(\psi+\psi_\mathrm{o}) & 0 \\ \omega_\mathrm{r}\mathcal{T}_{n,2}^{-1} & \tilde{\mathcal{T}}_n^{-1}(\psi+\psi_\mathrm{o}) \end{bmatrix} \right. \\
&\left. - \begin{bmatrix} \omega_\mathrm{r}\mathcal{T}_{n,2}^{-1} & 0 \\ \omega_\mathrm{r}^2\mathcal{T}_{n,3}^{-1} + \dot{\omega}_\mathrm{r}\mathcal{T}_{n,2}^{-1} & 2\omega_\mathrm{r}\mathcal{T}_{n,2}^{-1} \end{bmatrix} \right),
\end{aligned} \tag{A.3}
$$

$$
B = \begin{bmatrix} \mathcal{T}_n(\psi) & 0 \\ 0 & \mathcal{T}_n(\psi) \end{bmatrix} B^*(\psi)\mathcal{T}_{n\ \mathrm{c}}^{-1}(\psi+\psi_\mathrm{o}), \tag{A.4}
$$

$$
C = \mathcal{T}_{n,\mathrm{o}}(\psi)\left[C_1^*(\psi)\mathcal{T}_n^{-1}(\psi+\psi_\mathrm{o}) + \omega_\mathrm{r} C_2^*(\psi)\mathcal{T}_n^{-1} \quad C_2^*(\psi)\mathcal{T}_n^{-1}(\psi+\psi_\mathrm{o}) \right], \tag{A.5}
$$

$$
D = \mathcal{T}_{n,\mathrm{o}}(\psi) D^*(\psi)\mathcal{T}_{n,\mathrm{c}}^{-1}(\psi+\psi_\mathrm{o}), \tag{A.6}
$$

where $\mathcal{T}_{2,3}$ are the first and second time derivative of $\mathcal{T}$, independent of the azimuth offset ψ_o. The $(\cdot)^*$ notation refers to the system A, input B, output C and feed-through D matrices defined in the rotating frame, and the matrices $A^* \in \mathbb{R}^{r\times r}$ and $C^* \in \mathbb{R}^{q\times r}$ are partitioned as

$$
A^*(\psi) = \begin{bmatrix} 0 & I \\ A_\mathrm{K}^*(\psi) & A_\mathrm{C}^*(\psi) \end{bmatrix}, \tag{A.7}
$$

$$
C^*(\psi) = \begin{bmatrix} C_1^*(\psi) & C_2^*(\psi) \end{bmatrix}. \tag{A.8}
$$

As it is assumed that the rotating linearized models only include in- and outputs corresponding to rotating degrees of freedom, the matrices $\mathcal{T}_\mathrm{c}^{-1}$ and $\mathcal{T}_\mathrm{o}$ are equal to $\mathcal{T}^{-1}$. For obtaining the forward transformation matrix, the inverse matrices $\mathcal{T}^{-1}$, $\mathcal{T}_\mathrm{c}^{-1}$ and $\mathcal{T}_\mathrm{o}^{-1}$ are required.

B

Preventing tower resonance excitation by a quasi-LPV MPC framework

B.1. The affine LPV model representation and discretization

This section presents the process of converting the LPV model derived in Section 4.3.2 to its affine form. For this, the steady-state offset values of the state, input and output values are saved for each linearization. The offsets are indicated by a $\breve{(\cdot)}$, and the following relations

$$\hat{\boldsymbol{q}}(t, \boldsymbol{p}^*) = \boldsymbol{q}(t) - \breve{\boldsymbol{q}}(\boldsymbol{p}^*), \tag{B.1}$$
$$\hat{\boldsymbol{u}}(t, \boldsymbol{p}^*) = \boldsymbol{u}(t) - \breve{\boldsymbol{u}}(\boldsymbol{p}^*), \tag{B.2}$$
$$\hat{\boldsymbol{y}}(t, \boldsymbol{p}^*) = \boldsymbol{y}(t) - \breve{\boldsymbol{y}}(\boldsymbol{p}^*), \tag{B.3}$$

are substituted in Eq. (4.28), such that the affine form is obtained:

$$\dot{\boldsymbol{q}}(t) = \mathbf{A}(\boldsymbol{p})(\boldsymbol{q}(t) - \breve{\boldsymbol{q}}(\boldsymbol{p}^*)) + \mathbf{B}(\boldsymbol{p})(\boldsymbol{u}(t) - \breve{\boldsymbol{u}}(\boldsymbol{p}^*)) + \dot{\breve{\boldsymbol{q}}}(\boldsymbol{p}^*) \tag{B.4}$$
$$\boldsymbol{y}(t) = \mathbf{C}(\boldsymbol{p})(\boldsymbol{q}(t) - \breve{\boldsymbol{q}}(\boldsymbol{p}^*)) + \breve{\boldsymbol{y}}(\boldsymbol{p}^*), \tag{B.5}$$

in which $\boldsymbol{p}(t) = \boldsymbol{p}^*(t)$ indicates the current linear model in the LPV scheduling space (MathWorks, 2019). Because a finite set of linear models is taken, the scheduling variable might fall between two model scheduling points. In this case, either the nearest offsets corresponding to the current scheduling value are taken, or a linear interpolation is performed. When the models are defined on a fine enough grid, the advantage of increased accuracy by interpolation diminishes, and therefore the *nearest model* approach is employed.

As a sample-based and fixed time-step control setup is employed, the continuous-time system is converted to its discrete-time equivalent

$$\boldsymbol{q}(k+1) = \mathbf{A}_{\mathrm{d}}(\boldsymbol{p}_{\mathrm{k}})(\boldsymbol{q}(k) - \breve{\boldsymbol{q}}(\boldsymbol{p}_{\mathrm{k}}^{*})) + \mathbf{B}_{\mathrm{d}}(\boldsymbol{p}_{\mathrm{k}})(\boldsymbol{u}(k) - \breve{\boldsymbol{u}}(\boldsymbol{p}_{\mathrm{k}}^{*})) + \breve{\boldsymbol{q}}(\boldsymbol{p}_{\mathrm{k}}^{*}) \tag{B.6}$$

$$\boldsymbol{y}(k) = \mathbf{C}(\boldsymbol{p}_{\mathrm{k}})(\boldsymbol{q}(k) - \breve{\boldsymbol{q}}(\boldsymbol{p}_{\mathrm{k}}^{*})) + \breve{\boldsymbol{y}}(\boldsymbol{p}_{\mathrm{k}}^{*}), \tag{B.7}$$

in which k is the discrete time-step variable, and the matrix subscripts $(\cdot)_{\mathrm{d}}$ indicate the discrete time counterparts of the system and input matrices. Discretization of **A** and **B** is performed using a fourth order Runge-Kutta discretization method (Shampine et al., 1997), of which the matrix transformation relations are given by

$$\mathbf{A}_{\mathrm{d}} = \frac{1}{24}\mathbf{A}^4 t_{\mathrm{s}}^4 + \frac{1}{6}\mathbf{A}^3 t_{\mathrm{s}}^3 + \frac{1}{2}\mathbf{A}^2 t_{\mathrm{s}}^2 + \mathbf{A} t_{\mathrm{s}} + \mathrm{I}_{\mathrm{n}}, \tag{B.8}$$

$$\mathbf{B}_{\mathrm{d}} = \frac{1}{24}\mathbf{A}^3\mathbf{B} t_{\mathrm{s}}^4 + \frac{1}{6}\mathbf{A}^2\mathbf{B} t_{\mathrm{s}}^3 + \frac{1}{2}\mathbf{A}\mathbf{B} t_{\mathrm{s}}^2 + \mathbf{B} t_{\mathrm{s}} + \mathrm{I}_{\mathrm{n}}. \tag{B.9}$$

Note that the last term of Eq. (B.6), originating from the left-hand side of the equation, is in the discrete-time case taken at the current time instant, as the output for scheduling the next state offset $\breve{\boldsymbol{q}}$ is unavailable at time step k.

B.2. LPV FORWARD PROPAGATION MATRICES

This section defines the LPV forward-propagation matrices of Eq. (4.35):

$$\boldsymbol{Y}_{k+1} = \begin{bmatrix} y_{k+1} \\ y_{k+2} \\ \vdots \\ y_{k+N_p} \end{bmatrix}, \; \breve{\boldsymbol{Y}}_{k+1}(\mathbf{P}_k) = \begin{bmatrix} \breve{y}(\boldsymbol{p}_{\mathrm{k+1}}) \\ \breve{y}(\boldsymbol{p}_{\mathrm{k+2}}) \\ \vdots \\ \breve{y}(\boldsymbol{p}_{\mathrm{k+N_p}}) \end{bmatrix}, \; \Delta\boldsymbol{U}_k(\mathbf{P}_k) = \begin{bmatrix} u_k - \breve{u}(\boldsymbol{p}_{\mathrm{k}}) \\ u_{k+1} - \breve{u}(\boldsymbol{p}_{\mathrm{k+1}}) \\ \vdots \\ u_{k+\mathrm{N_p}-1} - \breve{u}(\boldsymbol{p}_{\mathrm{k+N_p-1}}) \end{bmatrix}$$

$$\mathbf{H}(\mathbf{P}_k) = \begin{bmatrix} C(\boldsymbol{p}_{k+1})A(\boldsymbol{p}_k) \\ C(\boldsymbol{p}_{k+2})A(\boldsymbol{p}_{k+1})A(\boldsymbol{p}_k) \\ \vdots \\ C(\boldsymbol{p}_{\mathrm{k+N_p}})A(\boldsymbol{p}_{k+\mathrm{N_p}-1})\dots A(\boldsymbol{p}_k) \end{bmatrix}, \quad \Delta\breve{\boldsymbol{X}}_k(\mathbf{P}_k) = \begin{bmatrix} \breve{x}(\boldsymbol{p}_{\mathrm{k}}) - \breve{x}(\boldsymbol{p}_{\mathrm{k+1}}) \\ \breve{x}(\boldsymbol{p}_{\mathrm{k+1}}) - \breve{x}(\boldsymbol{p}_{\mathrm{k+2}}) \\ \vdots \\ \breve{x}(\boldsymbol{p}_{\mathrm{k+N_p-1}}) - \breve{x}(\boldsymbol{p}_{\mathrm{k+N_p}}) \end{bmatrix},,$$

$$\mathbf{S}(\mathbf{P}_k) = \begin{bmatrix} C(\boldsymbol{p}_{k+1})B(\boldsymbol{p}_k) & 0 & \dots & 0 \\ C(\boldsymbol{p}_{k+2})A(\boldsymbol{p}_{k+1})B(\boldsymbol{p}_k) & C(\boldsymbol{p}_{k+2})B(\boldsymbol{p}_{k+1}) & \dots & 0 \\ \vdots & & \ddots & \vdots \\ C(\boldsymbol{p}_{\mathrm{k+N_p}})A(\boldsymbol{p}_{\mathrm{k+N_p-1}})\dots A(\boldsymbol{p}_{k+1})B(\boldsymbol{p}_k) & \cdots & & C(\boldsymbol{p}_{\mathrm{k+N_p}})B(\boldsymbol{p}_{\mathrm{k+N_p-1}}) \end{bmatrix},$$

$$\mathbf{L}(\mathbf{P}_k) = \begin{bmatrix} C(\boldsymbol{p}_{k+1}) & 0 & \dots & 0 \\ C(\boldsymbol{p}_{k+2})A(\boldsymbol{p}_{k+1}) & C(\boldsymbol{p}_{k+2}) & \dots & 0 \\ \vdots & & \ddots & \vdots \\ C(\boldsymbol{p}_{\mathrm{k+N_p}})A(\boldsymbol{p}_{k+\mathrm{N_p}-1})\dots A(\boldsymbol{p}_{k+1}) & \cdots & & C(\boldsymbol{p}_{\mathrm{k+N_p}}) \end{bmatrix},$$

$$\mathbf{D}(\mathbf{P}_k) = \begin{bmatrix} D(\boldsymbol{p}_{k+1}) & 0 & \cdots & 0 \\ 0 & D(\boldsymbol{p}_{k+2}) & \cdots & 0 \\ \vdots & & \ddots & \vdots \\ 0 & \cdots & & D(\boldsymbol{p}_{k+N_p}) \end{bmatrix}$$

C

THE DOT HYDRAULIC WIND TURBINE

C.1. DEFINITION OF HYDRAULIC INDUCTION, RESISTANCE AND CAPACITANCE

Hydraulic induction. The hydraulic induction L_H resembles the ease of acceleration of a fluid volume and is related to the fluid inertia I_f by

$$L_\mathrm{H} = f_\mathrm{c} I_\mathrm{f} = f_\mathrm{c} \frac{\rho L_\mathrm{l}}{A}, \tag{C.1}$$

with the assumption that the flow speed profile is radially uniform (Akers et al., 2006). For this reason, a distinction should be made between laminar and turbulent flows in circular lines: the induction of a laminar flow is generally corrected by a factor $f_\mathrm{c} = 4/3$, whereas a turbulent flow does not need correction with respect to the fluid inertia I_f (Bansal, 1989).

Hydraulic resistance. The hydraulic resistance dissipates energy from a flow in the form of a pressure decrease over a hydraulic element. In most cases, hydraulic resistances are taken as an advantage by means of control valves. For example, by adjusting a valve set point, one adjusts the resistance to a desired value. Mathematically, the hydraulic resistance relates the flow rate to the corresponding pressure drop,

$$\Delta p_\mathrm{R} = Q R_\mathrm{H}, \tag{C.2}$$

analogous to an electrical circuit in which the voltage over a resistive element equals the current times the resistance. The hydraulic resistance for a hydraulic line with a circular cross section and a laminar flow is

$$R_\mathrm{H,l} = \frac{8\mu L_\mathrm{l}}{\pi r_\mathrm{l}^4}, \tag{C.3}$$

which is a constant term independent of the flow rate. For a turbulent fluid flow, the computation of the resistance is more involved and results in a quantity that is dependent on the flow rate and effective pipe roughness. For simulation purposes this would require reevaluation of the resistance in each time step or for each operating point during linear analysis. Such a nonlinear time-variant (NLTV) system is employed in (Buhagiar et al., 2016), updating the resistive terms in each iteration for a hydraulic variable-displacement drivetrain with seawater under turbulent conditions.

Hydraulic capacitance. Because of fluid compressibility and line elasticity, the amount of fluid can change as a result of pressure changes in a control volume. The effective bulk modulus K_f of a fluid is defined by the pressure increase to the relative decrease in the volume:

$$dp = K_\mathrm{f}\frac{dV}{V_\mathrm{H}}, \qquad K_\mathrm{f} = V_\mathrm{H}\frac{dp}{dV}. \tag{C.4}$$

The equivalent bulk modulus (Merritt, 1967) of a compressible fluid without vapor or entrapped air in a flexible line with bulk modulus K_l is defined as

$$K_\mathrm{e} = \left(\frac{1}{K_\mathrm{f}} + \frac{1}{K_\mathrm{l}}\right)^{-1}. \tag{C.5}$$

Subsequently, the pressure change with respect to time is

$$\dot{p} = \frac{dp}{dt} = K_\mathrm{e}\frac{1}{V_\mathrm{H}}\frac{dV}{dt} = \frac{K_\mathrm{e}}{V_\mathrm{H}}Q = \frac{1}{C_\mathrm{H}}Q, \tag{C.6}$$

and thus the hydraulic capacitance C_H is directly proportional to the volume amount and gives the pressure change according to a net flow variation into a control volume.

C.2. MODEL DERIVATION OF A HYDRAULIC CONTROL VOLUME

For modeling the dynamics of a volume in a hydraulic line, analogies between mechanical and hydraulic systems are employed for convenience. First, the differential equation for a standard mass–damper–spring system driven by an external force F is given by

$$F = m\ddot{x} + c\dot{x} + kx. \tag{C.7}$$

For conversion to a hydraulic equivalent expression, the driving mechanical force is substituted by $F = \Delta pA$, the control volume mass is taken as $m = \rho V_\mathrm{H} = \rho AL_\mathrm{l}$, and the fluid inflow velocity defined as $\dot{x} = Q/A$. By rearranging terms, one obtains

$$\Delta p = \frac{\rho L_\mathrm{l}}{A}\dot{Q} + \frac{c}{A^2}Q + \frac{k}{A^2}\int Q dt, \tag{C.8}$$

which is further simplified into

$$\Delta p = L_\mathrm{H}\dot{Q} + R_\mathrm{H}Q + \frac{1}{C_\mathrm{H}}\int Q dt, \tag{C.9}$$

where L_H, R_H and C_H are the hydraulic induction, resistance, and capacitance (Esposito, 1969), respectively, and are defined in Appendix C.1. The former two of these three quantities depends on the flow Reynolds number, which shows whether the inertial or viscosity terms are dominant in the Navier–Stokes equations (Merritt, 1967). The Reynolds number is defined as

$$Re = \frac{D_\mathrm{l} v \rho}{\mu}, \tag{C.10}$$

where $D_\mathrm{l} = 2r_\mathrm{l}$ is the line diameter, and μ the fluid dynamic viscosity. For Reynolds numbers larger than 4000 the flow is considered as turbulent and the inertial terms are dominant, whereas for values smaller than 2300 the viscosity terms are deemed dominant.

For evaluation of the natural frequency ω_n and damping coefficient ζ for the considered system, the characteristic equation by neglecting the external excitation force ($\Delta p = 0$) is defined as

$$0 = \dot{Q} + \frac{R_\mathrm{H}}{L_\mathrm{H}} Q + \frac{1}{C_\mathrm{H} L_\mathrm{H}} \int Q dt \tag{C.11}$$

$$= \dot{Q} + 2\zeta\omega_\mathrm{n} Q + \omega_\mathrm{n}^2 \int Q dt. \tag{C.12}$$

Evaluating the quantities ω_n and ζ results in

$$\omega_\mathrm{n} = \sqrt{\frac{1}{C_\mathrm{H} L_\mathrm{H}}}, \tag{C.13}$$

$$\zeta_\mathrm{p} = \frac{R_\mathrm{H}}{2} \sqrt{\frac{C_\mathrm{H}}{L_\mathrm{H}}}. \tag{C.14}$$

The inverse result of Equation (C.9) is obtained (Murrenhoff, 2012), with flow Q as the external excitation and Δp as output:

$$Q = C_\mathrm{H} \Delta\dot{p} + \frac{1}{R_\mathrm{H}} \Delta p + \frac{1}{L_\mathrm{H}} \int \Delta p dt. \tag{C.15}$$

Now by evaluating the characteristic equation

$$0 = C_\mathrm{H} \Delta\dot{p} + \frac{1}{R_\mathrm{H}} \Delta p + \frac{1}{L_\mathrm{H}} \int \Delta p dt \tag{C.16}$$

$$= \Delta\dot{p} + \frac{1}{R_\mathrm{H} C_\mathrm{H}} \Delta p + \frac{1}{L_\mathrm{H} C_\mathrm{H}} \int \Delta p dt, \tag{C.17}$$

and using Equation (C.12), it is seen that the natural frequency remains unchanged with the result obtained in Equation (C.13), but the definition of the damping coefficient changes:

$$\zeta_\mathrm{Q} = \frac{1}{2R_\mathrm{H}} \sqrt{\frac{L_\mathrm{H}}{C_\mathrm{H}}}. \tag{C.18}$$

Finally, the differential equation defined by Equation (C.9) is expressed as a transfer function in

$$G_{\mathrm{Q}/\Delta\mathrm{p}}(s) = \frac{1/L_{\mathrm{H}}}{s + (R_{\mathrm{H}}/L_{\mathrm{H}}) + 1/(C_{\mathrm{H}}L_{\mathrm{H}}s)} \tag{C.19}$$

$$= \frac{s/L_{\mathrm{H}}}{s^2 + (R_{\mathrm{H}}/L_{\mathrm{H}})s + 1/(C_{\mathrm{H}}L_{\mathrm{H}})}, \tag{C.20}$$

and the same is done for Equation (C.15):

$$G_{\Delta\mathrm{p}/\mathrm{Q}}(s) = \frac{1/C_{\mathrm{H}}}{s + 1/(R_{\mathrm{H}}C_{\mathrm{H}}) + 1/(C_{\mathrm{H}}L_{\mathrm{H}}s)} \tag{C.21}$$

$$= \frac{s/C_{\mathrm{H}}}{s^2 + 1/(R_{\mathrm{H}}C_{\mathrm{H}})s + 1/(C_{\mathrm{H}}L_{\mathrm{H}})}. \tag{C.22}$$

BIBLIOGRAPHY

Akers, A., M. Gassman, and R. Smith (2006). *Hydraulic power system analysis*. Boca Raton, Florida: CRC press.

Al'tshul', A. D. and M. S. Margolin (1968). "Effect of vortices on the discharge coefficient for flow of a liquid through an orifice". In: *Hydrotechnical Construction* 2.6.

Artemis Intelligent Power (2018). `http://www.artemisip.com/sectors/wind/`. (last access: 6 September 2018).

Bak, C., F Zahle, R. Bitsche, T. Kim, A. Yde, L. Henriksen, P. Andersen, A. Natarajan, and M. Hansen (2013). "Design and performance of a 10 MW wind turbine". In: *Wind Energy*.

Bansal, R. (1989). *A Text Book of Fluid Mechanics and Hydraulic Machines: In MKS and SI Units*. New Delhi, India: Laxmi publications.

Bertelè, M., C. L. Bottasso, S. Cacciola, F. Daher Adegas, and S. Delport (2017). "Wind inflow observation from load harmonics". In: *Wind Energy Science* 2.2.

Bianchi, F. D., H. De Battista, and R. J. Mantz (2006). *Wind turbine control systems: principles, modelling and gain scheduling design*. Springer Science & Business Media.

Bir, G. (2008a). *User's Guide to MBC3*. NREL.

Bir, G. (2008b). "Multi-blade coordinate transformation and its application to wind turbine analysis". In: *46th AIAA Aerospace Sciences Meeting and Exhibit*.

Blaikie, D (2007). *Clayton windmills in Sussex, England*. `https://commons.wikimedia.org/w/index.php?curid=4039564`.

Borenstein, S. (2014). "With their mark on Earth, humans may name era, too". In: *AP News*. URL: `https://apnews.com/c999a20fb7114f818c0398c0e40720ab`.

Bos, R., M. Zaaijer, S. P. Mulders, and J. W. van Wingerden (2019). *FASTTool*. `https://github.com/TUDelft-DataDrivenControl/FASTTool`.

Bosch-Rexroth (2012). *Axial Piston Variable Motor A6VM - Sales information/Data sheet*. Tech. rep. Bosch-Rexroth.

Bossanyi, E. A. (2000). "The design of closed loop controllers for wind turbines". In: *Wind Energy* 3.3.

Bossanyi, E. A. (2003a). "Wind turbine control for load reduction". In: *Wind Energy* 6.3.

Bossanyi, E. A., P Wright, and P. A. Fleming (2010). *Controller field tests on the NREL CART2 turbine*. Tech. rep. NREL/TP-5000-49085. Golden, Colorado: National Renewable Energy Laboratory (NREL).

Bossanyi, E. (2003b). "Individual blade pitch control for load reduction". In: *Wind Energy* 6.2.

Bossanyi, E. and D. Witcher (2009). *Controller for 5MW reference turbine*. Tech. rep. Upwind.

Bossanyi, E. A., P. Fleming, and A. Wright (2012). "Field test results with individual pitch control on the NREL CART3 wind turbine". In: *50th AIAA Aerospace Sciences Meeting* *including the New Horizons Forum and Aerospace Exposition.* American Institute of Aeronautics and Astronautics (AIAA).

Bossanyi, E. A., P. A. Fleming, and A. D. Wright (2013). “Validation of individual pitch control by field tests on two-and three-bladed wind turbines”. In: *IEEE Transactions on Control Systems Technology (CST)* 21.4.

Bragg, S. (1960). “Effect of compressibility on the discharge coefficient of orifices and convergent nozzles”. In: *Journal of Mechanical Engineering Science* 2.1.

Brekke, H. (2001). *Hydraulic turbines: design, erection and operation.* Trondheim, Norway: Norwegian University of Science and Technology (NTNU).

Buhagiar, D., T. Sant, and M. Bugeja (2016). “A comparison of two pressure control concepts for hydraulic offshore wind turbines”. In: *Journal of Dynamic Systems, Measurement, and Control* 138.8.

Burton, T., N. Jenkins, D. Sharpe, and E. A. Bossanyi (2001). *Wind energy handbook.* Chichester, United Kingdom: John Wiley & Sons.

Cabrera, E., V. Espert, and F. Martínez (2015). *Symposium on Hydraulic Machinery and Cavitation.* Berlin, Germany: Springer.

Chapple, P, O. Dahlhaug, and P. Haarberg (2011). “Turbine driven electric power production system and a method for control thereof”. Pat. US007863767B2.

Cisneros, P. S., S. Voss, and H. Werner (2016). “Efficient nonlinear model predictive control via quasi-LPV representation”. In: *55th Conference on Decision and Control (CDC).* IEEE.

Dahleh, M., M. A. Dahleh, and G. Verghese (2011). *Lectures on Dynamic Systems and Control - Chapter 12 - Modal Decomposition of State-Space Models.* `https://ocw.mit.edu/courses/electrical-engineering-and-computer-science/6-241j-dynamic-systems-and-control-spring-2011/readings/MIT6_241JS11_chap12.pdf`. [Online; accessed 07-May-2019].

Department of Energy (DOE) (2015). *Levelized Cost of Energy (LCOE).* Presentation.

Diepeveen, N. F. B. (2013). “On the application of fluid power transmission in offshore wind turbines”. PhD thesis. Delft, The Netherlands: Delft University of Technology.

Diepeveen, N. F. B. and A Jarquin-Laguna (2014). “Wind tunnel experiments to prove a hydraulic passive torque control concept for variable speed wind turbines”. In: *Journal of Physics: Conference Series.* Vol. 555. IOP Publishing.

Diepeveen, N. F. B., S. P. Mulders, and J. van der Tempel (2018). “Field tests of the DOT500 prototype hydraulic wind turbine”. In: *11th International Fluid Power Conference.* Aachen.

Disario, G. (2018). “On the effects of an azimuth offset in the MBC-transformation used by IPC for wind turbine fatigue load reductions”. MA thesis. Delft University of Technology.

DNV-GL (2017). *Bladed.* `https://www.dnvgl.com/energy/generation/software/bladed/index.html`. [Online; accessed 14-November-2017].

DNV GL (2019). *Bladed.* `https://www.dnvgl.com/services/wind-turbine-design-software-bladed-3775`.

DTU Wind Energy (2019). *BasicDTUController.* `https://gitlab.windenergy.dtu.dk/OpenLAC/BasicDTUController`.

DTU wind energy (2019). *HAWC2 (Horizontal Axis Wind turbine simulation Code 2nd generation)*. http://www.hawc2.dk/hawc2-info.

Dykes, K., R. Damiani, O. Roberts, and E. Lantz (2018). *Analysis of ideal towers for tall wind applications*. Tech. rep. NREL/CP-5000-70642. https://www.nrel.gov/docs/fy18osti/70642.pdf. Golden, Colorado: National Renewable Energy Laboratory (NREL).

Esposito, A (1969). "A simplified method for analyzing hydraulic circuits by analogy". In: *Machine Design* 41.24.

Evans, M. A., M. Cannon, and B. Kouvaritakis (2015). "Robust MPC tower damping for variable speed wind turbines". In: *IEEE Transactions on Control Systems Technology (CST)* 23.1.

EWEA (2009). *The economics of wind energy*. Brussels, Belgium: EWEA.

Fingersh, L, M Hand, and A Laxson (2006). *Wind turbine design cost and scaling model*. Tech. rep. Golden, Colorado: National Renewable Energy Lab (NREL).

Fischer, T (2006). *Integrated Wind Turbine Design - Final report Task 4.1*. Tech. rep. Project UpWind.

Freebury, G. and W. D. Musial (2000). *Determining equivalent damage loading for full-scale wind turbine blade fatigue tests*. Tech. rep. Golden, Colorado: National Renewable Energy Laboratory (NREL).

Garcia, D., A. Karimi, and R. Longchamp (2005). "PID controller design for multivariable systems using Gershgorin bands". In: *IFAC Proceedings Volumes* 38.1.

Garrad Hassan. *Bladed 4.50*. (last access: 2019-07-01).

Garrad Hassan & Partners Ltd (2011). *Bladed User Manual*. Version 4.2.

Geels, F. W., B. K. Sovacool, T. Schwanen, and S. Sorrell (2017). "Sociotechnical transitions for deep decarbonization". In: *Science* 357.6357.

General Electric Renewable Energy (2019). *Haliade-X offshore wind turbine platform*. https://www.ge.com/renewableenergy/wind-energy/offshore-wind/haliade-x-offshore-turbine.

Germanischer Lloyd (2012). *Guideline for the certification of offshore wind turbines*. Germanischer Lloyd: renewables certification.

Geyler, M and P Caselitz (2007). "Individual blade pitch control design for load reduction on large wind turbines". In: *European Wind Energy Conference (EWEC)*.

Godfrey, K. (1993). *Perturbation signals for system identification*. Prentice Hall International (UK) Ltd.

Grant, M. and S. Boyd (2008). "Graph implementations for nonsmooth convex programs". In: *Recent Advances in Learning and Control*. Lecture Notes in Control and Information Sciences. http://stanford.edu/~boyd/graph_dcp.html. Springer-Verlag Limited.

Grant, M. and S. Boyd (2014). *CVX: Matlab Software for Disciplined Convex Programming, version 2.1*. http://cvxr.com/cvx. [Online; accessed 07-May-2019].

Gregory, R. (2005). *The industrial windmill in Britain*. Phillmore & Company, Limited.

Hägglunds (2015). *Compact CB - Product Manual*. Bosch Rexroth. Lohr am Main, Germany.

Hanema, J (2018). “Anticipative model predictive control for linear parameter-varying systems”. PhD thesis. Eindhoven, The Netherlands: Technische Universiteit Eindhoven.

Hansen, M. H. (2004). “Aeroelastic stability analysis of wind turbines using an eigenvalue approach”. In: *Wind Energy* 7.2.

Hansen, M. H. and L. C. Henriksen (2013). “Basic DTU wind energy controller”. In: *DTU Wind Energy*.

Hau, E. (2013). *Wind turbines: fundamentals, technologies, application, economics*. Berlin, Germany: Springer Science & Business Media.

Ho, W. K., T. H. Lee, and O. P. Gan (1997). “Tuning of Multiloop Proportional- Integral-Derivative Controllers Based on Gain and Phase Margin Specifications”. In: *Industrial and Engineering Chemistry Research*.

Holkar, K. and L. Waghmare (2010). “An overview of model predictive control”. In: *International Journal of Control and Automation* 3.4.

Hours, J.-H., M. N. Zeilinger, R. Gondhalekar, and C. N. Jones (2015). “Constrained spectrum control”. In: *IEEE Transactions on Automatic Control* 60.7.

Houtzager, I., J. W. van Wingerden, and M. Verhaegen (2013). “Wind turbine load reduction by rejecting the periodic load disturbances”. In: *Wind Energy* 16.2.

Hovgaard, T. G., S. Boyd, and J. B. Jørgensen (2015). “Model predictive control for wind power gradients”. In: *Wind Energy* 18.6.

Hružík, L., M. Vašina, and A. Bureček (2013). “Evaluation of bulk modulus of oil system with hydraulic line”. In: *EPJ Web of Conferences*. Vol. 45. EDP Sciences. Les Ulis, France.

IEC (2005). *IEC 61400-1 Third Edition 2005-08: Wind turbines - Part 1: Design requirements*. Tech. rep. International Electrotechnical Commission (IEC).

Jager, S. (2017). “Control Design and Data-Driven Parameter Optimization for the DOT500 Hydraulic Wind Turbine”. Master Thesis. Delft University of Technology.

Jain, A., E. Biyik, and A. Chakrabortty (2015). “A model predictive control design for selective modal damping in power systems”. In: *American Control Conference (ACC)*. American Control Conference (ACC). IEEE.

Jamieson, P. and G. Hassan (2011). *Innovation in wind turbine design*. Wiley Online Library.

Jarquin Laguna, A (2017). “Centralized electricity generation in offshore wind farms using hydraulic networks”. PhD thesis. Delft University of Technology.

Jelavić, M., V. Petrović, and N. Perić (2010). “Estimation based individual pitch control of wind turbine”. In: *Automatika* 51.2.

Johnson, W. (2012). *Helicopter theory*. Courier Corporation.

Jonkman, J., S. Butterfield, W. Musial, and G. Scott (2009). *Definition of a 5-MW reference wind turbine for offshore system development*. Tech. rep. Golden, Colorado: National Renewable Energy Laboratory (NREL).

KAMAT (2016). *Quintuplex Plunger Pump K80000-5G*. `https://www.kamat.de/en/plunger-pumps/k-80000-5g.html`. (last access: 6 September 2018).

Kempenaar, A. (2012). “Small Scale Fluid Power Transmission for the Delft Offshore Turbine”. MA thesis. Delft University of Technology.

Keyvani, A, M. S. Tamer, J.-W. van Wingerden, J. F. L. Goosen, and F Keulen (2019). “A comprehensive model for transient behavior of tapping mode atomic force microscope”. In: *Nonlinear Dynamics* 97.2.

Knudsen, T., T. Bak, and M. Soltani (2011). “Prediction models for wind speed at turbine locations in a wind farm”. In: *Wind Energy* 14.7.

Kooijman, H. J. T., C Lindenburg, D Winkelaar, and E. L. Van der Hooft (2003). “DOWEC 6 MW pre-design”. In: *Energy Research Center of the Netherlands (ECN)*.

Kotzalas, M. N. and G. L. Doll (2010). “Tribological advancements for reliable wind turbine performance”. In: *Philosophical Transactions of the Royal Society of London A: Mathematical, Physical and Engineering Sciences* 368.1929.

Kragh, K. and P. Fleming (2012). “Rotor Speed Dependent Yaw Control of Wind Turbines Based on Empirical Data”. In: *AIAA Aerospace Sciences Meeting* 1018.

Lahey, T. M. and T. Ellis (1994). *Fortran 90 programming*. Addison-Wesley Longman Publishing Co., Inc.

Larsen, T. J., H. A. Madsen, and K. Thomsen (2005). “Active load reduction using individual pitch, based on local blade flow measurements”. In: *Wind Energy* 8.1.

Leithead, W. E. and S. Dominguez (2005). “Controller design for the cancellation of the tower fore-aft mode in a wind turbine”. In: *44th Conference on Decision and Control (CDC)*. IEEE.

Liu, X, R Ortega, H Su, and J Chu (2009). “Identification of nonlinearly parameterized nonlinear models: application to mass balance systems”. In: *48h Conference on Decision and Control (CDC)*. IEEE.

Ljung, L. (1999). *System Identification: Theory for the User*. Prentice Hall.

Lu, Q, R Bowyer, and B. L. Jones (2015). “Analysis and design of Coleman transform-based individual pitch controllers for wind-turbine load reduction”. In: *Wind Energy* 18.8.

Maciejowski, J. (1989). *Multivariable Feedback Design*. Addison-Wesley.

Malcolm, D. J. and A. C. Hansen (2006). *WindPACT Turbine Rotor Design Study: June 2000 - June 2002 (Revised)*. Tech. rep. Golden, Colorado: National Renewable Energy Laboratory (NREL).

Manwell, J. F., J. G. McGowan, and A. L. Rogers (2010). *Wind energy explained: theory, design and application*. John Wiley & Sons.

MathWorks (2019). *Linear Parameter-Varying Models*. `https://mathworks.com/help/control/ug/linear-parameter-varying-models.html`. [Online; accessed 07-May-2019].

MathWorks (2019). *MATLAB / Simulink*. `https://www.mathworks.com`.

MathWorks (2019). *Symbolic Math Toolbox*. `https://mathworks.com/products/symbolic.html`. [Online; accessed 07-May-2019].

Menezes, E. J. N., A. M. Araújo, and N. S. B. da Silva (2018). “A review on wind turbine control and its associated methods”. In: *Journal of Cleaner Production* 174.

Merritt, H. E. (1967). *Hydraulic control systems*. Hoboken, New Jersey: John Wiley & Sons.

MHI - Mitsubishi Heavy Industries, Ltd. *SeaAngel 7 MW*. `https://www.mhi.com/`.

Mulders, S. P. (2015). “Iterative feedback tuning of feedforward IPC for two-bladed wind turbines: A comparison with conventional IPC”. MA thesis. Delft University of Technology.

Mulders, S. P. and J. W. van Wingerden (2018). "Delft Research Controller: an open-source and community-driven wind turbine baseline controller". In: *Journal of Physics: Conference Series*. Vol. 1037. 3. IOP Publishing.

Mulders, S. P. and J. W. van Wingerden (2019a). *Delft Research Controller (DRC)*. `https://github.com/TUDelft-DataDrivenControl/DRC_Fortran`.

Mulders, S. P. and J. W. van Wingerden (2019b). "On the importance of the azimuth offset in a combined 1P and 2P SISO IPC implementation for wind turbine fatigue load reductions". In: *American Control Conference (ACC)*. ACC / IFAC-ACE.

Mulders, S. P., N. F. B. Diepeveen, and J. W. van Wingerden (2018a). "Control design and validation for the hydraulic DOT500 wind turbine". In: *11th International Fluid Power Conference*. Aachen, Germany: RWTH Aachen University.

Mulders, S. P., N. F. B. Diepeveen, and J. W. van Wingerden (2018b). *Data set: Control design, implementation and evaluation for an in-field 500 kW wind turbine with a fixed-displacement hydraulic drivetrain*.

Mulders, S. P., A. K. Pamososuryo, G. E. Disario, and J. W. van Wingerden (2019a). "Analysis and optimal individual pitch control decoupling by inclusion of an azimuth offset in the multiblade coordinate transformation". In: *Wind Energy* 22.3.

Mulders, S. P., T. G. Hovgaard, J. D. Grunnet, and J.-W. van Wingerden (2019b). *Software implementation: Preventing wind turbine tower natural frequency excitation with a quasi-LPV model predictive control scheme (Version 1.0). Zenodo*. `http://doi.org/10.5281/zenodo.2672956`. [Online; accessed 07-May-2019].

Murrenhoff, H. (2012). *Grundlagen der Fluidtechnik: Teil 1: Hydraulik*. Herzogenrath, Germany: Shaker Verlag.

National Renewable Energy Loboratory (NREL) (2019). *FAST changelog*. `https://wind.nrel.gov/nwtc/docs/FAST_ChangeLog.txt`.

Navalkar, S. T., J. W. van Wingerden, E. Van Solingen, T Oomen, E Pasterkamp, and G. Van Kuik (2014). "Subspace predictive repetitive control to mitigate periodic loads on large scale wind turbines". In: *Mechatronics* 24.8.

Nelson, V. (2013). *Wind energy: renewable energy and the environment*. Ed. by A. Ghassemi. CRC press.

Nijssen, J. P. A., N. F. B. Diepeveen, and A. S. Kempenaar (2018). "Development of an interface between a plunger and an eccentric running track for a low-speed seawater pump". In: *11th International Fluid Power Conference*. Aachen, Germany: RWTH Aachen University.

NREL (2020). *ROSCO. Version 1.0.0*. URL: `https://github.com/NREL/rosco`.

NWTC (2019). *OpenFAST*. `http://openfast.readthedocs.io`. [Online; accessed 14-November-2017].

NWTC Information Portal (2014). *BModes*. `https://nwtc.nrel.gov/BModes`.

NWTC Information Portal (2015). *MLife*. `https://nwtc.nrel.gov/MLife`.

NWTC Information Portal (2016). *TurbSim*. `https://nwtc.nrel.gov/TurbSim`.

NWTC Information Portal (2019). *FAST v8.16*. `https://nwtc.nrel.gov/FAST8`. [Online; accessed 27-August-2019].

O'Brien, K. (2018). "Is the 1.5 degrees Celsius target possible? Exploring the three spheres of transformation". In: *Current Opinion in Environmental Sustainability* 31.

Oppenheim, A. V. (1999). *Discrete-time signal processing*. Pearson Education India.

Oppenheim, A., A. Willsky, and S. Nawab (2013). *Signals and Systems*. Pearson.
O'Rourke, C. J., M. M. Qasim, M. R. Overlin, and J. L. Kirtley (2019). "A Geometric Interpretation of Reference Frames and Transformations: dq0, Clarke, and Park". In: *IEEE Transactions on Energy Conversion* 34.4.
Ortega, R., F. Mancilla David, and F. Jaramillo (2013). "A globally convergent wind speed estimator for wind turbine systems". In: *International Journal of Adaptive Control and Signal Processing* 27.5.
Østergaard, K. Z., P. Brath, and J. Stoustrup (2007). "Estimation of effective wind speed". In: *Journal of Physics: Conference Series*. Vol. 75. Bristol, United Kingdom: IOP Publishing.
Pachauri, R. and L. Meyer (2014). "Climate Change 2014: Synthesis Report. Contribution of Working Groups I, II and III to the Fifth Assessment Report of the Intergovernmental Panel on Climate Change". In: *Intergovernmental Panel on Climate Change (IPCC)*.
Pao, L. Y. and K. E. Johnson (2009). "A tutorial on the dynamics and control of wind turbines and wind farms". In: *American Control Conference (ACC)*. St. Louis, Missouri.
Pao, L. Y. and K. E. Johnson (2011). "Control of wind turbines". In: *IEEE Control Systems* 31.2.
Pedersen, N. H., P. Johansen, and T. O. Andersen (2018). "Optimal control of a wind turbine with digital fluid power transmission". In: *Nonlinear Dynamics* 91.1.
Petrović, V., M. Jelavić, and M. Baotić (2015). "Advanced control algorithms for reduction of wind turbine structural loads". In: *Renewable Energy* 76.
Philander, S. G. (2008). *Encyclopedia of global warming and climate change*. Sage.
Piña Rodriguez, I. (2012). "Hydraulic drivetrains for wind turbines: Radial piston digital machines". MA thesis. Delft University of Technology.
Polinder, H., J. A. Ferreira, B. B. Jensen, A. B. Abrahamsen, K. Atallah, and R. A. McMahon (2013). "Trends in wind turbine generator systems". In: *IEEE Journal of Emerging and Selected Topics in Power Electronics* 1.3.
Putnam, P. C. (1947). *Power from the wind*. Van Nostrand Reinhold.
Ragheb, A. and M. Ragheb (2010). "Wind turbine gearbox technologies". In: *International Nuclear & Renewable Energy Conference (INREC)*. Piscataway, New Jersey: IEEE.
Rampen, W. (2006). "Gearless transmissions of large wind turbines-the history and future of hydraulic drives". In: *Artemis IP Ltd., Midlothian, UK*.
Rawlings, J. B., D. Angeli, and C. N. Bates (2012). "Fundamentals of economic model predictive control". In: *51st Conference on Decision and Control (CDC)*. IEEE.
Rawlings, J. B. and D. Q. Mayne (2009). *Model predictive control: Theory and design*. Nob Hill Pub. Madison, Wisconsin.
REpower (2004). REpower - Proven technology in new dimensions. Hamburg, Germany.
Rijksoverheid (2018). *Nuon krijgt vergunning voor windpark zonder subsidie*. `https://www.rijksoverheid.nl/actueel/nieuws/2018/03/19/nuon-krijgt-vergunning-voor-windpark-zonder-subsidie`. [Online; accessed 1 August 2019].
Rijksoverheid (2019a). "Klimaatakkoord". In: *Rijksoverheid*.
Rijksoverheid (2019b). *Windenergie op zee*. `https://www.rijksoverheid.nl/onderwerpen/duurzame-energie/windenergie-op-zee`. [Online; accessed 1 August 2019].

Risoe National Laboratory (2004). *Recommendations for design of offshore wind turbines (RECOFF)*. `https://cordis.europa.eu/project/rcn/54147`.

Rockström, J (2018). *Are we racing towards Earth's 'Hothouse' tipping point?* `https://www.leonardodicaprio.org/are-we-racing-towards-earths-hothouse-tipping-point/`.

Rockström, J., O. Gaffney, J. Rogelj, M. Meinshausen, N. Nakicenovic, and H. J. Schellnhuber (2017). "A roadmap for rapid decarbonization". In: *Science* 355.6331.

Rodriguez, A. G., A. G. Rodríguez, and M. B. Payán (2007). "Estimating wind turbines mechanical constants". In: *International Conference on Renewable Energies and Power Quality (ICREPQ)*. Vigo, Spain: EA4EPQ.

Rosenbrock, H. (1970). *State-Space and Multivariable Theory*. Thomas Nelson & Sons Ltd.

Rosenbrock, H. H. and D. Owens (1976). "Computer aided control system design". In: *IEEE Transactions on Systems, Man, and Cybernetics* 11.

Rybak, S. (1981). "Description of the 3 MW SWT-3 wind turbine at San Gorgonio Pass California". In: *Wind Energy Conference and Workshop (WW5)*. Vol. 1. San Gorgonio Pass, California: Bendix Corporation Energy, Environment and Technology Office.

Salter, S and M Rea (1984). "Hydraulics for Wind". In: *European Wind Energy Conference (EWEC)*.

Sasaki, M., A. Yuge, T. Hayashi, H. Nishino, M. Uchida, and T. Noguchi (2014). "Large capacity hydrostatic transmission with variable displacement". In: *9th International Fluid Power Conference (IFK)*. Vol. 9. Aachen, Germany: RWTH Aachen University.

Schlipf, D., D. J. Schlipf, and M. Kühn (2013). "Nonlinear model predictive control of wind turbines using LIDAR". In: *Wind energy* 16.7.

Schmitz, J., N. F. B. Diepeveen, N Vatheuer, and H. Murrenhoff (2012). "Dynamic transmission response of a hydrostatic transmission measured on a test bench". In: *EWEA 2012*. Copenhagen, Denmark: EWEA.

Schmitz, J., M. Vukovic, and H. Murrenhoff (2013). "Hydrostatic transmission for wind turbines: An old concept, new dynamics". In: *Symposium on Fluid Power and Motion Control*. Sarasota, Florida: ASME.

Schorbach, V. and P. Dalhoff (2012). "Two bladed wind turbines: antiquated or supposed to be resurrected". In: *European Wind Energy Association (EWEA)*.

SciPy.org (2017). *Interpolation (scipy.interpolate.RegularGridInterpolator)*. (last access: 1 July 2017).

Selvam, K., S. Kanev, J. W. van Wingerden, T. van Engelen, and M. Verhaegen (2009). "Feedback-feedforward individual pitch control for wind turbine load reduction". In: *International Journal of Robust and Nonlinear Control: IFAC-Affiliated Journal* 19.1.

Shampine, L. F., R. C. Allen, and S. Pruess (1997). *Fundamentals of numerical computing*. New York, United States: John Wiley & Sons.

Shan, M., J. Jacobsen, and S. Adelt (2013). "Field testing and practical aspects of load reducing pitch control systems for a 5 MW offshore wind turbine". In: *European Wind Energy Association (EWEA)*.

Sheng, S. (2013). *Report on Wind Turbine Subsystem Reliability – A Survey of Various Databases*. Tech. rep. NREL/PR-5000-59111. Golden, Colorado: National Renewable Energy Laboratory (NREL).

Sieros, G., P. Chaviaropoulos, J. D. Sørensen, B. H. Bulder, and P. Jamieson (2012). "Upscaling wind turbines: theoretical and practical aspects and their impact on the cost of energy". In: *Wind Energy* 15.1.

Silva, P., A. Giuffrida, N. Fergnani, E. Macchi, M. Cantù, R. Suffredini, M. Schiavetti, and G. Gigliucci (2014). "Performance prediction of a multi-MW wind turbine adopting an advanced hydrostatic transmission". In: *Energy* 64.

Skaare, B., B Hörnsten, and F. G. Nielsen (2011). "Energy considerations for wind turbines with hydraulic transmission systems". In: *European Offshore Wind Conference & Exhibition (EOW)*. 2. Amsterdam, The Netherlands.

Skaare, B., B. Hörnsten, and F. G. Nielsen (2013). "Modeling, simulation and control of a wind turbine with a hydraulic transmission system". In: *Wind Energy* 16.8.

Skogestad, S. and I. Postlethwaite (2007). *Multivariable feedback control: analysis and design*. Wiley New York.

Smulders, P. T., S Orbons, and C Moes (1984). "Aerodynamic interaction between two wind rotors set next to each other in one plane". In: *European Wind Energy Conference (EWEC)*.

Soltani, M. N., T. Knudsen, M. Svenstrup, R. Wisniewski, P. Brath, R. Ortega, and K. Johnson (2013). "Estimation of rotor effective wind speed: A comparison". In: *IEEE Transactions on Control Systems Technology* 21.4.

Spencer, M. D., K. A. Stol, C. P. Unsworth, J. E. Cater, and S. E. Norris (2013). "Model predictive control of a wind turbine using short-term wind field predictions". In: *Wind Energy* 16.3.

Spinato, F., P. J. Tavner, G. J. W. V. Bussel, and E. Koutoulakos (2009). "Reliability of wind turbine subassemblies". In: *IET Renewable Power Generation* 3.4.

Steffen, W. et al. (2018). "Trajectories of the Earth System in the Anthropocene". In: *Proceedings of the National Academy of Sciences* 115.33.

Stewart, J (2009). *Calculus - Early Transcedentals 6E*. Brooks/Cole.

Tavner, P. J., J Xiang, and F Spinato (2007). "Reliability analysis for wind turbines". In: *Wind Energy* 10.1.

Thake, J. (2000). *The micro-hydro Pelton turbine manual*. Practical Action Publishing. ISBN: 978-1-85339-460-7.

Thomsen, K. E., O. Dahlhaug, M. Niss, and S. Haugset (2012). "Technological advances in hydraulic drive trains for wind turbines". In: *Energy Procedia* 24.

Tofighi, E., D. Schlipf, and C. M. Kellett (2015). "Nonlinear model predictive controller design for extreme load mitigation in transition operation region in wind turbines". In: *Conference on Control Applications (CCA)*. IEEE.

Trostmann, E. (1995). *Water hydraulics control technology*. Boca Raton, Florida: CRC Press.

Umaya, M., T. Noguchi, M. Uchida, M. Shibata, Y. Kawai, and R. Notomi (2013). "Wind power generation-development status of offshore wind turbines". In: *Mitsubishi Heavy Industries Technical Review* 50.3.

Ungurán, R., S. Boersma, V. Petrović, J. W. van Wingerden, L. Y. Pao, and K. Martin (2019). "Feedback-feedforward individual pitch control design with uncertain measurements". In: *American Control Conference (ACC)*.

van der Hooft, E. and T. van Engelen (2004). “Estimated wind speed feed forward control for wind turbine operation optimisation”. In: *European Wind Energy Conference (EWEC)*. ECN-RX–04-126. ECN. London, United Kingdom.

van der Laan, M. P. et al. (2019). “Power curve and wake analyses of the Vestas multi-rotor demonstrator”. In: *Wind Energy Science* 4.2.

van der Tempel, J and D. P. Molenaar (2002). “Wind Turbine Structural Dynamics - A Review of the Principles for Modern Power Generation, Onshore and Offshore”. In: *Wind Engineering* 26.4.

van der Tempel, J. (2009). “Energy extraction system, has water pump attached to rotor, windmill for pumping water from sea, water system connected to water pump, for passing water pumped from sea, and generator connected to water system,” pat.

van Kuik, G., B. Ummels, and R. Hendriks (2008). “Perspectives on wind energy”. In: *Sustainable Energy Technologies*. Springer.

van Solingen, E, J Beerens, S. P. Mulders, R De Breuker, and J. W. van Wingerden (2016a). “Control design for a two-bladed downwind teeterless damped free-yaw wind turbine”. In: *Mechatronics* 36.

van Solingen, E., P. A. Fleming, A. Scholbrock, and J. W. van Wingerden (2016b). “Field testing of linear individual pitch control on the two-bladed controls advanced research turbine”. In: *Wind Energy* 19.3.

van Wingerden, J. W. (2018). *PBSID-Toolbox*. `https://github.com/jwvanwingerden/PBSID-Toolbox`.

Vestas (2016). *Vestas multi rotor concept demonstrator at Riso*. `https://www.vestas.com/~/media/files/multirotorfactsheet.pdf`.

Vukovic, M. and H. Murrenhoff (2015). “The Next Generation of Fluid Power Systems”. In: *Procedia Engineering* 106.

Waters, C. N. et al. (2016). “The Anthropocene is functionally and stratigraphically distinct from the Holocene”. In: *Science* 351.

White, F. M. (2011). *Fluid Mechanics*. 7th ed. New York: McGraw-Hill.

WindEurope (2019). *Wind energy in Europe in 2018 – Trends and statistics*. Tech. rep. Brussels, Belgium: WindEurope.

Wright, A. D. and M. J. Balas (2004). “Design of controls to attenuate loads in the controls advanced research turbine”. In: *Journal of Solar Energy Engineering* 126.4.

Wright, A. D. (2004). *Modern control design for flexible wind turbines*. Tech. rep. Golden, Colorado: National Renewable Energy Laboratory (NREL).

Wright, A. D., P. Fleming, and J.-W. van Wingerden (2011). “Refinements and tests of an advanced controller to mitigate fatigue loads in the controls advanced research turbine”. In: 49th American Institute of Aeronautics and Astronautics (AIAA).

Zhang, Z. (2007). “Flow interactions in Pelton turbines and the hydraulic efficiency of the turbine system”. In: *Institution of Mechanical Engineers, Part A: Journal of Power and Energy* 221.3. London, United Kingdom.

LIST OF ABBREVIATIONS

AEP	Annual Energy Production
BEM	Blade-Element Momentum
BO	Bayesian Optimization
CART	Control Advanced Research Turbine
CPC	Collective Pitch Control
DEL	Damage Equivalent Load
DNA	Direct Nyquist Array
DOE	Department of Energy
DOT	Delft Offshore Turbine
DOWEC	Dutch Offshore Wind Energy Converter
dq0	direct-quadrature-zero
DRC	Delft Research Controller
DTU	Technical University of Denmark
FAST	Fatigue, Aerodynamics, Structures, and Turbulence
FRF	Frequency-Response Function
GBN	Generalized Binary Noise
GE	General Electric
GM	Gain Margin
GUI	Graphical User Interface

HAWT	Horizontal Axis Wind Turbine
I&I	Immersion and Invariance
IEC	International Electrotechnical Commission
IPC	Individual Pitch Control
LCOE	Levelized Cost Of Energy
LIDAR	Light Detection and Ranging
LQG	Linear-Quadratic-Gaussian
LPV	Linear Parameter-Varying
LSS	Low-Speed Shaft
LTI	Linear Time-Invariant
MBC	Multiblade Coordinate
MHI	Mitsubishi Heavy Industries
MIMO	Multiple-Input Multiple-Output
MPC	Model Predictive Control
***n*P**	n-times-per-revolution
NLTV	Nonlinear Time-Variant
NREL	National Renewable Energy Laboratory
NWTC	National Wind Technology Center
NMPC	Nonlinear Model Predictive Control
PBSID	Predictor-Based-Subspace-IDentification
PCD	Pitch Circle Diameter
PI	Proportional Integral
PID	Proportional Integral Derivative

PM	Phase Margin
PMG	Permanent Magnet Generator
PSS	Power System Stabilizers
PV	Photovoltaic
qLPV	quasi-Linear Parameter-Varying
QP	Quadratic Program
RBS	Random Binary Signal
RC	Repetitive Control
RECOFF	Recommendations for Design of Offshore Wind Turbines
RGA	Relative Gain Array
RMPC	Robust Model Predictive Control
RWT	Reference Wind Turbine
SDFT	Selective Discrete Fourier Transform
SISO	Single-Input Single-Output
STFT	Short-Time Fourier Transform
SVD	Singular Value Decomposition
TM-AFM	Tapping Mode-Atomic Force Microscopy
TSR	Tip-Speed Ratio
UNFCC	United Nations Framework Convention on Climate Change
VS-VP	Variable-Speed Variable-Pitch
WindPACT	Wind Partnerships for Advanced Component Technology

Curriculum Vitæ

Sebastiaan Paul Mulders was born on the 28^{th} of January, 1991 in IJmuiden, municipality of Velsen, the Netherlands. He went to secondary school with classical education and languages, and received a double degree by the combination of *Nature & Technology* and *Nature & Health* educational profiles.

Directly after graduation from high school in 2009, he started his bachelor in Mechanical Engineering at the Delft University of Technology. During his bachelor studies, he did a minor in Applied Sciences, a final project on graphene growth, and joined the Formula Student engineering team. After receiving the bachelor's degree in 2013, he started his master in Systems and Control. Two years later, he graduated on data-driven and adaptive control methods for two-bladed wind turbines.

In January 2016, Sebastiaan started his PhD project in cooperation with Delft Offshore Turbine (DOT), under supervision of prof. dr. ir. Jan-Willem van Wingerden and dr. ir. Niels Diepeveen. The initial focus of the project was on the controller design for a DOT turbine with hydraulic drivetrain. The research results were later that year successfully implemented on a real-world prototype demonstrator. In later stages of the PhD, the emphasis shifted towards control advances for fatigue load mitigations, and the development of (educational) control software.

Throughout his PhD he published 5 articles in renowned scientific journals, and 10 conference papers at international conferences, where he spoke as a presenting author. He assisted in the MSc courses *Signal Analysis* and *Wind Turbine Design*, and supervised 7 master students in their graduation project. Furthermore, he developed and taught a self-produced Scientific Python course, and patented a novel predictive load preventing control strategy for large wind turbines. During the different educational phases, he simultaneously ran an IT consultancy company, providing services to business and private customers.

List of Publications

Journal publications

S.P. Mulders, T.G. Hovgaard, J.D. Grunnet and J.W. van Wingerden. Preventing wind turbine tower natural frequency excitation with a quasi-LPV model predictive control scheme. *Wind Energy*, 23(3), 2020 (in this thesis)

J.A. Frederik, B.M. Doekemeijer, S.P. Mulders and J.W. van Wingerden. The helix approach: using dynamic individual pitch control to enhance wake mixing in wind farms. Submitted to: *Wind Energy*, 2019

S.P. Mulders, A.K. Pamososuryo, G.E. Disario and J.W. van Wingerden. Analysis and optimal individual pitch control decoupling by inclusion of an azimuth offset in the multiblade coordinate transformation. *Wind Energy*, 22(3), 2019 (in this thesis)

S.P. Mulders, N.F.B. Diepeveen and J.W. van Wingerden. Control design, implementation, and evaluation for an in-field 500 kW wind turbine with a fixed-displacement hydraulic drivetrain. *Wind Energy Science*, 3(2), 2018 (in this thesis)

E. van Solingen, S.P. Mulders and J.W. van Wingerden. Iterative feedback tuning of wind turbine controllers. *Wind Energy Science*, 2(1), 2017

E. van Solingen, J. Beerens, S.P. Mulders, R. de Breuker and J.W. van Wingerden. Control design for a two-bladed downwind teeterless damped free-yaw wind turbine. *Mechatronics*, 36, 2016

Patents

S.P. Mulders, J.W. van Wingerden, T.G. Hovgaard and J.D. Grunnet. Structural vibration mitigation using model based control. PA 2019 70248, 2019

Conference papers

S.P. Mulders, A.K. Pamososuryo and J.W. van Wingerden. Efficient tuning of Individual Pitch Control: A Bayesian Optimization Machine Learning approach. In *The Science of Making Torque from Wind (TORQUE)*, Delft, Netherlands, 2020

S.P. Mulders, M.B. Zaaijer, R. Bos and J.W. van Wingerden. Wind turbine control: open-source software for control education, standardization and compilation. In *NAWEA/WindTech*, Amherst, Massachusetts, USA, 2019 (in this thesis)

S.P. Mulders and J.W. van Wingerden. On the importance of the azimuth offset in a combined 1P and 2P SISO IPC implementation for wind turbine fatigue load reductions. In *American Control Conference (ACC)*, Philadelphia, Pennsylvania, USA, 2019 (in this thesis)

N. Moustakis, S.P. Mulders, J. Kober and J.W. van Wingerden. A Practical Bayesian Optimization Approach for the Optimal Estimation of the Rotor Effective Wind Speed. In *American Control Conference (ACC)*, Philadelphia, Pennsylvania, USA, 2019

S.P. Mulders, N.F.B. Diepeveen and J.W. van Wingerden. Extremum Seeking Control for optimization of a feed-forward Pelton turbine speed controller in a fixed-displacement hydraulic wind turbine concept. In *WindEurope*, Bilbao, Spain, 2019

S.P. Mulders and J.W. van Wingerden. On the averaging in the multi-blade coordinate transformations for wind turbines: an $\mathscr{H}_\infty$ model matching approach. In *Conference on Control Technology and Applications (CCTA)*, Copenhagen, Denmark, 2018

S.P. Mulders and J.W. van Wingerden. Delft Research Controller: An open-source and community-driven wind turbine baseline controller. In *The Science of Making Torque from Wind (TORQUE)*, Milan, Italy, 2018 (in this thesis)

S.P. Mulders, N.F.B. Diepeveen and J.W. van Wingerden. Control design and validation for the hydraulic DOT500 wind turbine. In *International Fluid Power Conference (IFK)*, Aachen, Germany, 2018 (in this thesis)

N.F.B. Diepeveen, S.P. Mulders and J. van der Tempel. Field tests of the DOT500 prototype hydraulic wind turbine. In *International Fluid Power Conference (IFK)*, Aachen, Germany, 2018

S.P. Mulders, S. Jager, N.F.B. Diepeveen and J.W. van Wingerden. Control design and optimization for the DOT500 hydraulic wind turbine. In *Wind Energy Science Conference (WESC)*, Copenhagen, Denmark, 2017 (in this thesis)

S.P. Mulders, E. van Solingen, J.W. van Wingerden and J. Beerens. Iterative tuning of feedforward IPC for two-bladed wind turbines. In *The Science of Making Torque from Wind (TORQUE)*, Munich, Germany, 2016